

THESIS ON NATURAL AND EXACT SCIENCES B237

**High-Accuracy Reference Standards
for Quantitative Two-Photon
Absorption Spectroscopy**

SOPHIE DE REGUARDATI DI CASTELFRANCO



TALLINN UNIVERSITY OF TECHNOLOGY

School of Science
Department of Cybernetics
Division of Physics

This dissertation was accepted for the defense of the degree of Doctor of Philosophy in Engineering Physics on June 30th, 2017

Supervisor : Prof. Aleksander Rebane, Department of Chemical Physics, National Institute of Chemical Physics and Biophysics, Tallinn, Estonia

Opponents: Dr. Arnulf Rosspeinter, Department of Physical Chemistry, University of Geneva, Switzerland

Dr. Koit Muring, Institute of Physics, University of Tartu, Estonia

Defense: August 17th 2017, 11:00 am

Room U02-102

Tallinn University of Technology, Ehitajate tee 5, Tallinn

Declaration:

Hereby I declare that this doctoral thesis, my original investigation and achievement, submitted for the doctoral degree at Tallinn University of Technology has not been submitted for doctoral or equivalent academic degree.

Sophie de Reguardati



REPUBLIC OF ESTONIA
MINISTRY OF EDUCATION
AND RESEARCH



© Sophie de Reguardati, 2017

ISSN 1406-4723

ISBN 978-9949-83-136-4 (publication)

ISBN 978-9949-83-137-1 (PDF)

LOODUS- JA TÄPPISTEADUSED B237

**Kõrgtäpsusega standardid
kvantitatiivses kahefootonses
neeldumisspektroskoopias**

SOPHIE DE REGUARDATI DI CASTELFRANCO

TABLE OF CONTENTS

LIST OF PUBLICATIONS	8
LIST OF ABBREVIATIONS AND SYMBOLS.....	9
1 INTRODUCTION.....	11
2 THEORETICAL CONSIDERATIONS.....	14
2.1 Main concepts of one and multiphoton absorption	14
2.2 Relation between absorption cross-section and molecular dipole moments	17
2.2.1 Semi-classical approach	17
2.2.2 1PA probability, transition dipole moment and oscillator strength.....	20
2.2.3 2PA probability and permanent dipole moment	23
2.2.4 Parity selection rule for one- and two-photon transition....	25
2.3 Sum-over-states (SOS) versus few-essential-states (FES) model.....	26
2.3.1 Dipolar contribution to SOS.....	27
2.3.2 Origin of permanent electric dipole moment in organic chromophores	27
2.3.3 FES model	30
2.4 Emerging applications for two-photon absorption	33
2.4.1 Possibility of tight 3D-localized excitation.....	33
2.4.2 Deeper tissue penetration due to lower scattering of near-infrared (NIR).....	35
2.4.3 Limiting maximum photon flux for eye- and sensor protection.....	36
2.5 Overview of experimental techniques for measuring absolute 2PA cross section in organic chromophores	39
2.5.1 Direct Methods	39
2.5.2 Indirect Methods	46
2.6 Selection of an experimental technique for measuring absolute cross-section with higher precision	47

2.6.1	Comparison of the experimental technique to optimize control of the 2PA phenomena.....	47
2.6.2	Absolute 2PA cross-section determination using a modified 2PIF method	49
2.6.3	Determining 2PA cross-section of an unknown fluorophore using 2PIF reference standard method	51
2.7	Current state of the art of 2PA reference standards.....	52
3	AIM OF THE STUDY	55
4	ESTABLISHING TWO-PHOTON ABSORPTION STANDARDS IN THE 680 - 1050 NM RANGE	56
4.1	Experimental set-up for measuring absolute 2PA cross-section using 2PIF method	56
4.2	Evaluation and selection of fluorophore/solvent systems suitable as 2PA standards	61
4.3	Protocol for higher accuracy measurements of the absolute 2PA cross-section.....	65
4.3.1	Sample preparation and procedure for extinction coefficient determination.....	65
4.3.2	Procedure for evaluating the excitation beam parameters .	68
4.3.3	Procedure for 1PA and 2PA fluorescence signals determination.....	72
4.4	Verification of 2PA spectral shape obtained from an independent experiment.....	76
4.5	Determination of the maximum absolute cross-section for each standards.....	78
4.6	Confirmation of the fidelity of the established standard 2PA cross-section spectra.....	80
5	SOME APPLICATIONS OF THE NEW STANDARDS	86
5.1	Estimation of the permanent dipole moment change in the lowest-energy electronic transition	86
5.2	Determination of 6MI dipole moment change by measuring its 2PA cross-section using reference standards	89
	CONCLUSION	93
	ABSTRACT	94

KOKKUVÕTE.....	95
REFERENCES.....	96
ACKNOWLEDGEMENTS	105
CURRICULUM VITAE	106
ELULOOKIRJELDUS.....	107
APPENDICES.....	109
APPENDIX A: Saturation effect in 2PA absorption	111
APPENDIX B: Temporal pulse broadening through optics	115
APPENDIX C: Determination of magnification factor	125
APPENDIX D: Auto-correlator calibration for measuring the pulse temporal profile	129
APPENDIX E: Beam profile at various wavelengths.....	133
APPENDIX F: Molecular structure of reference standards	137
APPENDIX G: 2PA shape function comparison between independent 2PIF measurements	141
APPENDIX H: Absorption spectra of reference standards	147
APPENDIX I: Pair-wise comparison of 2PA cross-section.....	155
APPENDIX J: Publication I.....	159
APPENDIX K: Publication II	175
APPENDIX L: Publication III	193

LIST OF PUBLICATIONS

The present doctoral thesis is based on the following papers, which are referred to in the text by their Roman numerals:

- I** de Reguardati, S., Pahapill, J., Mikhailov, A., Stepanenko, Y. and Rebane, A., “High-accuracy reference standards for two-photon absorption in the 680-1050 nm wavelength range”, *Opt. Express* 24(8), 9053-9066 (2016).

- II** de Reguardati, S., Pahapill, J., Rammo, M. and Rebane, A., “Improving the fidelity of two-photon absorption reference standards”, *Proc. SPIE 10094* (2017).

- III** Mikhaylov, A., Lindquist, J. R., Callis, P. R., Kohler, B., Pahapill, J., de Reguardati, S., Rammo, M., Uudsemaa, M., Trummal, A. and Rebane, A., “Femtosecond two-photon absorption spectra and permanent electric dipole moment change of tryptophan, 2-aminopurine and related intrinsic and synthetic fluorophores”, *Proc. SPIE 10069* (2017).

AUTHOR’S OWN CONTRIBUTION

- I** Selection and evaluation of suitable fluorophores, testing and optimizing the set-up for measuring the absolute two-photon cross-section with high accuracy, carrying out the experiment, analysis of the results and a major part of writing the paper.

- II** Establishing the protocol for cross-checking of the standards, carrying out the experiments, analysis of the data and writing the paper.

- III** Carrying out the experiment on the characterization of the fluorescent-base analog to guanine, analysis of the results.

LIST OF ABBREVIATIONS AND SYMBOLS

KBFI	Keemilise ja Bioloogilise Füüsika Instituut or National Institute of Chemical Physics and Biophysics
MSU	Montana State University
1PA	One-photon absorption
2PA	Two-photon absorption
ESA	Excited-state absorption
OPL	Optical-power limiting
2PIF	Two-photon induced fluorescence
SOS	Sum-over-states
FES	Few-essential-states
IR	Infrared
UV	Ultraviolet
FWHM	Full width at half maximum
HOMO	Highest occupied molecular orbital
LUMO	Lowest unoccupied molecular orbital
cw	Continuous wave
DCM	Dichloromethane
DMSO	Dimethylsulfoxide
BDBAS	4,4'-bis(di-n-butylamino)stilbene
BDPAS	4,4'-bis(diphenylamino)-stilbene
AF455	7,7',7''-(1,3,5-triazine-2,4,6-triyl)tris[9,9-didecyl-N,N-diphenyl 9H-Fluoren-2-amine
THF	Tetrahydrofuran
MeTHF	2-methyltetrahydrofuran
Rh 6G	Rhodamine 6G
C153	Coumarin 153
MetOH	Methanol
Φ	Photon flux (number of photons per unit area and time)
c	Velocity of light in vacuum

h	Planck's constant
N_a	Avogadro constant
μ_0	Vacuum permeability
ϵ_0	Vacuum permittivity
e	Elementary charge
α	Fine structure constant
ν	Frequency
ω	Angular frequency
λ	Wavelength
σ_{nPA}	n-photon absorption cross-section
N_g	Population density in the ground state
N_f	Population density in the final excited state
C	Concentration
ϵ	Extinction coefficient or molecular absorptivity
n	Refractive index
$\vec{\mu}$	Electric dipole moment
z_R	Rayleigh length
w_0	Beam waist
T	Transmittance
I	Intensity or irradiance
F	Fluorescence signal
ϵ_r	Dielectric constant
W	Laser average power
Q	Quantum yield
ϕ	Differential quantum yield
g_P	Shape factor

1 INTRODUCTION

The process of instantaneous two-photon absorption (2PA) was first predicted by Maria Goeppert-Mayer in 1931 [3], who theoretically considered quantum-mechanical probability of a transition from ground electronic state to an excited electronic state via simultaneous absorption of two photons, where the transition energy equals the combined energy of the two photons. Her pioneering work provided an estimate of the peak 2PA cross section of a typical optical absorber, $\sigma_{2PA} = 10^{-50} \text{ cm}^4 \text{ s photon}^{-1}$. This value is now broadly adopted as a convenient unit (GM) of the 2PA efficiency in organic chromophores as many common organic molecules have a 2PA cross-section in the range of 0.1-10 GM. Molecules specifically designed to be highly efficient two-photon absorbers can present considerably higher values, typically in the 10^3 - 10^5 GM range such as dendrimers[4] and squaraines [5]. In contrast to one-photon absorption (1PA), where the transition probability scales linearly with the photon flux (number of incident photons per unit area per unit time), the rate of 2PA increases as the square of the photon flux. Because σ_{2PA} is generally rather small, in order to achieve practical efficiency, i.e. a two-photon transition rate comparable to that of 1PA, one would need a high photon flux, on the order of $10^{30} \text{ photon cm}^{-2} \text{ s}^{-1}$. Regular photon-emitters such as incandescent lamps have relatively low irradiance. The capability to produce sufficiently high optical intensity became available only after the invention of the laser. For this reason, the first observation of 2PA was reported only in 1961 by W. Kaiser and C. G. Garret [6], who used a pulsed ruby laser to illuminate a crystal of CaF_2 containing luminescent Eu^{2+} ions. This pioneering experiment also confirmed the so-called parity selection rule, according to which, in systems with inversion symmetry, two-photon transitions are allowed only between states of equal parity. This property is now widely used to investigate excited levels that are forbidden in one-photon absorption.

Due to proliferation of high-intensity lasers, especially wavelength-tunable femtosecond lasers, which became broadly available about 25 years ago, the utility of 2PA has grown from a mere scientific curiosity into a thriving field of research and applications, covering as diverse areas as biological microscopy [7-15], two-photon photodynamic therapy [16-24] and photonic materials processing e.g. three-dimensional (3D) ultrahigh density optical data storage [25-29], 3D microfabrication [34-39], optical power limiting [35-38].

Driven by expanding uses of 2PA, many new molecular systems performing 2PA with increasing efficiency were designed and tested [39-40]. However, quantitative characterization of the molecular σ_{2PA} and its dependence on the excitation laser wavelength is still posing practical issues. This is because accurate determination of σ_{2PA} requires precise knowledge of the photon flux, which is prone to considerable experimental uncertainty in pulsed laser. Consequently, the residual experimental errors in 2PA spectroscopy remain

large, often exceeding 20-50 %. There are also lingering discrepancies between results reported by different laboratories and/or using different measurement techniques. These problems are exacerbated in situations where the excitation photon wavelength needs to be varied in broad range of wavelengths, such as in the case of local electric field measurement [41-42]. A convenient solution, for at least some of these issues, consists in referencing the 2PA measurements with respect to so-called reference standards, where the σ_{2PA} spectra have been previously accurately characterized. Such “calibration” reduces the technical cost associated with often tedious laser characterization, thus reducing variability in the 2PA measurements and potentially opening up 2PA measurement abilities for labs with even simple laser equipment. The idea of two-photon standards emerged in 1996 [43] by Xu et al., then was resumed in 2008 by Makarov et al. [44], who established absolute two-photon cross-section spectra for 15 different fluorescent systems with estimated accuracy of $\sim 20\%$. However, this level of accuracy is often inadequate and our goal is to improve the 2PA standards in term of accuracy and choice of fluorophores, e.g. more stable in a larger concentration range.

Improving the accuracy of two-photon standards will lead to better agreement between 2PA measurement results obtained from experiments performed under different conditions, as well as more effective calibration of fluorophores in multi-photon microscopy. Higher accuracy is perhaps most critical in the emerging field of quantitative 2PA spectroscopy, which has the potential of measuring the strength of intra- and intermolecular electric fields, by taking advantage of the relation between σ_{2PA} and the change of permanent electric dipole moment upon transition from the ground state to an excited states [42]. Furthermore, to verify different models that express σ_{2PA} in terms of molecular parameters, accurate quantitative measurements are a necessity.

In this thesis, we aim to establish calibrated absolute reference standards for 2PA with improved accuracy, better than 10%, by careful characterization of the photon flux that effectively excites the sample, estimate the number of molecules excited and the efficiency of the fluorescence detection. Once this is accomplished, one can measure the 2PA of any other chromophore by comparison with one suitable standard. The thesis follows almost the chronological order of the past 4 years of work.

In section 2, we introduce the main concepts of 2PA. We will derive formulas that relate the 2PA cross-section of a chromophore to its molecular parameters. We highlight few practical advantages of 2PA and how they are used in the emerging applications of two-photon absorption. We will discuss what can be achieved in term of two-photon standards and which experimental methodology is the most suitable for our objectives. After the experimental methodology selection, we establish the theoretical bases of our experimental set-up and review the current state of the art of 2PA reference standards.

Section 3 summarizes our motivation and lays out the approach that we have taken in this project.

In section 4, we present our set of 10 fluorescent standards, covering the 680 – 1050 nm excitation range and with fluorescence in the visible region. We will describe our experimental set-up and the methodology for carrying-out an absolute two-photon experiment. We will explain how to optimize the experiments, in term of solution concentration, tracking the quadraticity of the 2PA fluorescence signal, and how we treated the data to gain in precision. We will point out how we post-confirmed our absolute cross-section spectra by cross-checking our data.

In section 5 we analyze some of the measured 2PA in term of permanent dipole change and also, as an example of application of the standards, we determine the 2PA cross-section spectrum of a fluorescent probe, which can replace guanine in DNA.

2 THEORETICAL CONSIDERATIONS

2.1 Main concepts of one and multiphoton absorption

From a microscopic point of view, an atom or a molecule can be excited through the absorption of light. In one-photon absorption (1PA), the photon energy, with frequency ν (and wavelength λ), matches the energy difference between the ground state and the excited state,

$$h\nu = \frac{hc}{\lambda} = E, \quad (1)$$

where h is the Planck's constant, c is the velocity of light and E is the transition energy.

The excitation may also occur by simultaneous absorption of multiple photons, whose energy adds up to the energy of the excited compound

$$\sum h\nu_i = E, \quad (2)$$

For instance, in case of two-photon absorption (2PA):

$$h\nu_1 + h\nu_2 = E. \quad (3)$$

In a degenerate case with a pure monochromatic source, the two photons have the exact same frequency ν ,

$$2h\nu = E. \quad (4)$$

Comparison between 1PA transition (blue arrow) and degenerate 2PA transition (two red arrows) from the ground state S_0 to the first excited state S_1 is shown in Figure 1. Note that here we assume that the molecule has no inversion symmetry, and thus the same state can be reached by 1PA and 2PA.

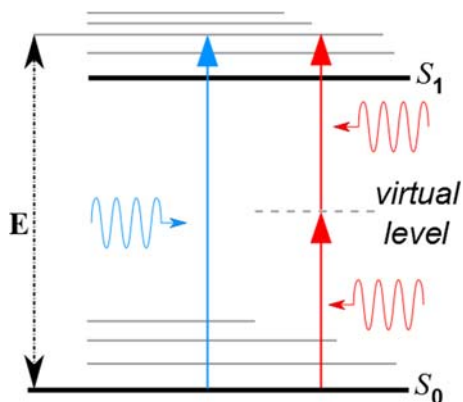


Figure 1: Scheme of 1PA (blue vertical arrow) and 2PA (red vertical arrows) in an energetic description of a molecule. Grey lines correspond to vibrational levels associated with a pure electronic level (black line). Dashed line – virtual intermediate state.

The 2PA is a simultaneous or instantaneous event in the sense that there are no real intermediate energy levels that are populated in this process. This effect is to be distinguished from stepwise absorption, in which case there are real intermediate levels involved that are populated at some point in time. The 2PA takes place through a so-called virtual intermediate level [45], exact meaning of which will be elucidated later in this thesis. Since there is no real intermediate eigenstates involved, the law of energy conservation seems violated. However, Heisenberg's principle states that uncertainty in the energy of the virtual state ΔE_v can be very large during a very short time interval τ_v : $\Delta E_v \tau_v \geq \hbar$, so that the law of energy conservation is relaxed during very short times. In fact, we may estimate the lifetime of the virtual state from the energy mismatch, ΔE_v , between the transition energy and the photon energy. For example, if the lowest transition energy is 3.1 eV, and the absorbed photon energy is 1.55 eV, with the corresponding wavelength 800 nm, then the energy mismatch is $\Delta E_v = 1.55$ eV corresponding to a virtual state lifetime $\tau_v \approx 4 \times 10^{-16}$ s, which is on the order of one wave oscillation period. During that short time, which is sometimes associated with the lifetime of the virtual state, a second photon can be absorbed to satisfy energy conservation.

From a macroscopic point of view, the attenuation of a monochromatic light beam propagating through an absorbing medium can be described by a phenomenological expansion series,

$$\frac{d\Phi_t}{dz} = -\sigma_{1PA}N_g\Phi_t - \sigma_{2PA}N_g\Phi_t^2 - \sigma_{3PA}N_g\Phi_t^3 - \dots, \quad (5)$$

where Φ_t is the photon flux through the sample (number of photons per unit area and time), z is the propagation distance in the medium, σ_{nPA} is the degenerated absorption of n photons cross section, and N_g is the population density in the ground state (number of molecules per unit of volume).

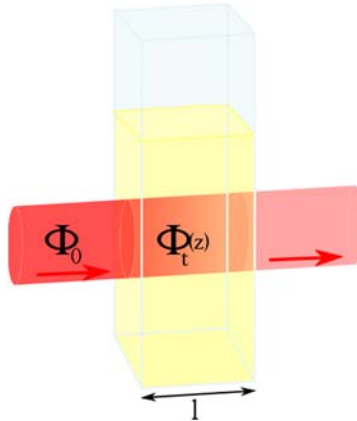


Figure 2: Propagation of a collimated monochromatic beam through an absorbing solution in an optical cuvette.

The first term of the expansion series correspond to the 1PA process, the second term to the 2PA, the third term to the 3PA etc.

In most cases, these different absorption processes occur at different wavelengths, which mean that, for the photon flux, each term of the expansion series can be treated separately. The first term gives the equation:

$$\frac{d\Phi_t}{dz} = -\sigma_{1PA}N_g\Phi_t, \quad (6)$$

and leads to the well-known Beer-Lambert's law of linear extinction

$$\Phi_t(z) = \Phi_0 e^{-\sigma_{1PA}N_g z}, \quad (7)$$

where Φ_0 is the incoming collimated photon flux, i.e. before the beam enters the absorbing solution as shown in Figure 2. The 1PA cross-section characterizes the molecule's ability to absorb one photon, with angular frequency ω , at a time and is related to the so called molecular extinction coefficient ϵ_{1PA} through

$$\sigma_{1PA}(\omega) = \ln(10) \frac{\epsilon_{1PA}(\omega)}{N_a}, \quad (8)$$

where N_a is the Avogadro constant. For example, typical organic fluorophores such as a coumarin or a rhodamine dye possess peak extinction coefficient values, $\epsilon_{1PA} \sim 10,000 \text{ cm}^{-1} \text{ M}^{-1}$ and $\sim 100,000 \text{ cm}^{-1} \text{ M}^{-1}$, respectively, which translates into corresponding peak absorption cross sections of, $\sigma_{1PA} = 10^{-20} \text{ cm}^2$ and 10^{-19} cm^2 .

The second term in (5) leads to the equation:

$$\frac{d\Phi_t}{dz} = -\sigma_{2PA}N_g\Phi_t^2. \quad (9)$$

The 2PA cross-section is expressed in $\text{cm}^4 \text{ s photon}^{-1}$ and is rather small so the value are usually presented in GM unit, where $1 \text{ GM} = 10^{-50} \text{ cm}^4 \text{ s photon}^{-1}$. For instance, coumarin dyes typically present maximum value for 2PA cross-section on the order of, $\sigma_{2PA} \sim 10 \text{ GM}$, while 2PA maximum in rhodamines may be an order of magnitude larger, $\sigma_{2PA} \sim 100 \text{ GM}$. Some specially designed 2-photon enhanced chromophores such as squaraines [5], conjugated dendrimers [4] and some tetrapyrroles [46] may reach $\sigma_{2PA} \sim 10^3 - 10^5 \text{ GM}$. But even so, to achieve a 2PA transition probability that is comparable to that of 1PA transition probability, one needs a very high photon flux

$$\Phi_0 \cong \sigma_{1PA}/\sigma_{2PA} \cong 10^{28} - 10^{30} \text{ photon cm}^{-2} \text{ s}^{-1}. \quad (10)$$

Currently, the most practical way to reach such high photon flux values is by using mode-locked lasers producing ultrashort pulses. For example, consider a femtosecond mode-locked Ti:Sapphire laser operating at 800 nm wavelength that has pulse duration 100 fs, and pulse repetition rate of 100 MHz. If the beam is focused to a nearly diffraction-limited spot of 1 μm in diameter, then average power of 10 mW will produce photon flux on the order of $10^{27} \text{ photon cm}^{-2} \text{ s}^{-1}$, which roughly corresponds to the excitation parameters typically used in two-photon microscopes [7, 15].

Solution of Equation (9) gives the following expression for the photon flux as a function of the propagation distance z

$$\Phi_t(z) = \frac{\Phi_0}{1+z\sigma_{2PA}N_g\Phi_0}. \quad (11)$$

Because beam attenuation caused by 2PA is usually quite small, Equation (11) can be in turn expanded in a series as:

$$\Phi_t(z) \approx \Phi_0 - z\sigma_{2PA}N_g\Phi_0^2. \quad (12)$$

Another alternative way to describe 2PA strength used in literature is in terms of so-called the 2PA coefficient β , which is related to our definition of the absorption cross section as

$$\beta = \frac{\sigma_{2PA}N_gN_a}{h\nu}, \quad (13)$$

2.2 Relation between absorption cross-section and molecular dipole moments

2.2.1 Semi-classical approach

Here we are going to derive relations that express the absorption cross-section in terms of microscopic parameters, such as molecular transition frequencies and molecular dipole moments. We will be using semi-classical theory of light-matter interaction, where the medium is composed of atoms or molecules, which is described by the theory of quantum mechanics, while the light is described by the classical Maxwell theory. This approach is commonly applied to a variety of non-linear optical phenomena, and is also used in this thesis to describe the properties of 2PA transitions in organic chromophores.

Let \hat{H}_0 represent the stationary Hamiltonian operator of the unperturbed, isolated molecule. Stationary energy eigenfunctions $u_n^0(\vec{r})$, satisfy the equation,

$$\hat{H}_0 u_n^0(\vec{r}) = E_n u_n^0(\vec{r}), \quad (14)$$

where, $E_n = \hbar\omega_n$, is the n^{th} eigenstate energy and ω_n is the corresponding angular frequency. Functions $u_n^0(\vec{r})$ form a complete set of orthonormal solutions.

For the type of organic chromophores considered here, the by far largest contribution to the interaction energy between light and the absorber stems from the electric component of the oscillating field and the electric dipole of the chromophore. All higher-order interaction terms, such as electric quadrupole and magnetic dipole are much smaller in value, and will be neglected. For simplicity, we consider a monochromatic plane-polarized wave, propagating in positive z -axis direction. The amplitude of the electric field is:

$$\vec{E}(t) = E \cos(kz - \omega t)\vec{e}, \quad (15)$$

where k is the propagation constant, \vec{e} is the unit polarization vector ($\vec{e} \cdot \vec{e} = 1$), ω is angular frequency and E the amplitude. For a planar wave in a non-magnetic medium, the electric polarization vector \vec{e} and magnetic polarization vector \vec{b} are mutually perpendicular, and are also perpendicular with respect to the propagation vector:

$$\vec{B}(t) = B \cos(kz - \omega t)\vec{b} \text{ and } \vec{b} \perp \vec{e}. \quad (16)$$

The amplitude of the magnetic component is related to that of the amplitude of the electric field by $B = \frac{n}{c}E$, where $\frac{c}{n}$ is the phase velocity of light in the medium of refractive index n . A momentary snapshot of the wave, presenting spatial dependence of both E and B , is shown in Figure 3.

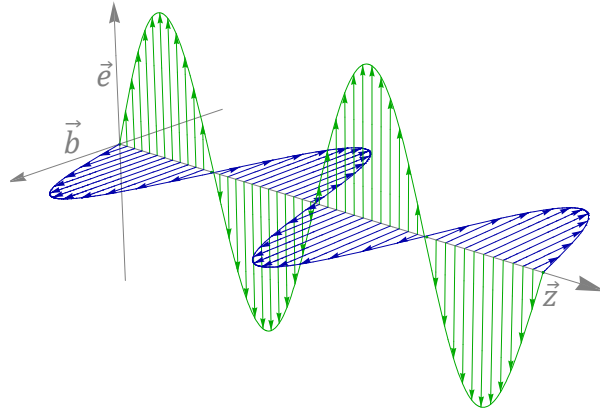


Figure 3: Schematic of a vertically linearly polarized electromagnetic wave propagating in free space in the \vec{z} direction, at a time t . The evolution of the electric field \vec{e} with the propagating distance is represented in green and evolution of the magnetic field \vec{b} is in blue.

The energy flux carried by a monochromatic beam is given by Poynting vector:

$$\vec{S} = \frac{1}{\mu_0} \vec{E} \wedge \vec{B} = \frac{n}{\mu_0 c} E^2 \cos^2(kz - \omega t) \vec{z}, \quad (17)$$

where the vacuum permeability $\mu_0 = 4\pi \times 10^{-7} \text{ kg m A}^{-2} \text{ s}^{-2}$.

The irradiance or power per unit area (sometimes called illumination intensity) I is given by the absolute value of Poynting vector, averaged over at least one oscillation period

$$I = \langle |\vec{S}| \rangle = \frac{n}{2c\mu_0} E^2. \quad (18)$$

Therefore, in SI unit, the photon flux corresponding to a monochromatic linearly polarized plane wave of angular frequency ω and amplitude E is

$$\Phi = \frac{I}{\hbar\omega} = \frac{n}{2c\mu_0\hbar\omega} E^2 = \frac{nc\varepsilon_0}{2\hbar\omega} E^2, \quad (19)$$

where ϵ_0 is the vacuum permittivity (linked with vacuum permeability through the relation $\epsilon_0\mu_0c^2 = 1$).

A chromophore positioned at $z = 0$, in an external electromagnetic field \vec{E} is described by the following Hamiltonian \hat{H} :

$$\hat{H} = \hat{H}_0 + \hat{V}(t), \quad (20)$$

where $\hat{V}(t)$ is the interaction energy between the atom and the applied electromagnetic field,

$$\hat{V}(t) = -\vec{\mu} \cdot \vec{E}(t), \quad (21)$$

where $\vec{\mu}$ is the electric dipole moment of the molecule. The absolute value of the interaction energy is in most cases very small compared to the unperturbed energy, and may be thus considered as a small perturbation of \hat{H}_0 .

In the time-dependent perturbation calculation, we will assume that the electric field is switched on at time $t = 0$, and vanished at $t < 0$. The perturbed wavefunction, $\Psi(\vec{r}, t)$, must satisfy the time-dependent Schrödinger equation

$$\hat{H}\Psi(\vec{r}, t) = [\hat{H}_0 + \hat{V}(t)]\Psi(\vec{r}, t) = i\hbar \frac{\partial}{\partial t} \Psi(\vec{r}, t). \quad (22)$$

To solve this equation, we represent Ψ as a linear superposition of unperturbed eigenfunctions

$$\Psi(\vec{r}, t) = \sum_n a_n(t) u_n^0(\vec{r}) e^{-i\omega_n t}, \quad (23)$$

where $a_n(t)$ is the probability amplitude of finding the molecule at the n^{th} energy level at the time t . When multiplied from left with $u_k^0(\vec{r})^*$ (i.e. complex conjugate of $u_k^0(\vec{r})$) and integrated over r-coordinate, Equation (21) leads to a system of coupled differential equations for the determination of the time-dependent coefficients $a_n(t)$ ($n = 1, 2, 3, \dots, k, \dots$):

$$\left\{ \begin{array}{l} \frac{da_1(t)}{dt} = -\frac{E(e^{i\omega t} + e^{-i\omega t})}{2i\hbar} \sum_n a_n(t) \vec{\mu}_{1n} \cdot \vec{e} e^{-i(\omega_n - \omega_1)t} \\ \dots \\ \frac{da_k(t)}{dt} = -\frac{E(e^{i\omega t} + e^{-i\omega t})}{2i\hbar} \sum_n a_n(t) \vec{\mu}_{kn} \cdot \vec{e} e^{-i(\omega_n - \omega_k)t} \\ \dots \end{array} \right. \quad (24)$$

where $\vec{\mu}_{kn}$ is the dipole moment matrix element between k^{th} and n^{th} level,

$$\vec{\mu}_{kn} = \langle k | \vec{\mu} | n \rangle = \iiint u_k^0(\vec{r})^* \cdot \vec{\mu} \cdot u_n^0(\vec{r}) d^3\vec{r}. \quad (25)$$

If, as we have already assumed, the perturbation alters the probability amplitudes only by a very small amount, then the coefficients $a_n(t)$ can be represented as a series in powers of the interaction energy:

$$a_n(t) = a_n^0 + a_n^1(t) + a_n^2(t) \dots, \quad (26)$$

where the first term corresponds to the 0-th approximation, 2nd term corresponds to 1st approximation etc. Initially, i.e. at $t < 0$, the molecule is considered to be in the lowest-energy (ground) state that we will recognize with the subscript g ,

$$a_g^0 = 1 ; \dots ; a_k^0 = 0 ; \dots \quad (27)$$

The perturbation is small, such that $a_g(t) \approx 1$ and $a_n(t) \ll a_g(t)$. Then we may assume that every higher order term in the series (26) is much smaller than the preceding lower order term.

2.2.2 IPA probability, transition dipole moment and oscillator strength

The second term in the Equation (25) corresponds to the first order of approximation, and gives the probability that, at time $t > 0$, the molecule can be found in the state f :

$$\frac{da_f^1(t)}{dt} = -\frac{E(e^{i\omega t} + e^{-i\omega t})}{2i\hbar} e^{i\omega_{fg}t} \vec{\mu}_{fg} \cdot \vec{e}, \quad (28)$$

where $\omega_{fg} = \omega_f - \omega_g = \frac{E_f - E_g}{\hbar}$.

The solution of this differential equation, with the initial condition $a_n^1(0) = 0$ for $n \neq g$ leads to

$$a_f^1(t) = \frac{E}{2\hbar} \left[\frac{1 - e^{i(\omega_{fg} - \omega)t}}{(\omega - \omega_{fg})} - \frac{1 - e^{i(\omega_{fg} + \omega)t}}{(\omega_{fg} + \omega)} \right] \vec{\mu}_{fg} \cdot \vec{e}, \quad (29)$$

If the transition occurs from a lower-energy state to a higher-energy state, i.e. $\omega_{fg} > 0$, then for positive frequency, $\omega > 0$, the first term in the bracket becomes resonant and predominates when, $\omega \sim \omega_{fg}$. This situation corresponds to the one-photon absorption. The second term, which would predominate if $\omega_{fg} < 0$, i.e. transition from higher-energy initial state to a lower-energy final state, corresponds to stimulated one-photon emission. Stimulated emission is not relevant to the experiments described in this thesis, so in what follows, we retain the first term in Equation (29) and will discard the second term [52]. The corresponding probability of finding the system in the excited state, at a time $t > 0$, is given by

$$P_{g \rightarrow f}^{(1)}(t) = |a_f^1(t)|^2 = \frac{E^2}{4\hbar^2} |\vec{\mu}_{fg} \cdot \vec{e}|^2 \left[\left| \frac{\sin\left(\frac{\omega_{fg} - \omega}{2}t\right)}{\frac{(\omega - \omega_{fg})}{2}} \right|^2 \right]. \quad (30)$$

In the limit, where t tends to *infinity*, the function enclosed in square brackets becomes very narrow, with a high peak value, and may be represented by a Dirac delta function, $2\pi t\delta(\omega_{fg} - \omega)$. Thus, for large t , the probability of finding the molecule in the excited state becomes:

$$\lim_{t \rightarrow \infty} P_{g \rightarrow f}^{(1)}(t) = \frac{\pi E^2 t}{2\hbar^2} |\vec{\mu}_{fg} \cdot \vec{e}|^2 \delta(\omega_{fg} - \omega). \quad (31)$$

This relation, known as Fermi's Golden Rule, satisfies energy conservation between photon frequency and the energy change of the system, $E_f - E_g = \hbar\omega$. However, in practical spectroscopy, where transitions occur not only between well-defined electronic states, but may involve a large number of other degrees of freedom, such as vibrations, rotations etc, organic chromophores often exhibit rather broad-band absorption spectra, which are difficult to reconcile with the Dirac δ -delta function presented in Equation (31). To accommodate the inevitable line-broadening, we replace the δ -function with a normalized continuous distribution. For instance, an absorption transition of organic chromophores often exhibits Gaussian-like bands, and in this case

$$g_M(\omega) = \sqrt{\frac{4 \ln(2)}{\pi \Delta\omega^2}} e^{-\frac{4 \ln(2)}{\pi \Delta\omega^2} (\omega - \bar{\omega}_{fg})^2}, \quad (32)$$

where $\Delta\omega$ is the full width at half maximum (FWHM) of the distribution centered at frequency $\bar{\omega}_{fg}$. The normalization condition reads,

$$\int_0^\infty g_M(\omega) d\omega = 1. \quad (33)$$

The appropriately amended Equation (31) becomes

$$P_{g \rightarrow f}^{(1)}(t) = \frac{\pi E^2 t}{2\hbar^2} |\vec{\mu}_{fg} \cdot \vec{e}|^2 g_M(\omega). \quad (34)$$

The rate of transition, $R_{g \rightarrow f}(t)$, is defined as the fraction of molecules that are excited to the final state during unit time. The transition rate corresponding to probability (34) is expressed as

$$R_{g \rightarrow f}^{(1)}(t) = \frac{\pi E^2}{2\hbar^2} |\vec{\mu}_{fg} \cdot \vec{e}|^2 g_M(\omega). \quad (35)$$

In order to evaluate the absorption cross section, we consider again a beam propagating through the sample, as shown in Figure 2. The number of photons absorbed in a thin layer of thickness Δz per unit area and per unit time is

$$\Delta\Phi_t = \sigma_{1PA} N_g \Phi_t \Delta z. \quad (36)$$

On the other hand, since each absorbed photon produces one excited molecule,

$$\Delta\Phi_t = \Delta z N_g R_{g \rightarrow f}^{(1)}(t) = \Delta z N_g \frac{\pi E^2}{2\hbar^2} |\vec{\mu}_{fg} \cdot \vec{e}|^2 g_M(\omega), \quad (37)$$

Combining (35) and (36), and taking into account the definition of photon flux (18), leads to the expression of the 1PA cross-section in SI unit

$$\sigma_{1PA}(\omega) = \frac{\pi\omega}{nc\epsilon_0\hbar} |\vec{\mu}_{fg} \cdot \vec{e}|^2 g_M(\omega). \quad (38)$$

So far we have assumed that the transition dipole moment vector is oriented in the same direction for all chromophores contained in the sample. In reality, the orientations of solvated molecules is random, and in liquid phase, also constantly changing. To take this random orientation into account, the scalar product in Equation (38) needs to be averaged over all possible orientations of $\vec{\mu}_{fg}$ vector with respect to the excitation polarization. The isotropic averaging gives

$$\begin{aligned}\langle |\vec{\mu}_{fg} \cdot \vec{e}|^2 \rangle &= \frac{1}{8\pi^2} \int_0^\pi \int_0^{2\pi} \int_0^{2\pi} |\vec{\mu}_{fg} \cdot \vec{e}|^2 \sin\theta \, d\theta d\varphi d\chi, \\ \langle |\vec{\mu}_{fg} \cdot \vec{e}|^2 \rangle &= \frac{1}{3} |\vec{\mu}_{fg}|^2,\end{aligned}\quad (39)$$

where θ , φ and χ are the Euler angles defined in the following Figure 4.

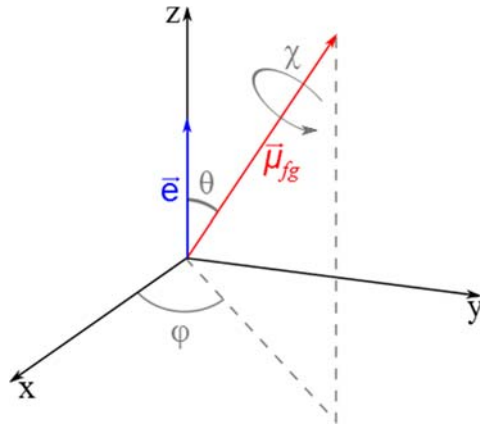


Figure 4: Direction of the electric polarization \vec{e} and the transition dipole moment $\vec{\mu}_{fg}$ in the laboratory reference, where X, Y, and Z are the frame axes. θ , φ and χ are the Euler angles that relate the dipole moment direction. A rotational average integrates over the full ranges of θ , φ and χ to account for the range of molecule orientations in a bulk sample.

Therefore, for randomly-oriented chromophores, the one-photon absorption cross section is given by the expression

$$\sigma_{1PA}(\omega) = \frac{\pi\omega}{3nc\epsilon_0\hbar} |\vec{\mu}_{fg}|^2 g_M(\omega). \quad (40)$$

The transition dipole moment, which is a measure of the transition strength, may be obtained by integrating the 1PA cross-section over the transition line shape:

$$|\vec{\mu}_{fg}| = \sqrt{\frac{3nc\epsilon_0\hbar}{\pi} \int \frac{\sigma_{1PA}(\omega)}{\omega} d\omega}. \quad (41)$$

This formula can be also rewritten in term of extinction coefficient thanks to Equation (8),

$$|\vec{\mu}_{fg}| = \sqrt{\frac{3nc\epsilon_0\hbar\ln(10)}{\pi N_a} \int \frac{\epsilon_{1PA}(\lambda)}{\lambda} d\lambda}. \quad (42)$$

2.2.3 2PA probability and permanent dipole moment

Once the expression for the 1st order term, $a_n^1(t)$, is known, we insert it into the equation for the second-order term. The second order probability amplitude of finding the systems in the final state f if, at $t = 0$, the system is the state g arises from the equation:

$$\begin{aligned} \frac{da_f^2(t)}{dt} &= -\frac{E(e^{i\omega t} + e^{-i\omega t})}{2i\hbar} \sum_m a_m(t) \vec{\mu}_{fm} \cdot \vec{e} e^{-i(\omega_m - \omega_f)t}, \\ &= \frac{iE^2}{4\hbar^2} \sum_m \frac{(\vec{\mu}_{mg} \cdot \vec{e})(\vec{\mu}_{fm} \cdot \vec{e})}{(\omega - \omega_{mg})} \left[e^{i(\omega_{fm} - \omega)t} + e^{i(\omega_{fm} + \omega)t} - e^{i(\omega_{fg} - 2\omega)t} - \right. \\ &\quad \left. e^{i\omega_{fg}t} \right], \end{aligned} \quad (43)$$

where $\omega_{fm} = \omega_f - \omega_m$ and $\omega_{fg} = \omega_f - \omega_g = \frac{E_f - E_g}{\hbar}$.

Here the state m plays the role of an intermediate state, which system may or may not populate on its way from g to f . Because we are looking only for instantaneous transition from a lower-energy state g to a higher-energy state f , and disregard transitions related to stimulated emission, we keep in the right-hand side of the Equation (43) only the term corresponding to 2PA,

$$\frac{da_f^2(t)}{dt} = \frac{iE^2}{4\hbar^2} \sum_m \frac{(\vec{\mu}_{mg} \cdot \vec{e})(\vec{\mu}_{fm} \cdot \vec{e})}{(\omega_{mg} - \omega)} e^{i(\omega_{fg} - 2\omega)t}. \quad (44)$$

Integrating over time, gives the following solution

$$a_f^2(t) = \frac{E^2}{4\hbar^2} \sum_m \frac{(\vec{\mu}_{mg} \cdot \vec{e})(\vec{\mu}_{fm} \cdot \vec{e})}{(\omega_{mg} - \omega)} \times \left[\frac{e^{i(\omega_{fg} - 2\omega)t} - 1}{(\omega_{fg} - 2\omega)} \right]. \quad (45)$$

The probability $P_{g \rightarrow f}^{(2)}(t)$ of finding the molecule at the final level f is

$$P_{g \rightarrow f}^{(2)}(t) = \frac{E^4}{16\hbar^4} \left| \sum_m \frac{(\vec{\mu}_{mg} \cdot \vec{e})(\vec{\mu}_{fm} \cdot \vec{e})}{(\omega_{mg} - \omega)} \right|^2 \times \left[\left| \frac{\sin\left(\frac{\omega_{fg} - 2\omega}{2}t\right)}{\frac{(\omega_{fg} - 2\omega)}{2}} \right|^2 \right]. \quad (46)$$

The function enclosed on brackets has a sharp maximum if $2\omega \approx \omega_{fg}$. Again, as in the case of 1-photon transition discussed above, in the limit of long observation time, the sharply peaked function turns into Dirac δ -function, reflecting the law of conservation of energy:

$$\lim_{t \rightarrow \infty} P_{g \rightarrow f}^{(2)}(t) = \frac{\pi E^4 t}{8\hbar^4} \left| \sum_m \frac{(\vec{\mu}_{mg} \cdot \vec{e})(\vec{\mu}_{fm} \cdot \vec{e})}{(\omega_{mg} - \omega)} \right|^2 \delta(\omega_{fg} - 2\omega). \quad (47)$$

This Equation (47) shows that in the second-order transition, the molecule gains energy equal to $2\hbar\omega$, which corresponds to the absorption of two photons of identical energy. If we now assume that the energy of a single photon is far detuned from resonances due to any of the states m , $|\omega_{mg} - \omega| \approx |\omega|$, then one-photon transition, if we choose to talk about such process under current circumstances, may occur only over a very short time interval, $\sim\omega^{-1}$, and is, therefore, of vanishing significance. Nevertheless, the probability (47) contains a sum over all such potential intermediate (one-photon absorbing) states, which amounts to what is called virtual intermediate level, shown as horizontal dashed line in Figure 1. We underline that the virtual energy level is a mathematical construct only, and does not correspond to any real eigenstate energy of the system.

As previously mentioned, absorbers with line-broadened absorption profiles cannot be fitted with a Dirac-delta function, so we shall use again the normalized line shape function in the Equation (47)

$$P_{g \rightarrow f}^{(2)}(t) = \frac{\pi E^4 t}{8\hbar^4} \left| \sum_m \frac{(\vec{\mu}_{mg} \cdot \vec{e})(\vec{\mu}_{fm} \cdot \vec{e})}{(\omega_{mg} - \omega)} \right|^2 g_M(2\omega), \quad (48)$$

where the normalization condition reads

$$\int_0^\infty g_M(2\omega) d\omega = 1, \quad (49)$$

The corresponding transition rate is

$$R_{g \rightarrow f}^{(2)}(t) = \frac{\pi E^4}{8\hbar^4} \left| \sum_m \frac{(\vec{\mu}_{mg} \cdot \vec{e})(\vec{\mu}_{fm} \cdot \vec{e})}{(\omega_{mg} - \omega)} \right|^2 g_M(2\omega). \quad (50)$$

From Figure 2, the number of photons absorbed in a thin layer of thickness Δz per unit area and per unit time is

$$\Delta\Phi_t = \sigma_{2PA} N_g \Phi_t^2 \Delta z. \quad (51)$$

Since two photons absorbed produce one excited state, then there are $N_f = \frac{\Delta\Phi_t}{2}$ molecules excited,

$$\frac{\Delta\Phi_t}{2} = \Delta z N_g R_{g \rightarrow f}^{(2)}(t). \quad (52)$$

Combining Equations (50), (51), (52) and using the definition of photon flux (18) leads to the expression of the 2PA cross-section:

$$\sigma_{2PA}(\omega) = 2(2\pi)^3 \frac{\alpha^2 \omega^2}{n^2 e^4} \left\langle \left| \sum_m \frac{(\vec{\mu}_{mg} \cdot \vec{e}) \times (\vec{\mu}_{fm} \cdot \vec{e})}{(\omega_{mg} - \omega)} \right|^2 \right\rangle g_M(2\omega), \quad (53)$$

where $\alpha = \frac{1}{4\pi\epsilon_0} \frac{e^2}{\hbar c}$ is the fine-structure constant and e is the electron charge. This last expression is in SI unit, the conversion with GM unit follows the rule 1 GM = 10^{-50} cm⁴ s photon⁻¹. The isotropic average considers all possible orientations of transition dipole moment with respect to the excitation polarization in the

volume investigated and will be evaluated for a few practical cases considered below.

2.2.4 Parity selection rule for one- and two-photon transition

If a molecule is centrosymmetric, i.e. if its structure displays inversion center, then its electronic states can be classified according to parity as *g* (gerade) or *u* (ungerade). Spectroscopic selection rule called *Laporte rule* specifies that allowed one-photon transitions in such molecules must involve a change in parity, either $g \rightarrow u$ or $u \rightarrow g$. Consequently, if a molecule is centrosymmetric, then linear absorption spectrum is dominated by parity-changing transitions, whereas those between same parity states are forbidden. The symmetry notation *u* and *g* refers to the operation of inversion, which requires starting at an arbitrary point in the molecule, travelling straight through the center, and then continuing outwards an equal distance from the center. This operation of inversion is represented by an arrow in Figure 5 depicting simple molecular orbitals. The orbital is designated *g* (for gerade or even) if the phase is the same, and *u* (for ungerade, uneven) if the phase changes sign in an inversion operation.

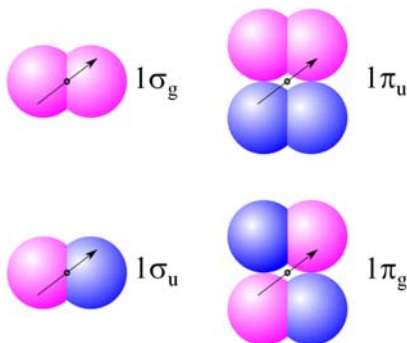


Figure 5: Simplest molecular orbitals (named 1σ and 1π) for a diatomic molecule where positive phase of the orbital is colored in blue, whereas magenta color stands for a negative phase.

2.2.4.1 Laporte rule for one-photon transitions

Mathematically speaking, Laporte rule originates from transformation properties of the transition matrix elements of the form

$$\langle i | \vec{\mu} \cdot \vec{e} | j \rangle, \quad (54)$$

where *i* and *j* are two arbitrary states. Since the dipole moment operator is odd upon inversion of all three Cartesian coordinates, the value of the matrix element must vanish if *i* and *j* are of the same parity. By extension, matrix elements describing permanent electric dipole moment $\langle i | \vec{\mu} \cdot \vec{e} | i \rangle$, vanish for all states that have definite parity.

In the context of organic chromophores, if they possess inversion symmetry, then purely electronic transitions between opposite parity states have dominant electronic transition dipole moments and large extinction coefficient, whereas those between same parity states are weak or unobservable. Also, organic molecules with centrosymmetric structure cannot have permanent electric dipole moments. However, forbidden transitions can become allowed if the center of symmetry is disrupted, i.e. if the inversion symmetry is broken. In such cases, nominally forbidden transitions, including permanent dipoles, gain in strength, often in proportion to the degree by which the symmetry is broken. Disruption of the center of inversion symmetry occurs for various reasons, and serves as an important spectroscopic indicator of molecular environment.

2.2.4.2 Parity selection rule for two-photon transitions

The sum in the expression for the 2PA cross-section can be re-written in terms of transition matrix elements

$$\sum_m \frac{\langle g | \vec{\mu} \cdot \vec{e} | m \rangle \langle m | \vec{\mu} \cdot \vec{e} | f \rangle}{(\omega_{mg} - \omega)}. \quad (55)$$

Let us assume that all involved eigenstates possess either g or u parity. It is then easy to observe that if the initial state and final state are of different parity, then the whole sum vanishes. Indeed, for the $g \rightarrow m$ transition matrix element to be different from zero, m must be of opposite parity with respect to g . But then, m and f must be of the same parity, which means that the product of the two matrix elements in the numerator vanishes. This leads directly to extension of Laporte parity rule to two-photon transitions, stating that allowed two-photon transitions occur in systems with inversion symmetry only between states with the same parity.

Thus, in molecules with an inversion center, transitions that are one-photon allowed are two-photon forbidden and vice-versa – two-photon allowed transitions should be forbidden in one-photon absorption. This is so-called alternative parity selection rule, and it can be extended to include any higher-order multi-photon transitions as well.

2.3 Sum-over-states (SOS) versus few-essential-states (FES) model

Equation (53) represents a sum-over-states (SOS) consisting of infinite number of terms, which includes values of transition dipole moments, their interferences and transition frequencies for all excited electronic states. It requires calculating both ground and excited-states eigenfunction and the transition dipole moments between them. Various quantum computational methods aim to calculate the 2PA cross-section from Equation (53). In practice, only a small fraction of the information required in SOS is available from experiments; higher energy states are particularly difficult to fully characterize. Although the two-photon cross-

section consists of contributions from all eigenstates, in many practical situations, 2PA spectra description are reasonably well described by considering only few lowest energy states. Resort to the few essential states models provide useful clues for structural optimization in the chromophore design for particular applications.

2.3.1 Dipolar contribution to SOS

To gain better insight into the inner workings of the 2PA cross section, let us note that the sum in SOS expression includes all states, i.e. counting also the initial and final states. Let us re-write the sum in way that separates out the terms corresponding to the matrix elements $\vec{\mu}_{gg}$ and $\vec{\mu}_{ff}$:

$$\sigma_{2PA}(\omega) = 2(2\pi)^3 \frac{\alpha^2 \omega^2}{n^2 e^4} \left\langle \left| \frac{(\vec{\mu}_{gg} \cdot \vec{e})(\vec{\mu}_{fg} \cdot \vec{e})}{-\omega} + \frac{(\vec{\mu}_{fg} \cdot \vec{e})(\vec{\mu}_{ff} \cdot \vec{e})}{(\omega_{fg} - \omega)} + \sum_{m \neq f, g} \frac{(\vec{\mu}_{mg} \cdot \vec{e})(\vec{\mu}_{fm} \cdot \vec{e})}{(\omega_{mg} - \omega)} \right|^2 \right\rangle g_M(2\omega). \quad (56)$$

The first two terms, containing to the permanent dipole moments of the initial- and final states, can be further combined into one term if we assume that for the lowest energy transition $\omega \cong \frac{1}{2} \omega_{fg}$:

$$\frac{(\vec{\mu}_{gg} \cdot \vec{e})(\vec{\mu}_{fg} \cdot \vec{e})}{-\omega} + \frac{(\vec{\mu}_{fg} \cdot \vec{e})(\vec{\mu}_{ff} \cdot \vec{e})}{(\omega_{fg} - \omega)} \cong \frac{(\vec{\mu}_{fg} \cdot \vec{e})(\Delta\vec{\mu}_{fg} \cdot \vec{e})}{\omega}, \quad (57)$$

where $\Delta\vec{\mu}_{fg} = \vec{\mu}_{ff} - \vec{\mu}_{gg}$ is the change of the permanent electric dipole moment upon transition between g and f . In the context of centrosymmetric chromophores, where permanent dipole moments all vanish, this contribution has no consequence. However, in systems with no inversion symmetry, and, especially in those chromophores with inherently large permanent dipole moments (so-called dipolar chromophores), the above dipole term can have a strong or even dominant contribution to the 2PA cross-section [54].

2.3.2 Origin of permanent electric dipole moment in organic chromophores

An electric dipole moment is a measure of the separation of positive and negative electrical charges within a system. In molecules, it originates from the electron density distribution regarding to the nuclei, which is manifested as a separation between the centers of positive and negative charges. With Coumarin 153 (C153) as an example, Figure 6 shows the highest occupied molecular orbital (HOMO) and lowest unoccupied molecular orbital (LUMO), where one electron occupying that orbital is likely to be found. It is possible to see displacement of the electron probability density from the central aromatic ring in HOMO to the left ring with the trifluoromethyl group in LUMO, which means that upon excitation of one electron, the electron probability density changes

along the axis of the molecule and, as a consequence, the dipole moment changes from ground to the excited state.

This change of the dipole moment upon electronic excitation has often a large influence on solvation dynamics, especially in polar solvents, which is largely governed by the interactions of solute and solvent dipole moments. Hence, understanding how the molecular dipole moments behave in the ground and excited states is critical for optimizing solvent-dependent properties of materials, including absorption and fluorescence spectra as well photo-initiated charge separation [1]. Also, the conformations of flexible biomolecules like peptides depend on the relative orientations of the backbone dipole moments, the α -helix being the consequence of aligned microscopic dipole moments of the peptide bonds [56]. The conformations might be subjected to geometry changes upon the changed dipole-dipole interactions between the different moieties after electronic excitation.

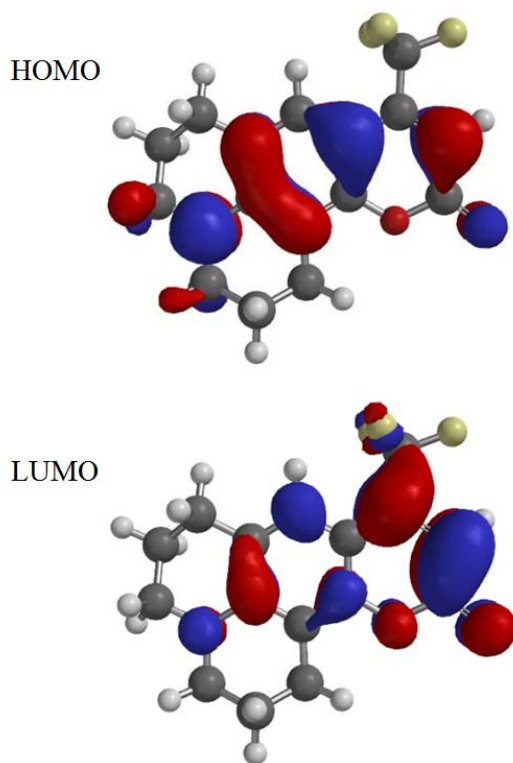


Figure 6: Comparing the molecular orbitals HOMO and LUMO for C153, calculated with by DFT B3LYP/6-31G(d). Form A. Leniak, Polish Academy of Sciences, Warsaw, Poland [102].

The values of molecular dipole moments are usually expressed in Debye units, where $1 \text{ D} = 3.33564 \times 10^{-30} \text{ C m}$. The permanent dipole moments of

organic chromophores generally lie between 0 and 30 D. 1 D roughly corresponds to the value of the product of elementary charge e with a typical charge separation of about 10^{-8} cm. There are various techniques of determining molecular dipole moment like solvatochromism of absorption and fluorescent bands [56] and vibrational Stark spectroscopy [101] to name a few. It is natural that each of the methods possesses its advantages and disadvantages.

Solvatochromism is caused by differential solvation of the ground and first excited state chromophore. If the chromophore is more stabilized in the ground state than in the excited state with increasing solvent polarity, a blue shift in the absorption and fluorescence spectra will result; whereas larger stabilization in the first excited state relative to that in the ground state, with increasing polarity, will lead to a red shift. The Lippert-Mataga equation describes the Stoke shift, between absorption peak λ_A and emission peak λ_{em} , in terms of change in dipole moment, based on the Onsager model for solvation, where the point dipole is in a spherical cavity cut from a dielectric medium. Unfortunately, this method is approximate and contains many assumptions. The fluorophore is supposed to have no specific interaction with the solvent, ignoring hence hydrogen bonding or charge transfer interaction to name a few. The polarizability of the fluorophore is also ignored and the ground and excited state dipole moments are assumed to point in the same direction. Finally, no clear prescription for the selection of the cavity radius a can be found in the literature. Therefore the solvatochromism method is valid only for a limited range of rigid systems [1], whereas larger non-spherical chromophores would need more complex expressions that describe the chromophore shape in adequate detail.

Stark spectroscopy measures the changes of an isolated absorption band of a frozen sample (i.e. immobilized) in the presence of an externally applied electric field, due to the dependence of ground and excited energy levels and transition dipoles on the local electric field \vec{E}_{loc} [101]

$$\Delta\omega \cong \frac{-1}{\hbar} \left(\Delta\vec{\mu}_{fg} \cdot \vec{E}_{loc} + \frac{1}{2} \Delta\alpha_{fg} \vec{E}_{loc} \cdot \vec{E}_{loc} \right), \quad (58)$$

where $\Delta\alpha_{fg}$ is the change of molecular polarizability from ground to excited state, where the polarizability α refers to the redistribution of a molecule's electron density due to an electric field. In the first order, the shift of the transition angular frequency $\Delta\omega$ is proportional to the dipole moment change and the local electric field \vec{E}_{loc} . Usually, this shift is much smaller than the bandwidth of the broad absorption bands. The extinction coefficient spectrum is affected by the presence of the external field and the dipole moment difference is then extracted from the decomposition of the derivative extinction coefficient spectrum [101]. Stark spectroscopy requires cooling of the samples to cryogenic temperatures in order to achieve narrow line shapes, thus limiting its versatility. The multi-parameter fitting of the extinction coefficient change, required in Stark spectroscopy, can be delicate. Finally, to our knowledge, no method has

been developed to determine the exact magnitude of the local electric field strength acting on by the molecule.

Table 1: Literature values of the dipole moments of Coumarin 153 determined by different methods [49].

Reference	Methodology	$\Delta\mu_{fg}$ (D)
Rechthaler et al.	Solvatochromic shift for a cavity radius 4.76 Å	6.5
Maroncelli et al.	Solvatochromic shift for a cavity radius 3.9 Å	4.1
	Solvatochromic shift for a cavity radius 5.85 Å	7.5
Peteanu et al.	Stark effect in toluene	5.8
	Stark effect in MeTHF	7.0

As an example, Table 1 lists the determined change in dipole moment for Coumarin 153, reported in the literature and obtained using different techniques. The change in permanent dipole moment ($\Delta\mu_{fg}$), obtained by solvatochromism shift, varies from 4.1 to 7.5 D depending on the cavity radius used in the solvatochromism method. Values obtained by Stark spectroscopy are in the 6.0 – 7.0 D range, depending on the solvent.

2.3.3 FES model

The SOS summarizes the contributions of transitions between all possible states. A quantitative description of the experimentally measured 2PA cross sections and 2PA spectra may be achieved by truncation of the SOS expression on the assumption that only a few excitation paths actually contribute the most. Under such assumption, the 2PA cross sections of the low-energy excited states may be described to be due to transitions from the ground state g directly to the final state f without interaction with any intermediate energy states (two level model), as shown in Figure 7 (a). The two-level model showing a 2PA resonance requires a permanent dipole moment difference between the ground and the first excited state. This model fails however, to describe centrosymmetrical molecules since they possess negligible permanent dipole moments. Including an intermediate state i , as shown in Figure 7 (b) is necessary to describe the 2PA behavior of a centrosymmetric chromophore.

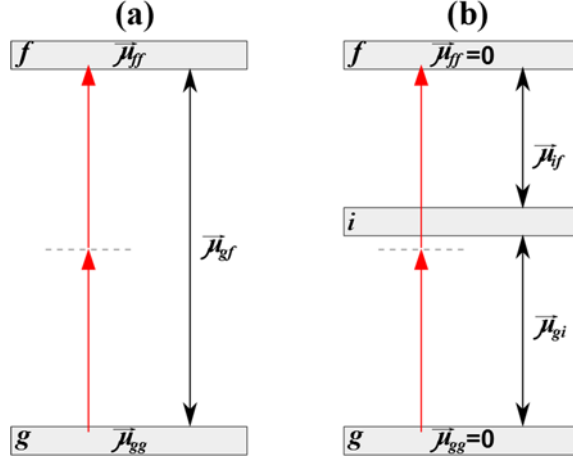


Figure 7: Basic versions of few-essential energy levels model. **a)** Two-level model for non-centrosymmetric chromophore with non-zero permanent dipole moment difference. **b)** Three-level model for centrosymmetric chromophore with a zero permanent dipole moment difference.

2.3.3.1 Two level model of 2PA

According to the two-level model, the contribution of the intermediate states in SOS can be ignored for the lowest energy transition $\omega \cong \frac{1}{2} \omega_{fg}$,

$$\sigma_{2PA}(\omega) = 2(2\pi)^3 \frac{\alpha^2 \omega^2}{n^2 e^4} \left\langle \left| \frac{(\vec{\mu}_{fg} \cdot \vec{e})(\Delta \vec{\mu}_{fg} \cdot \vec{e})}{\omega} \right|^2 \right\rangle g_M^{2PA}(2\omega). \quad (59)$$

This simplification of the summation is valid for chromophores which permanent dipole moment changes upon excitation, hence for non-centrosymmetrical molecules.

For randomly orientated molecules in a solvent, isotropic averaging yields the following expression:

$$\begin{aligned} \langle |(\vec{\mu}_{fg} \cdot \vec{e})(\Delta \vec{\mu}_{fg} \cdot \vec{e})|^2 \rangle &= \frac{1}{8\pi^2} \int_0^\pi \int_0^{2\pi} \int_0^{2\pi} |\vec{\mu}_{fg} \cdot \vec{e}|^2 |\Delta \vec{\mu}_{fg} \cdot \vec{e}|^2 \sin\theta \, d\theta d\phi d\chi, \\ \langle |(\vec{\mu}_{fg} \cdot \vec{e})(\Delta \vec{\mu}_{fg} \cdot \vec{e})|^2 \rangle &= \frac{P(\beta)}{15} |\vec{\mu}_{fg}|^2 |\Delta \vec{\mu}_{fg}|^2, \end{aligned} \quad (60)$$

where β is the angle between the transition dipole moment $\vec{\mu}_{fg}$ and the change of static dipole moment $\Delta \vec{\mu}_{fg}$ in the body-fixed coordinate system as shown in Figure 8. The expression $P(\beta)$ depends on excitation polarization. For linearly polarized light $P(\beta) = (2 \cos^2(\beta) + 1)$ whereas for circularly polarized light $P(\beta) = 1/2(\cos^2(\beta) + 3)$.

Therefore,

$$\sigma_{2PA}(\omega) = 2(2\pi)^3 \frac{\alpha^2}{15n^2 e^4} P(\beta) |\vec{\mu}_{fg}|^2 |\Delta \vec{\mu}_{fg}|^2 g_M^{2PA}(2\omega). \quad (61)$$

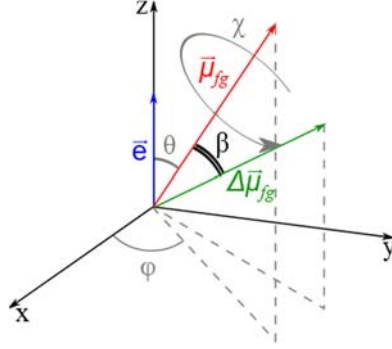


Figure 8: Direction of the electric polarization \vec{e} of the excitation beam, the transition dipole moment $\vec{\mu}_{fg}$ and the dipole moment change $\Delta\vec{\mu}_{fg}$ in the laboratory reference, where X , Y , and Z are the frame axes. θ , φ and χ are the Euler angles. A rotational average integrates over the full ranges of θ , φ and χ to account for the range of molecule orientations in a bulk sample.

For a pure electronic transition, the 1PA and 2PA line shapes coincide. Then we can combine to the Equation (40) with the Equation (61), which leads to

$$|\Delta\vec{\mu}_{fg}| = \sqrt{\frac{5\epsilon_0\hbar cn}{P(\beta)} \frac{\omega}{\sigma_{1PA}(\omega)} \sigma_{2PA}(\omega/2)}, \quad (62)$$

where $\sigma_{2PA}(\omega/2)$ is the peak 2PA cross-section and $\sigma_{1PA}(\omega)$ is the peak 1PA cross-section at half the wavelength.

Hence, comparing 1PA and 2PA, providing that the two-level model can be applied, is an all-optical method alternative to the standard techniques for the determination of permanent dipole moment change.

For optical excitation of molecules in a solvent, the electric field acting on the molecule may differ from the applied electric one. This difference between externally applied and actual electric field strength is often accounted for so-called local field factor L [2]: $\vec{E}_{LOC}(t) = L \vec{E}(t)$. The most used expression is the Lorentz field factor given by the expression $L = \frac{n^2+2}{3}$. It modifies Equation (62) as follows:

$$|\Delta\vec{\mu}_{fg}| = \sqrt{\frac{5\epsilon_0\hbar c n}{P(\beta) L^2} \frac{\omega}{\sigma_{1PA}(\omega)} \sigma_{2PA}(\omega/2)}. \quad (63)$$

2.3.3.2 Three level model for a centrosymmetric molecule

If the chromophore possesses a center of inversion, then the inverse symmetry leads to two important properties which profoundly influence 2PA behavior. Firstly, electronic transitions between energy levels follow parity selection rules. Secondly, the static dipole moments are all equal to zero: $\vec{\mu}_{ff} = \vec{\mu}_{gg} = 0$. Simplest description for centrosymmetric molecules is by considering initial –

gerade– ground state g , –gerade– final excited state f and the –ungerade– intermediate one i . Taking into account isotropic averaging leads to

$$\sigma_{2PA}(\omega) = 2(2\pi)^3 \frac{\alpha^2 L^4 \omega^2}{15n^2 e^4} P(\alpha) \frac{|\vec{\mu}_{ig}|^2 \times |\vec{\mu}_{fi}|^2}{(\omega_{ig} - \omega)^2} g_M(2\omega), \quad (64)$$

where α is the angle between transition dipole moments $\vec{\mu}_{ig}$ and $\vec{\mu}_{fi}$ and P is the same function as in Equation (61).

2.4 Emerging applications for two-photon absorption

The main reason why 2PA process has become so popular recently in varied applications is because it exhibits not one, but several unique attributes that linear absorption phenomenon lacks. In what follows we briefly address some of these properties presented along with some illustrative examples.

2.4.1 Possibility of tight 3D-localized excitation

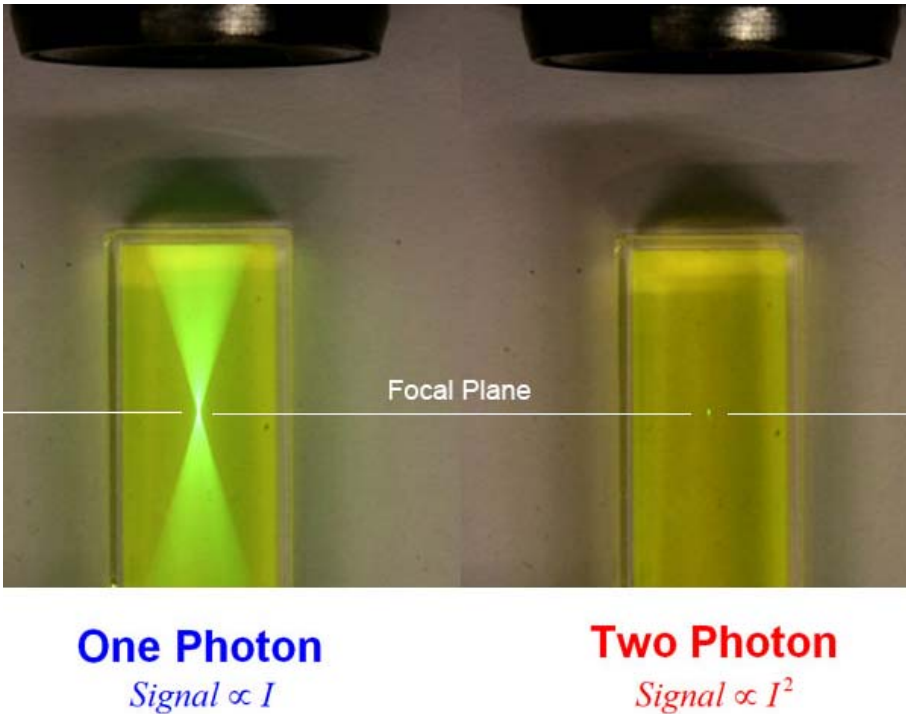


Figure 9: Comparison of 1PA and 2PA fluorescence with focused excitation beam. Both cuvettes contain Fluorescein solution. From Cornell University, Xu research group, Ithaca, USA [60].

Figure 9 shows the fluorescence emission arising from the illumination of two cuvettes containing identical Fluorescein solutions. In both cuvettes, the laser

was focused through a microscope objective to a tight spot in the focal plane of the objective. On the left side, the excitation wavelength is tuned to the one-photon absorption peak of Fluorescein, while on the right side the wavelength is 800 nm, which corresponds to a 2PA transitions. As the picture shows, 1PA-induced fluorescence occurs along the whole path of the laser, whereas 2PA phenomenon is sharply located in a small volume $\sim \lambda^3$ at the focus, where the photon flux is the highest. This property is providing, for nearly diffraction-limited 3D, confinement of the excitation volume in 2PA.

An application that successfully exploits inherent 3D localization of 2PA is microfabrication by laser-induced polymerization. This fabrication method provides exceptional control and flexibility in producing 3D structures that cannot be manufactured by any other means, and has been used, for example, to construct miniature medical devices, including scaffolds for artificial tissue growth [30]. If one can use a resin that photopolymerizes under illumination with a focused ultrafast IR laser, then solid polymer can be formed at the focal point of an objective lens, usually aided by a special 2PA-active photoinitiator. By moving the focal point around in three-dimensional space to solidify the medium at different points, practically any micro-object with desired complex geometry can be created. Left side of Figure 10 sketches the basic principle of 3D fabrication by 2PA. A 2PA photosensitive layer of resin is encapsulated between two glass-plates. The sample is mounted on a three-axis nanopositioning stage for controlled motion in all directions. The excitation beam, for inducing polymerization of the resin at the focal point, is projected into the sample with a microscope objective lens.

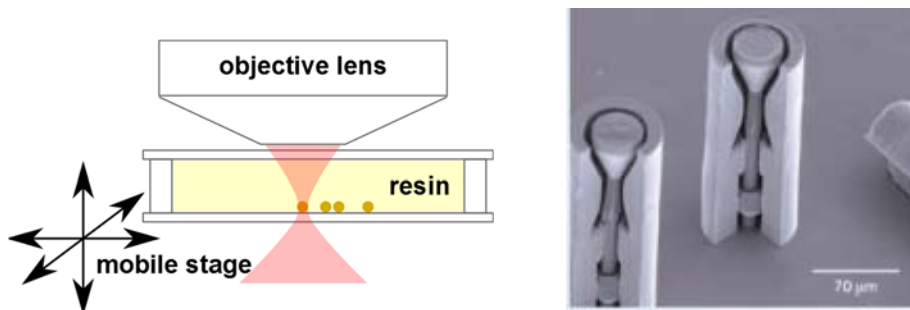


Figure 10: (Left) Schematic of 3D fabrication method by 2PA. (Right) example of 3D microfabrication: microvalve designed to prohibit the reversal of blood flow in human veins. Only part of the valve cover was built to enable visualization of the interior. The dimensions of the valve can be changed by simply scaling the computer design to fit the patient's vein's diameter, and its fabrication takes only a few minutes. From Foundation for Research and Technology Hellas (FORTH), Greece [30].

Right panel of Figure 10 presents a 3D microfabrication of microvalves for biomedical application, made with a biocompatible silicon hybrid resin. The scale of the valve is on the order of 100 μm with the smallest features as fine as

few μm . The 2PA spectrum of the photoinitiator can be determined using reference standard in a direct method. Knowing the 2PA spectrum of the photoinitiator allows selecting the excitation wavelength and photoinitiator concentration in the sample to optimize the speed and quality of printing.

2.4.2 Deeper tissue penetration due to lower scattering of near-infrared (NIR)

Visible (VIS) wavelengths are widely used for microscopic imaging of thin biological samples such as tissue slices, but visible light is not well suited for thick samples or deep tissues, because the light is strongly absorbed and scattered by cells organelles. VIS and UV wavelengths can also cause various types of damages such as protein denaturation, leading to disorganization and even death of cells under study. Most importantly, strong tissue scattering, where the mean path length of VIS photons is only a few tens of μm , obscures sharp images and creates detrimental background at the expense of desired signal such as fluorescence. In near-IR, especially in the so-called tissue transparency window, 750 – 1200 nm, the effect of absorption and tissue scattering is at least one order of magnitude less than in the VIS range, but, few fluorophores can be excited at such long wavelengths via 1PA.

Two-photon excitation of fluorescence can take full advantage of the superior penetration ability of NIR light. Because scattered photons have almost no probability of producing two-photon induced fluorescence, and also because of the large difference between excitation wavelength and the fluorescence emission wavelengths, scattered laser photons can be effectively rejected from the detector with efficient filters, such that 2PA fluorescence microscope images show almost no detrimental background. Besides, there is empirical evidence that reducing photon energy often provides better photostability of fluorescent proteins [41].

Combining the above with the 3D-localized excitation, multiphoton microscopy has revolutionized biological imaging, especially regarding study of deep tissues. Figure 11 shows a network of neurons in an intact mouse cortex expressing yellow fluorescent proteins. The image is reconstructed from *in vivo* conventional single photon microscopy (left) and two-photon microscopy (right). In single photon microscopy, only layers 200~300 μm deep from the surface can be seen. The fine detail of tuft dendrites is hidden by noise arising from the background scattering. Better resolution is achieved by two-photon microscopy, which allows seeing clearly up to 600 μm deep from the surface showing the whole parts of dendrites and cell bodies of neurons.

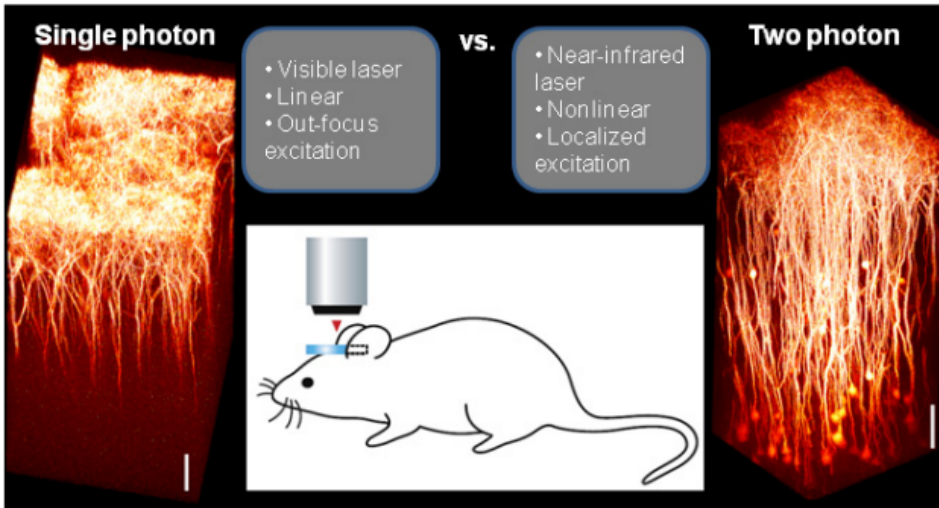


Figure 11: *In vivo* comparison of conventional single photon microscopy and two-photon microscopy imaging the intact cortex of YFP-H line mouse, expressing yellow fluorescent proteins (YFPs) in many layer V pyramidal neurons. Scale bar, 100 μm . From College of Korean Medicine, Seoul, Korea [61].

This example is using 2PA excitation of a fluorescent protein expressed *in situ*. To improve 2PA microscopy, it is important to develop fluorescent proteins with increased 2-photon brightness and higher photostability. These parameters can be quantitatively characterized by referencing relative to accurate 2PA reference standard, e.g. in order to identify useful mutations [41].

Another example which takes advantage of the deep penetration of NIR light is two-photon photodynamic therapy (PDT) as a local light-activated treatment to destroy tumor tissue. The key point of the technique is the use of photosensitizer with high 2PA cross-section which localizes with better affinity toward cancer cells and/or tumor tissue. After illumination of the region of interest, the photosensitizer is excited by 2PA generates toxic singlet oxygen by energy transfer, which attack tumor cells [16, 24].

2.4.3 Limiting maximum photon flux for eye- and sensor protection

Proliferation of various types of lasers, including high power sources, in everyday- as well as in military-related applications presents significant hazards to the eyesight of military personnel, aircraft pilots or optical sensor. For instance, US and UK governments currently invest in the development of a laser weapon system whose power is estimated to be between 15 and 50 kW [62]. There is also myriad of accident yearly in laboratories resulting in severe tissue or eye damage to individuals due to exposure to high intensive light.

While it is possible to protect the human eye from a conventional laser pointer with a proper wavelength filter, static filters are not appropriate for frequency-agile and pulsed lasers. Currently, the research is focused on the development of optical power limiting (OPL) materials that are transparent under ordinary ambient light conditions, but absorb or block intense laser light over a broad wavelength range extending into the NIR for specific time intervals. For example, the maximum safe level allowed to enter an eye is estimated to be around $0.2 \mu\text{J}$ in the VIS region for pulses less than 17 ms [63]. For a given sample thickness, the transmitted photon flux by 1PA is proportional to the incoming photon flux (see Equation (7)), whereas it decreases quadratically with the incoming photon flux in case of 2PA (see Equation (12)). Hence 2PA materials might offer a protection for high laser intensity and are under investigation.

Figure 12 shows a comparison of energy transmitted by 1PA (line) and 2PA (triangle symbols) enhanced by excited state absorption (ESA) through 10 mm path-length cuvette of 4,4'-bis(di-n-butylamino)stilbene (BDBAS) in acetone, with a concentration of 0.14 M, using a 5 ns pulse Nd:YAG-pumped dye laser focused to 0.0025 cm^2 near the exit window of the cuvette. The incident energy was modified with the help of neutral-density filters. Only 11% of input energy of $160 \mu\text{J}$ is transmitted in the case of 2PA, and only 4% transmission was measured for $1000 \mu\text{J}$ input energy pulses. In contrast, the energy transmitted is 95% in 1PA, independently of the incoming energy. 1PA and 2PA transmittance curves converge at the origin.

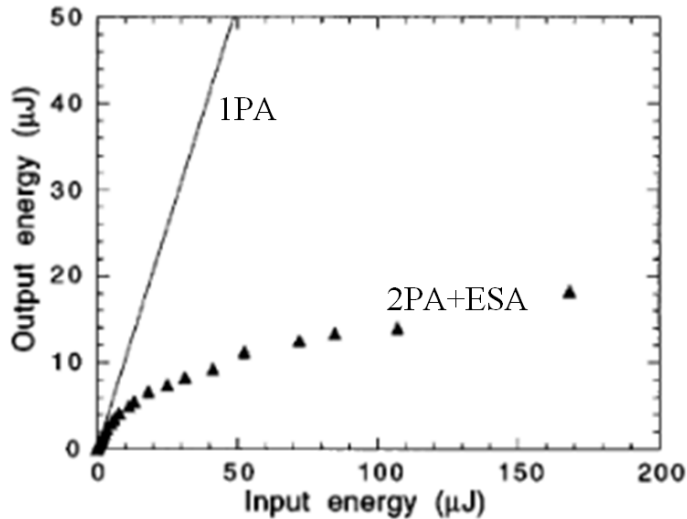


Figure 12: Comparison between the OPL response (triangle) and linear transmission (line) for BDBAS in acetone at a concentration of 0.14 M in a 10 mm cell. Nonlinear transmission was performed at 600 nm with 5 ns laser pulses and an $f/5$ optical system. From Jet Propulsion Laboratory and Beckman Institute, California, USA [63].

From this study, the effective cross-section was found to be 1.2×10^4 GM for BDBAS in acetone at 610 nm and 1.3×10^4 GM for 4,4'-bis(diphenylamino)-stilbene (BDPAS) in toluene at 700 nm. Compared to our own measurements (see appendix H Figure H.3) this value is 70 times larger than the intrinsic 2PA cross-section for BDPAS in toluene (Figure H.3 in appendix H). The difference is due to excited-state absorption (ESA), which can be described by two steps during the pulse duration: an instantaneous 2PA step followed by a very fast relaxation to the lowest excited-state S_1 and then the last step with ESA process to a higher level $S_n > S_1$. ESA can also occur in the triplet states, if there is significant inter-system crossing. Figure 13 is a visual scheme of 2PA followed by ESA in the energy level diagram.

Because of the participation of ESA, the cross-section measured in this experiment is said to be an effective cross-section, and its value depends upon experimental conditions, especially upon the pulse width and laser intensity. Approximately, the so called 2PA effective cross-section σ_{2PA}^{eff} , for a given pulse duration, is found to increase linearly with the photon flux [72]

$$\sigma_{2PA}^{eff} = \sigma_{2PA} + u\sigma_{ESA}\Phi, \quad (65)$$

where u is a constant, related to the concentration and pulse duration, and σ_{ESA} is the excited state one-photon cross-section.

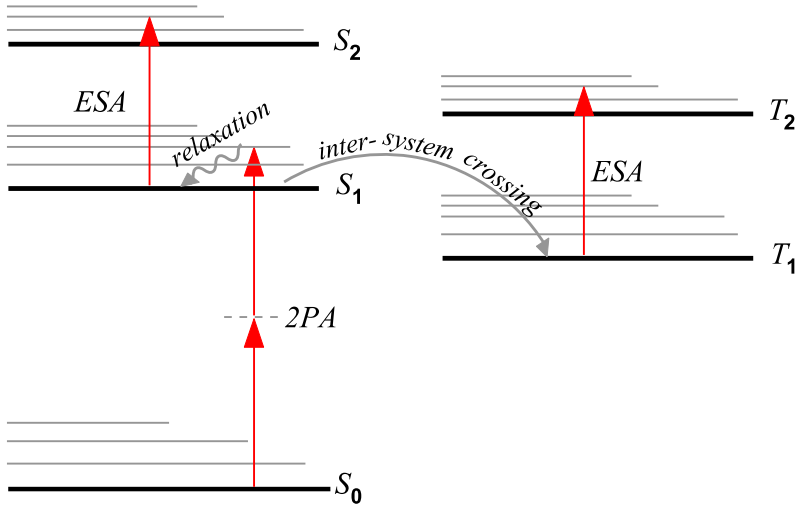


Figure 13: Jablonsky diagram of and 2PA followed by ESA. Grey lines correspond to higher order of vibrational levels corresponding to the pure electronic transition. Grey lines correspond to vibrational levels associated with a pure electronic level (black line).

There is still much improvement and research needed to optimize the efficiency of OPL materials. For instance, from Figure 12, with input energy

larger than 50 μJ , the nonlinear transmitted energy slowly increases from 10 μJ , which is far beyond allowed limits for eye safety [63]. Hence, using reference standard to track the changes in 2PA efficiency is an important tool in the developing of improved compounds for OPL.

2.5 Overview of experimental techniques for measuring absolute 2PA cross section in organic chromophores

There are two principal techniques for measuring the value of $\sigma_{2\text{PA}}$. Direct methods observe the number of transmitted photons, and calculate $\sigma_{2\text{PA}}$ using the relative change of the photon flux before and after passing through the 2PA medium. Indirect methods infer $\sigma_{2\text{PA}}$ by measuring secondary effects induced by 2PA, such as luminescence emission, generation of heat, generation of sound etc. In the following section we will present a brief description of different experimental approaches that aim to measure the absolute two-photon cross-section. We will discuss how each method is reflected in the choice of experimental conditions and how the experimental observables of interest are related to the 2PA cross-section.

2.5.1 Direct Methods

When a beam of light travels through an absorbing sample, the corresponding sample transmittance function, T , is defined as the ratio between the number of photons at the output vs. the number of photons at the input,

$$T = \frac{\Phi_{out}}{\Phi_{in}}. \quad (66)$$

As long as absorption saturation and other side-effects may be neglected, the 2PA transmittance decreases with increasing incident photon flux, as described by Equation (11). If this dependence is known from an experiment, then, provided that the incident photon flux and other relevant parameters such as chromophore concentration and sample thickness are also known, one can use the nonlinear transmittance directly to determine $\sigma_{2\text{PA}}$. The main advantage of the direct measurement is that it is broadly applicable to a variety of nonlinear absorbers, including liquids, solids, thin films etc. However, there are also some fundamental as well as practical limitations. One of the fundamental limitation stems from the fact that if the chromophores can undergo excited state absorption from the states created initially through 2PA, then that may create artifacts that are difficult to distinguish from “true” 2PA. Main practical limitation stems from the fact that the transmittance is not a zero-background measurement, meaning that if the change of the transmittance is small, $\Delta T \ll 1\%$, then utmost care must be taken to achieve sufficient accuracy of the experiment. Typical change of transmittance in direct 2PA experiments is on the order of a few percent, $\Delta T \sim 1 - 5\%$. To determine $\sigma_{2\text{PA}}$ with, say, 20% accuracy, one would need to measure the transmittance itself with an accuracy of at least \sim

1%. This accuracy should be compared with typical accuracy provided by commercial optical power meters and other photodetectors, which is also $\sim 1\%$. As an example, let us estimate the maximum transmittance change in a generic direct 2PA experiment. According to Equation (12), the maximum change of the transmittance is determined by the product, $\sigma_{2PA}N_g\Phi l$. Assuming, $\sigma_{2PA} = 100$ GM, chromophore concentration 100 mM and path length $l = 1$ mm, we can estimate that to achieve 1% maximum transmittance change, the peak photon flux must be on the order of, $\Phi \sim 2 \times 10^{27}$ photon $\text{cm}^{-2} \text{s}^{-1}$. The photon energy at wavelength 800 nm is, $h\nu = 2.5 \times 10^{-19}$ J, which means that the minimum irradiance needed to observe 1% transmittance change under current conditions would be about, $I \sim 4 \times 10^8$ W cm^{-2} . Achieving this high irradiance typically requires ultrashort laser pulses with duration ~ 100 fs or less, but may also require focusing of the beam to a small spot to further increase the photon flux. On the other hand, minimum focus spot size (beam waist), w_0 , is limited by the requirement that the sample thickness should be larger than the diffraction length (Rayleigh length) of the focus, which for a Gaussian beam leads to a relation

$$l \geq z_R = \frac{\pi w_0^2}{\lambda}. \quad (67)$$

For example, at 800 nm, the smallest beam waist, in 1 mm thick sample, is about $w_0 \sim 16$ μm . Using this value, and a 2PA cross-section of $\sigma_{2PA} = 100$ GM, we can estimate the required average laser power, CW or pulsed, to induce 1% changes for different concentrations. Estimations are presented in Table 2.

Table 2: Example of order of magnitude of sample concentration, photon flux and average laser power required to detect a transmittance change of 1% with a collimated beam of 16 μm diameter set at 800 nm passing through 1 mm of sample thickness whose 2PA cross-section is $\sigma_{2PA} \sim 100$ GM.

N_g molar (M)	Φ (photon $\text{cm}^{-2} \text{s}^{-1}$)	I (W cm^{-2})	CW laser power (W)	Pulsed laser power (W) 100fs 76 MHz
10^{-6}	10^{32}	10^{14}	10^{10}	10^5
10^{-3}	10^{29}	10^{11}	10^7	10^2
1	10^{26}	10^8	10^4	10^{-1}
100	10^{24}	10^6	10^2	10^{-3}

Considering that the femtosecond laser doesn't exceed 1W at output in the whole wavelength range, then the concentration minimum threshold is mM (Table 2), therefore direct method requires molecules with high solubility.

Another practical issue that may limit tight focusing is an optical damage to materials, including damage of glass walls of the cuvette containing the sample,

which, for femtosecond laser pulses, typically occurs at $I > 100 \text{ GW cm}^{-2}$. Successful direct 2PA measurement must deal with these various limitations and two main approaches are described below.

2.5.1.1 Open-aperture Z-scan

The popular so-called open aperture z-scan technique was first introduced in 1989 by Shaik-Bahae et al. [68], where the photon flux is varied by moving the sample along the propagation direction (z-direction) of a focused laser beam. Figure 14 presents a scheme of this technique: a pulse laser is tightly focused by a $\sim 20 \text{ cm}$ focal length lens. A thin sample mounted on a moving stage can translate along the beam path over $\sim 20 \text{ mm}$ distance through the focal point. The transmitted light power is collected by a photodetector PD2. To compare with the excitation beam power, a small portion of the excitation light is reflected on a glass plate and collected with a photodetector PD1.

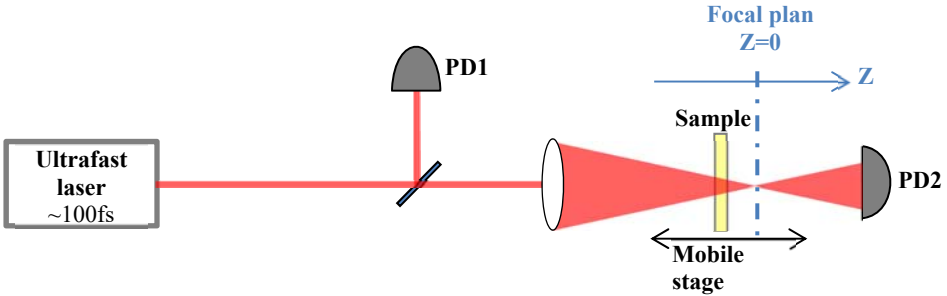


Figure 14: Schematic of Z-scan set-up for determining two-photon cross-section.

For a given pulse energy, the spot size changes along z-direction, with the highest photon flux occurring at the focal plane $z = 0$. If the spatial intensity profile of the beam is known, then the flux-dependent transmittance function may be determined by moving the sample to different z-positions, and measuring the corresponding pulse energy before and after the sample. Typically, this measurement is performed symmetrically using both positive- and negative z-displacements, because any significant deviations from a symmetric result relative to the focal plane may indicate potential artifacts e.g. thermal lensing, sample bleaching, etc. The resulting transmittance function, $T(z)$, also known as absorptive z-scan signature or trace, has a characteristic symmetric shape with a single minimum at $z = 0$. The 2PA cross section is obtained by comparing the experimental z-scan signature with appropriate model, which, in general, represents a nonlinear fitting function (see below).

Figure 15 shows the 2PA data, of a z-scan experiment, of Rhodamine 6G in methanol in a 1 mm thick sample measured by an open-aperture Z-scan technique using a 76-MHz pulse repetition rate mode-locked Ti:Sapphire femtosecond oscillator [69]. Figure 15 a) shows the z-scan trace (circles) at 806 nm, where the beam waist was $w_0 = 17 \mu\text{m}$ at focal plan; red line represents the

nonlinear fit. Maximum transmittance change achieved in this case is about 25%. Figure 15 b) shows the 2PA spectrum, where the σ_{2PA} values are extracted from z-scan measurements at different wavelengths.

Most implementations of z-scan techniques, including the example in Figure 15, rely on a non-linear fit based on the assumption that the excitation laser beam has spatial and temporal intensity profile that can be accurately described by Gaussian functions.

A difficulty with this approach is that, even if the transmission change is quite clearly imprinted in the z-scan trace, σ_{2PA} remains subject to significant experimental uncertainty. This is because the experimental curve fitting model is a nonlinear function of the fitting parameter(s), the accuracy of the fit depends crucially on the quality of the experimental data, much more than in case of a linear fit. This is manifest in the 2PA spectrum, where data points at different wavelengths display a substantial scatter, especially when compared to our 2PA spectrum for the same chromophore (Figure H.10 of appendix H) obtained with another technique explained and detailed in this thesis.

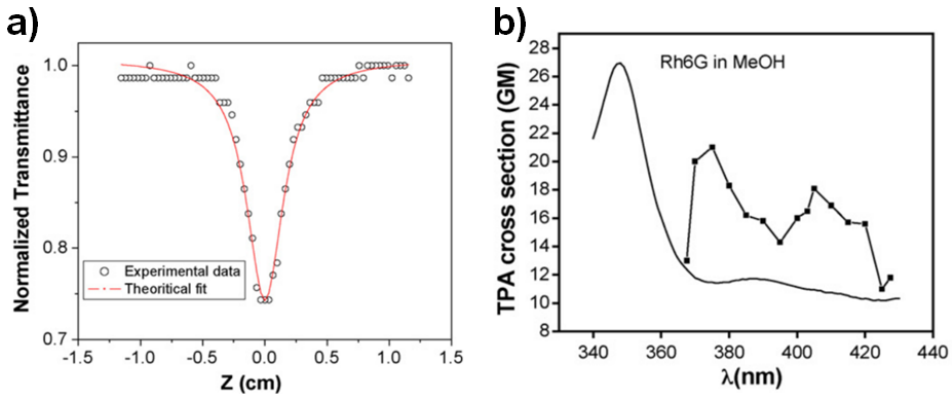


Figure 15: **a)** Absorptive Z-scan signature of Rhodamine 6G in methanol at 806 nm (black circles) and its best fit (red line). **b)** Comparison of 2PA spectrum (connected squares) and 1PA spectrum (solid line, Y scale not shown) for Rhodamine 6G in methanol, plotted in arbitrary scale at the same y-axis, of Rhodamine 6G in methanol. At the x-axis, the 2PA spectrum is plotted against half the excitation wavelength value to allow comparison of the transition wavelengths for the 1PA and 2PA. From Indian Institute of Technology, Kanpur [69].

Fitting of z-scan traces suffers further problems in conditions, where the transmittance change is small, experimental data is noisy or where the actual beam intensity profile deviates from the assumed model (or both). If the beam shape is not perfectly Gaussian, or if the beam parameters are not known, then an alternative approach to evaluate z-scan data could be used based on reference standards [99]. In this case, the measurement at each wavelength is performed twice, with the sample under study and with a known sample with well-

characterized σ_{2PA} value. This could alleviate some experimental errors, and may even relax the requirement for short sample path length. However, because the fitting of the reference the sample data is still essentially nonlinear, the reference standard-based approach has so far not been widely adopted in z-scan experiments. Nevertheless, because the z-scan is, at least conceptually, rather straightforward, this direct measurement techniques remain popular among many researchers.

2.5.1.2 Nonlinear transmission (NLT)

Limitations of z-scan method become most apparent if the maximum attainable change of the sample transmittance is small, e.g. less than 1%. Under such conditions, it would be an advantage if instead of nonlinear fitting one could derive σ_{2PA} value by applying linear fit to the experimental data. This approach is exploited in the so-called nonlinear transmission (NLT) measurement, where the beam size passing through the sample is fixed, while the incident photon flux is varied, e.g. by using a variable filter or attenuator. Figure 16 presents a scheme of this technique: a collimated pulse laser is directed through the sample. A variable neutral density filter modulates the incoming photon flux. The transmitted laser power is measured with a photodetector PD2 and compared to the incoming laser power, which is measured by reflecting a portion of the incoming photon flux through a reference photodetector PD1.

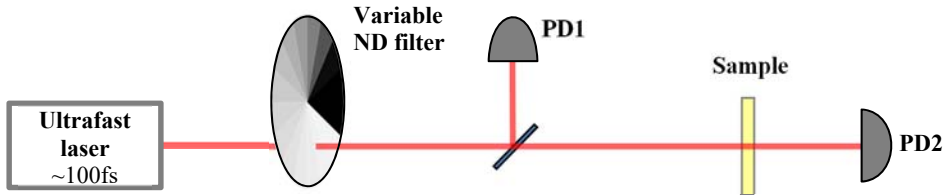


Figure 16: Schematic of NLT set-up for determining two-photon cross-section.

Let us assume that the beam incident on the sample is nearly collimated and that the maximum change of the transmittance is small, $\Delta T < 1\%$. Then from Equation (12) we can express the transmittance function through a sample of thickness l as follows

$$\Delta T(P_0) \cong -\sigma_{2PA} N_g l g_P P_0, \quad (68)$$

where $P_0 = \iiint \Phi_0 dx dy dt$ is the total number of incident photons per pulse and g_P is a shape factor that depends only on the laser beam intensity profiles,

$$g_P = \frac{\iiint \Phi_0^2 dx dy dt}{(\iiint \Phi_0 dx dy dt)^2}, \quad (69)$$

As long as the transmittance function is linear with the number of incident photons or incident pulse energy, the slope of this dependence is proportional to the 2PA cross-section. Figure 17 shows the “raw” dependence of the

transmittance, for L-tryptophan in H₂O on the incident pulse energy at different laser excitation wavelengths. Because the 2PA cross section of tryptophan is low, $\sigma_{2PA} < 1$ GM (see publication III in appendix L), maximum change of the transmittance does not exceed 0.5%. This allows to use linear fit function (dashed lines), which is least susceptible to scatter of experimental data.

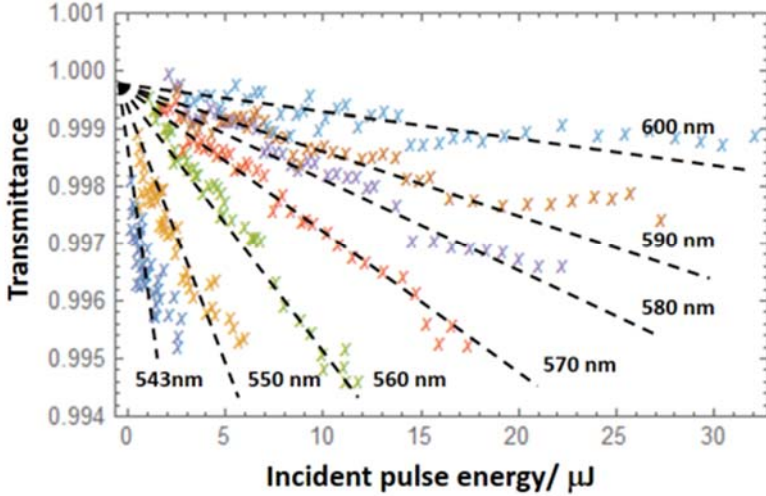


Figure 17: Example of NLT measurement of L-tryptophan in H₂O solution using wavelength-tunable femtosecond optical parametric amplifier (OPA). Dependence of the sample transmittance on the incident pulse energy is plotted as squared, where each color refers to an excitation wavelength. Linear fit functions to experimental data are shown by dashed lines. Data from A. Rebane group, Montana State University, unpublished.

Deriving σ_{2PA} value from the measured slope of the transmittance function using Equation (68) requires knowledge not only of the total number of incident photons, P_0 , but also of the spatial and temporal distribution shape factor, g_p . Especially in the case of high pulse energy tunable femtosecond lasers utilizing optical parametric amplification (OPA), the beam shape is often far from Gaussian, and varies considerably from one OPA tuning wavelength to another. Therefore, rather than reshaping the beam profile or measuring the beam parameters at every wavelength, it is more convenient to rely on reference standards. Assuming that the temporal and spatial profile of laser intensity do not change in the course of the measurement, one can determine the transmittance change of a known two-photon standard, ΔT_{ref} , under the same illumination conditions. Knowing the absolute 2PA spectrum, $\sigma_{2PA,ref}$ and the concentration of the reference, $N_{g,ref}$ one can define an experimental correction function

$$corr(\lambda) = \sigma_{2PA,ref}(\lambda) \frac{N_{g,ref}}{\Delta T_{ref}(\lambda)}, \quad (70)$$

where subscript *ref* stands for reference standard.

The correction function is then used to correct or normalize the “raw” slopes of the sample under study, according to the equation

$$\sigma_{2PA}(\lambda) \cong corr(\lambda) \frac{\Delta T(\lambda)}{N_g}. \quad (71)$$

Figure 18 shows the uncorrected “raw” data arising from NLT slopes of L-tryptophan (black squares) and the correction function obtained with 9-Chloroanthracene in methylene chloride as reference (blue dots) [44]. The final corrected 2PA spectrum of L-tryptophan is obtained by multiplying the “raw” spectrum with the correction function (red circles) and is shown in publication III (appendix L).

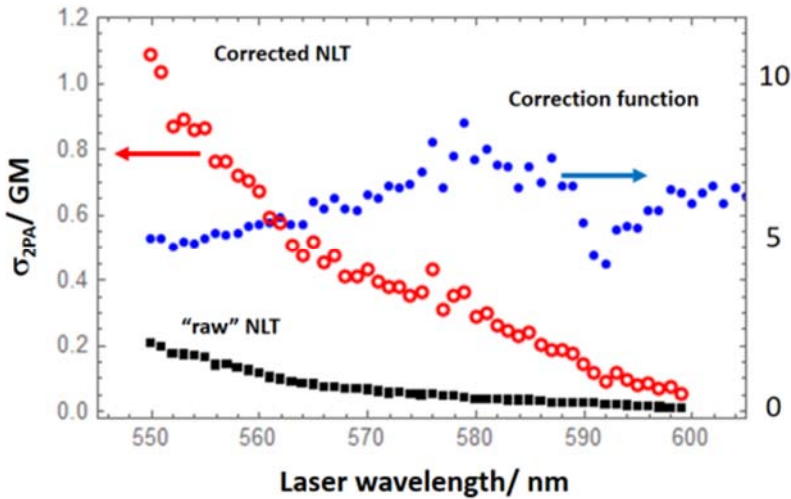


Figure 18: Example of NLT measurement of L-tryptophan in H_2O solution using wavelength-tunable femtosecond optical parametric amplifier (OPA). Uncorrected “raw” (black squares) NLT slopes, correction function relative to 9-Chloroanthracene in methylene chloride (blue dots) and corrected 2PA spectrum of l-tryptophan (red circles). Data from A. Rebane group, Montana State University, unpublished.

It should be underlined that Equation (68) is valid only if the maximum transmittance change is relatively low. The maximum allowed transmittance change, ΔT_{\max} , depends critically on the actual beam shape. In general, the more smooth and Gaussian-like the beam shape is, the higher is the value of ΔT_{\max} . In the above experiment, the sample thickness was 10 cm and the beam spot size was accordingly increased, $w_0 > 200 \mu\text{m}$, to accommodate the diffraction Equation (67). If sufficient laser pulse energy is available, the NLT method allows measuring samples with long optical path length, which may be an advantage if the 2PA cross section or sample concentration (or both) is low. The

key, of course, is the ability to accurately detect very small changes in the transmittance, on the order of 0.1% or less, as illustrated in Figure 17.

2.5.2 Indirect Methods

An indirect method relies on the recording of the signal produced by the molecule as a result of 2PA excitation and in turn is potentially background-free. After absorbing two photons, a molecule is promoted to an excited electronic state and after an initial relaxation to the lowest excitation level S_1 , according to Kasha-Vavilov rule, the remaining energy can be released to the environment through one or more physical processes, like luminescence (shown in green in Figure 19), and detected with the appropriate detector. Excitation signal is detected with a photodetector PD1, via the reflection of a portion of the incoming photon flux, and the induced energy released is detected by the appropriate detector Det.

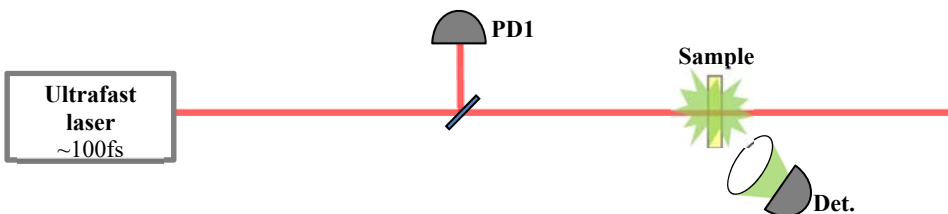


Figure 19: Generic indirect measurement method for determining two-photon cross-section. Excitation power can be monitored by a photodetector PD1 which collects a portion of the incident photon flux reflected from a glass-plate. The signal generated by 2PA is collected by an appropriate detector Det.

The most common indirect method for measuring absolute 2PA cross-section is the two-photon induced fluorescence (2PIF). This method takes advantages of fact that the number of emitted fluorescence photons is proportional to the number of molecules N_f excited by 2PA.

$$F_{2PA} = \eta Q N_f, \quad (72)$$

where F_{2PA} is the number of the fluorescence photons detected, η is the detection efficiency, Q the chromophore quantum yield in the selected solvent and N_f the number of molecules excited by 2PA. If the fraction of molecules excited is low and the beam is approximately collimated over throughout the thickness l of the sample, then we can neglect the dependence of the intensity on z , and we can deduce, from Equation (12), that:

$$\begin{aligned} N_f &= \frac{1}{2} \iiint (\Phi_0 - \Phi_t) dx dy dt, \\ N_f &\cong \frac{l \sigma_{2PA} N_g}{2} \iiint \Phi_0^2 dx dy dt. \end{aligned} \quad (73)$$

Since the signal detected is background-free, more diluted solution or lower laser power can be used as long as the signal is above the threshold of the detector. By monitoring the number of fluorescence photon emitted, it is possible to obtain relative or absolute 2PA spectra, knowing the photon flux and the detection efficiency over the wavelength range studied. Again, by the use of reference standards, the tedious laser and detection system characterization can be alleviated by applying a correction function obtained with the standard under the exact same conditions as the sample under study.

$$\begin{aligned} corr(\lambda) &= \sigma_{2PA_{ref}} \frac{Q_{ref} N_{g_{ref}}}{F_{2_{ref}}}, \\ \sigma_{2PA}(\lambda) &= corr(\lambda) \frac{F_2}{Q N_g}, \end{aligned} \quad (74)$$

where subscript *ref* stands for reference standard.

This technique can only be applied to fluorescent molecules with appreciable quantum yield efficiency. Disadvantages include problems of reabsorption that may influence fluorescence studies of molecules that display small Stokes shifts.

2.6 Selection of an experimental technique for measuring absolute cross-section with higher precision

2.6.1 Comparison of the experimental technique to optimize control of the 2PA phenomena

The measurement of 2PA cross-section still poses a number of experimental problems and experimental uncertainties of the most recent standards are above 20% [44]. We will compare different techniques and select the optimal one. The technique chosen must be sensitive to 2PA and ensure a control that 2PA is the only process being measured. Furthermore, the 2PA cross-section must be extracted from the measured data without the reliance of complicated fitting models or assumptions. The following Table 3 summarizes some the advantages and drawbacks of the different techniques presented in the previous section.

Direct methods are simpler than indirect method in the set-up design. One major drawback is that NLT or Z-scan need high excitation power and high concentration of the solutions under investigation, which can lead to other nonlinear phenomena and to saturation (see appendix A). For instance, in 2000, Oulianov and al [103] studied 4 fluorophores, Rhodamine 6G and B in methanol, (4-[N-(2-hydroxyethyl)-N-(methyl)amino phenyl]-49-(6-hydroxyhexyl) stilbene in methanol and N,N,N-tris[4-{2-/4-{5-[4-/tert-butyl)phenyl]-1,3,4-oxidiazol-2yl}phenyl)-1-propyl}phenyl]-amine in dichloromethane, for which two different techniques of 2PA measurements were compared. Namely, the absolute nonlinear transmission method (NLT) and the two-photon induced fluorescence (2PIF) using Rhodamine B as standard and following Equation (74). The laser system emitted at 802 nm pulses with 1.2 ps

duration, 700 μJ energy and 100 Hz repetition rate. The incident laser was focused with a waist estimated at 44 μm . The 2PA cross-sections measured by NLT for some of the molecules were 7 to 11 times smaller compared to the ones obtained by the 2PIF method. They suggested that one has to be very careful using NLT methods for 2PA cross-sections as other nonlinear effects come into play, and that substantially smaller values measured by NLT might be due to stimulated emission or scattering processes.

Another limitation in the direct method is the difficulty to distinguish 2PA from ESA, which reduces the accuracy of the determined $\sigma_{2\text{PA}}$. In the case of the 2PIF method, the number of molecules excited is measured via fluorescence signal. Hence the quadratic dependency of the number of photons emitted versus the number of excitation photons is a practical tool to assure that 2PA is the unique phenomena occurring.

Table 3: Main advantages and drawbacks of the different techniques for measuring 2PA cross-section.

Method	Advantages	Drawbacks
direct	Simplicity of the technique Applicable to any 2PA absorber	Not selective for 2PA process only. Favour ESA process Requires accurate measurement in a small dynamic range ($\Delta T < 1\%$) Needs highly soluble molecules Low signal-to-noise ratio
	Z-scan	Nonlinear fitting model and its optimization
	NLT	Linear fitting
indirect	Selective for 2PA process High dynamic range	Labour and time consuming Need calibration of the detection channel
	2PIF	Background-free signal Needs high fluorescence yield $QY > 0.01$

Direct method must measure small changes in the transmittance signal. Accurate measurement in a small dynamic range can be difficult regarding detector error margin as well as the impact scattering may have in the highly concentrated solution, which can contribute to the background signal. In that regard, 2PIF method is background free, in a sense that a measured fluorescence signal occurs only via 2PA, which offers a high dynamic range.

Therefore, 2PIF method is selected, because it offers greater specificity and accuracy in the measurements, although this approach does place more constraints on the samples being investigated, e.g. the sample must be soluble and fluorescent with high quantum yield.

2.6.2 Absolute 2PA cross-section determination using a modified 2PIF method

The fluorescence excitation method offers high sensitivity for the 2PA detection but relies on careful characterization of the excitation laser pulse properties, the knowledge of the number of molecules excited in the process and efficiency of the detection system. A direct comparison with 1PA emission allows the calibration of the efficiency of the detection channel and fluorescence quantum yield. The subscript f for the final excited state will be replaced by the subscripts $2PA$ and $1PA$ for the physical parameters that may encounter ambiguity. Using this notation, the number of fluorophore excited by one laser pulse from Equation (73) rewrites

$$N_{2PA} = \frac{1}{2} \sigma_{2PA} l N_g \int_{\text{pulse}} \iint_{\text{Beam area}} \Phi_{2PA}^2 dx dy dt. \quad (75)$$

In the absence of ground-state depletion and photobleaching, the density of molecules in the ground state N_g is constant. To extract the value of the 2PA cross-section σ_{2PA} from Equation (75), one needs the explicit spatial and temporal characteristics of the excitation photon flux. For a laser pulse defined by a Gaussian spatial and temporal shape, the photon flux is

$$\Phi_{2PA} = \Phi_{2PA}^0 \times \exp\left(-\frac{2(x-x_c)^2}{w_x^2}\right) \times \exp\left(-\frac{2(y-y_c)^2}{w_y^2}\right) \times \exp\left(-\frac{2(t-t_c)^2}{\tau^2}\right), \quad (76)$$

where Φ_{2PA}^0 is the peak value at coordinates $\{x_c, y_c, t_c\}$, w_x and w_y are the beam waist and τ is the pulse temporal width at which the photon flux drop to $1/e^2$ of the peak value. The corresponding full widths at half maximum are given by, respectively: $\Delta x = w_x \sqrt{\ln 4}$, $\Delta y = w_y \sqrt{\ln 4}$ and $\Delta t = \tau \sqrt{\ln 4}$.

The peak photon flux is related to the average laser power (in W) by a power meter:

$$W_{2PA} = \hbar \omega_{2PA} \langle \iint_{-\infty}^{+\infty} \Phi_{2PA} dx dy \rangle_{\text{time}}, \quad (77)$$

$$W_{2PA} = \hbar\omega_{2PA} \times \Phi_{2PA}^0 \times f \times \left(\frac{\pi}{2\ln 4}\right)^{3/2} \Delta t \Delta x \Delta y,$$

where f is the pulse repetition rate (in Hz).

Once the laser source photon flux is determined, the integral in Equation (75) becomes

$$N_{2PA} = \sqrt{2} \left(\frac{\ln 2}{\pi}\right)^{3/2} \frac{\sigma_{2PA} l N_g}{(\hbar\omega_{2PA})^2} \frac{W_{2PA}^2}{f^2 \Delta t \Delta x \Delta y}. \quad (78)$$

Next, let us evaluate the average fluorescence signal, with an integration time T larger than the pulse duration, detected within an emission window centered on the registration wavelength λ_{reg} ,

$$F_{2PA} = f T N_{2PA} \int_{\lambda_{reg}} \eta(\lambda_{em}) \varphi(\lambda_{em}) d\lambda_{em}, \quad (79)$$

where $\eta(\lambda_{em})$ is the differential detection efficiency and $\varphi(\lambda_{em})$ is the differential fluorescence quantum yield:

$$\begin{aligned} \eta(\lambda_{em}) &= \frac{d\eta}{d\lambda_{em}}, \\ \text{and } \varphi(\lambda_{em}) &= \frac{dQ}{d\lambda_{em}}, \end{aligned} \quad (80)$$

Combining Equation (78) and (79) we can see that the 2PA cross-section spectrum is proportional to the 2PIF signal, corrected to excitation laser parameters

$$\sigma_{2PA} = \frac{K}{N_g} \frac{F_{2PA}}{W_{2PA}^2} (\hbar\omega_{2PA})^2 \Delta t \Delta x \Delta y, \quad (81)$$

where K is a constant factor depending on the system fluorescence quantum yield, the detection efficiency and the laser repetition rate:

$$K = \frac{f(\pi/\ln 2)^{3/2}}{l T \sqrt{2} \int_{\lambda_{reg}} \eta(\lambda_{em}) \varphi(\lambda_{em}) d\lambda_{em}}. \quad (82)$$

As we have already seen, so far, measurement of σ_{2PA} is a multi-step process. If one strives, as we do here, towards ultimate accuracy of the σ_{2PA} measurement, then it is imperative to critically analyze each and every compound that makes up the combined measurements. From this perspective, it is practical to address separately the measurement of the 2PA spectral profile function (relative 2PA spectrum) and absolute value of σ_{2PA} . In fact, best results are achieved if these two measurements are performed in two dedicated experiments.

To obtain the 2PA spectral shape, the factor K can be set to normalize the 2PA spectrum and is then referred to K^{norm} ,

$$\sigma_{2PA}^{a.u} = \frac{K^{norm}}{C} \frac{F_{2PA}}{W_{2PA}^2} (\hbar\omega_{2PA})^2 \Delta t \Delta x \Delta y. \quad (83)$$

By measuring the intensity of the fluorescence, F_{2PA} , the average power, W_{2PA} , the pulse duration Δt , and the beam size, Δx and Δy , all as a function of wavelength, one can obtain the corrected 2PA spectrum in relative units. As the second step, the 2PA spectral shape is rescaled by at least one wavelength point, where the absolute 2PA cross-section is measured with sufficient accuracy. To obtain the absolute 2-photon cross section, we need to know the value of K in Equation (81). If the Kasha-Vavilov rule is obeyed, then we are allowed to assume that the fluorescence spectrum and the quantum efficiency are independent of the excitation wavelength. This allows the number of molecules excited through 2PA process N_{2PA} to be evaluated based on the relative signal of the 1PA and 2PA excited fluorescence, provided that the registration is carried out under exactly the same conditions. After been excited with a pulse laser set at λ_{2PA} to promote 2PA, the same region is excited with a continuous beam set at λ_{1PA} to promote 1PA, leaving all other conditions exactly the same. In case of 1PA,

$$F_{1PA} = TN_{1PA} \int_{\lambda_{reg}} \eta(\lambda_{em}) \varphi(\lambda_{em}) d\lambda_{em}, \quad (84)$$

where N_{1PA} is deduced from the Beer-Lambert law (Equation (7)):

$$N_{1PA} = \frac{W_{1PA}}{\hbar\omega_{1PA}} (1 - e^{-\sigma_{1PA} N g l}), \quad (85)$$

where W_{1PA} is the average beam power for 1PA.

By combining Equations (81), (84) and (85) the 2PA cross-section for fluorescent chromophores is

$$\sigma_{2PA} = \frac{1}{\sqrt{2}} \left(\frac{\pi}{\ln 2} \right)^{3/2} \frac{W_{1PA}}{W_{2PA}^2} \frac{(\hbar\omega_{2PA})^2}{\hbar\omega_{1PA}} \frac{F_{2PA}}{F_{1PA}} f \Delta t \Delta x \Delta y \frac{(1 - e^{-\sigma_{1PA} N g l})}{\ln g}. \quad (86)$$

By comparing both single and two-photon absorption, it is possible to determine the absolute 2PA cross-section of a molecule σ_{2PA} for a given wavelength λ_{2PA} .

2.6.3 Determining 2PA cross-section of an unknown fluorophore using 2PIF reference standard method

A suitable reference standard should be selected, such that it has sufficiently overlapping absorption and emission wavelength range with the sample under study: the larger is the overlap of their fluorescence spectra, the smaller is the potential measurement error caused by limited dynamic range of the detector. Since relative 2PA cross-section, with reference standard, aims to alleviate the excitation beam and detection system characterization, the following methodology is not restricted to our 2PIF method and can be applied to any 2PIF measurement, for example where the photon flux is focused.

If the excitation wavelengths, the photon flux, the beam parameters and the fluorescence detection conditions for the sample and the standard are the same, then the ratio between the corresponding cross sections derived from Equation

(86) leads to the expression for the sample 2PA cross-section with respect to the standard:

$$\sigma_{2PA}^{sample} = \frac{F_{2PA}^{sample}}{F_{2PA}^{ref}} \frac{N_g^{ref}}{N_g^{sample}} \frac{\varphi^{sample}(\lambda_{reg})}{\varphi^{ref}(\lambda_{reg})} \sigma_{2PA}^{ref} \quad (87)$$

The known cross-section of the standard and its measured fluorescence signal substitutes to the excitation photon flux characterization in Equation (81):

$$(\hbar\omega_{2PA})^2 \Delta t \Delta x \Delta y = \frac{W_{2PA}^2}{F_{2PA}^{ref}} N_g^{ref} \sigma_{2PA}^{ref} \quad (88)$$

The fluorescence signal is integrated over a narrow wavelength interval λ_{reg} , typically 1-5 nm or less, such as the detection spectral efficiency can be considered as nearly constant and therefore cancels out in the quotient. This implies as well that even though different spectrometer may be used for the 2PA experiment and the determination of the relative quantum yield, the detector response cancels out in both ratios $\frac{F_{2PA}^{sample}}{F_{2PA}^{ref}}$ and $\frac{\varphi^{sample}(\lambda_{reg})}{\varphi^{ref}(\lambda_{reg})}$. Thus the ratio between the quantum efficiencies can be obtained using a spectrofluorimeter in 1PA excitation mode [74] set at the same registration wavelength λ_{reg} than the 2PA experiment and with the exact same bandwidth, while using sufficiently diluted solutions controlled by their optical density OD ($OD_{max} < 0.5$) according to the formula:

$$\varphi(\lambda_{reg}) = \frac{\int_{\lambda_{reg}} F_{1PA}(\lambda_{em}) d\lambda_{em}}{1 - 10^{-OD(\lambda_{1PA})}} \quad (89)$$

This implies that reference standard and the sample must overlap sufficiently in their 1PA spectra to provide a suitable common excitation wavelength, λ_{1PA} . Refractive index of the solvent does not appear in this formula because it cancels out in the relative cross-section expression (87).

In the case of the determination of the 2PA spectral shape function of the sample, then under the same condition mentioned earlier, Equation (87) simplified into:

$$\sigma_{2PA}^{sample, au} = K^{norm} \frac{F_{2PA}^{sample}}{F_{2PA}^{ref}} \sigma_{2PA}^{ref} \quad (90)$$

This relation shows that a corrected 2PA spectral change is obtained by means of comparison between the fluorescence excitation spectra of the sample with the one of the standard, obtained under the same conditions.

2.7 Current state of the art of 2PA reference standards

Most, if not all, applications of 2PA rely on the on knowledge of the σ_{2PA} value. In many cases, one also needs to know the 2PA spectrum over a broad range of wavelengths. Knowing the 2PA spectra of biological markers will allow, for

example, selecting a common 2PA excitation wavelength for usable fluorescence signals in a multi-labelled 2PA microscopy. Monitoring the 2PA spectrum of a chromophore aids in the design of derivative compounds with extended uses and increased efficiency, especially for imaging or microfabrication, or with broader 2PA spectrum as required for optical power limiting. As in any kind of advanced spectroscopy, extracting useful information from the observed features requires correct interpretation of the measured 2PA cross-section spectra with enough accuracy. Quantitative 2PA spectroscopy with the help of FES model is used for establishing structure-properties relations for various organic and inorganic chromophores and is a key for designing of new efficient 2PA. The comparison of 2PA cross-section σ_{2PA} results from different techniques is not always straightforward and experimental conditions employed may vary significantly. One major issue is the characterization of the excitation photon flux which sometimes has a complex dependence of laser alignment etc.

Therefore, in 1996 Xu and Webb [43] proposed the use of 2PA standards that can be used to avoid photon flux characterization of the excitation beam. In this pioneering work, they used a ~ 80 -MHz pulse repetition rate mode-locked Ti:Sapphire femtosecond laser to measure the absolute 2PA cross-section using the 2PIF method for eleven common fluorophores. The 2PA cross section measurements were performed in the excitation wavelength range 690 - 1050 nm by exciting fluorescence in fluorophore solution with a tightly focussed laser beam. The evaluation of the absolute 2PA cross-section relied on the quantitative evaluation of the fluorescence signal collection efficiency, which was estimated to be $\sim 30\%$ reliable. Also, the spatial distribution of the incident light was not directly measured but assumed to be the point-spread function for diffraction-limited focus, perhaps leading to another substantial error. Finally, the determination of the absolute cross-section required the knowledge of fluorescence quantum yield, accurate value of which is not always available. Therefore absolute cross-section spectra were determined for only three of the eleven fluorophores, and only so-called two-photon action cross-section was estimated for the other fluorophores, which consists of the product of the 2PA cross-section with the fluorescence quantum yield. Nevertheless, this work has served as a main benchmark for comparison of 2PA spectra after it was published.

Important improvements in the absolute measurement of σ_{2PA} were made in 2008 by Makarov et al. [44]. In their case, the excitation beam was only slightly focussed, which allowed for direct measurement of the beam spatial profile. They carried out measurements of a set of 15 standards using 1 kHz pulse repetition rate femtosecond optical parametric amplifier (OPA), tunable over the range of wavelengths 550-1600 nm. They first characterized the spectral shape correction function, which relies on the laser spatial profile and temporal profile, dependent on the wavelength. However, poor day-to-day reproducibility of the beam parameters at the low pulse repetition rate adversely affected the

correction function of the 2PA spectral shapes, leading to substantial degree of discrepancy. The 2PA fluorescence signal was calibrated relative to 1PA fluorescence in the same sample, which gave more reliable σ_{2PA} values, compared to Xu and Webb method, with estimated accuracy of 20 - 30%.

Absolute two-photon cross-section determination poses the problem of reliability in the excitation beam and in the number of excited molecules characterization. In the emerging area of quantitative two-photon spectroscopy, higher accuracy 2PA cross-sections spectra of reference standards are necessary to determine the strength of intra- and intermolecular electric fields. There are at least three possible ways, in which the current 2PA reference standards should be improved. Firstly, the choice of the standards must be screened. The selected standards must be photostable, they must be free of any chemical equilibrium over a broad range of concentration to be applied in indirect as well as direct methods. In addition, they must cover a broad range of visible and near IR wavelength regions. Secondly, the 2PA spectra shape, in an arbitrary scale, must be smooth and precise. This requires the knowledge of the excitation photon flux parameters and assurance that no other nonlinear phenomena are in competition. Thirdly, the absolute cross-section at the maximum of two-photon absorption for each standard must be measured with higher accuracy, in order to rescale the corresponding 2PA shape spectrum. This last implies, among other requirements, more constraints regarding the precision in the determination of the number of molecules excited by 2PA. To reach this objective, the 2PIF method allows controlling and optimizing every critical parameter involved in the determination of absolute two-photon cross-section as well as determining the final error bar.

To achieve higher accuracy and fidelity, two independent measurements were performed, one focusing on improving the 2PA spectral shape, the other specifically devoted to the improvement of the absolute 2PA cross-section σ_{2PA} accuracy. The 2PA shape functions were measured by A. Rebane group at Montana State University, whereas the work on absolute cross sections was performed at the Estonian National Institute of Chemical Physics and Biophysics. As a preliminary result, Figure 20 below shows the comparison of the 2PA cross-section spectrum for Fluorescein in water buffer pH11 obtained by Xu et al. [43], Makarov et al. [44] and in this study. The shape presented in this study is much smoother than previous results. The absolute 2PA cross-section is smaller, but as we will see, we reached a measured accuracy of 8%.

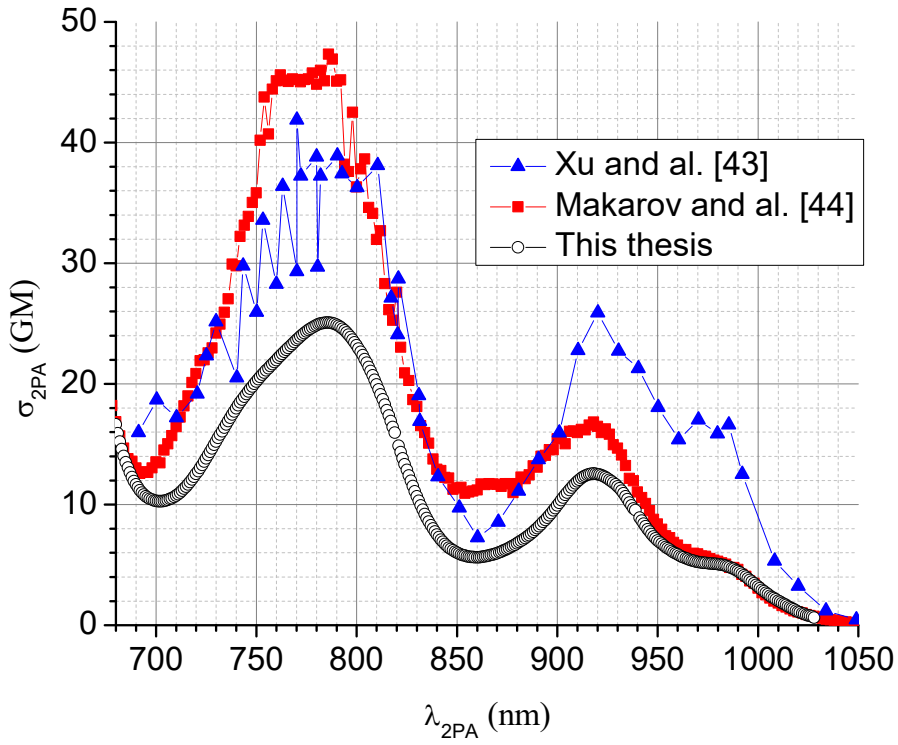


Figure 20: Absolute 2PA cross-section spectrum for Fluorescein in water buffer pH 11. Blue triangles are the first data obtained by Xu et al. [43]. Red squares are the data obtained by Makarov et al. [44] and black circles are the improved data obtained in this study.

3 AIM OF THE STUDY

This thesis is focused on absolute 2PA cross-section σ_{2PA} determination and aims to:

1. Finding suitable standards for 2PA in the visible-near IR region;
2. Develop an experimental set-up and protocol in order to measure the value of σ_{2PA} with a precision better than 10%, preferably 5%;
3. Verify the 2PA spectral shape function determined independently, in a different experiment (not part of this thesis).

4 ESTABLISHING TWO-PHOTON ABSORPTION STANDARDS IN THE 680 - 1050 NM RANGE EXPERIMENTAL SET-UP FOR MEASURING ABSOLUTE 2PA CROSS-SECTION USING 2PIF METHOD

Schematic of the setup is shown in Figure 21. The laser system comprises a 76-MHz pulse repetition rate mode-locked Ti:Sapphire femtosecond oscillator (Coherent Mira 900F) pumped by 10 W cw frequency-doubled Nd:YVO₄ laser (Coherent Verdi V-10). Potential residual short-wavelength pump emissions emanating from the laser output were cut off by a color glass long-pass filter (LPF1). This laser has a spatial TEM₀₀ mode well described by two-axis Gaussian function (see Equation (77)). A series of diaphragms were used to align the laser beam such that it passed near the center of all the optical elements.

The femtosecond laser wavelength was tuned manually in the range 690 - 960 nm with the average output power varying in the range 0.5 – 1.5 W. The fundamental laser spectrum was measured with a diffraction grating spectrometer (OceanOptics USB4000) to which a weak reflection was conveyed through an optical fiber.

A combination of focusing and collimating lenses (L1, 500 mm and L3, 150 mm) positioned at a distance ~ 800 mm from each other acted as an inverted telescope to reduce beam diameter up to ~ 0.3 mm at the sample location, while maintaining a nearly constant profile along the sample thickness of interest, set at $l = 2$ mm.

The spatial profile of the fundamental wavelength beam at the sample location (sample removed) was measured with the CCD-camera based beam profiler (Thorlabs BC106-VIS). The camera and the focusing lens L4 (150 mm) are placed after the sample location, in an arrangement to image the beam at the sample location with a magnification of ~ 3 . The calibration of the magnification factor was performed using a calibrated micrometer scale with 50 μm division (Thorlabs R1L3S1P), positioned at the sample holder (see appendix C). The incident beam on the camera was attenuated by an integrated 20 dB absorbing filter. A continuously variable neutral density filter wheel ND2 (Thorlabs NDC-100C-4) was placed in front of the camera to further adjust the laser power to avoid CCD saturation. The power reflected by the glass plate GP4 was sufficiently weak to minimize any thermal lensing in the beam profile imaging path.

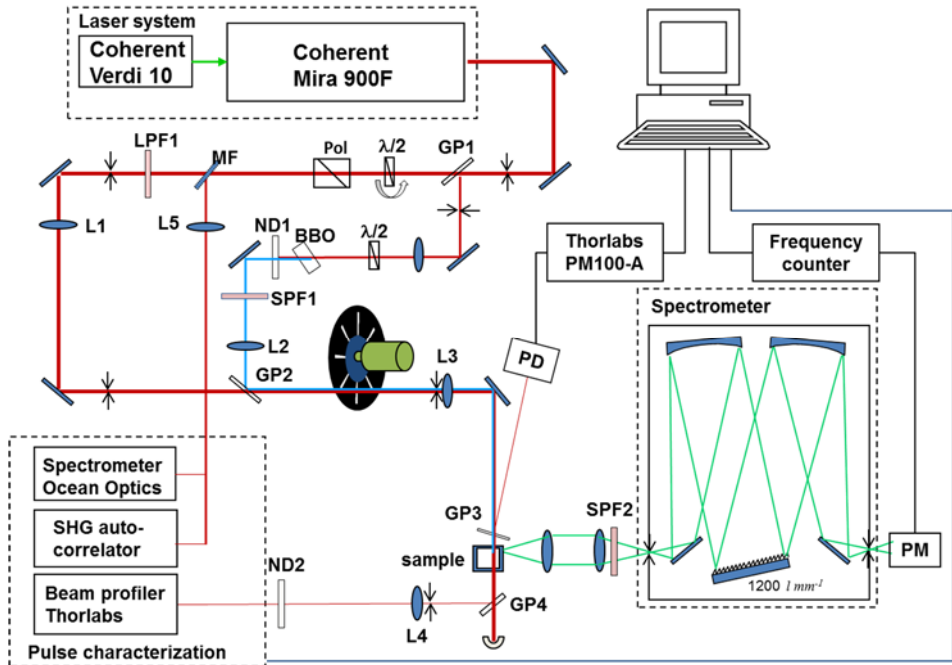
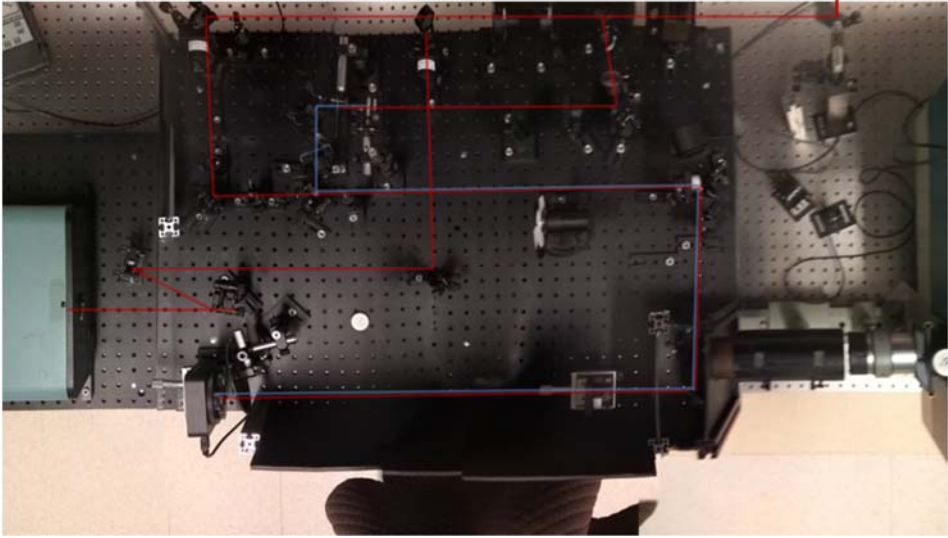


Figure 21: (Up) Picture of the experimental set-up mounted on an optical table. (Down) Schematic of the experimental set-up; L – focusing lenses; ND – neutral density filter wheel; SPF – short-pass glass filter; LPF – long-pass glass filter; GP – glass plate; PM – photomultiplier; PD - photodetector; Pol - Glan-Taylor polarizer; GP – glass plate. Red line stands for the fundamental beam path; blue line stands for the generated SHG beam path. Green lines show the fluorescence detection beam path.

To generate the 1PA excitation beam, single reflection ($\sim 4\%$) off a glass plate (GP1) was focused on a Type I phase matched BBO crystal of 6 mm thickness that generated second harmonic (blue) light. A $\lambda/2$ plate in front of the SHG crystal rotated the pump beam polarization to horizontal direction in order to assure that SHG had the same (vertical) polarization as the fundamental beam. Therefore the 1PA excitation occurs at half the wavelength of the 2PA excitation: $\lambda_{1PA} = \frac{1}{2}\lambda_{2PA}$. Residuals of the fundamental wavelength (red) were cut off by glass short-pass filter (SPF1) placed after the BBO crystal. At short wavelengths, ~ 700 nm, the glass plate was replaced by a flip mirror to compensate for decrease in the laser output power. After GP2 the two beams followed the same path and were incident on the same spot at the sample. A focusing lens (L2, 125 mm) which combines with L3 and a diaphragm placed before L3 were used to shape the blue beam such as to have the same or smaller spot size as the red beam at the sample location over the measured path length. The exact collimation of the blue beam regarding red beam was ensured by their center coincidence on the CCD-camera profiler.

Figure 22 shows the side view of fluorescence of a solution of Fluorescein along 1PA and 2PA excitation paths. Blue laser for 1PA excitation was shifted slightly off center to allow the comparison. Both beams display roughly constant emission intensity along the path which suggests a constant beam profile throughout the sample. Although the blue beam shows a fluorescence induced emission arising from a larger volume in Figure 22, this excitation can be further reduced thanks to the iris in front of L3 to better match the red beam diameter.

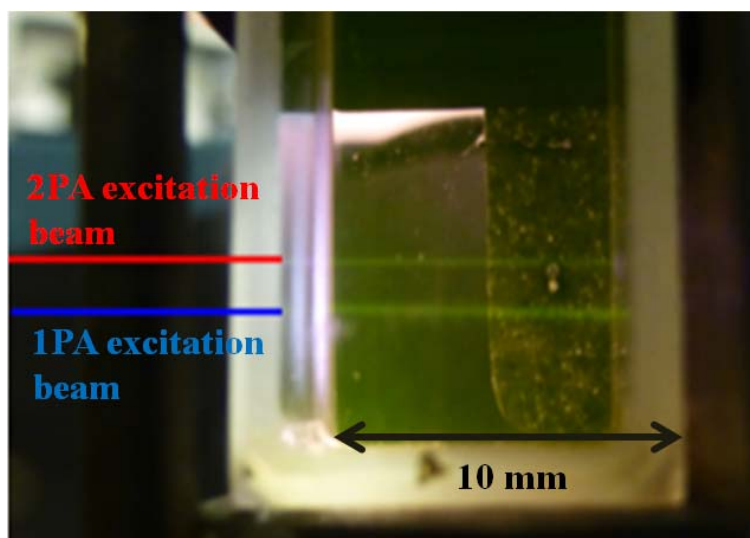


Figure 22: Example of fluorescence signal excited simultaneously by 1PA and 2PA in a Fluorescein solution. The two excitation beams are represented with blue line for 1PA and red line for 2PA. For the purpose of this photo, 1PA excitation beam was shifted down below the 2PA excitation beam.

Fluorescence signal was collected from the first 2 mm section of the sample solution at 90° from the excitation direction. The rest of the solution fluorescence was masked by a sheet of thick black paper. The 2 mm horizontal fluorescence track was imaged with $\sim 1:1$ magnification on the entrance slit of a scanning diffraction grating spectrometer (LOMO MDR-12). The height of the vertical spectrometer slit is much larger than the fluorescence image. Scattered laser light was additionally suppressed by a stack of short-pass color glass filters (SPF2). Inside the spectrometer, the spectral dispersion occurs in the horizontal plane by diffraction on a $1200 \text{ lines mm}^{-1}$ grating. The combination of the rotating grating and adjusting the exit slit, typically set at 2 mm, permits the selection of a small 6 nm portion of the fluorescence spectrum centered on λ_{reg} , which was detected with a photon counting module (Hamamatsu H6240-01) coupled to a frequency counter with PC readout. By selecting a small spectral width around the maximum, we measured a stable signal with reduced background signal.

The red beam power at the sample was varied manually rotating a $\lambda/2$ plate that was positioned in front of a Glan-Taylor linear polarizer (GL10-B Thorlabs) (Pol). The relative average power of the fundamental beam at the sample was monitored by reflecting a portion of the incident beam to an integrating sphere silicon photodetector (Thorlabs S140C) coupled to an optical power meter (Thorlabs PM100A). The signal from the integrated sphere detector was compared to that obtained with another optical power meter (Coherent FieldMate) with a thermoelectric probe (Coherent Powermax PM10) placed directly in front of the sample with the $\lambda/2$ plate rotated to a position where the signal is at maximum.

Absolute blue beam power for 1PA was measured with an integrating sphere silicon photodetector (Thorlabs S140C) or with a standard silicon photodetector (Thorlabs S120VC) placed directly in front of the sample.

A flip mirror MF (Figure 21) was redirecting the laser to a modified second harmonic auto-correlator (INRAD 5-14A). The eventual broadening of the pulse through the optical elements from GP1 to sample is below 0.5% (see appendix B). Figure 23 shows a scheme (left) and a picture of the auto-correlator used for the determination of the temporal width of the excitation laser pulse. Briefly, a variable delay was produced by rotating glass plates (glass thickness 1 mm) and non-collinear second harmonic generation was produced in 0.1 mm BBO crystal, SHG signal was measured by the use of a photo-detector connected to Keysight oscilloscope (DSOS404A). Further details about the auto-correlator calibration are presented in appendix D.

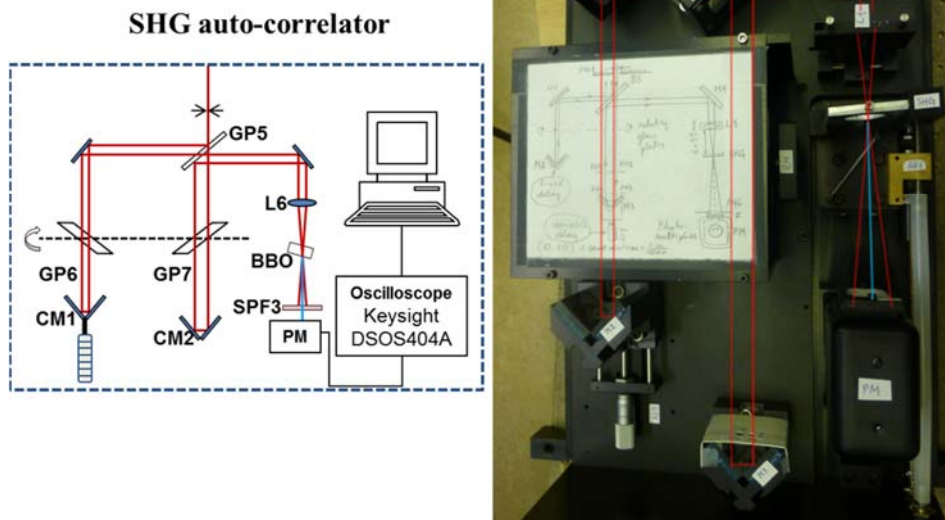


Figure 23: Schematic (left) and photo (right) of the SHG auto-corellator, modified by A. Rebane. L – focusing lens; GP – glass plate; CM – corner mirror; SPF – short-path filter.

To minimize potential detrimental effect of thermal lensing (refraction of light due to change of index of refraction with temperature) in the sample solution, especially for tetrahydrofuran (THF) and methanol solutions, the beam profile was also recorded after passing through the sample, while stirring the solution. If the thermal distortions were still observed to change the beam diameters by 5 - 10% or more, then the average laser power was reduced by factor 10 using a 100 Hz optical chopper (Thorlabs MC2000) that was inserted before the lens L3, where the spot size was at the minimum. As an example, Figure 24 shows how the beam profile tends to lens due to thermal effect in the solvent. Figure 24 a) is the beam profile recorded for the excitation beam and Figure 24 b) is the reduced beam profile after installing a cuvette filled with MetOH in the sample holder. Stirring the solution helps to dissipate the local heat, but in case of MetOH it wasn't enough to reconstitute perfectly the beam profile onto the camera, underlying that some distortion are still present. While using the optical chopper, we can see in Figure 24 d) that distortion is absent.

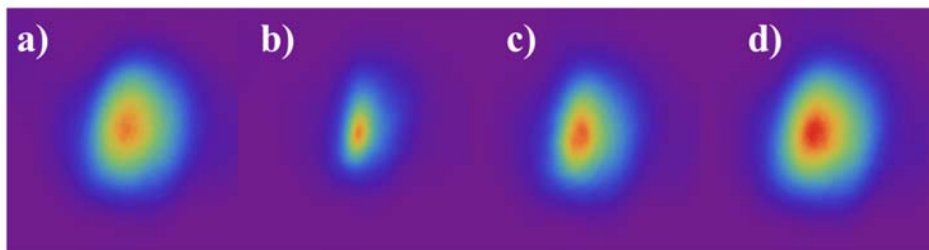


Figure 24: Beam profile image in a color scale of a) the excitation beam; b) the excitation beam after crossing a 10 mm cuvette filled with MetOH; c) the excitation beam after crossing a 10 mm cuvette filled with MetOH stirred and d) the excitation beam after crossing a 10 mm cuvette filled with MetOH while the average power is reduced with the use of the chopper.

4.1 Evaluation and selection of fluorophore/solvent systems suitable as 2PA standards

Standards should be selected such as to facilitate their use, i.e. they should be commercially available, or at least can be synthesized without any major difficulties. They must preferably show a sufficiently large 2PA cross-section in the selected range of excitation wavelengths. The standards should be well soluble under ambient conditions up to mM concentration (minimal aggregation) and the solutions should be stable both in the dark as well as under stringent illumination conditions. The set of standard should cover a sufficiently large emission wavelengths range as explained in paragraph 2.7.3. Because in our method we determine the 2PA cross-section by direct comparison of the 2PA fluorescence emission and 1PA fluorescence emission, our standard must present enough strength for 1PA and 2PA for the same transition in the visible region.

Fluorescein dianion in water buffer pH11 was proposed as a standard by Xu et al. [43] and Makarov et al. [44]. It offers high quantum yield of fluorescence ~ 0.9 and a relatively large peak 2PA cross-section ~ 40 GM, accompanied by high photostability and excellent solubility. On the other hand, Rhodamine B (Rhodamine 610), which was also proposed previously, appeared in different solvents as a mixture of at least three different forms: (a) intensely colored protonated cation form; (b) zwitterion and (c) colorless lactone [83-85]. In water, the equilibrium between zwitterion and lactone form has a reported value of $pK_a = 8.3$ whereas in methanol the equilibrium between zwitterionic and cationic form has $pK_a = 3.1$. We observed that, in deuterated water, zwitterionic form tends to aggregate at concentrations as low as 10^{-5} M as manifested by a distinct change of the 1PA spectrum with the rise of the dimer absorbance peak at 523 nm as shown in Figure 25. According to literature, this effect appears in slightly

more concentrated solution in pure water [85]. Our estimation is that 1% of molecules are dimer at 10^{-5} M and up to 40% at 10^{-4} M concentration.

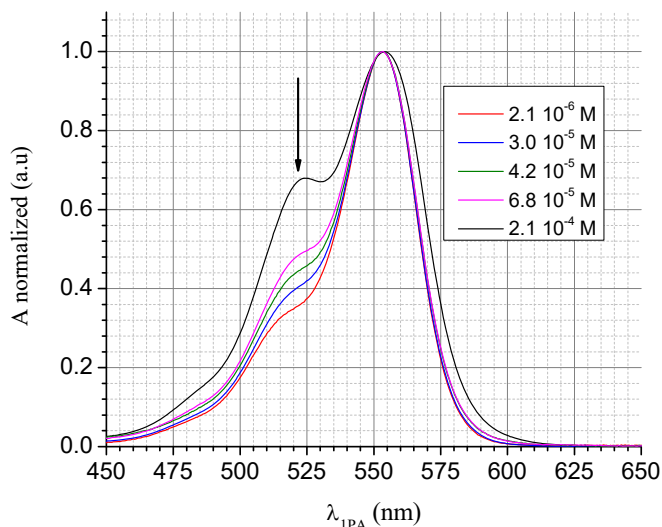


Figure 25: Changes observed in the shape of absorbance spectrum of Rhodamine B in deuterated water with concentration ranging from 10^{-6} M to 10^{-4} M. With increasing concentration, the absorption band of the dimer centered on 523 nm becomes more prominent.

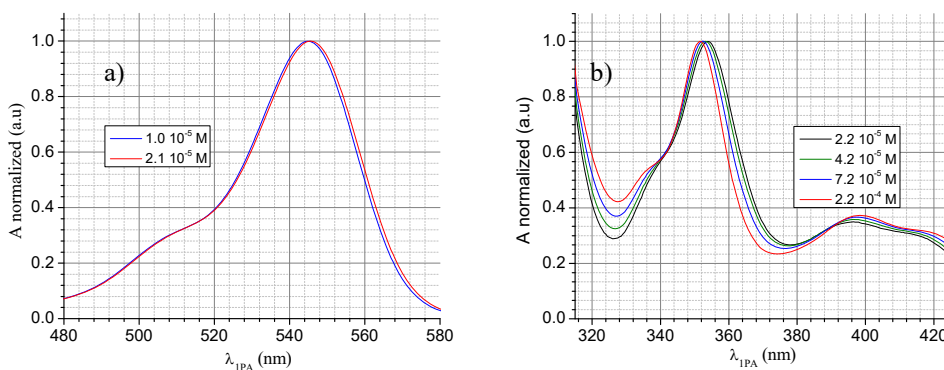


Figure 26: a) Bathochromic shift of 2 nm for the maximum absorption peak for Rhodamine B in methanol, when raising the concentration from 1.0×10^{-5} M to 2.1×10^{-5} M, b) Hypsochromic shift of the peak corresponding a higher transition when raising the concentration from 2.2×10^{-5} M to 2.2×10^{-4} M.

We found that in methanol, with increasing concentration, the equilibrium is displaced toward the cationic form due to increases of the acidity and is visible in the 1PA spectrum for concentration as low as 10^{-5} M by a bathochromic shift of the maximum

peak and more noticeable hypochromic shift of a higher electronic transition band at 355 nm as shown in Figure 26.

Therefore water or heavy water solutions of Rhodamine B can be considered as transition systems between solutions of monomers and aggregates in the whole range of usual studies. Because the different monomers and aggregates might have different optical properties, and their proportion is subject to change depending on the exact concentration, we excluded Rhodamine B as a viable high accuracy standard. In contrast, Rhodamine 6G has a unique form and doesn't suffer from aggregation, at least up to 1 mM concentration. Therefore Rhodamine 6G in methanol is preferred in our set of standards.

Perylene, Lucifer yellow and Chloroanthracenes from Makarov et al. [44], Cascade Blue, DiI, Indo-1, DAPY and Dansyl hydrazine from Xu et al. [43] are all covering essentially the same region <750 nm with relatively low 2PA cross section peak, $\sigma_{2PA} < 10$ GM. Because some of the biological markers absorb in the near-UV region, we must propose at least one standard in this region. We kept 9-Chloroanthracene in this study since it offers the highest cross-section, among the fluorophores cited before, and presents great stability, more than a month. We also include, as an alternative, 4,4'-bis-(diphenylamino)stilbene (BDPAS) proposed by Makarov et al. [44], which has low stability in solution, about 1 week, but has a relatively high 2PA cross-section, up to ~ 150 GM.

7,7',7''-(1,3,5-triazine-2,4,6-triyl)tris[9,9-didecyl-N,N-diphenyl 9H-Fluoren-2-amine CAS Registry Number, 517874-02-13 (AF455) was synthesized by Kannan et al. [89] and present a large 2PA cross-section maximum of ~ 200 GM, which is highly desired for accurate measurements. Therefore, for the intermediate wavelengths region, 720 – 1050 nm, we focused our interest on Prodan, Coumarin 153 and AF455. These 3 dyes also present red shift solvatochromism, more pronounced in their fluorescence than in their absorbance spectra, with increasing the solvent polarity. The solvatochromism shifts observed for Prodan and C153, when the solvent changes from toluene to dimethylsulfoxide (DMSO), and for AF455, when the solvent changes from toluene to tetrahydrofuran (THF), are presented in the following Table 4.

Table 4: Solvatochromism shift with increasing the solvent polarity. Initial solvent is toluene for all the chromophores. Data are deduced from our measurements shown in Appendix H.

Comp.	λ_{1PA} shift (nm)	λ_{em} shift (nm)	Solvent polarity increase
Prodan	9	45	0.345
C153	19	72	0.345
AF455	4	51	0.129

Solvatochromism can be used as an advantage when applied to 2PA spectroscopy using a reference standard. Indeed, if Prodan, C153 or AF455 is chosen because of its good 1PA spectrum overlapping with the sample, one can tune the fluorescence with

the right ratio of toluene and either DMSO or THF in order that the fluorescence emission spectra of the standard match better the one of the sample. The new proposed reference fluorophores set comprises both commercial organic dyes such as 9-Chloroanthracene in DCM, Prodan in toluene, Prodan in DMSO, Coumarin 153 (C153) in toluene, C153 in DMSO, Fluorescein dianion in water buffer pH 11 and Rhodamine 6G (Rh 6G) in methanol (MetOH), but also custom-synthesized compounds such as BDPAS in DCM, AF455 in toluene, AF455 in THF. This set covers 680 - 1050 nm excitation wavelength range in 2PA. The molecular structure of these chromophores is presented in appendix F. Their combined fluorescence emission spectra, shown in Figure 27, cover the 375 – 600 nm range.

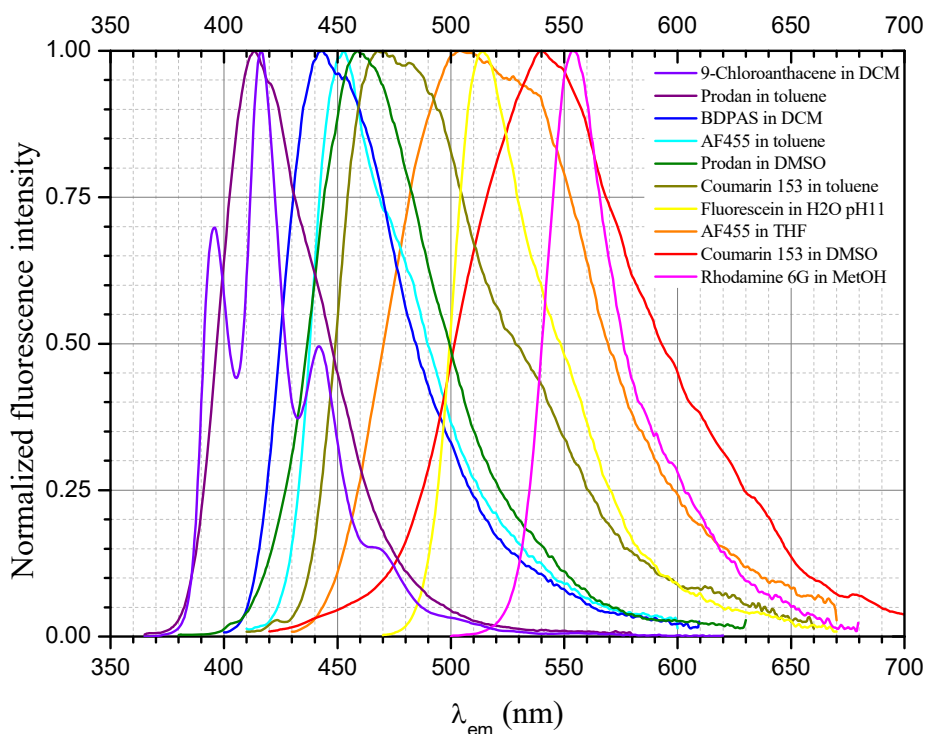


Figure 27: Normalized fluorescence spectra of the selected standards.

4.2 Protocol for higher accuracy measurements of the absolute 2PA cross-section

The determination of the 2PA cross-section needs precise measurement of 9 parameters which are:

- The 2PA excitation beam temporal profile and the pulse duration Δt ,
- The 2PA excitation beam spatial profile and the vertical and horizontal spot size Δx and Δy ,
- The sample concentration, N_g , and its extinction coefficient spectrum in the solvent used,
- The 2-photon excited fluorescence signal F_{2PA} and the corresponding average excitation power W_{2PA} ,
- The 1-photon excited fluorescence signal F_{1PA} and the corresponding excitation power W_{1PA} .

4.2.1 Sample preparation and procedure for extinction coefficient determination

Prodan, Coumarin 153 (C153), Fluorescein, 9-Chloroanthracene (9-ChlA) and Rhodamine 6G (Rh 6G) were obtained from Aldrich and were used as received. 4,4'-Bis(diphenylamino)-stilbene (BDPAS) was custom-synthesized by K. Schanze group (U of Florida) as described in [86]. AF455 was provided by Dr. S. Tan from the Air Force Research Laboratory. The synthesis of AF455 is described in [87-88]. All solvents were purchased from Sigma-Aldrich and were used without further purification.

Stock solutions were prepared by mixing 10 mL of solvent with 1 - 3 mg of dry dye, weighted with 1% precision, using Mettler-Toledo Model AT2611 analytical balance.

A set of daughter solutions with maximum absorbance in the range $OD = 0.5 - 1.5$ were prepared from the stock solution. This range provides most reliable measurements of OD with the spectrophotometer (Shimadzu UV-3600Plus).

Linear absorption spectra were obtained with Shimadzu UV-3600Plus spectrophotometer in a dual beam configuration, using pure solvent as reference. The sample and the reference were contained in 10 mm quartz cuvettes. To ensure that no impurities were added in the solutions during the dilution step and to exclude possible dimerization or aggregation of the dye in the solution, the normalized spectrum for each daughter solution were compared. When the normalized spectra did superimpose perfectly, then the absorption value at the peak versus the concentration was fitted with a linear model as shown in Figure

28. The slope of the fit is the molar extinction coefficient in $M^{-1} cm^{-1}$ at the maximum of the absorption band.

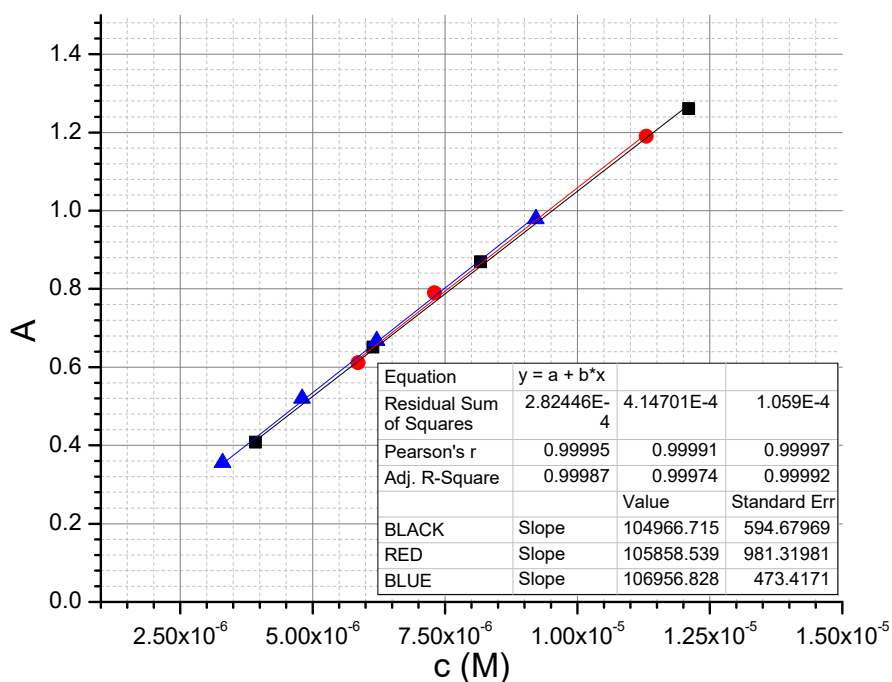


Figure 28: Molar extinction coefficient determination for AF455 in THF at the absorption peak 415 nm. Each set of solution arising from the same stock solution share the same color representation. Square symbols represent the absorbance measured for the corresponded concentration whereas straight line is the best fit.

Because a potential error may arise from the weighting of the dry dye, the procedure was repeated two times, by preparing 2 more stock solutions, which allowed us to check the reproducibility of the determined extinction coefficient and to estimate the error made in this measurement. Average extinction coefficients determined at the maximum of the absorption band along with the associated estimated error are presented in Table 5. The average extinction value determined at the maximum was used to rescale the normalized spectrum, thus providing the molar extinction coefficient spectrum of the standard. The standard extinction coefficient spectra are presented in Appendix H.

Table 5: Molar extinction coefficient values determined at the absorption peak.

Comp.	Solvent	$\epsilon_{1PA}(\lambda_{1PA})$ M ⁻¹ cm ⁻¹ (nm)	Error %
BDPAS	DCM	5.26 10 ⁴ (388)	2%
Prodan	toluene	1.98 10 ⁴ (349)	4%
Prodan	DMSO	1.75 10 ⁴ (358)	1%
C153	toluene	2.00 10 ⁴ (408)	6%
C153	DMSO	1.85 10 ⁴ (427)	6%
AF455	toluene	1.17 10 ⁵ (419)	2%
AF455	THF	1.06 10 ⁵ (415)	1%
Fluorescein	H2O pH11	8.86 10 ⁴ (491)	6%
Rh 6G	MetOH	1.22 10 ⁵ (528)	6%
9-ChlA	DCM	8.02 10 ³ (570)	4%

To determine the absolute 2PA cross-section, the standard linear absorbance at the excitation wavelength $\lambda_{1PA} = \frac{1}{2}\lambda_{2PA}$, must be well below OD = 0.2 to limit primary inner filter effect, i.e. to ensure a relatively constant fluorescence signal along the beam path through the sample. This OD corresponds to a depletion of less than 10% in the 1PA excitation photon flux over the 2 mm pathlength for which the fluorescence is detected. Samples were prepared by dissolving dry dye in the solvent. The normalized spectrum was compared with the normalized extinction coefficient spectrum to make sure that the dye was completely dissolved and that no impurities were added. Then the ratio of the absorbance and the extinction coefficient spectra give the concentration value thought the Beer-Lambert's law:

$$C = \frac{A}{\epsilon_{1PA}l}. \quad (91)$$

In practice, best estimation of the sample concentration is obtained by averaging the determined concentration from Equation (91) at different wavelength, where the absorbance is in the 0.05 - 1.5 range. The standard deviation of the concentrations estimated in this manner, usually below 5%, will be included in the final error calculation of the 2PA cross-section.

4.2.2 Procedure for evaluating the excitation beam parameters

The 2PA excitation beam profile was measured in the absence of sample.

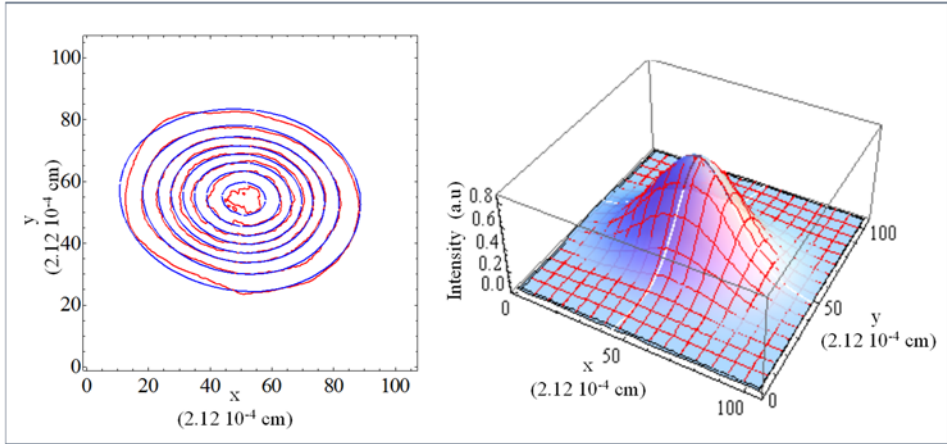


Figure 29: Example of beam profile (red matrix) and its asymmetrical Gaussian fit for $\lambda=812 \text{ nm}$ presented in a topographic (left) and 3D (right) view using Mathematica program.

Figure 29 shows the contour plot (left) and 3D rendering (right) of the beam profile at a selected wavelength, 812 nm. The x and y axis are scaled according to known camera pixel size ($6.45 \mu\text{m}$) and also by taking into account the magnification factor. The beam profile is elliptic, slightly rotated from horizontal direction, and may show some asymmetry. Thus, the best fit to the experimental profile was obtained with an asymmetric Gaussian function which is shown in red lines in Figure 29.

In Appendix E, we collected some example of beam profiles at different wavelengths and determined on different days. Figure 30 summarize the full-width at half maximum values on the main elongation direction. The data shows little reproducibility of the beam profile at a single wavelength. The laser spatial beam profile varied as a function of wavelength but also changed from day to day depending on the alignment of the laser. The beam size, on average, increases up to 50% when changing the wavelength from 680 nm to 950 nm.

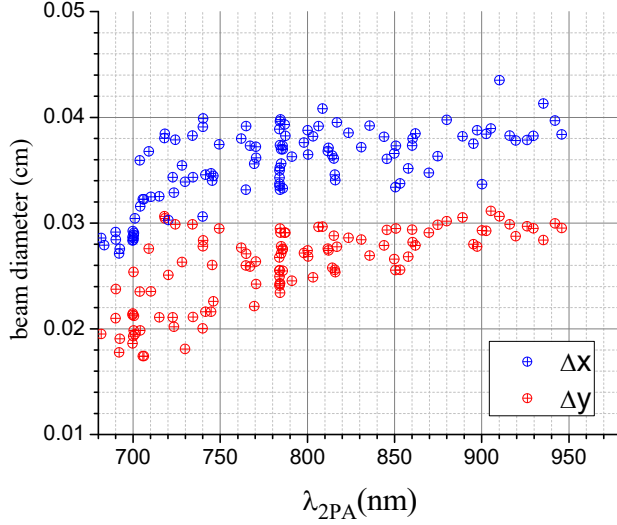


Figure 30: Full width at half maximum of the beam profile measured at different wavelengths and different days.

The beam diameter lies within 0.02 – 0.04 cm. Neglecting the wavelength dependence of the beam diameter can result in a 2PA cross-section error as large as 200%. The beam ellipticity ($e = 1 - D_{min}/D_{max}$) changes from 0.28 to 0.37. Ignoring this ellipticity could result in up to 50% error in the 2PA cross-section.

Since we used asymmetric Gaussian fit, the product $\Delta x \Delta y$ of the full-width at half maximum in Equations (83) and (86) was amended by a shape correction factor, g_p , which was evaluated based on the asymmetric Gaussian fit model as

$$g_p = \frac{\ln 4}{\pi} \frac{\iint \Phi_{2PA} dx dy}{\iint \Phi_{2PA}^2 dx dy}. \quad (92)$$

Maximum error of the beam shape measurement was estimated by relative quadratic mean between the image and the fit and taking into account 2% due to the estimated accuracy of the magnification factor,

$$\Delta g_p = \frac{\sqrt{\iint (\Phi_{2PA} - fit)^2 dx dy}}{\sqrt{\iint \Phi_{2PA}^2(x,y) dx dy}}. \quad (93)$$

Maximum error was found to be around 7% which constitutes the largest contribution to the overall error bar of the absolute σ_{2PA} value. One large contribution to this error is due to the poorly defined background. The background does not contribute to 2PA, consequently if σ_{2PA} measurements show good reproducibility, then we would be allowed to reduce the final error bar.

The pulse temporal intensity profile was also obtained for each wavelength. Figure 31 shows in blue symbols the oscilloscope trace of the SHG auto-correlation function measured at 786 nm rescaled according to the delay induced

in the auto-correlator. The resulting signal was well fitted with a Gaussian function, showed in red line. We estimated a maximum experimental error of the pulse temporal full-width at half maximum Δt to be about 2 %, this error may result from beam misalignment and detector response nonlinearity in the auto-correlator.

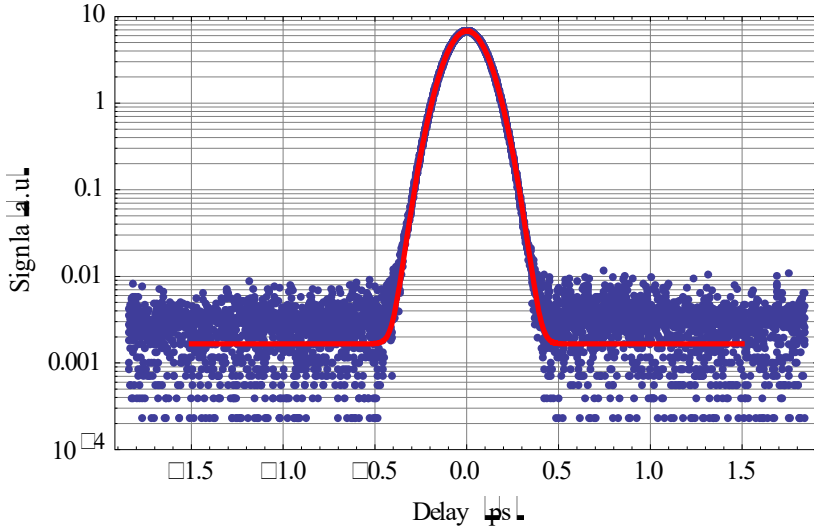


Figure 31: Example of auto-correlation function (blue dot) and its Gaussian fit (red line) for $\lambda=786$ nm with Chi-square exceeding 0.999 using Origin program.

The pulse duration taken at different days versus wavelength is presented in Figure 32. The pulse duration has a global tendency to decrease by about 40% from 200 fs below 700 nm to 120 fs close to 980 nm. As in the case of the beam profile measurement, the day-to-day data points show a substantial spread. Because of the absence of reproducibility, the pulse duration was measured every time for each day and wavelength.

Another useful indicator, for the pulse characterization, is the time-bandwidth product, which shows how close is the pulse to the transform limit set by its spectral width. The minimum value for a Gaussian profile is 0.441. The theoretical pulse duration estimated from laser spectral width are represented in magenta crosses in Figure 32 and have a smaller value than the measured one represented in black symbols and show a decrease from 200 fs at 680 nm to 100 fs close to 980 nm. Determining the pulse duration from the spectral bandwidth could result in above $\sim 11\%$ and up to 40% error in the 2PA cross-section. We note that if the wavelength dependence of the pulse duration would be neglected, by assuming the overall pulse duration of 100 fs, given by the manufacturer, then it results in up to 50% error in the 2PA cross-section determination.

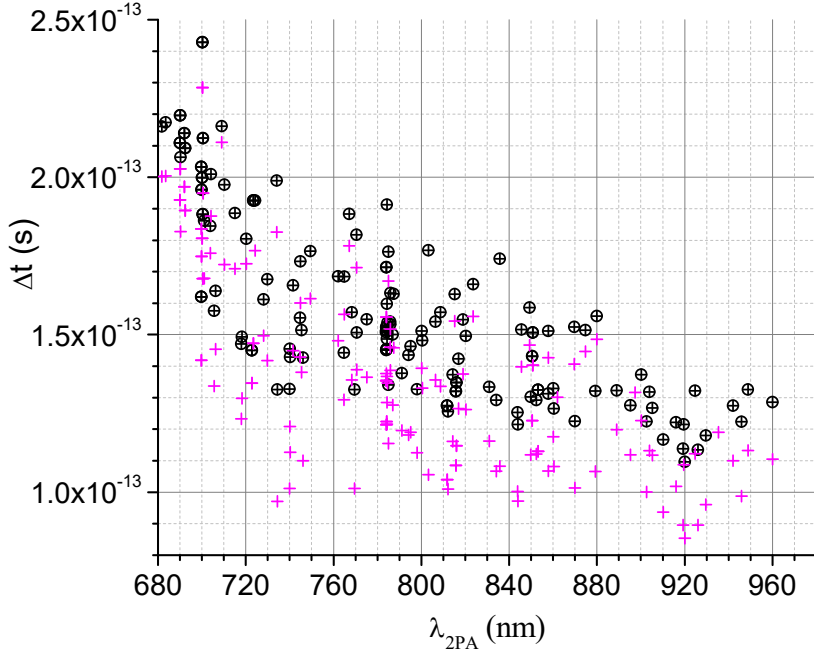


Figure 32: Pulse duration at different wavelength and at different days of measurements. Black symbols are the measured pulse duration via the auto-correlator. Magenta crosses are the estimated minimum pulse duration Δt_0 deduced from the measured spectral bandwidth.

The calculated time-bandwidth product is randomly spread over the wavelength range as shown in Figure 33 a). Its distribution, in Figure 33 b), shows a peak at ~ 0.49 and a mean value of ~ 0.51 . This indicates that the pulses are slightly chirped:

$$\Delta t^2 = \Delta t_0^2 + \left(\frac{4\beta \ln 2}{\Delta t_0} \right)^2, \quad (94)$$

where Δt_0 is the chirp-free duration of the transform limited pulse and β the linear chirp coefficient [90].

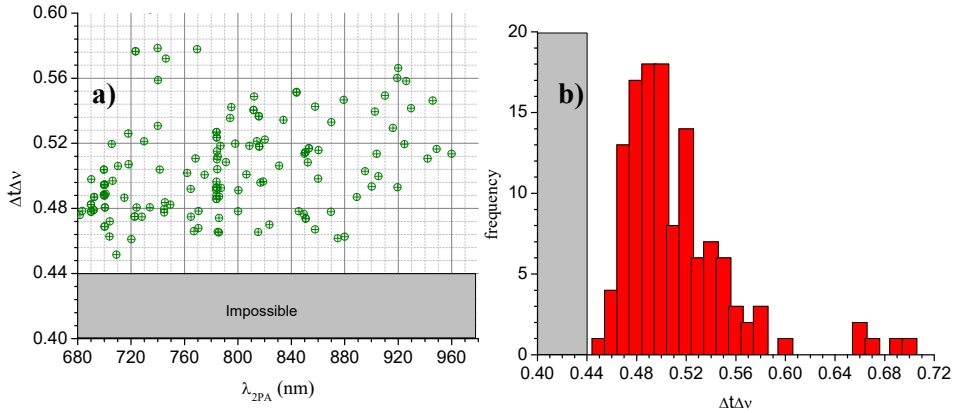


Figure 33: Time-bandwidth product calculated from the pulse duration fit and spectral fit with Gaussian functions. **a)** Time-bandwidth value versus the wavelength. **b)** Distribution of all the time-bandwidth value.

As long as the 2PA cross-section does not depend on the pulse duration, the presence of a chirp may be neglected. Comparison with two-photon shape from independent set-up, carried out below, will indicate if the chirp has any detrimental effect or not.

4.2.3 Procedure for 1PA and 2PA fluorescence signals determination

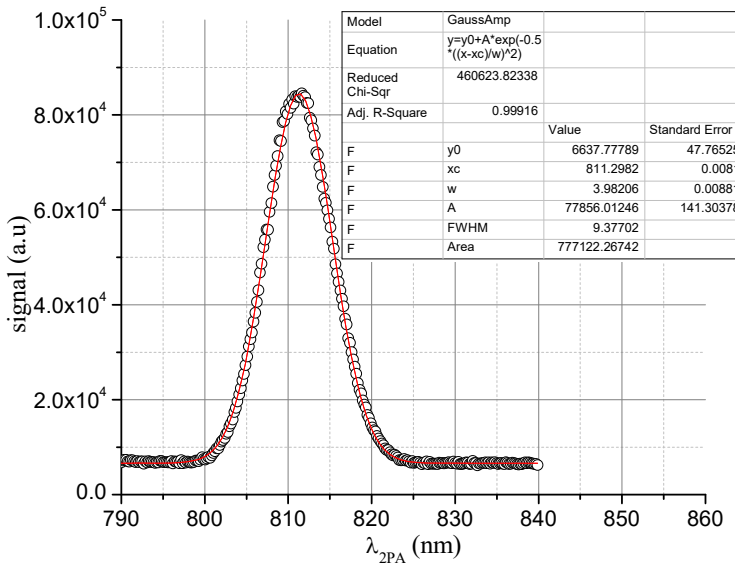


Figure 34: Example of fundamental laser spectrum (black circles) set at 811 nm with a full width at half maximum of 9.4 nm fitted with a Gaussian function (red line) using Origin program.

During the 1PA and 2PA fluorescence acquisition, the position laser spectrum, as shown in Figure 34, was carefully tracked to not deviate more than 0.2 nm from the set position. If the deviation is larger than 0.2 nm, the 2PA dependency on the excitation signal shift from quadratic dependence, but most importantly the wavelength conversion in the BBO decreases in efficiency and the 1-photon excitation fluorescence would not correspond to the prior measured excitation beam power, leading to an increased error in the determined absolute 2PA cross-section.

At each acquisition, to guarantee the quadratic power dependence of the 2PIF signal on the excitation power, the power is gradually attenuated by rotating the $\lambda/2$ plate in front of the Glan-Taylor polarizer. The average fluorescent signal F_{2PA} and average power W_{2PA} were measured simultaneously with 1s integration time and averaged over 100 acquisitions. The log-log dependence of the resulting average 2PIF signal F_{2PA} on the average power W_{2PA} was fitted with a linear function using bivariate York method, which iteratively minimizes the distance between data points and the fitted line in the x- and y-direction. York method may be considered a more precise fitting method than the least-square fitting, which doesn't include uncertainties in the x-values.

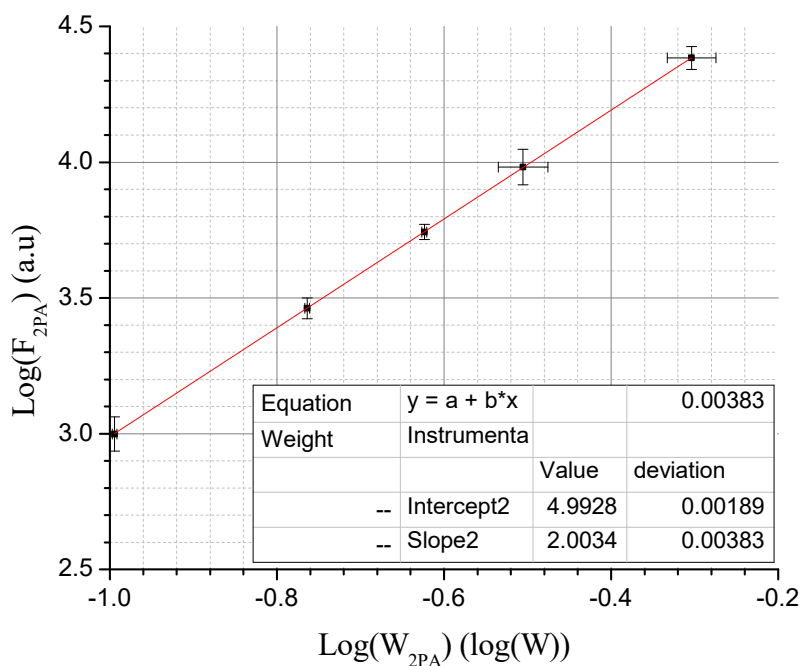


Figure 35: Example of the quadratic power dependence using log-log linear fit of F_{2PA} vs. W_{2PA} recorded for Coumarin 153 in toluene at 816 nm. Experimental data (black squares) are fitted with linear regression using York method (red line) existing in Origin program and show a power law coefficient of 2.00.

Figure 35 Shows, in black symbols with x- and y- error bars, an exemplary power dependence of the measured fluorescent signal for Coumarin 153 in toluene at 816 nm excitation wavelength. Solid red line stands for the York fit. Using York method, we measured a 2PIF signal dependence on the power of 2.003 ± 0.004 and a deduced ratio $\frac{F_{2PA}}{W_{2PA}} = 98365 \pm 0.5\%$.

Most of our measurements showed a power law coefficient in the 1.98 - 2.02 range. We accepted measurements with a power law coefficient in the 1.96 - 2.04 range. Figure 36 shows a compilation of the power law coefficient arising from York fitting for all the measurements performed. They appear to be randomly distributed around the central value 2.00 with a deviation, which doesn't exceed 0.02. This ensured that 2PA was not accompanied by other spurious phenomena such as residual linear absorption, thermal lensing and saturation.

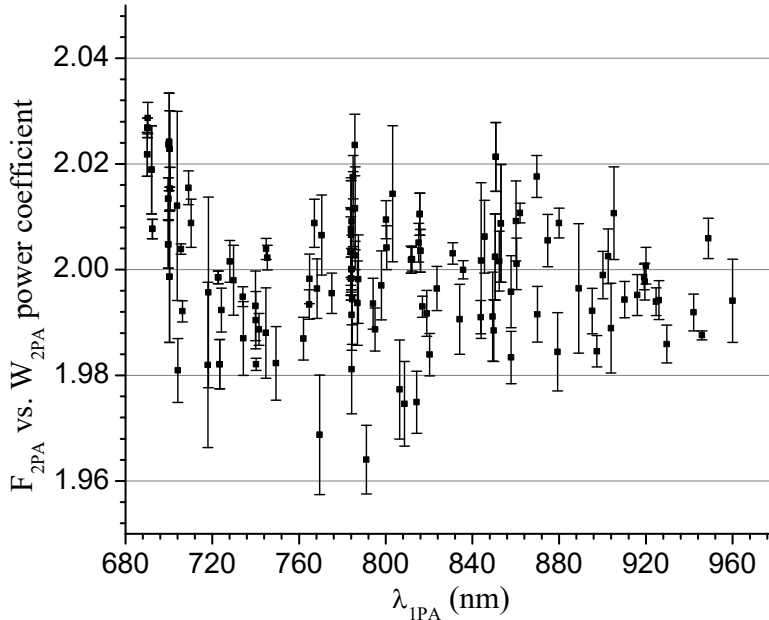


Figure 36: Power law coefficient of the 2PIF signal on the excitation power at different wavelength with different standard sample. Data points are cumulative over all the experiments performed.

To provide increased accuracy, in Equations (83), for the determination the 2PA shape function, and in Equation (86), for the determination of the absolute 2PA cross-section, the intercept of the fit (*intercept2* in Figure 35) to the power of 10 was used in the place of the quotient:

$$\frac{F_{2PA}}{W_{2PA}^2} = 10^{Intercept2}. \quad (95)$$

The standard error given by the fit (Figure 35) was included in the final cross-section error estimation.

The 1-photon excitation beam power was adjusted by using continuously variable metal-coated filter wheel (ND1). The power W_{1PA} was measured immediately before the start of the fluorescence signal acquisition F_{1PA} to minimize possible laser power drift. Both average power W_{1PA} and average fluorescent signal F_{1PA} were measured with an integration time of 1 s and averaged over 100 acquisitions. The resulting F_{1PA} signal vs. incoming power W_{1PA} was fitted with a linear function using York method to verify the linear relation. Figure 37 shows, in black symbols, average fluorescence signal F_{1PA} versus the average power W_{1PA} for Coumarin 153 in toluene at 816 nm excitation wavelength, with the same solution and geometry as for the 2PA fluorescence detection (Figure 35). Blue line stands for the best York fit.

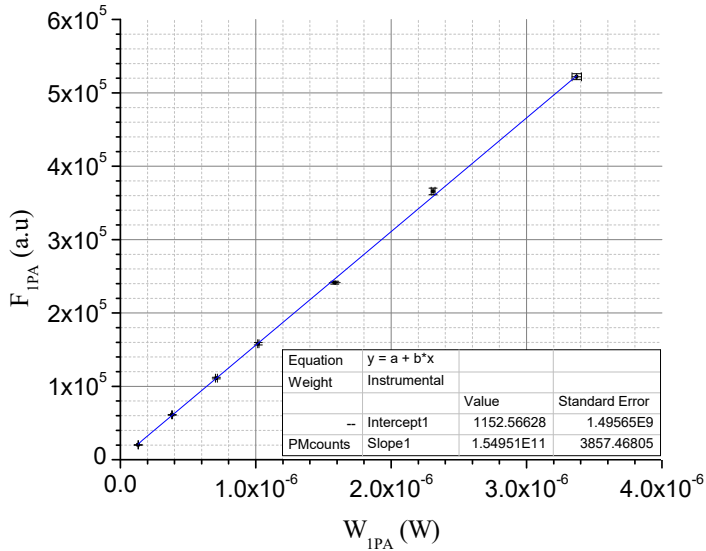


Figure 37: Example of the linear dependence of the fluorescence signal F_{1PA} vs. the blue beam power W_{1PA} after 1-photon absorption recorded for Coumarin 153 in toluene at 816 nm. Experimental data (black point with error bars) are fitted with linear regression using York method (red line) existing in Origin program with R-squared of 0.999.

For increased accuracy in the absolute 2PA cross-section determination, the slope of the fit (*slope1* in Figure 37) was used in Equations (86) in the place of the quotient:

$$\frac{F_1}{W_1} = slope1. \quad (96)$$

The standard deviation given by the fit was included for the 2PA cross-section error bar estimation.

4.3 Verification of 2PA spectral shape obtained from an independent experiment

As we pointed out earlier, the reference standards developed here comprise two different set-up data: (a) 2PA spectral shape and (b) absolute value of σ_{2PA} at selected wavelength. High accuracy spectral shape were obtained in a series of independent experiments performed at Montana State University (MSU) as described in paper I in appendix J. In this thesis we focus on the absolute σ_{2PA} , however, we also performed, to some degree, spectral shape measurements exploiting Equation (83) to verify the results obtained at MSU.

Figure 38 presents the 2PA shape function of Fluorescein in a water buffer pH 11 measured by two complimentary experiments, where the red data points stand for the measurements performed in this thesis (KBFI) and the grey open circles stand for the measurements performed in MSU.

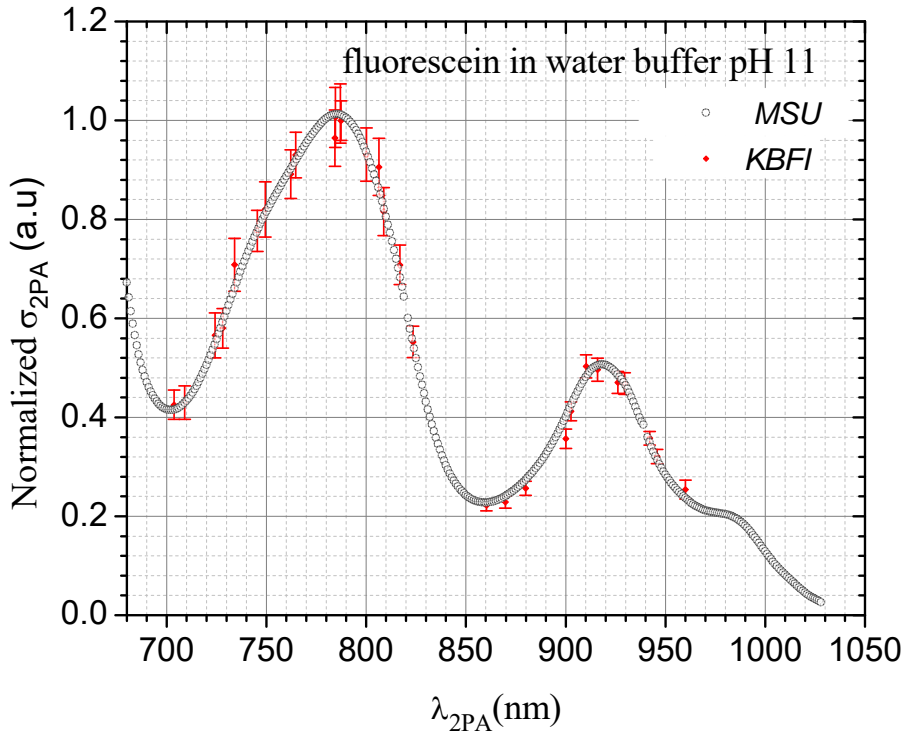


Figure 38: Comparison between independent 2PIF measurement techniques for the determination of 2PA shape function for Fluorescein in water buffer pH 11. Grey circles - with scanning laser set-up, red symbols - with manually tuned laser.

2PA shape functions for other standards are presented in Appendix G. We focus mainly on Fluorescein in water buffer pH 11 and Rhodamine 6G in MetOH because these 2 dyes present an absorption spectrum with at least 2 absorption peaks, as shown in Figure 38, hence 2PA shape showing high dynamic variations is the better choice to confront results. One might expect that different measurement systems behave slightly differently, especially regarding excitation photon flux parameters, leading to deviation outcome. Nevertheless, we achieve a good agreement between the two totally independent measurements, which serve as a confirmation of the high accuracy of both experiments.

The cumulative deviation error, over all wavelengths, estimated of our relative 2PA measurement compared to the one obtained in MSU is presented in Figure 39. The deviation error is symmetrically spread around the mean value -0.1% with a standard deviation of 3.9% . This allows us to estimate that the overall uncertainty of the 2PA shape functions presented here is about 5% , in accordance with the estimation provided in paper I in appendix J. Since the two experiments were truly independent, we conclude that the relative accuracy of the photon flux measurement and, accordingly, the relative beam spatial and temporal profiles accuracy, was also about 5% or better. As a consequence, it also attests that the observed pulse chirp has no significant consequence and that the determined error on the shape correction factor can be reduced (Equation (93)).

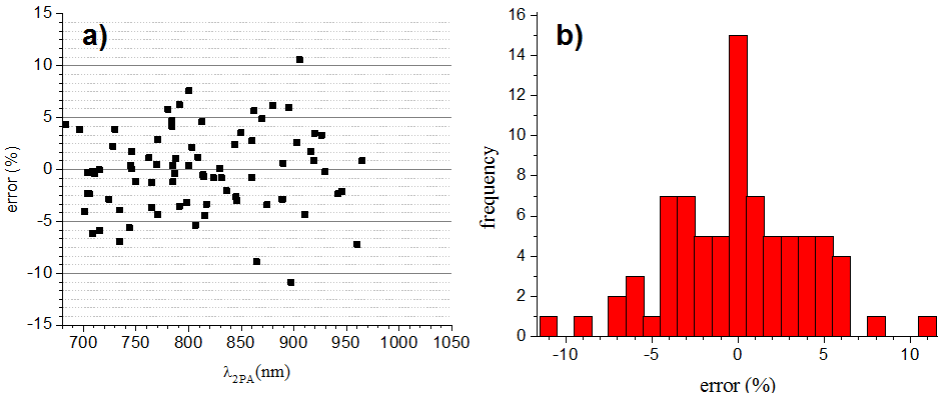


Figure 39: Discrepancy in the determination of the 2PA shape function $\sigma_{2PA}^{a.u}$ between the two independent set up cumulated from all the experiments performed. **a)** presents the error in % versus the laser tuning wavelength. **b)** presents the histogram of the error distribution obtained.

4.4 Determination of the maximum absolute cross-section for each standards

In the case of the absolute cross section measurement, there is an additional uncertainty due to the measurement of the 1-photon excited fluorescence. Firstly, for this measurement, the 1-photon excitation beam should be aligned to illuminate the exact same sample volume, or smaller, as the 2PIF excitation beam. If the beams are even slightly misaligned, then the two fluorescence signals may no longer be collected from the exact same sample volume. Secondly the maxima of the 2-photon and 1-photon spectra do not always coincide. When we tune the 2-photon excitation wavelength near the peak of the 2PA spectrum, then the corresponding 1-photon excitation wavelength may be located where the linear absorbance is very low or changes abruptly, thus making it difficult to accurately determine how many photons are absorbed in the sample. In this last case, any fluctuation of the laser away from the settled wavelength may have a significant impact on the accuracy of the determined fluorescence yield. To minimize this potential error we made sure that the laser peak wavelength remains constant during the measurements by tracking its spectral distribution continuously.

The main difficulty for Fluorescein in water buffer pH 11 and Rh6G in methanol stems from the fact that in their corresponding 1PA and 2PA spectral shapes do not match (see Appendix H, Figure H.7 and H.10). As a consequence, it is a challenge to find a concentration of the solution suitable simultaneously for one-photon and two-photon measurements. On one hand, the OD, at half the wavelength value for the 2PA peak, must be in the range of 0.05 to 0.2 in the 350 nm region such that 2PIF measurement is in accordance to our experimental conditions. On the other hand, it corresponds then to a high concentration leading to a saturated 1PA spectrum, even in 1 mm cuvette, thus hampering exact spectrophotometric evaluation of the concentration. As a consequence, our reported absolute 2PA for Fluorescein in paper I (Appendix J) was ~6% overestimated, essentially because of erroneous concentration estimation. Correction was made on the consideration of portion of the 1PA spectrum, which were perfectly superimposed with the extinction coefficient spectrum and by rejecting the range below 360 nm, where the solvent start absorbing as well.

The quadratic error in the 2PA cross-section, $\Delta\sigma_{2PA}$, is calculated based on the standard deviation obtained for the linear fit for 1PA and 2PA excitation fluorescence relative to the excitation power, the standard deviation of the average concentration based on the comparison of OD and extinction coefficient spectra, an estimated accuracy of 2% for the temporal profile and the cumulative relative quadratic mean deviation of the beam spatial profile,

$$\frac{\Delta\sigma_{2PA}}{\sigma_{2PA}} = \sqrt{\left(\frac{\Delta K_{2PA}}{K_{2PA}}\right)^2 + \left(\frac{\Delta K_{1PA}}{K_{1PA}}\right)^2 + \left(\frac{\Delta N_g}{N_g}\right)^2 + \left(\frac{\Delta g_p}{g_p}\right)^2 + 2\%}, \quad (97)$$

where $K_{2PA} = \frac{F_{2PA}}{W_{2PA}^2}$ and $K_{1PA} = \frac{F_{1PA}}{W_{1PA}}$. We can point out that, with our methodology, where we use shape correction factor and the ratio of fluorescence signal with respect to the excitation power, 5 parameters out of the 9 separated measurements are required for the absolute 2PA cross-section determination and the corresponding estimated error, hence improving the accuracy of the result.

As mentioned earlier, the determined error of the beam profile, due to the background contribution, gives the biggest contribution to the final error of about 7% whereas our 2PA shape function, including beam profile error, is estimated to be 5% maximum. Since we repeated at least twice the cross-section determination, then by evaluating the mean value, the final error was reduced as well and stayed below 8% for all the standards as shown in Table 6.

Table 6: σ_{2PA} and $\Delta\sigma_{2PA}$ values are obtained by averaging over all measurements performed.

	Comp.	Solvent	$\sigma_{2PA}(\lambda_2)$ GM (nm)	$\Delta\sigma_{2PA}$ ±%
1	BDPAS	DCM	175 (690) 138 (700)	8 8
2	Prodan	toluene	19 (700)	6
3	Prodan	DMSO	20 (723)	8
4	C153	toluene	17 (816)	5
5	C153	DMSO	17 (851)	7
6	AF455	toluene	404 (784)	7
7	AF455	THF	392 (784)	6
8	Fluorescein	H2O pH11	24 (785) 6.0 (858)	5 8
9	Rh 6G	MetOH	79 (812) 202 (692)	8 8
10	9-Chloroanthracene	DCM	0.043 (740)	8

The peak cross section value for BDPAS in DCM is $\sigma_{2PA} = 175 \pm 14$ GM, is less than was reported earlier [44], which we attribute to relatively rapid photo-degradation and low dark stability of the solution [92] leading to an underestimation of the 1PA fluorescence signal. These side effects were avoided

in current experiments. The 2PA spectrum rapidly drops to 20 GM at 750 nm and falls below 1 GM at longer wavelength. The solvatochromic shift is ~ 23 nm for Prodan with increasing the solvent polarity from toluene to DMSO, but the maximum value for the cross-section is practically the same, 19 GM. Same effect is to be noticed for C153 with a 2PA cross-section peak of ~ 17 GM independently of the solvent, but with a shift of 35 nm while increasing solvent polarity from toluene to DMSO. Remarkable feature is that the 2PA and 1PA profiles practically coincide in the range $\lambda_{2PA} = 740 - 1000$ nm for C153 and Prodan. The peak cross section of Fluorescein in water buffer pH 11 is $\sigma_{2PA} = 24 \pm 1.2$ GM at 780 nm. This is again about factor 2 less than the earlier reported value [44], most likely because, in previous experiment, this wavelength coincides with degeneracy of the OPA, where the beam parameters may deteriorate. In our current measurement this issue did not occur.

Rh 6G in MeOH cross section at 810 nm is $\sigma_{2PA} = 79 \pm 6$ GM, and correlates well with the value reported in [44] and is shown in Figure H.10 from appendix H. Both the absolute value and the shape function are higher at 690 nm compared to the value reported previously. This discrepancy is most likely caused by the narrow spectral band, at $\lambda_{2PA} = 680 - 710$ nm. The spectral FWHM of the excitation pulses in that particular wavelength range was measured to be $\Delta\lambda_{2PA} = 3 - 4$ nm, i.e. is comparable to the half-width of the named band. For comparison, in the earlier measurements the pulses were spectrally about factor of two broader, which may explain why the spectral feature appears more pronounced in the current data. Below 700 nm, the laser average power was low leading to a small fluorescence signal but also the laser was less stable. Hence the 2PA cross-section spectrum was rescaled preferably with the absolute cross-section determined at 812 nm. Finally 9-Chloroanthracene in dichloromethane presents a cross-section of 0.043 ± 0.004 GM at 740 nm, which is about 1.5 less than the value published in [44]. In our case, we concentrate the solution for the 2PA fluorescence recording and the registration wavelength was set at the second peak of emission to alleviate secondary inner filter effect from 1-photon excitation. If such care is not taken, the resulting absolute 2PA cross-section might be overestimated.

4.5 Confirmation of the fidelity of the established standard 2PA cross-section spectra

In the previous section, we estimated the maximum error of the absolute 2PA cross-section value to be about 8%. However, experimental errors exceeding that margin may still be present. Our goal here is to minimize the probability of such accidental experimental errors. Because this task is still practically difficult, we propose, instead of repeating the absolute measurements, to verify the fidelity of the current best characterized data set by carrying out a pair-wise comparison between different standards under identical excitation and detection conditions.

The general idea is to use the reference technique, described in 2.6.3, where one standard is considered as a “sample” for which the cross-section has to be determined with respect to another suitable “standard” taken from the rest of the set using Equation (87). By doing so, we can verify the correspondence between the absolute 2PA cross-section and the relative 2PA cross-section, thus revealing potential discrepancies.

We note that since the 2PIF detection is typically performed in a different setup from the differential quantum yield measurement, potential systematic errors may occur from erroneous differential quantum yield measurements due to mismatch in the wavelength calibration of different spectrometers, light source correction functions etc. However, since our 2PA shape was already verified with a substantially smaller maximum error of 5 %, and then as long as the difference between the absolute cross-section and relative cross-section determination is sufficiently small, e.g. less than 8%, this additional error contribution may be neglected.

Our next step is to pair up each of the 10 standards from previous chapter with a matching partner from the same set, such that 2PA and fluorescence emission spectra have sufficient overlap. We have all together 10 of such matching pairs. Figure 40 shows the 2PA and 1PA spectra, along with the fluorescence emission spectra for selected 9 pairs (out of 10 pairs studied) that allows a comparison via the reference technique: (a) 9-Chloroanthracene in DCM vs. Prodan in toluene, (b) 9-Chloroanthracene in DCM vs. BDPAS in DCM, (c) BDPAS in DCM vs. Prodan in in DMSO, (d) BDPAS in DCM vs. C153 in toluene, (e) Prodan in DMSO vs. C153 in toluene, (f) C153 in toluene vs. AF455 in THF, (g) C153 in toluene vs. AF455 in toluene, (h) C153 in DMSO vs. Rhodamine 6G in MetOH and (i) C153 in DMSO vs. Fluorescein in water buffer pH 11. As already mentioned, one of the criteria for choosing the particular pairs was sufficient overlap between their respective absorption spectra (solid lines). The second criterion was overlap between the fluorescence spectra (dash lines). Common fluorescence detection wavelength is indicated by a vertical straight line. For all these pairs, one system is considered as “sample” and the other one is considered as “standard”. We then determined the 2PA cross-section of the “sample” relative to the “standard” at the same wavelength, where we performed absolute 2PA cross-section determination, for a direct comparison of our measurements. We did as well measurements at some other wavelengths to confirm the 2PA shape as long as the 1PA and 2PA overlap of the pair allowed it.

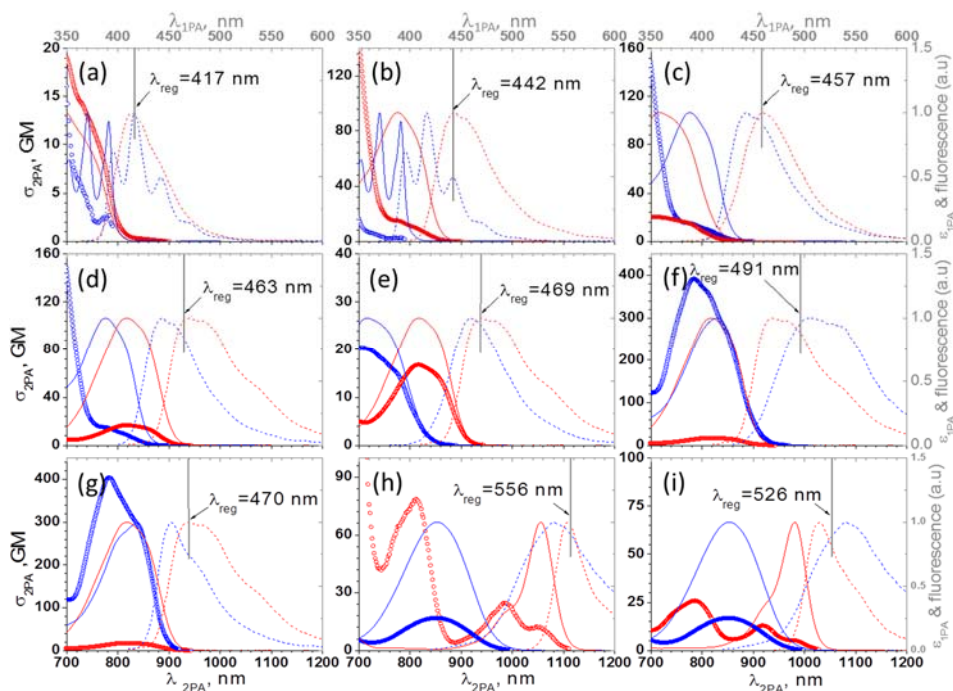


Figure 40: Normalized 1PA spectra (line, right and top axis), normalized fluorescence spectra (dash, right and top axis) and 2PA spectra (circle, bottom and left axis) of: (a) 9-Chloroanthracene in DCM (blue) vs. Prodan in toluene (red); (b) 9-Chloroanthracene in DCM (blue) vs. BDPAS in DCM (red); (c) BDPAS in DCM (blue) vs. Prodan in DMSO (red); (d) BDPAS in DCM (blue) vs. Coumarin 153 in toluene (red); (e) Prodan in DMSO (blue) vs. C153 in toluene (red); (f) AF455 in THF (blue) vs. C153 in toluene (red); (g) AF455 in toluene (blue) vs. C153 in toluene (red); (h) C153 in DMSO vs. Fluorescein in water buffer pH 11 (red); (i) C153 in DMSO (blue) vs. Rhodamine 6G in methanol (red). The common chosen fluorescence detection wavelength λ_{reg} for each pair is also indicated. Note that we had to enhance 10 times the 2PA spectrum of 9-Chloroanthracene in DCM in (a) and in (b) for a better visualization.

Figure 41 summarizes the results of the pair-wise comparison experiments. The absolute 2PA spectra from previous section are shown in circles using a unique color for each standard. The relative 2PA cross-sections are indicated with square symbols, where the color refers to the used reference standard. The pair-wise relative 2PA was then compared with the ratio between the absolute σ_{2PA} values for the same excitation wavelength. The discrepancy between the two ratios values at selected wavelengths expressed in % terms is presented in appendix I.

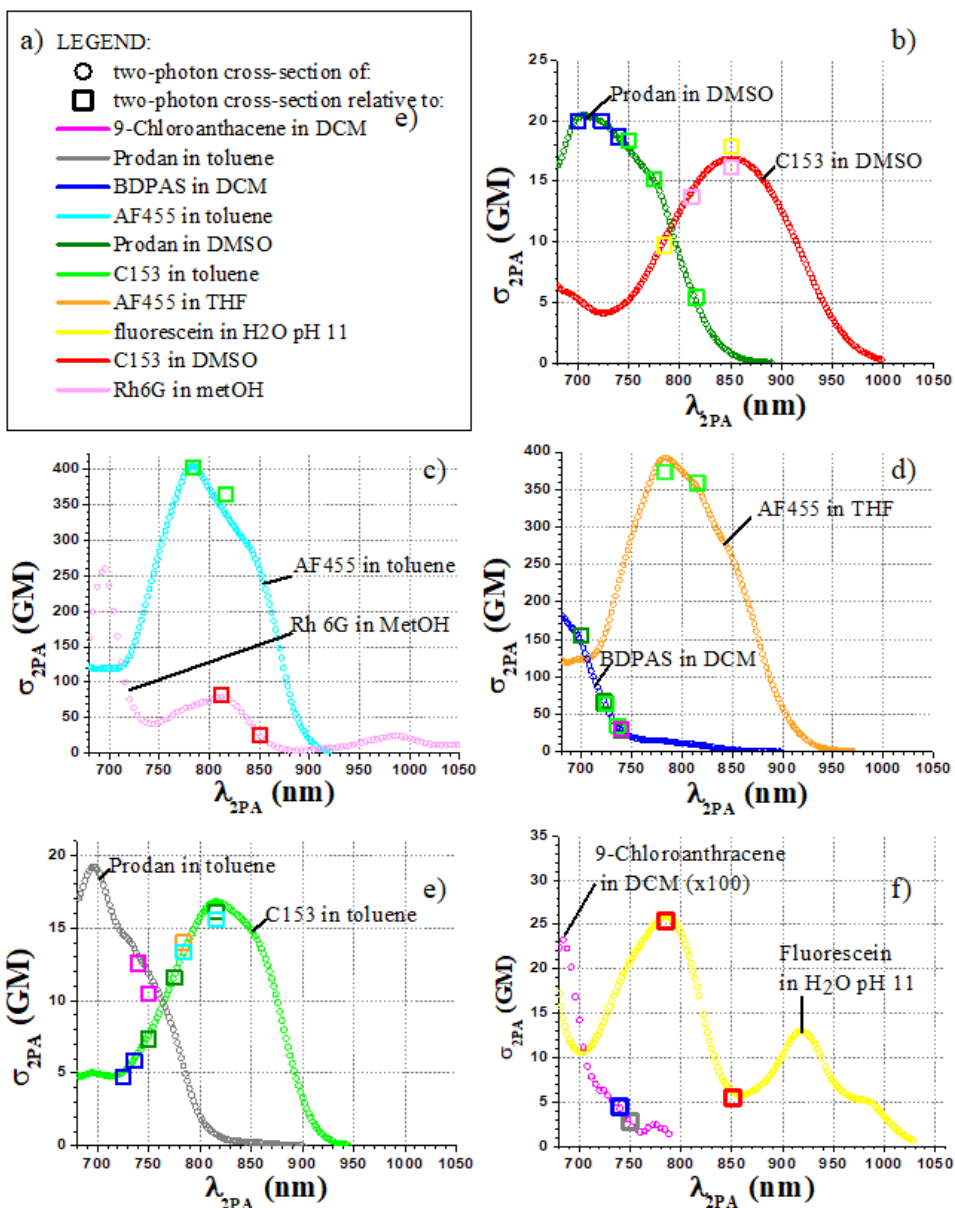


Figure 41: Comparison of sample relative 2PA cross-section calculated with the reference compared to its absolute value for the same wavelength. Each color stands for a standard as explained in the legend (a).

For BDPAS in DCM, there is relatively poor overlap with the absorption and fluorescence of Prodan in toluene, which may be responsible for some marked deviations. Indeed, their 1PA absorption maxima are displaced by ~ 40 nm making it difficult to find a suitable common excitation wavelength, and their

corresponding fluorescent maxima are also shifted by 30 nm, leading to a difficult choice of the common λ_{reg} . With our choice $\lambda_{\text{reg}} = 457$ nm, we found a deviation of -17.1% at 701 nm and -28.7% at 750 nm excitation. Thus, this may be revealing some additional uncertainty, especially regarding the spectral mismatch. Relative to Prodan in DMSO the fluorescence registration wavelength was 14 nm away for the maximum of the emission for BDPAS in DCM, but still a relatively flat region (Figure 40 (c)). The deviation from the absolute value is $+1.0\%$ at 700 nm. With 4 selected wavelengths in the 720 - 740 nm region, the deviations are in the range from 0.3 % relatively to Prodan in toluene at 723 nm, to 8.1 % relatively to C153 in toluene at 725 nm, while the registration occurred 10 – 15 nm away from the emission peak of BDPAS in DCM. Figure 41 d) shows also a good correlation between the relative 2PA cross-section and the absolute spectrum. Therefore our absolute 2PA cross-section value for BDPAS in dichloromethane is as well validated.

C153 in toluene cross-section was measured relatively to 4 other standards and is shown in Figure 41 e). The fluorescence detection wavelength was close to its maximum at 468 nm when compared to BDPAS in DCM (Figure 40 (d)), Prodan in DMSO (Figure 40 (e)) and AF455 in toluene (Figure 40 (g)). In contrast, the fluorescence detection wavelength was 22 nm away to longer wavelength from the fluorescence peak, when compared to AF455 in THF (Figure 40 (f)). Nevertheless, since the fluorescence spectrum of C153 in toluene is broad, the fluorescence spectrum is still nearly flat in this region, thus limiting the relative differential quantum yield error. The discrepancy ranges from -7.5% to $+5.3\%$ for all the measurements and one can see from Figure 41 e) that the 2PA relative spectrum does well reproduce the absolute one in the 720 - 820 nm range. At the 2PA peak, $\lambda_{2\text{PA}} = 816$ nm, we report a deviation of -4% relatively to Prodan in DMSO, -1.8% relatively to AF455 in THF and -7.2% relatively to AF455 in toluene which might suggest that the absolute cross-section is slightly lower than the one reported in Table 6. However, this deviation is still less than 8 %, thus confirming our previous absolute two-photon cross-sections for C153 in toluene and in turn validates the accuracy of its whole 2PA spectrum.

Conversely, assuming that the absolute 2-photon cross-section spectra for Coumarin 153 in toluene and BDPAS in DCM are exact, then using those two standards, we found for Prodan in DMSO a deviation of -0.9% at its 2PA peak at 700 nm. Otherwise, the deviation does not exceed 4.6 % for the 6 points covering the 700 – 816 nm range, which is almost the whole range of the spectrum as shown in Figure 41 b). Hence we can affirm that this standard, as reported in Table 6, is accurate also within 8%. AF455 in THF and in toluene were both compared to C153 in toluene and showed at their 2PA peak a deviation of -0.3% for AF455 in toluene and -5.0% for AF455 in THF. Since we trust our 2PA shape, the good agreement with only 2 points, as shown in Figure 41 c) and 41 d) is enough to attest the validity of the whole 2PA absolute spectra for these dyes.

Comparison of 9-Chloroanthracene in DCM to BDPAS in DCM at 740 nm gave a deviation of -6.3% while the recording wavelength 442 nm correspond to the 3rd emission peak for 9-Chloroanthracene in DCM and main peak for BDPAS in DCM as shown in Figure 40 (b). Relative to Prodan in toluene the deviation was $+3.9\%$ at 740 nm and $+13.6\%$ at 750 nm while the registration was set to the common maximum peak ~ 417 nm of these two dyes as shown in Figure 40 (a). We have to point out that the 2PA shape for 9-Chloroanthracene is slightly noisy for longer wavelength and therefore is responsible for the resulting deviation is higher at 750 nm. The good agreement found at 740 nm confirmed our absolute measurement for 9-Chloroanthracene at this wavelength. Conversely, the relative cross-section determined for Prodan in toluene with respect to 9-Chloroanthracene in DCM is 3.7% off compared to the absolute value, therefore we are allowed to assert that the larger deviation found for Prodan in toluene relatively to BDPAS in DCM is the consequence of the poor overlap in their emission spectra and that the absolute 2PA spectrum determined for Prodan in toluene is sufficiently accurate as state above.

Based on the pair-wise comparison of Fluorescein in buffer pH11 and C153 in DMSO, we firstly noticed a deviation of $\sim 12\%$ at the 2PA peak for Fluorescein. It is originated from an overestimation of the absolute 2-photon cross-section for Fluorescein because of an inaccurate evaluation of the Fluorescein concentration. After correction of the absolute 2PA σ_{2PA} , Fluorescein showed a deviation at its 2PA peak of $+4.6\%$ relatively to C153 in DMSO, while the fluorescence is recorded at the Fluorescein emission peak, which is slightly away to longer wavelength from C153 in DMSO peak, as shown in Figure 40 (h). We also measured the cross-section at the first minimum of Fluorescein at 851 nm and found a deviation of -5.8% . Using the same reference standard, Rhodamine 6G in MeOH showed a deviation at its 2PA peak of $+3.8\%$ while the registration wavelength occurred in between the fluorescence peak of these two dyes as shown in Figure 40 (i). Conversely, C153 in DMSO gave at 851 nm a deviation $+6.1\%$ relatively to Fluorescein in water buffer pH11 and -3.7% relatively to Rhodamine 6G. Therefore, this trio cross-comparison presents 2PA cross-section deviations smaller than the 8% compared to their absolute one as shown in Figure 41 b), c) and f). It confirms the accuracy to our absolute measurements presented in Table 6.

5 SOME APPLICATIONS OF THE NEW STANDARDS

In previous chapters, we have established the 2PA spectra and 2PA cross-section of a series of fluorophores with record-breaking accuracy. In this chapter, we are going to apply this new information to find answers to some interesting questions in molecular physics, such as the permanent dipole moment change in the lowest-energy dipole-allowed transition and measuring the 2PA spectrum of a fluorescent analog of a DNA base.

5.1 Estimation of the permanent dipole moment change in the lowest-energy electronic transition

The standards selected presumably possess a non-zero permanent dipole moment difference between the ground and excited state. Nevertheless, we might be tempted to analyze the 1PA and 2PA spectra of the systems in term of permanent dipole moment using the two-level model described in section 2.3.3. From Equation (63) with vertical polarization, and supposing that the two vector $\vec{\mu}_{fg}$ and $\Delta\vec{\mu}_{fg}$ are parallel (e.g. $\beta=0$), the difference in permanent dipole moment from the ground to the excited state can be evaluated simply by comparison of the 2PA and 1PA cross-section spectra:

$$\begin{aligned} |\Delta\vec{\mu}_{fg}| &= c \sqrt{\frac{5\epsilon_0 h N_A}{3 \ln 10}} \frac{3}{n^2+2} \sqrt{\frac{n \sigma_{2PA}(2\lambda)}{\lambda \epsilon_{1PA}(\lambda)}}, \\ |\Delta\vec{\mu}_{fg}| &= 4.55 \cdot 10^3 \frac{3}{n^2+2} \sqrt{\frac{n \sigma_{2PA}(2\lambda)}{\lambda \epsilon_{1PA}(\lambda)}}, \end{aligned} \tag{98}$$

with the 2PA cross-section σ_{2PA} expressed in GM, extinction coefficient ϵ_{1PA} in M cm^{-1} and the wavelength λ in nm. Note that this equation is known to be empirically valid only if the 1PA and 2PA shape coincide, considering the lowest transition $S_0 \rightarrow S_1$, at least for the pure electronic transition (0-0). The calculated difference in dipole moments, where 1PA and 2PA shape coincide in the long wavelength range, is shown in green points superposed to the absorption spectra for all standards in appendix H.

We see in Appendix H that Prodan and C153 dyes show a similar shape for 1PA and 2PA spectra extending across the whole band, including vibronic components (Figure H.2, H.5, H.6 and H.9). For instance, Figure 42 shows the example of C153 in DMSO, where the extinction coefficient spectrum and the two-photon cross-section are scaled such as they superimpose. The ratio $\frac{\sigma_{2PA}(2\lambda)}{\epsilon_{1PA}(\lambda)}$ is constant over the whole $S_0 \rightarrow S_1$ transition band, which allows determining the permanent dipole moment difference with Equation (98) for the whole band, without any distinction of the vibrational bands, which compose it.

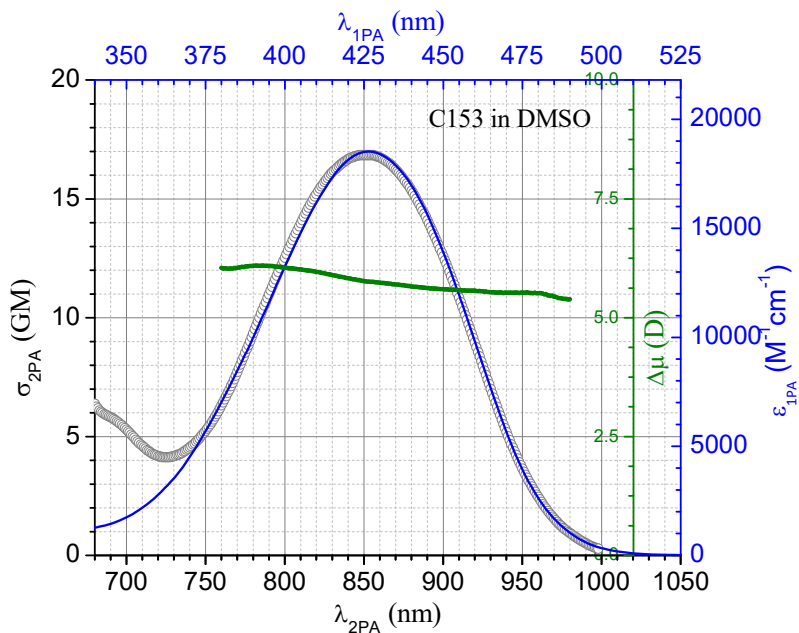


Figure 42: 2PA cross-section spectrum (black circles), absolute 2PA cross-section measured (red squares with error bar), extinction coefficient (blue line) and difference in permanent dipole moment (green squares) from ground to excited state for Coumarin 153 in DMSO.

Table 7: Experimental values of transition dipole moment and change in dipole moment for C153 obtained in this study and obtained in literature with Stark effect or solvatochromism shift methods, where the estimated cavity radius is also indicated.

Solvent	μ_{01} D	$\Delta\mu_{01}$ D	Method.	ref.
Toluene	8.0	5.6	All optical	This study
DMSO	8.3	5.7	All optical	This study
-	-	6.5	Solvatochromic shift $a=4.76 \text{ \AA}$	[107]
-	-	4.1	Solvatochromic shift $a=3.9 \text{ \AA}$	[108]
-	-	7.5	$a=5.85 \text{ \AA}$	
toluene	-	5.8	Stark effect	[49]
MeTHF	-	7.0	Stark effect	[49]

The resulting average transition dipole and permanent dipole moment difference for $S_0 \rightarrow S_1$ transition for Prodan and C153 are listed in Table 7 and 8. For both dyes, the effect of increasing solvent polarity leads to a small increase in the permanent dipole moment difference.

On the overall, in the case of C153, we found a good agreement with both Stark effect spectroscopy and solvatochromism methodology. This supposes that considering pure solvent dielectric response or completely ignoring specific solute-solvent interaction are equally successful at predicting the dipole moment change.

Table 8: Experimental values of transition dipole moment and change in dipole moment for Prodan obtained in this study and obtained in literature with Stark effect or solvatochromism shift methods, where the estimated cavity radius is also indicated.

Solvent	μ_{01} D	$\Delta\mu_{01}$ D	Method.	ref.
Toluene	8.0	6.2	All optical	This study
DMSO	8.2	7.0	All optical	This study
-	-	8.0	Solvatochromic shift, a=4.2 Å	[104]
-	-	7.0	Solvatochromic shift, a=4.7 Å	[105]
-	-	4.3	Solvatochromic shift, a=4.2 Å	[106]
-	-	4.9	Solvatochromic shift, a=4.6 Å	
cyclohexane	-	12.7	Stark effect	[58]
1,4-dioxane	-	14.0	Stark effect	[58]

Compared to literature values, the values of permanent dipole moment difference for Prodan lies between the one obtained by solvatochromism and the one obtain by Stark spectroscopy. Solvatochromism measurements depend on the appreciation for the cavity radius. With a radius of 4.7 Å, the intrinsic permanent dipole moment difference matches our estimation for C153 in DMSO, but there is no argument stating that this radius value is more valid than another. Values obtained by Stark spectroscopy are about twice our determined one, but rely on different solvents.

For the other standards, we note that the 1PA and the 2PA are very different at short wavelengths. In particular, the wavelength corresponding to the 2PA peak is not, as one could expect, the double of the wavelength corresponding to the 1PA peak, but is shorter instead. In such case, Equation (98) is restricted to

lowest-energy vibronic transition 0-0 located at the longest-wavelength part of both 1PA and 2PA spectra. Indeed, if we calculate the ratio $\frac{\sigma_{2PA}(2\lambda)}{\epsilon_{1PA}(\lambda)}$ from our experimental data, then the ratio appears more or less constant in the longest-wavelength part, which indicates that both 1PA and 2PA are due to the same 0-0 transition. The permanent dipole moment difference values, calculated with Equation (98) in this restricted region, are shown in Table 9.

9-Chloroanthracene signal was too weak and a bit noisy in the long wavelength range, so we can only obtain upper value estimate ~ 0.4 D.

Table 9: Experimental values of the change in dipole moment of the pure electronic transition (0-0) with its estimated central wavelength λ_{0-0} and the transition dipole moment over the whole electronic transition $S_0 \rightarrow S_1$.

Comp.	Solvent	μ_{01} D	$\Delta\mu_{01}$ D	λ_{0-0} (nm)
BDPAS	DCM	13.5	5.7	410
AF455	toluene	12.4	7.0	420
AF455	THF	13.0	5.6	426
Fluorescein	H2O pH11	12.6	1.4	491
Rh 6G	MetOH	13.7	1.7	529

5.2 Determination of 6MI dipole moment change by measuring its 2PA cross-section using reference standards

The pteridine nucleoside analog 6-methylisoxanthopterin (6MI) is a fluorescent analog to DNA base guanine with the fluorescence emission in the 450 nm region with high quantum yield (~ 0.7) and 1PA peak at 343 nm. It has found use as promising fluorophore probe for monitoring DNA and RNA conformations. Because living cells absorb light in the ranges from 200 - 360 nm overlapping with the 6MI spectrum, it is of increasing interest to explore the 2-photon absorption properties of this system [97][98] in the so-called tissue transparency window (750 nm-1200 nm), where tissue scattering[1, 32, 33] and photo-damage to cells [7] are both greatly reduced.

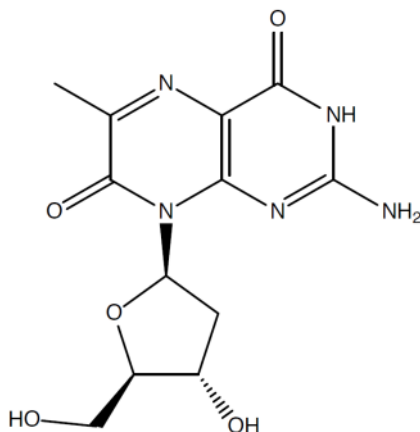


Figure 43: Chemical structure of 6MI

The chemical structure of 6MI in Figure 43 shows that 6MI resembles to guanosine. 6MI was purchased from Fidelity Systems, Inc. and was dissolved in 1 M phosphate buffer pH 7. This solvent was chosen to simulate human cell environment but also to avoid ionization of the N3 proton of 6MI whose pK_a is approximately 8.3. The peak extinction coefficient at 344 nm was estimated to be $\epsilon_{IPA} \sim 1.00 \times 10^4 \text{ M}^{-1} \text{ cm}^{-1}$. From our set of standards, BDPAS and 9-Chloroanthracene present a good 1PA and fluorescence spectra overlap with 6MI. Figure 44 presents the comparison of normalized 1-photon absorption and fluorescence spectra between 6MI in phosphate buffer pH=7 and this two chosen standards. 6MI and BDPAS share the same wavelength 442 nm for their fluorescence peak, while it corresponds to the 3rd peak for 9-Chloroanthracene. The absorption peak of 6MI lies in a flat absorption region in BDPAS in DCM spectrum, which makes this standard very suitable for relative cross-section determination. For 9-Chloroanthracene, the 3rd absorption peak is quite close to 6MI maximum absorption. Therefore, the fluorescence registration wavelength was set at 442 nm, the 6MI peak. As was explained in section 2.6.3, the linear fluorescence was excited at different wavelength, where the absorption spectra are close to constant. To compare with BDPAS, we illuminated both samples at 295 nm, 307 nm, 310 nm, 329 nm, 343 nm, 350 nm and 353 nm and found a differential quantum yield for 6MI relative to BDPAS of 0.92 ± 0.06 . The same procedure with excitation at 335 nm, 343 nm, 349 nm, 352 nm, and 359 nm, corresponding to the extrema of 9-Chloroanthracene absorption spectrum, resulted in a differential quantum yield for 6MI relative to 9-Chloroanthracene of 3.6 ± 0.2 .

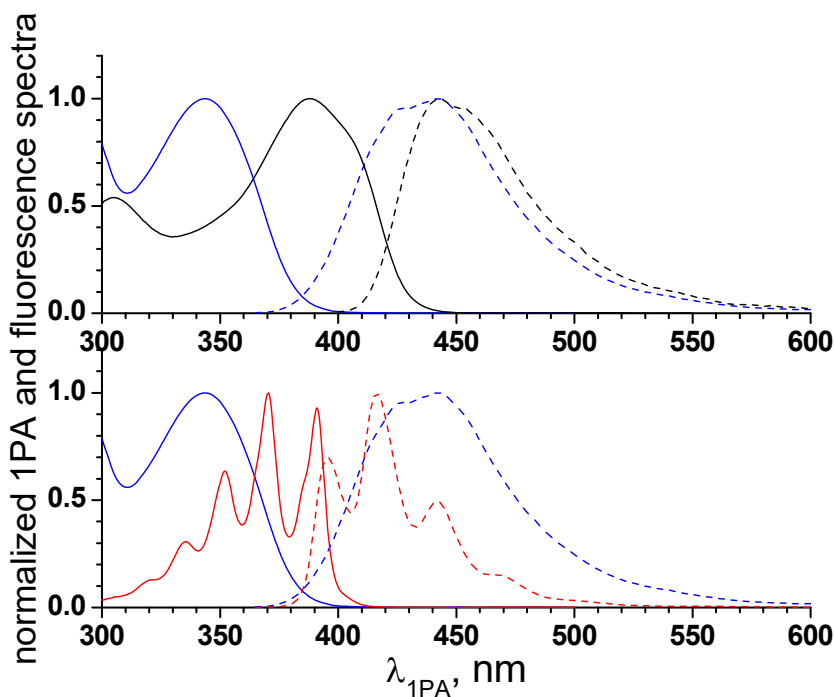


Figure 44: Normalized 1-photon absorption (solid line) and fluorescence spectra (dash line) of 6MI in phosphate buffer pH7 (blue), BDPAS in DCM (upper panel, black) and 9-chloroanthracene in DCM (lower panel, red).

Figure 45 shows, for the first time, the 2PA spectrum of 6MI in water pH7 in the 770-750 nm range. Grey circles correspond to the measurement of relative shape, according to Equation (83), which was then scaled according to the 2PA cross-section measured at few selected wavelength with respect to BDPAS in DCM (black points) and 9-Chloroanthracene in DCM (red point) standards. The maximum value determined is $\sigma_{2PA} \sim 1.5 \text{ GM}$ at the short wavelength edge of the laser tuning range $\sim 700 \text{ nm}$. Since the 6MI cross-section determined with both standards do overlap well, one can interpret it as another proof of the accuracy and reliability of our standard absolute two-photon cross-section spectra.

Main advantage of the relative 2PA cross-section determination is the time saving to get results, and the separation in two sub-tasks, which can be optimized independently: the relative fluorescence efficiency determination and the relative 2PIF signal acquisition. This last one can be enhanced by using more concentrated solutions, giving rise to increased signal and better signal-to-noise ratio. The only consideration is to record the fluorescence signal away from the absorption band to avoid inner-filter effect.

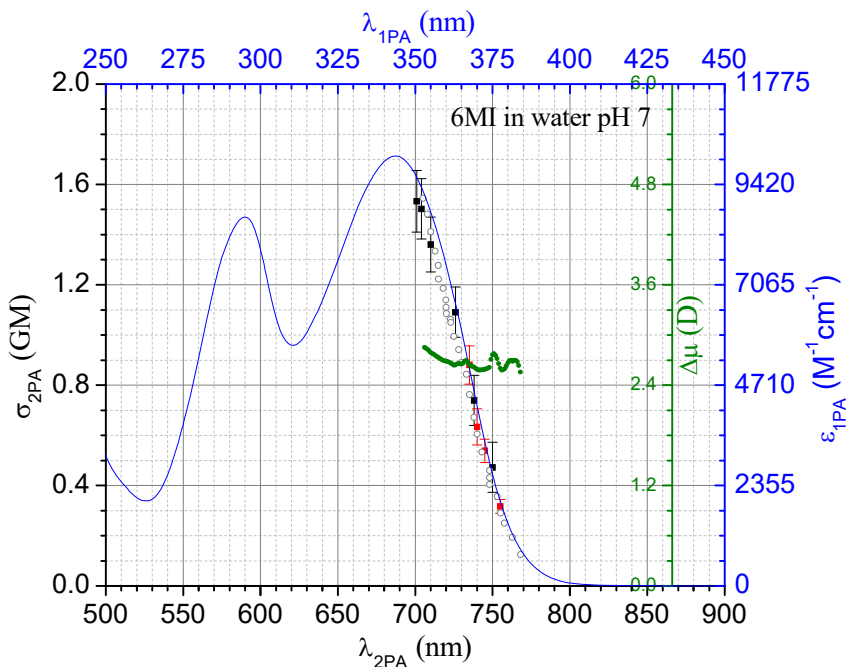


Figure 45: rescaled 2PA shape spectrum (grey circles, left and bottom axis) and extinction coefficient spectrum (blue line, right and top axis) of 6MI in phosphate buffer pH=7. Relative cross-section with respect to BDPAS in DCM (black) and to 9-Chloroanthracene in DCM (red). Difference in permanent dipole moment (green squares) from ground to excited state.

6-MI is sensitive to its nearest neighbors and base stacking, making it a very useful real-time probe of DNA conformation. The fluorescence quenching by base stacking is not well understood, hence tracking the 2PA and evaluating the dipole moment change evolution upon the stacking dynamic of double strand DNA might give some first clues. Indeed, since the determination of the 2PA cross-section relative to a standard is faster compared to the absolute determination, one can follow the fluorescence signal change due to DNA base pairing, if the excitation conditions remain constant.

Our measured 2PA spectral shape in Figure 45 appears to follow closely the shape of the 1PA spectrum. Using the same approach as in the previous section, we evaluated the ratio between the 2PA and 1PA, from which we estimated the change of permanent electric dipole moment in the $S_0 \rightarrow S_1$ transition (green symbols in Figure 45). The mean value is $|\Delta\vec{\mu}_{10}| = 2.7 \pm 0.2\text{D}$ which is close to the value of 3.2 D obtained by Kodali et al. [109] using Stark spectroscopy in frozen LiCl glasses at 77K.

CONCLUSION

We established a set of reference standards for the 2PA measurements in the 680 to 1050 nm wavelength range with unprecedentedly high accuracy of 8% using an improved femtosecond fluorescent excitation method. The standards were carefully selected such as they offer a great solubility, photostability and the solutions do not manifest presence of multiple forms of the fluorophores.

We designed a set-up for measuring 2PA cross-section based on the indirect fluorescence excitation method, which uses comparison to 1-photon excitation fluorescence to evaluate the number of molecules excited by 2PA. We performed precise measurements of the laser parameters, including temporal and spatial profile. The final quadratic error was calculated based on the standard deviation determined for each parameter involved in the absolute 2PA cross-section determination.

We checked the reliability of our standard by pair-wise comparison among them using the relative method and confirmed the 8% accuracy limit.

As an example of application of the standards, we estimate the change of permanent electric dipole moment upon excited state transition in the fluorophores studied and also measure, for the first time, the 2PA cross-section spectrum of a fluorescent DNA base analog.

Improved accuracy of the reference standard might provide reproducible determination of the relative two-photon cross-section of a sample, independently of the method employed. Most especially, it is crucial for quantitative spectroscopy for determining the dipole moment change upon excitation of a 2PA absorbing solvated molecule. To improve the accuracy below 8%, one possible and tedious next step would be, in order to draw some statistic, to repeat the same measurement multiple times.

In the future, if the dipole moment properties of a chromophore are well known, then local electric field in a biological process can be probed with 2PA. For instance it is theoretically predicted that proteins comprising charged group may generate large local electrostatic field $\vec{E}_{LOC} \approx 10^6 - 10^8 \text{ V cm}^{-1}$. Also DNA binding involves change of the local electrostatic field and quantitative 2PA spectroscopy with high accuracy of fluorescent-labeled DNA would be able to measure and interpret the binding processes.

ABSTRACT

This dissertation describes nonlinear-optical experiments, where we have measured, with a record-breaking accuracy, the absolute femtosecond two-photon absorption cross-section and -spectra of a selected series of organic fluorophores dissolved in organic solvents. The accuracy of this data, which covers the two-photon excitation wavelength range 680 – 1050 nm, is estimated to be better than 8% , and was confirmed by meticulous measurement of all key experimental parameters involved, including the temporal pulse shape of the femtosecond laser, spatial laser beam profile, fluorophore concentration etc. The accuracy of the data set was also verified by pair-wise cross-checking between 10 different standards thus further reducing potential experimental errors. As a result, the data presented here serves a valuable technical benchmark or reference standard, that other researcher will be able to effectively apply in their research, e.g. to calibrate multi-photon absorption measurements and related nonlinear-optical experiments. In particular, by using these standards one is able to largely circumvent tedious characterization of the complex photon flux functions, which otherwise constitute a major source of experimental errors in contemporary ultrafast multi-photon spectroscopy and nonlinear optics. We anticipate that this work is going to facilitate development of new and improved two-photon active chromophores for a broad range of applications including but not limited to multi-photon microscopy, microfabrication, and optical limiting.

KOKKUVÕTE

Käesolevas väitekirjas on teostatud eksperimendid mittelineaarse optika vallas, kus on muu hulgas rekordilise täpsusega mõõdetud rea orgaaniliste fluorofooride kahe footoni neeldumise absoluutne ristlõige ja selle sõltuvus ergastava valguse lainepikkusest ehk kahe footoni neeldumise spekter. Saadud spektrite täpsus on hinnanguliselt parem kui 8%, kusjuures need spektrid katavad summarselt laia kahe footoni ergastuse rakendusele enim huvi pakkuvat lainepikkuste vahemikku 680–1050 nm. Nimetatud mõõtmistäpsuse kinnituseks on läbi viidud kõigi eksperimendis oluliste parameetrite üksikasjalik uuring, sh femtosekundlaseri impulsi ajalise kestvuse ja ergastava valguskimbu footonite ruumilise jaotuse mõõtmine, fluorofoori lahuse kontsentratsiooni määramine jne. Lisaks on kahefotoonse neeldumise ristlõike numbrilise väärtuste juhusliku vea võimaluse vähendamiseks läbi viidud 10 erineva standardi omavaheline paariviisiline võrdlus, mis omakorda kinnitab 8% absoluutse täpsuse hinnagut. Nimetatud mõõtmiste tulemusena on loodud põhjalikult kontrollitud andmebaas, mis on omataoliste hulgas kõrge täpsuse ja usaldusväärsuse poolest unikaalne. Kasutades loodud andmebaasi, on võimalik oluliselt tõhustada mittelineaarse spektroskoopia eksperimente, s.h. femtosekundlaserite footonite voo omaduste määramist, mis on paljudel juhtudel mõõtmisvea peamine põhjus. Töö teine oluline praktiline tulem seisneb selles, et välja töötatud uudne meetodika tõhustab optimeeritud materjalide väljaarendamist mitmete mittelineaarse optika rakenduste tarbeks.

REFERENCES

- [1] Lakowicz, J. R., [Principles of Fluorescence Spectroscopy, 3rd edition], Springer (2006).
- [2] Southerland, R. L., [Handbook of Nonlinear Optics, 2nd edition], Marcel Dekker (2003).
- [3] Göppert-Mayer, M., “Über Elementarakte mit zwei Quantensprüngen,” *Ann. Phys.* 401 (3), 273–294 (1931).
- [4] Dobrizhev, M., Karotki, A., Rebane, A. and Spangler, C. W., “Dendrimer molecules with record large two-photon absorption cross section”, *Opt. Lett.* 14, 1081-1083 (2001).
- [5] Chung, S.-J., Zheng, S., Odani, T., Beverina, L., Fu, J., Padilha, L. A., Biesso, A., Hales, J. M., Zhng, X., Schmidt, K., Ye, A., Zojer, E., Barlow, S., Hagan, D. J., Van Stryland, E. W., Yi, Y., Shuai, Z., Pagani, G. A., Bredas, J.-L., Perry, J. W., and Marder, S. R., “Extended Squaraines Dyes with Large Two-Photon Absorption Cross-sections”, *J. Am. Chem. Soc.* 128(45), 14444-14445 (2006).
- [6] Kaiser, M. and Garrett, C. G. B., “Two-Photon Excitation in $\text{CaF}_2:\text{Eu}^{2+}$ ”, *Phys. Rev. Lett.* 7(6), 229-231 (1961).
- [7] Denk, W., Strickler, J. H. and Webb, W. W., “Two-photon laser scanning fluorescence microscopy”, *Science* 248, 73-76 (1990).
- [8] Williams, R. M., Piston, D. W. and Webb, W. W., “Two-photon molecular excitation provides intrinsic 3-dimensional resolution for laser-based microscopy and microphotochemistry”, *FASEB J*, 8, 804-813 (1994).
- [9] Denk, W. and Svoboda, K., “Photon Upmanship: Why Multiphoton Imaging is More Than a Gimmick”, *Neuron* 18, 351-357 (1997).
- [10] Zipfel, W. R., Williams, R. M. and Webb, W. W., “Nonlinear magic: multiphoton microscopy in the biosciences”, *Nat. Biotechnol.* 21, 1369-1377 (2003).
- [11] Shear, J. B., “Multiphoton-Excited Fluorescence in Bioanalytical Chemistry”, *Anal. Chem.* 71, 589A-605A (1999).
- [12] Williams, R. M., Zipfel, W. R. and Webb, W. W., “Multiphoton Microscopy in Biological Research”, *Curr. Opin. Chem. Biol.* 5, 603-608 (2001).
- [13] Oheim, M., Michael, D. J., Geisbauer, M., Madsen, D. and Chow, R. H., “Principles of two-photon excitation fluorescence microscopy and other nonlinear imaging approaches”, *Adv. Drug Deliv. Rev.* 58, 788-808 (2006).
- [14] Bewersdorf, J., Rainer, P. and Hell, S.W., “Multifocal multiphoton microscopy”, *Opt. Lett.* 23, 665-667 (1998).
- [15] Xu, C., Zipfel, W., Shear, J. B., Williams, R. M. and Webb, W. W., “Multiphoton fluorescence excitation: New spectral windows for biological nonlinear microscopy”, *PNAS* 93 (20), 10763-10768 (1996).

- [16] Bhawalkar, J. D., Kumar, N. D., Zhao, C. F. and Prasad, P. N., "Two-photon photodynamic therapy", *J. Clin. Laser Med. Surg.* 15 (5), 201-204 (1997).
- [17] Leupold, D. and Kochevar, I. E., "Multiphoton photochemistry in biological systems. Introduction", *Photochem. Photobiol.* 66, 562-565 (1997).
- [18] Frederiksen, P. K. and Jorgensen, O. P. R., "Two-Photon Photosensitized Production of Singlet Oxygen", *J. Am. Chem. Soc.* 123, 1215-1221 (2001).
- [19] Brown, S., "Photodynamic Therapy: Two photons are better than one," *Nat. Photon.* 2, 394-395 (2008).
- [20] Ogawa, K. and Kobuke, Y., "Recent Advances in Two-Photon Photodynamic Therapy", *Anticancer Agents Med. Chem.* 8(3), 269-279 (2008).
- [21] Gao, D., Agayan, R. R., Xu, H., Philbert, M. A. and Kopelman, R., "Nanoparticles for Two-Photon Photodynamic Therapy in Living Cells", *Nano Lett.* 6(11), 2383-2386 (2006).
- [22] Fisher, W. G., Partridge, W. P. Jr., Dees, C. and Watcher, E. A., "Simultaneous Two-Photon Activation of Type-I Photodynamic Therapy Agents", *Photochem. and Photobiol.* 66(2), 141-155 (1997).
- [23] Collins, H. A., Khurana, M., Moriyama, E. H., Mariampillai, A. M., Dahlstedt, E., Balaz, M., Kuimova, M. K., Drobizhev, M., Yang, V. X. D., Phillips, D., Rebane, A., Wilson, B. C. and Anderson, L., "Blood-vessel closure using photosensitizers engineered for two-photon excitation", *Nat. Photon.* 2, 420-424 (2008).
- [24] Kim, S., Ohulchanskyy, T. Y., Pudavar, H. E., Pandey, R. K. and Prasad, P. N., "Organically Modified Silica Nanoparticles Co-encapsulating Photosensitizing Drug and Aggregation-Enhanced Two-Photon Absorbing Fluorescent Dye Aggregates for Two-Photon Photodynamic Therapy", *J. Am. Chem. Soc.* 129 (9), 2669-2675 (2007).
- [25] Parthenopoulos, D. A. and Rentzepis, P. M., "Three-Dimensional Optical Storage Memory", *Science* 245 (4920), 843-845 (1989).
- [26] Glezer, E. N., Milosavljevic, M., Huang, L., Finlay, R. J., Her, T.-H., Callan, J. P. and Mazur, E., "Three-dimensional optical storage inside transparent materials", *Opt. Lett.* 21 (24), 2023-2025 (1996).
- [27] Cumpston, B. H., Sundaravel, P. A., Barlow, S., Dyer, D. L., Ehrlich, J. E., Erskine, L. L., Heikal, A. A., Kuebler, S. M., Lee, I.-Y. S., McCord-Maughon, D., Qin, J., Rockel, H., Rumi, M., Wu, X.-L., Marder, S. R. and Perry, J. W., "Two-photon polymerization initiators for three-dimensional optical data storage and microfabrication", *Nature* 398, 51-54 (1999).
- [28] Strickler, J. H. and Webb, W. W., "Three-dimensional optical data storage in refractive media by two-photon point excitation", *Opt. Lett.* 16 (22), 1780-1782 (1991).
- [29] Walked, E. and Rentzepis, P. M., "Two-photon technology: A new dimension" *Nat. Photon.* 2, 406-408 (2008).

- [30] Farsari, M. and Chichkov, B. ., “Materials processing: Two-photon fabrication”, *Nat. Photon.* 3, 450-452, (2009)
- [31] Zhou, W., Kuebler, S. M., Braun, K. L., Yu, T., Cammack, K., Ober, C. K., Perry, J. W. and Marder, S. R., “An efficient Two-Photon-Generated photoacid Applied to Positive-Tone 3D Microfabrication”, *Science* 10, 1106-1109 (2002).
- [32] Maruo, S., Nakamura, O. and Kawata, S., “Three dimensional microfabrication with two-photon-absorbed photopolymerization”, *Opt. Lett.* 22 (2), 132-134 (1997).
- [33] Ovsianikov, A., Viertl, J., Chichkov, B., Oubaha, M., MacCraith, B., Sakellari, L., Giakoumaki, A., Gray, D., Vamvakaki, M., Farsari, M. and Fotakis, C., “Ultra-low Shrinkage Hybrid Photosensitive Material for Two-Photon Polymerization Microfabrication”, *ACS Nano.* 2 (11), 2257-2262 (2008).
- [34] Weiss, T., Hildebrand, G., Schade, R. and Liefelth, K., “Two-Photon polymerization for microfabrication of three-dimensional scaffolds for tissue engineering application”, *Eng. Life Sci.* 9 (5), 384-390 (2009).
- [35] Ehrlich, J. E., Wu, X. L., Lee, I.-Y. S., Hu, Z.-Y., Rockel, H., Marder, S. R. and Perry J. W., “Two-photon absorption and broadband optical limiting with bis-donor stilbenes”, *Opt. Lett.* 22 (24), 1843-1845, (1997).
- [36] Spangler, C. W., “Recent development in the design of organic materials for optical power limiting”, *J. Mater. Chem.* 9, 2013-2020 (1999).
- [37] Morel, Y., Irimia, A., Najechalski, P., Kervella, Y., Stephan, O. and Baldeck, P.L., “Two-photon absorption and optical power limiting of bifluorene molecule”, *J. Chem. Phys.* 114, 5391-5396 (2001).
- [38] Du, Y., Dong, N., Zhang, M., Zhu, K., Na, R., Zhang, S., Sun, N., Wang, G. and Wang, J., “Covalent functionalization of graphene oxide with porphyrin and porphyrin incorporated polymers for optical limiting”, *Phys. Chem. Chem. Phys.* 19, 2252-2260 (2017).
- [39] Albota, M., Beljonne, D., Bredas, J.-L., Ehrlich, J. E., Fu, J.-Y., Heikal, A. A., Hess, S. E., Kogej, T., Levin, M. D., Marder, S. R., McCord-Maughon, D., Perry, J. W., Rockel, H., Rumi, M., Subramaniam, G., Webb, W. W., Wu, X-L and Xu, C., “Design of Organic Molecules with Large Two-Photon Absorption Cross Sections”, *Science* 11 (281), 1653-1656 (1998).
- [40] Reinhardt, B., Brott, L. L., Clarson, S. J., Dillard, A. G., Bhatt, J. C., Kannan, R., Yuang, L., He, G. S. and Prasad, P. N., “Highly Active Two-Photon Dyes: Design, Synthesis, and Characterization toward Application”, *Chem. Mater.* 10 (7), 1863-1874 (1998).

- [41] Drobizhev, M., Makarov, N. S., Tillo, S. E., Hughes, T. E. and Rebane, A., “Two-photon absorption properties of fluorescent proteins”, *Nat. Methods* 8, 393-399 (2011).
- [42] Rebane, A., Wicks, G., Drobizhev, M., Cooper, T., Trummal, A. and Uudsemaa, M., “Two-photon voltmeter for measuring a molecular electric field”, *Angew. Chem. Int. Ed. Engl.*, 54 (26), 7582-7586 (2015).
- [43] Xu, C. and Webb, W. W., “Measurement of two-photon excitation cross sections of molecular fluorophores with data from 690 to 1050 nm”, *J. Opt. Soc. Am. B* 13, 481-491 (1996).
- [44] Makarov, N. S., Drobizhev, M. and Rebane, A., “Two-photon absorption standards in the 550-1600 nm excitation wavelength range”, *Opt. Express* 16(6), 4029-4047 (2008).
- [45] Peticolas, W. L. “Multiphoton spectroscopy”, *Ann. Rev. Phys. Chem.* 18, 233-260 (1967).
- [46] Friese, D. H., Mikhaylov, A., Kreszewski, M., Poronok, Y. M., Rebane, A., Ruud, K. and Gryco, D. T., “Pyrrolo[3,2-b]pyrroles- from unprecedented solvatochromism to two-photon absorption”, *Chemistry* 21 (50), 18364-18374 (2015).
- [47] Rebane, A., Drobizhev, M., Makarov, N. S., Beuerman, E., Tillo, S. and Hughes, T., “New all-optical method for measuring molecular permanent dipole moment difference using two-photon absorption spectroscopy”, *J. Lumin.* 130, 1619-1623 (2010).
- [48] Abe, T. and Iweibo, I., “The experimental and theoretical expressions for the molecular electronic oscillator strength in solution”, *J. Chem. Phys.* 83, 1546-1550, (1985).
- [49] Chowdhury, A., Locknar, S. A., Premvardhan, L. and Peteanu, L. A., “Effects of Matrix Temperature and Rigidity on the Electronic properties of Solvatochromic Molecules: Electroabsorption of Coumarin 153”, *J. Phys. Chem. A* 103, 9614-9625 (1999).
- [50] Schiff, L. I., [Quantum Mechanics], McGraw-Hill, New-York (1955).
- [51] Vallee, R. A. L., Van der Auweraer, M., de Stryver, F. C., Beljonne, D. and Orrit, M., “A microscopic Model for the Fluctuations of Local Field and Spontaneous Emission of Single Molecules in Disordered Media”, *Chem. Phys. Chem.* 6, 81-91 (2006).
- [52] Heitler, W., [The quantum theory of radiation, 3rd edition], Dover publications, Inc. (1954).
- [53] Struve, W. S., [Fundamentals of Molecular Spectroscopy], Wiley (1989).

- [54] Meath, W. J., and Power, E. A., “On the importance of permanent moments in multiphoton absorption using perturbation theory”, *J. Phys. B: At. Mol. Opt. Phys.* 17(5), 763 (1984).
- [55] Lim, E., [Excited States, Volume 3], Elsevier Inc. (1977).
- [56] Hol, W. G. J., Van Duijnen, P. T and Berendsen, H. J. C., “The α -helix dipole and the properties of proteins”, *Nature* 273, 443-446 (1978).
- [57] Lippert E., “Dipolmoment Und Elektronenstruktur Von Angeregten Molekullen”, *Z Naturforsch A Astrophys. Phys. Physikalisch Chem.* 10(7), 541–545 (1955).
- [58] Nemkovich, N. A. and Baumann, W., “Molecular Stark-effect spectroscopy of Prodan and Laurdan in different solvents and electric dipole moments in their equilibrated ground and Franck-Condon excited state”, *J. Photochem. Photobiol. A* (185), 26-31 (2007).
- [59] Rebane, A., Wicks, G. R., Drobizhev, M., Cooper, T., Trummal, A. and Uudsemaa, M., “Two-Photon Voltmeter for Measuring a Molecular Electric Field”, *Angew. Chem. Int. Ed. Eng.* 54(26),7582-7586 (2015).
- [60] <http://xu.research.engineering.cornell.edu/research>
- [61] Kim, W. and Kim S. W., “Neural circuit remodeling and structural plasticity in the cortex during chronic pain”, *Korean J Physiol. Pharmacol.* 20(1), 1-8, (2016).
- [62] Coffey, V. “High-energy lasers: new advances in defense applications”, *Opt. Photonics News*, 25(10), 28-35 (2014).
- [63] Miller, M. J., Mott, A. G. and Ketchel, B. P., “General Optical Limiting Requirements”, *Proc. SPIE* 3472 (24), (1998).
- [64] Ehrlich, J. E., Wu, X. L., Lee, I.-Y. S., Hu, Z.-Y., Rockel, H., Marder, S. R. and Perry J. W., “Two-photon absorption and broadband optical limiting with bis-donor stilbenes”, *Opt. Lett.* 22(24), 1843-1845, (1997).
- [65] Zheng, W., Li, D., Zeng, Y., Luo, Y. and Qu, J. Y., “Two-photon excited hemoglobin fluorescence”, *Biomed. Opt. Express* 2 (10), 71-79 (2010).
- [66] Li, D., Zheng, W., Zhang, W., Teh, S. K., Zeng, Y., Luo, Y. and Qu, J. Y., “Time-resolved detection enables standard two-photon fluorescence microscopy for in vivo label-free imaging of microvasculature in tissue”, *Opt. Lett.* 36 (14), 2638-2640 (2011).
- [67] Sun, Q., Zheng, W., Wang, J., Luo, Y. and Qu, J. Y., “Mechanism of two-photon excited hemoglobin fluorescence emission”, *J. Biomed. Opt.* 20 (10), 105014 (2015).
- [68] <http://omlc.org/spectra/hemoglobin/>

- [69] Sheik-Bahae, M., Said, A. A., Tai-Huei, W., Hagan, D. J. and Van Stryland, E. W., "Sensitive measurement of optical nonlinearities using a single beam", *IEEE J. Quant. Electron.* 26(4), 760-769 (1989).
- [70] Nag, A. and Goswami, D., "Solvent effect on two-photon absorption and fluorescence of rhodamine dyes", *J. Photochem. Photobiol. A Chem.* 206, 188-197, (2009).
- [71] M. A. Albota, C. Xu, W. W. Webb, "Two-photon fluorescence excitation cross sections of biomolecular probes from 690 to 960 nm," *Appl. Opt.* 37, 7352-7356 (1998).
- [72] M. Rumi, and J. W. Perry, "Two-photon absorption: an overview of measurements and principles", *Adv.in Opt. and Photon.* 2, 451-518 (2010).
- [73] F. Terenziani, C. Katan, E. Badaeva, S. Tretiak, and M. Blanchard-Desce, "Enhanced Two-photon Absorption of Organic Chromophores: Theoretical and Experimental Assessments", *Adv. Mater.* 20, 4641-4678 (2008).
- [74] A. M. Broumer, "Standards for photoluminescence quantum yield measurements in solution (IUPAC Technical Report)", *Pure Appl. Chem.* 83 (12), 2213-2228 (2011).
- [75] Würth, C., Grabolle, M., Pauli, J., Spieles, M. and Resch-Genger, U., "Relative and absolute determination of fluorescence quantum yields of transparent samples," *Nat. Protoc.* 8 (8), 1535-1550 (2013).
- [76] B. Gu, Y. Sun, W. Ji, "Two-photon-induced excited-state nonlinearities", *Opt. Express* 16, 17745-177751 (2008).
- [77] B. Gu, W. Ji, P. S. Patil, S. M. Dharmaprakash, H-T Wang, "Two-photon induced excited state absorption : Theory and experiment", *Appl. Phys. Lett.* 92, 091118 (2008)
- [78] Y. Gao and M. J. Potasek, "Effects of excited-state absorption on two-photon absorbing materials", *Appl. Opt.*, 45, No 11, 2521-2528 (2006)
- [79] Kubista, M., Sjoback, R., Eriksson, S. and Albinsson, B., "Experimental Correction for the Inner-filter Effect in Fluorescence Spectra", *Analyst* 119, 417-419 (1994).
- [80] <http://refractiveindex.info>
- [81] Yariv, A. and Yeh, [Photonics, 6th edition], Optical Electronics in Modern Communication, (Oxford University Press, 2007).
- [82] Rosete-Aguilar, M., Estrada-Silva, F.C., Bruce, N. C., Roman-Moreno, C. J. and Ortega-Martinez, R. "Calculation of temporal spreading of ultrashort pulses propagation through optical glasses", *Revista Mexicana de Fisika* 54, (2) 141-148 (2008).
- [83] Gu, B., Sun, Y. and Ji, W., "Two-photon-induced excited-state nonlinearities", *Opt. Express* 16 (22), 17745-177751 (2008).

- [84] Arbeloa, I. L., Ojeda, P. R., "Molecular forms of rhodamine B," *Chem. Phys. Lett.* **79**, 347-350 (1981).
- [85] Hinckley, D. A., Seybold, P. G., Borris, D. P., "Solvatochromism and thermochromism of rhodamine solutions," *Spectrochim. Acta A Mol. Spectrosc.* **42**, 741-754 (1986).
- [86] Mchedlov-Petrosyan, N. O. and Kholin, Y. V., "Aggregation of Rhodamine B in water," *Russ. J. of App. Chem.*, **77** (3), 414-422 (2004).
- [87] Dubinina, G. G., Price, R. S., Abboud, K. A., Wicks, G., Wnuk, P., Stepanenko, Y., Drobizhev, M., Rebane, A. and Schanze, K. S., "Phenylene vinylene platinum(II) acetylides with prodigious two-photon absorption," *J. Am. Chem. Soc.* **134** (47), 19346-9 (2012).
- [88] Kannan, R., Tan, L.-S. and Vaia, R. A., "Two-photon responsive chromophores containing electron accepting cores," *US Patent 6,555,682* (2003).
- [89] Kannan, R., He, G. S., Lin, T.-C., Prasad, P. N., Vaia, R. A. and Tan, L.-S., "Toward highly active two-photon, absorbing liquids. Synthesis and characterization of 1,3,5-triazine-based octupolar molecules," *Chem. Mater.* **16** (1), 185-194 (2004).
- [90] Hong, K.-H., Sung, J. H., Lee, Y. S. and Nam, C. H., "Temporal characterization of chirped femtosecond laser pulses," *Opt. Commun.* **213**, 193-200 (2002).
- [91] de Reguardati, S., Pahapill, J., Mikhailov, A., Stepanenko, Y. and Rebane, A., "High-accuracy reference standards for two-photon absorption in the 680-1050 nm wavelength range," *Opt. Express* **24** (8), 9053-9066 (2016).
- [92] N. S. Makarov, M. Drobizhev, A. Rebane, "Two-photon absorption standards in the 550-1600 nm excitation wavelength range," *Opt. Express* **16** (6), 4029-4047 (2008).
- [93] G. G. Dubinina, R. S. Price, K. A. Abboud, G. Wicks, P. Wnuk, Y. Stepanenko, M. Drobizhev, A. Rebane, K. S. Schanze, "Phenylene vinylene platinum(II) acetylides with prodigious two-photon absorption", *J. Am. Chem. Soc.* **134** (47,) 19346-9 (2012).
- [94] Samanta, A. and Fessenden, R. W., "Excited State Dipole Moment of PRODAN as Determined from Transient Dielectric Loss Measurements", *J. Phys. Chem. A.* **104**, 8972-8975 (2000).
- [95] Maroncelli, M. and Fleming, G. R., "Picosecond solvation dynamics of coumarin 153: The importance of molecular aspects of solvation", *J. Chem. Phys.* **86** (11), 6221- 6239 (1987).
- [96] Kuzyk, M. G., Perez-Moreno, J., Zhou, J., Ramini, S. K., Hung, S.-T. and Clays, K., "Experimental verification of a self-consistent theory of the first-

- second- and third-order (non)linear optical response”, *Phys. Rev. A* 84, 033837 (2011).
- [97] Cho, S. H., Chang, W. S., Kim, K. R. and Hong, J. W., “Measurement of UV absorption of single living cell for cell manipulation using NIR femtosecond laser”, *Appl. Surf. Sci.* 255 (9), 4974-4978 (2009).
- [98] Siede, W. and Doetsch, P. W., [DNA Damage Recognition], CRC Press (2005).
- [99] Bridges, E. R., Fischer, G. L. and Boyd, R. W., “Z-scan measurement technique for non-Gaussian beams and arbitrary sample thicknesses”, *Opt. Lett.* 20 (17), 1821-1823 (1995).
- [100] Mataga, N., Kaifu, Y. and Koizumi, M., “Solvent effects upon fluorescence spectra and the dipole moments of excited molecules”, *Bull. Chem. Soc. Jpn.* 61, 962-975 (1955).
- [101] Liptay, W., “Electrochromism and Solvatochromism”, *Angew. Chem. Int. Ed Engl.* 8 (3), 177-188 (1969).
- [102] https://www.researchgate.net/post/What_are_the_HOMO_and_LUMO_levels_of_Coumarin-153
- [103] Oulianov, D. A., Tomov, I. V., Dvornikov, A. S. and Rentzepis, P. M., “Observations on the measurement of two-photon absorption cross-section” *Opt. Commun.* 191, 235–243 (2001).
- [104] Balter, A., Nowak W., Pawelkiewicz W. and Kowalczyk, A. D. “Some remarks on the interpretation of the spectral properties of Prodan”, *Chem. Phys. Lett.* 143 (6), 565–570 (1988).
- [105] Catalan, J., Perez, P., Laynez, J., and Blanco, F., « Analysis of the solvent effect on the photophysics properties of 6-Propionyl-2-(dimethylamino)naphthalene (PRODAN)”, *J. Fluoresc.* 1 (4), 215–223 (1991).
- [106] Kawski, A., Kuklinski, B. and Bojarski, P., “Thermochromic shifts of absorption and fluorescence spectra and excited state dipole moment of PRODAN”, *Z Naturforsch. A Phys. Sci.* 55 (5), 550-554 (2000).
- [107] Rechthaler, K. and Kohler, G., “Excited state properties and deactivation pathway of 7-aminocoumarins”, *Chem. Phys.* 189, 99-116 (1994).
- [108] Horng, M. L., Gardecki, J. A., Papazyan, A. and Maroncelli, M., “Subpicosecond Measurements of Polar Solvation Dynamics: Coumarin 153 Revisited”, *J. Phys. Chem.* 99 (48), 17311-17337 (1995).
- [109] Kodali, G., Narayanan, M. and Stanley, R. J., “Excited-State Electronic Properties of 6-Methylisoxanthopterin (6-MI): An Experimental and Theoretical Study”, *J. Phys. Chem. B* 116 (9), 2981-2989 (2012).

- [110] Bestvater, F., Spiess, E., Stobrawa, G., Hacker, M., Feurer, T., Porwol, T., Berchner-Pfannschmidt, U., Wotzlaw, C. and Acker, H., "Two-photon fluorescence absorption and emission spectra of dye relevant for cell imaging", *J. Microsc.* (208), 108-110 (2002).
- [111] Mütze, J., Iyer, V., Macklin, J. J., Colonell, J., Karsh, J., Petrášek, Z., Schwille, P., Looger, L. L., Lavis, L. D. and Harris, T. D., "Excitation Spectra and Brightness Optimization of Two-Photon Excited Probes", *Biophys. J.* 102 (4), 934-944 (2012).
- [112] Velasco, M. G. M., Allgeyer, E. S., Yuan, P., Grutzendler, J. and Bewersdorf, J., "Absolute two-photon excitation spectra of red and far-red fluorescent probes", *Opt. Lett.* 40 (21), 4915-4918 (2015).
- [113] Makarov, N. S., Campo, J., Hales, J. M. and Perry, J. W., "Rapid, broadband two-photon-excited fluorescence spectroscopy and its application to red-emitting secondary reference compounds", *Opt. Mat. Express* 1 (4), 551-563 (2011).
- [114] Penzkofer, A. and Wiedmann, J., "Orientation of transition dipole moments of rhodamine 6G determined by excited state absorption", *Opt. Commun.* 35 (1), 81-86 (1980).
- [115] Jagatap, B. N. and Meath, J. "Contributions of permanent dipole moments to molecular multiphoton excitation cross section", *J. Opt. Soc. Am. A* 19 (11), 2673-2681 (2002).

ACKNOWLEDGEMENTS

This dissertation is the result of almost 4 years of work and adaptation in a new life.

First, I would like to express my greatest gratitude to my supervisor, Prof. Aleksander Rebane, for his support and helpful discussions. Under his supervision I had an amazing opportunity to work in a rich initial training network worn by a common and interdisciplinary goal. The field of 2PA is so wide, that I think I will never know enough on the subject.

I would like to thank Dr. Raivo Stern, who welcomed me in KBFI and helped my first step there.

I would like to thank Jüri Pahapill, engineer-physicist. His help with many experiments is invaluable; as well he was my human back-up memory when I forgot things or procedures. Without him, I definitely would not have succeeded this PhD. Thanks to Matt Rammo, master student, who came to learn and give a hand.

I would like to thank everyone working at KBFI, for our gathering coffee break, discussion and exchange of good ideas. Especially Liis and Jasper, with who I was mostly hanging out. Thanks to Charlie, a native English speaker in the team is valuable, especially when it is forbidden to write the thesis in French!

I would like to thank my very first guru, M. Jean-François de Backer, who after so many years stays at pole position when I have to think who was my best physics teacher. Without him, I am pretty sure I wouldn't have continued my studies in physics field.

Great thank to my husband, who is responsible to our relocation in Estonia and thus my involvement in this PhD. After these year, I feel like Tallinn is my home and I had a heart-broken to leave this place.

Finally and most importantly, my PhD best success were undoubtedly my two organic synthesis, namely my two kids Philippe and Elisabeth who are able to make my life full of joy and meaningful.

CURRICULUM VITAE

Name	Sophie de Reguardati
Date and place of birth	January 24, 1983, France
E-mail address	sophie.de.reguardati@kbfi.ee
Education	2012-2017 Doctoral studies at Tallinn University of Technology in Engineering Physics Tallinn, Estonia 2008 –2009 Master degree at ENS Cachan, France on Molecular nano- and bio-photonics for telecommunications and biotechnologies 2007 – Agregation diploma of Physics, France
Language competence/skills	French, native (C2) English, fluent (B2)
Employment	2012-2017 early stage researcher at National Institute of Chemical Physics and Biophysics, Tallinn, Estonia 2010-2012 scientific communication at National Museum of Natural History (Paris, France) for secondary school public 2009-2010 teacher of physics and chemistry in secondary school in Paris, France
Research activity	Establishment of two-photon standards with high accuracy cross-section determination

ELULOOKIRJELDUS

Ees- ja perekonnanimi	Sophie de Reguardati
Sünniaeg- ja koht	24.01.1983, Prantsusmaa
E-maili aadress	sophie.de.reguardati@kbfi.ee
Haridus	2012-2017 Doktoriope Tallinna Tehnikaülikoolis tehnilise füüsika erialal, Tallinn, Eesti. Dokoritöö teema: Kõrgtäpsusega standardid kvantitatiivse kahe footoni neeldumisspektroskoopia tarbeks. 2008 –2009 Magistriõpe, ENS Cachan, Prantsusmaa. Magistritöö teema: Molekulaarne nano- ja biofotoonika telekommunikatsiooni ja biotehnoloogia tarbeks. 2007 – Diplomiõpe füüsika erialal, Prantsusmaa.
Keelte valdamine	Prantsuse keel, emakeel (C2) Inglise keel, vabalt (B2)
Töökohad	2012-2017 Teadur, Keemilise ja Bioloogilise Füüsika Instituut (KBFI), Tallinn, Eesti; 2010-2012 Teadussuhtluse spetsialist gümnaasiumi õpilastele, National Museum of Natural History, Paris, France. 2009-2010 füüsika ja keemia õpetaja, Gümnaasium, Paris, France
Teaduslik uurimistöö	Orgaaniliste süsteemide mitme footoni neeldumise mittelineaarne spektroskoopia ja tehnika (füüsikaline keemia)

APPENDICES

APPENDIX A: Saturation effect in 2PA absorption

When saturation in 2PA occurs, then the ground-state is depleted such as the population density N_g is not constant anymore. In general N_g is a function of time and space. When a fluorophore is promoted to an excited state, then, in general, it cannot absorb at the same wavelength unless it returns to the ground state.

The rate of excitation from the ground state is governed by the equation:

$$\frac{dN_g}{dt} = \frac{N_f}{\tau_{fl}} - \frac{1}{2}\sigma_{2PA}N_g\Phi^2, \quad (\text{A.1})$$

where τ_{fl} is the ground state recovery time identified as fluorescence lifetime of the fluorophore. Note that Equation (A.1) neglects stimulated emission supposing that the number of molecules excited remains small.

If we assume that the recovery is much faster than the time interval between two excitation pulses, $\tau_{fl} < 1/f$, then each consecutive pulse encounters the medium, where all chromophores are in the ground state. For 76-MHz repetition rate, $1/f=13.2$ ns, which exceeds typical value for fluorescence lifetime $\sim 1 - 4$ ns, thus legitimizes this equation. In this situation, the material is in the same condition every time a new pulse arrives and the total number of photon absorbed is additive in the number of pulses.

Table A.1: Typical of fluorescence lifetime values for a few solvated chromophores [1].

Chromophore	Fluorescence lifetime
Fluorescein in buffer pH=11	4.0 ns
Prodan in water	1.4 ns
Rhodamine 6G in water	4.1 ns
Coumarin 6 in ethanol	2.5 ns

On the other hand, laser pulse duration $\Delta t \sim 100$ fs is much shorter than the recovery time so we can assume that no excited chromophore decays to the ground state within the pulse duration. We can therefore neglect the first term of Equation (A.1):

$$\frac{dN_g}{dt} = -\frac{1}{2}\sigma_{2PA}N_g\Phi^2, \quad (\text{A.2})$$

with $\Phi = \Phi_0 \times e^{-\frac{2(\ln 2 \times t)^2}{\Delta t^2}}$ for a Gaussian photon flux.

By integration over pulse duration, we find the fraction of population remaining in the ground state is:

$$\frac{N_g}{N_g(0)} = e^{-\frac{\sqrt{\pi}}{8\ln(4)}\sigma_{2PA}\Delta t\Phi_0^2}. \quad (\text{A.3})$$

Assuming a constant pulse duration $\Delta t \sim 100$ fs, the fraction of population in the ground depends on the peak of the photon flux as shown in Figure A.1.

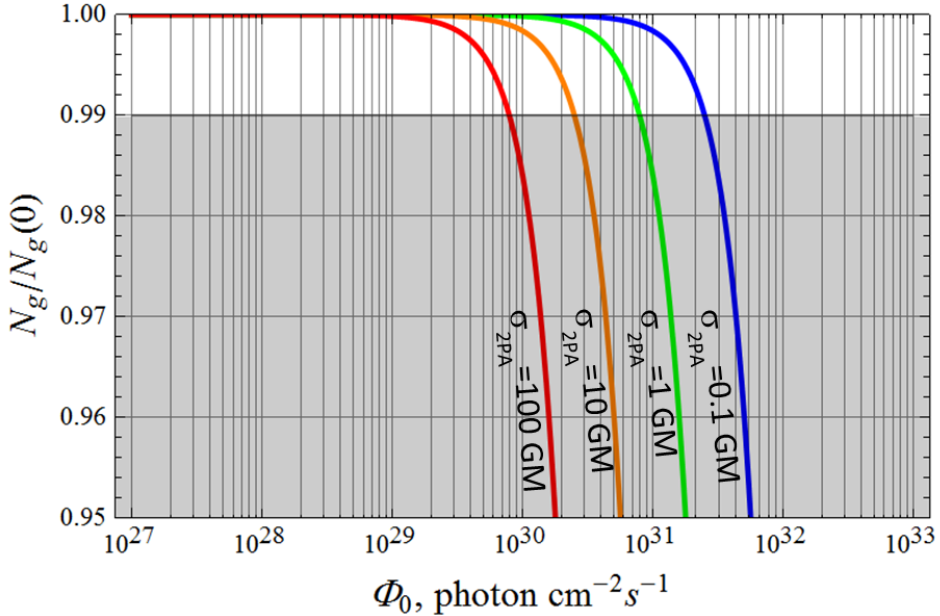


Figure A 1: Dependence of the relative population in the ground state as a function of the photon flux peak for different 2PA cross-section values. By setting of $\frac{N_g}{c} \geq 99\%$ the grey zone symbolizes the forbidden region.

For a 2PA cross-section of 100 GM, maximum saturation at 0.1% is reached with a photon flux of 7.9×10^{29} photon $\text{cm}^{-2} \text{s}^{-1}$. Considering a beam waist of ~ 0.3 mm and wavelength 800 nm, this limit correspond to an average power of $\sim 10^4$ W which is far above the maximum power ~ 1 W used in our experiment. Because we are using diluted solution, then the variation of the density in the ground state $N_g(t)$ is negligible. This is not the case for direct method, where high concentration and more focus beam are used such as in the direct method.

APPENDIX B: Temporal pulse broadening through optics

The chromatic dispersion of optical materials causes an optical pulse to spread as it propagates through the material. The pulse spreading is produced by the dependence of the group velocity on the frequency. The effect is more dramatic for ultrashort pulses since they have great spectral width.

1. Parameterization of the system

1.1. Description of a pulse

A pulse is an optical field of finite time duration and can be made by adding different monochromatic plane waves with different frequency. For a monochromatic wave and using the complex notation, the amplitude of the wave at the $z=0$ position can be expressed as $\tilde{E}(0, \omega)$.

Taking into account time dependence:

$$\tilde{E}(0, \omega, t) = e^{j\omega t} \tilde{E}(0, \omega), \quad (\text{B.1})$$

and adding up all waves, the pulse is then seen as a Fourier integral:

$$E(0, t) = \int \tilde{E}(0, \omega, t) d\omega = \int e^{j\omega t} \tilde{E}(0, \omega) d\omega. \quad (\text{B.2})$$

The pulse envelop $\tilde{E}(0, \omega)$ in the spectral domain appears to be the inverse Fourier integral of the initial temporal profile:

$$\tilde{E}(0, \omega) = \int e^{-j\omega t} E(0, t) dt. \quad (\text{B.3})$$

A temporal Gaussian pulse, centered on the pulsation ω_0 , is given by

$$E(0, t) = e^{-\ln 4 \left(\frac{t}{\tau_0}\right)^2} e^{j\omega_0 t + \varphi}, \quad (\text{B.4})$$

where τ_0 represents the full width at half maximum duration of the intensity peak. For instance FigureB.1 represent such a pulse, considering real part of Equation (B.4), with a central angular frequency or pulsation $\omega_0 = 2.35 \times 10^{15}$ rad s^{-1} corresponding to the wavelength $\lambda_0 = 800$ nm and a duration $\tau_0 = 10^{-13}$ s.

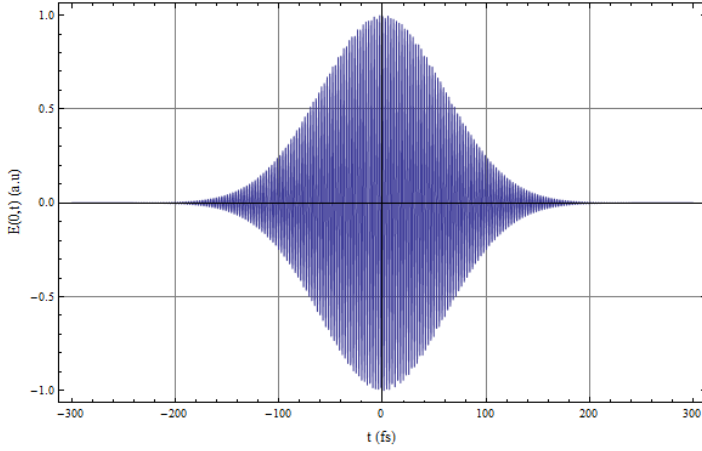


Figure B.1: Example of a pulse with 2.35 rad fs^{-1} central pulsation and duration 100 fs

The phase φ can be time-dependent if the pulse is chirped. In case of transform-limited Gaussian pulse, it remains constant and with the adequate time origin can be put at 0.

In the spectral domain, the calculation of the inverse Fourier (B.3) integral gives:

$$\tilde{E}(0, \omega) = \sqrt{\frac{\pi}{\ln 4}} \tau_0 e^{-\frac{\tau_0^2}{4 \ln 4} (\omega - \omega_0)^2}, \quad (\text{B.5})$$

which is also a Gaussian centered on ω_0 . The corresponding spectral intensity has a full width at half maximum $\Delta\omega = \frac{4 \ln 4}{\tau_0}$ and is represented in Figure B.2.

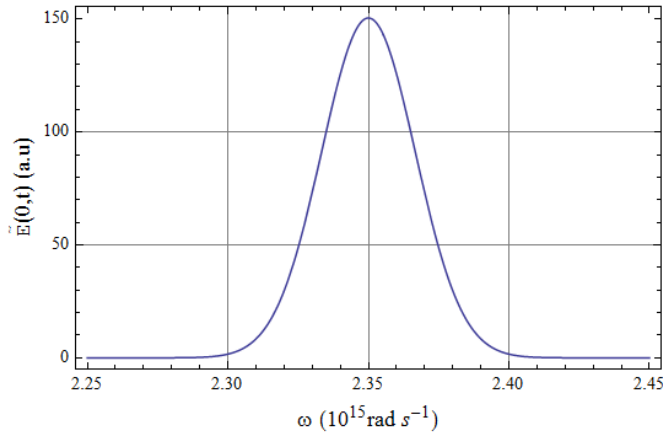


Figure B.2: Fourier transformation of pulse from Figure B.1

In the case of a femtosecond laser $\tau_0 = 100 \text{ fs}$ centered on the wavelength $\lambda_0 = 800 \text{ nm}$ then:

$$\begin{aligned}\Delta\omega &\approx 5.5 \cdot 10^{13} \text{ rad s}^{-1}, \\ \omega_0 &= \frac{2\pi}{\lambda_0} c \approx 2 \cdot 10^{15} \text{ rad s}^{-1}.\end{aligned}\tag{B.6}$$

Therefore $\frac{\Delta\omega}{\omega_0} \approx 0.02 \ll 1$, e.g. the pulse is narrowly concentrated in the neighborhood of ω_0 and move slowly compare to the vibration ω_0 .

1.2. Dispersive optics

The temporal profile of a short optical pulse is altered as it travels through a dispersive optical system. This occurs because the spectral components that constitute the pulse are phase shifted by different retardation and/or attenuated.

The transmission through a linear optical system can be characterized by a transfer function $H(\omega, z)$, which is the factor that multiplies, in the spectral domain, the input pulse to generate the output pulse after crossing the distance z through the system

$$\tilde{E}(z, \omega) = H(\omega, z) \tilde{E}(0, \omega).\tag{B.7}$$

A transparent medium is characterized by its refractive index $n(\omega)$ which depends on the light's frequency. In case of there is no attenuation, the transfer function is only a phase filter:

$$H(\omega, z) = e^{-jn(\omega)\frac{\omega}{c}z} = e^{-jk(\omega)z},\tag{B.8}$$

were $n(\omega)\frac{\omega}{c} = k(\omega)$ the wave vector.

A transparent homogeneous isotropic non-magnetic medium can be described by its refractive index using the Sellemeier formula:

$$n^2(\lambda) - 1 = \frac{B_1\lambda^2}{\lambda^2 - c_1} + \frac{B_2\lambda^2}{\lambda^2 - c_2} + \frac{B_3\lambda^2}{\lambda^2 - c_3},\tag{B.9}$$

were the wavelength in vacuum λ expressed in μm . Figure B.3 presents such dependence on the example of BK7 glass.

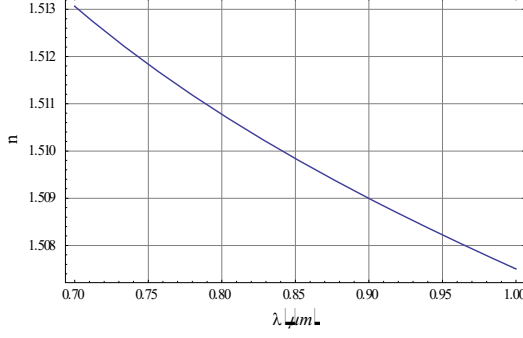


Figure B 3: dependence of glass BK7 refractive index upon the wavelength over the range available by mode-locked Ti:Sapphire femtosecond oscillator (Coherent Mira 900F).

2. Pulse broadening calculation

2.1. Exact calculation

At the output of the medium with refractive index $n(\omega)$ and length d , the resulting pulse is obtained by multiplying with the transfer function characterizing the medium

$$\tilde{E}(d, \omega) = H(\omega, d) \tilde{E}(0, \omega) = e^{-jk(\omega)d} \sqrt{\frac{\pi}{\ln 4}} \tau_0 e^{-\frac{\tau_0^2}{4 \ln 4} (\omega - \omega_0)^2}. \quad (\text{B.10})$$

In the time-domain, the pulse is given by Fourier transformation:

$$\begin{aligned} E(d, t) &= \int e^{j\omega t} \tilde{E}(d, \omega) d\omega \\ &= \int e^{j\omega t} e^{-jk(\omega)d} \sqrt{\frac{\pi}{\ln 4}} \tau_0 e^{-\frac{\tau_0^2}{4 \ln 4} (\omega - \omega_0)^2} d\omega. \end{aligned} \quad (\text{B.11})$$

Since the input pulse is centered on ω_0 , we can do the transformation $\Omega = \omega - \omega_0$, thus:

$$E(d, t) = \sqrt{\frac{\pi}{\ln 4}} \tau_0 \int e^{j(\Omega + \omega_0)t} e^{-jk(\Omega + \omega_0)d} e^{-\frac{\tau_0^2}{4 \ln 4} \Omega^2} d\Omega. \quad (\text{B.12})$$

Because this integral over Ω is restricted over the low-frequency band $\Delta\omega \ll \omega_0$, the pulse envelop will be slowly varying relatively to the period of the carrier $\frac{2\pi}{\omega_0}$.

2.2. Approximation using group velocity

With the condition that the envelope varies slowly, one can expand $k(\Omega + \omega_0)$ to a Taylor series about the center optical frequency ω_0 :

$$k(\Omega + \omega_0) = k(\omega_0) + \left. \frac{dk}{d\omega} \right|_{\omega=\omega_0} \Omega + \left. \frac{1}{2} \frac{d^2k}{d\omega^2} \right|_{\omega=\omega_0} \Omega^2 + \dots \quad (\text{B.13})$$

Considering the system parameterization, $k(\Omega + \omega_0)$ is real and lead to the identification with the group velocity $v_g = \left. \frac{dk}{d\omega} \right|_{\omega=\omega_0}$:

$$\left. \frac{d^2k}{d\omega^2} \right|_{\omega=\omega_0} = \left. \frac{d}{d\omega} \left(\frac{1}{v_g} \right) \right|_{\omega=\omega_0} = - \frac{1}{v_g^2} \left. \frac{dv_g}{d\omega} \right|_{\omega=\omega_0}. \quad (\text{B.14})$$

In the quadratic approximation, the derivative of order higher than 2 are neglected. The calculation of the integral (B.12) is then simplified:

$$E(d, t) = \sqrt{\frac{\pi}{\ln 4}} \tau_0 e^{j(\omega_0 t - k(\omega_0) d)} \int e^{-j \left(\frac{d}{v_g} - t \right) \Omega} e^{- \left(j a d + \frac{\tau_0^2}{4 \ln 4} \right) \Omega^2} d\Omega, \quad (\text{B.15})$$

were $a = \left. \frac{1}{2} \frac{d^2k}{d\omega^2} \right|_{\omega=\omega_0}$ the chirping factor.

The integration can be carried out by using the ‘‘Siegman’s lemma’’ namely:

$$\int e^{-Ay^2 - 2By} dy = \sqrt{\frac{\pi}{A}} e^{B^2/A}; \quad \text{Re}[A] > 0, \quad (\text{B.16})$$

After identification, it appears that the output pulse has the shape:

$$E(d, t) = \frac{2\pi}{\sqrt{\frac{4jad\ln 4}{\tau_0^2} + 1}} e^{j \left(\omega_0 t - k(\omega_0) d + 4ad \frac{\left(t - \frac{d}{v_g} \right)^2}{\left(\frac{\tau_0^2}{\ln 4} \right)^2 + 16 a^2 d^2} \right)} e^{- \frac{\ln 4 \left(t - \frac{d}{v_g} \right)^2}{\tau_0^2 + 16 a^2 d^2 \frac{\ln 4^2}{\tau_0^2}}}, \quad (\text{B.17})$$

The intensity of the pulse is therefore:

$$I(d, t) = |E(d, t)|^2 = \frac{4\pi^2}{\frac{4jad\ln 4}{\tau_0^2} + 1} e^{- \frac{2\ln 4 \left(t - \frac{d}{v_g} \right)^2}{\tau_0^2 + 16 a^2 d^2 \frac{\ln 4^2}{\tau_0^2}}}, \quad (\text{B.17})$$

The output pulse is also Gaussian, delayed by $\frac{d}{v_g}$ and with a full-width at half

maximum duration $\tau = \tau_0 \sqrt{1 + \left(\frac{8ad\ln 2}{\tau_0^2} \right)^2}$

2.3. Chirping factor a

The chirping a is calculated from the dependence of the refractive index n on the wavelength.

The group velocity can be calculated

$$\begin{aligned} \frac{1}{v_g} = \frac{dk}{d\omega} \Big|_{\omega=\omega_0} &= -\frac{\lambda^2}{2\pi c} \frac{dk}{d\lambda} \Big|_{\lambda=\lambda_0} = -\frac{\lambda^2}{c} \frac{d}{d\lambda} \left(\frac{n}{\lambda} \right) \Big|_{\lambda=\lambda_0}, \\ \frac{1}{v_g} &= \frac{n(\lambda) - \lambda \frac{dn}{d\lambda}}{c} \Big|_{\lambda=\lambda_0}, \end{aligned} \quad (\text{B.18})$$

where λ_0 is the central wavelength defined by $\omega_0 = \frac{2\pi c}{\lambda_0}$.

Therefore:

$$\begin{aligned} a = \frac{1}{2} \frac{d^2 k}{d\omega^2} \Big|_{\omega=\omega_0} &= -\frac{1}{2v_g^2} \frac{dv_g}{d\omega} \Big|_{\omega=\omega_0} = \frac{\lambda^2}{4\pi c v_g^2} \frac{dv_g}{d\lambda} \Big|_{\lambda=\lambda_0}, \\ a &= \frac{\lambda_0^3}{4\pi c^2} \frac{d^2 n}{d\lambda^2} \Big|_{\lambda=\lambda_0}. \end{aligned} \quad (\text{B.19})$$

The derivation of the refractive index can be calculated from the Sellmeier formula leads to:

$$\begin{aligned} \frac{d^2 n}{d\lambda^2} \Big|_{\lambda=\lambda_0} &= \frac{\left(-\frac{2B_1\lambda_0^3}{(\lambda_0^2 - C_1)^2} + \frac{2B_1\lambda_0}{\lambda_0^2 - C_1} - \frac{2B_2\lambda_0^3}{(\lambda_0^2 - C_2)^2} + \frac{2B_2\lambda_0}{\lambda_0^2 - C_2} - \frac{2B_3\lambda_0^3}{(\lambda_0^2 - C_3)^2} + \frac{2B_3\lambda_0}{\lambda_0^2 - C_3} \right)^2}{4 \left(1 + \frac{B_1\lambda_0^2}{\lambda_0^2 - C_1} + \frac{B_2\lambda_0^2}{\lambda_0^2 - C_2} + \frac{B_3\lambda_0^2}{\lambda_0^2 - C_3} \right)^{3/2}} \\ &+ \frac{\frac{8B_1\lambda_0^4}{(\lambda_0^2 - C_1)^3} - \frac{10B_1\lambda_0^2}{(\lambda_0^2 - C_1)^2} + \frac{2B_1}{\lambda_0^2 - C_1} + \frac{8B_2\lambda_0^4}{(\lambda_0^2 - C_2)^3} - \frac{10B_2\lambda_0^2}{(\lambda_0^2 - C_2)^2} + \frac{2B_2}{\lambda_0^2 - C_2} + \frac{8B_3\lambda_0^4}{(\lambda_0^2 - C_3)^3} - \frac{10B_3\lambda_0^2}{(\lambda_0^2 - C_3)^2} + \frac{2B_3}{\lambda_0^2 - C_3}}{2 \sqrt{1 + \frac{B_1\lambda_0^2}{\lambda_0^2 - C_1} + \frac{B_2\lambda_0^2}{\lambda_0^2 - C_2} + \frac{B_3\lambda_0^2}{\lambda_0^2 - C_3}}} \end{aligned} \quad (\text{B.20})$$

3. Application considering elements on the set-up

3.1. Optical element

The laser beam crosses different lenses, beam splitter, a half wave plate and -Glan-Taylor polarizer. Those transparent medium can attenuate the power and also broaden the pulse that reaches the sample. Only what matter are their length and their chemical composition. Hence focal of lenses is irrelevant for the phenomenon. Therefore the pulse duration measured by redirecting the beam from position MF may be underestimated.

Regarding the schematics of the set-up in Figure 22, L1 and L5 are equivalent: they are both made of glass N-BK7 and have same thickness. Therefore, the possible pulse elongation due to L5 has the same effect that the one due L2 for reaching the sample. Therefore, the optical components that need to be discussed are GP2, GP5 and L3.

3.2. Broadening through lens (L3)

The lens has thickness 2.3 mm at its center and is made of N-BK7. Figure A.4 presents the enlargement of the pulse after L3 depending on the wavelength. In any cases the enlargement is smaller than 0.01%, e.g. beyond even its detection.

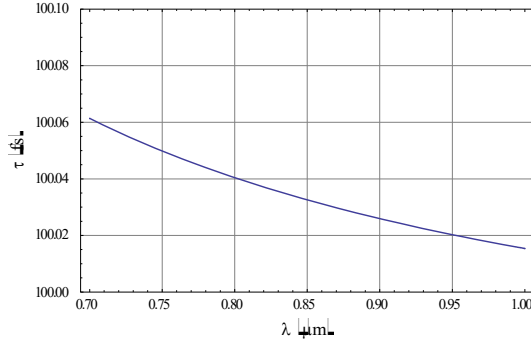


Figure B.4: 100 fs pulse broadening through L3.

3.3. Broadening through beam-splitter (BS2)

Beam-splitter thickness is 4 mm, thus the distance crossed by the laser is $d \sim 4\sqrt{2} = 5.66 \text{ mm}$. Its composition is N-BK7.

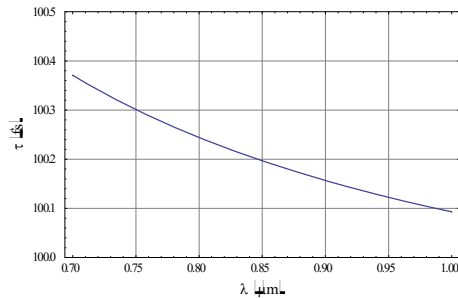


Figure B.5: 100 fs pulse broadening through GP2 considered made of N-BK7.

From Figure B.5, one can see that the pulse elongation is negligible. Elongation through GP5 will give similar results.

To conclude, pulse elongation through the optical elements is negligible. Therefore the pulse duration can be measured on the beam path, where it is physically convenient.

APPENDIX C: Determination of magnification factor

L4 position is adjusted such as the red beam passes through it center. Then the red beam is spread using a piece of white paper placed in front of the sample location. L4 position is further adjusted on the optical axis to image a micrometer ruler placed at the sample location. Figure C.1 shows the image of the microscale form on the camera. The image is sharp, testifying the good positioning of the lens.

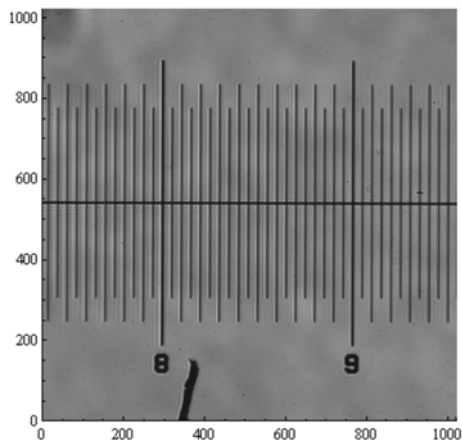


Figure C.1: Example of the ruler image after adjusting L4 lens position for red beam set at 692 nm.

A chosen horizontal profile can be selected showing the intensity distribution, where each minimum stand for a line black marker from the microscale, as shown in Figure C.2.

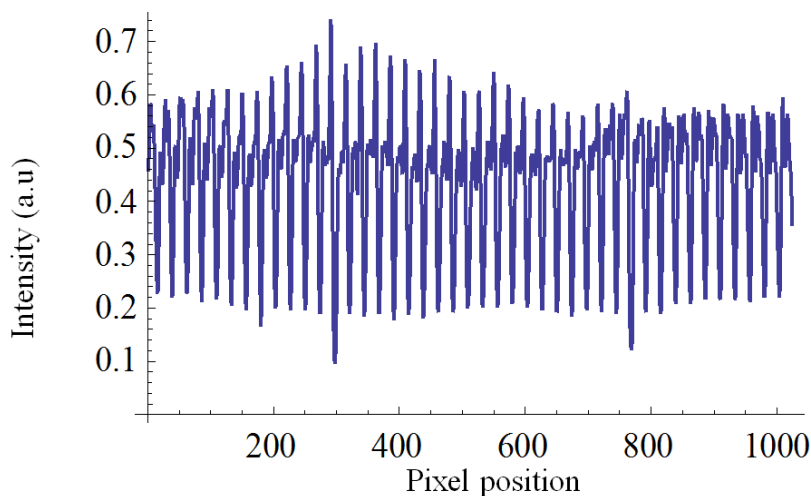


Figure C.2: Example of intensity profile from the 450th vertical position of the previous image C.1.

If we call \min_1 the position of the first minimum and \min_2 the position of the last minimum, N the number of markers from \min_1 to \min_2 , since one pixel size is $6.45 \mu\text{m}$, then the magnification factor is given by:

$$mag = \frac{6.45(\min_2 - \min_1)}{50(n-1)}. \quad (\text{A.1})$$

Position of \min_1 and \min_2 may be between two possible pixels. Minimizing \min_1 for one pixel and maximizing \min_2 for 1 pixel gives a deviation of 2% which will be considered as a fixed error in this measurement.

APPENDIX D: Auto-correlator calibration for measuring the pulse temporal profile

In the auto-correlator modified by A. Rebane, shown in Figure 22, every single pulse with envelope function $I(t)$ was split in two identical copies on an uncoated glass plate GP5. The resulting beams were reflected back from corner mirrors (CM1, CM2) while passing on their way twice through 1 mm thick rotating glass plates (GP6, GP7) set at 60 degrees with respect to each other and acting as a variable delay between the two beams. The retro reflected beams were again recombined on GP5 and focused with lens L6 (60 mm) to a common spot in 0.1 mm BBO crystal producing a non-collinear second harmonic generation beam.

According to the Snell-Descartes' law of refraction law and the fact the two glass plates are set at $\theta_r = 60^\circ$ relative to each other, the total time delay between the two beams is:

$$\Delta\tau_{\pm} = L \frac{\Delta\tau_{\text{auto}} = \Delta\tau^+ - \Delta\tau^-, \quad n_2 - n_1 \left(\frac{n_1}{n_2} \sin^2(\theta \pm \theta_r/2) \right) + \cos(\theta \pm \theta_r/2) \sqrt{1 - \frac{n_1^2}{n_2^2} \sin^2(\theta \pm \theta_r/2)}}{c \sqrt{1 - \frac{n_1^2}{n_2^2} \sin^2(\theta \pm \theta_r/2)}}, \quad (\text{D.1})$$

where θ is the rotational angle as illustrated on Figure D.1, n_1 is the refractive index of the air set at unity and n_2 is the refractive index of the glass. Refractive index depends on wavelength and can be described by Sellmeier equation.

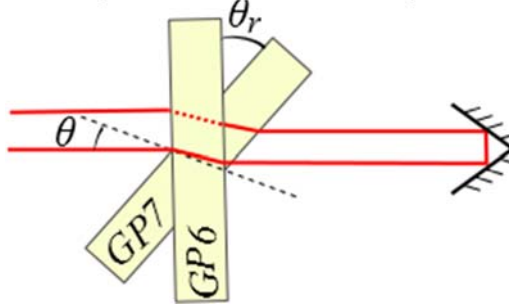


Figure C. 1: Profile scheme of the delay system made from two glass plate GP6 and GP7.

The delayed two beams are parallel but slightly separated when they reach the lens L6, which refracts them along mutually converging path that cross in the type I second harmonic crystal BBO. An output second harmonic beam at half the laser wavelength appears after the crystal, traveling in a direction that bisects the angle between the two input beams. The SHG intensity as a function of time was detected with a photomultiplier (PM) and digitized with 4 GHz oscilloscope Keysight DSOS404A. A blue glass filter (SGF) was used to reject residual fundamental wavelength. Since the detector response is slow compared to the pulse envelope function, the integrated measured intensity is:

$$S_{SHG} \propto \int I(t)I(t - \Delta\tau_{\text{auto}})dt. \quad (\text{D.2})$$

An optical fork sensor detected the passage of GP7 edge, allowing the determination of the rotational speed and consequently the conversion of the oscilloscope time axis into θ .

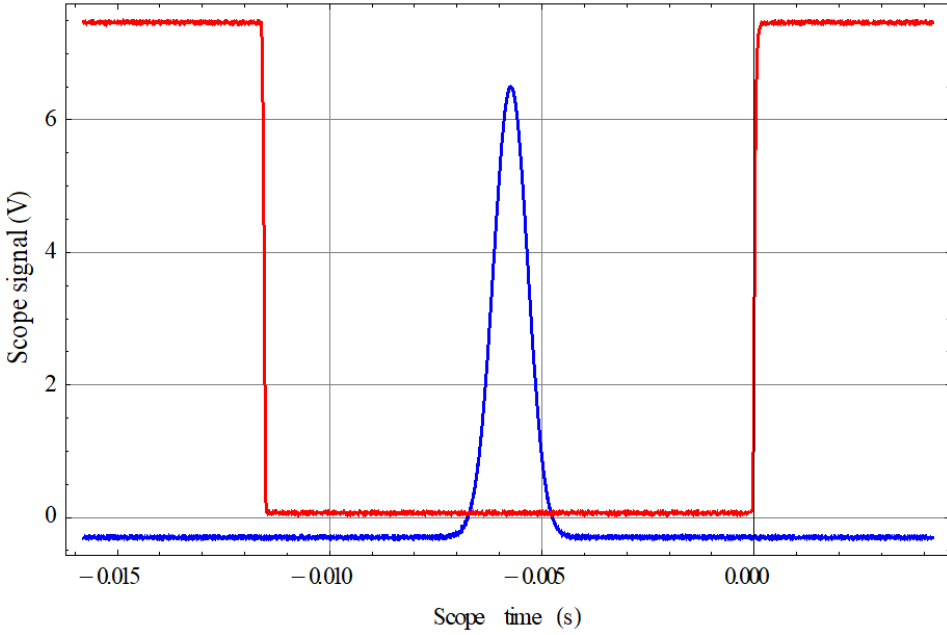


Figure 46: Example of the oscilloscope trace from the auto-correlator with the laser set at 786 nm. Blue line is the signal of the SHG and red line is the signal from the internal optical fork detecting the glass passage to the vertical position.

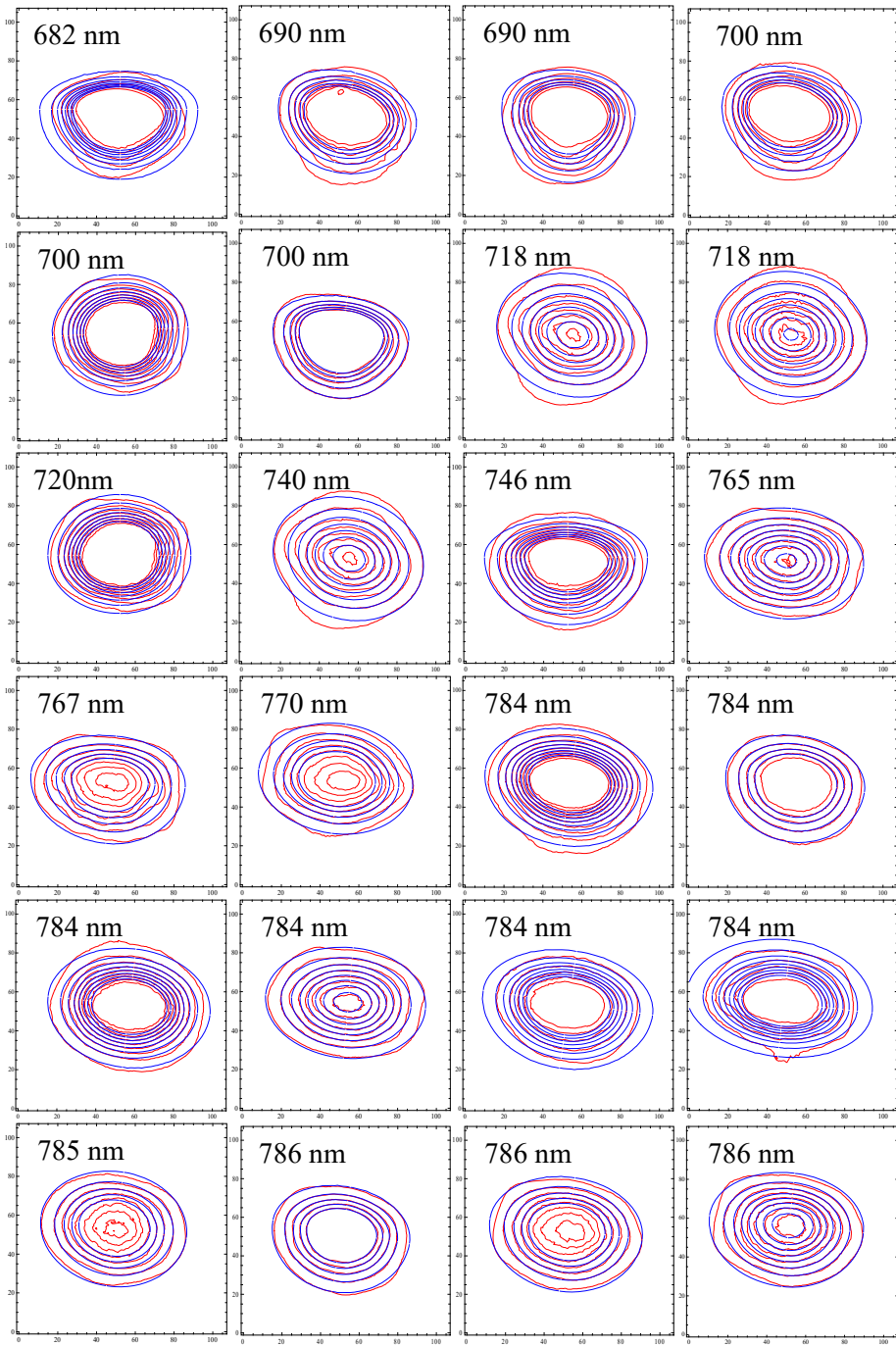
One rotation of the glass plate occurs within 0.068 s. The oscilloscope is set with 0.02s scanning speed and acquires 10000 points. Therefore:

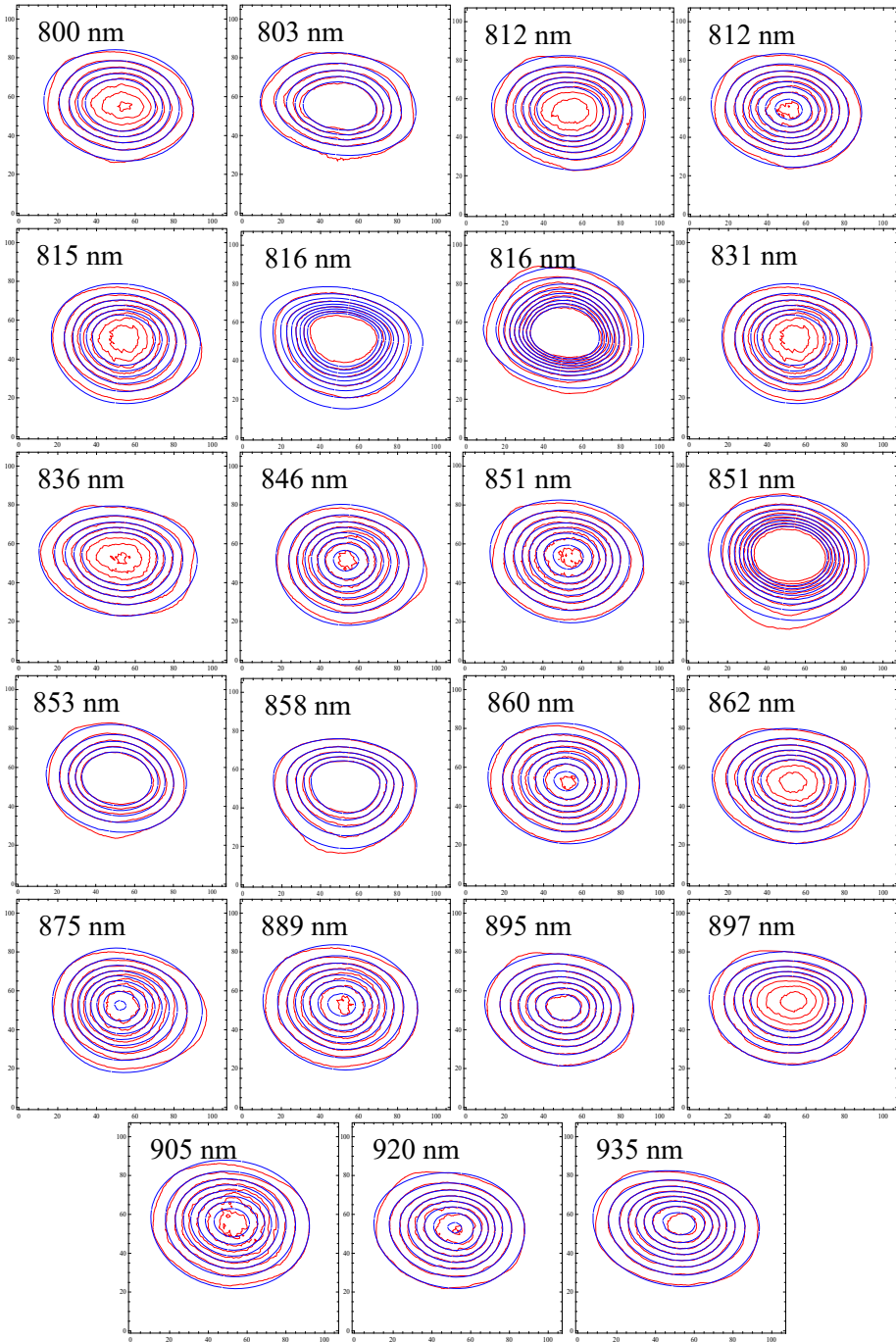
$$\theta = \frac{360}{0.068} \frac{0.02}{10000} i, \quad (\text{D.3})$$

where i is the i th point of the acquisition.

According Equation (D.2), the auto-correlator trace S is always symmetrical and therefore doesn't reveal the exact shape of $I(t)$. Nevertheless, maximum degree of pulse asymmetry can be identified as a deviation from exact Gaussian shape.

APPENDIX E: Beam profile at various wavelengths





APPENDIX F: Molecular structure of reference standards

Figure F.1 shows the chemical structures of the fluorophores chosen to be part of the 2PA reference standard set. These 7 chromophores are: 4,4'-bis(diphenylamino)-stilbene (BDPAS), Prodan, Coumarin 153 (C153), 7,7',7''-(1,3,5-triazine-2,4,6-triyl)tris[9,9-didecyl-N,N-diphenyl]9H-Fluoren-2-amine (AF455), Fluorescein dianion, Rhodamine 6G (Rh6G) and 9-Chloroanthracene.

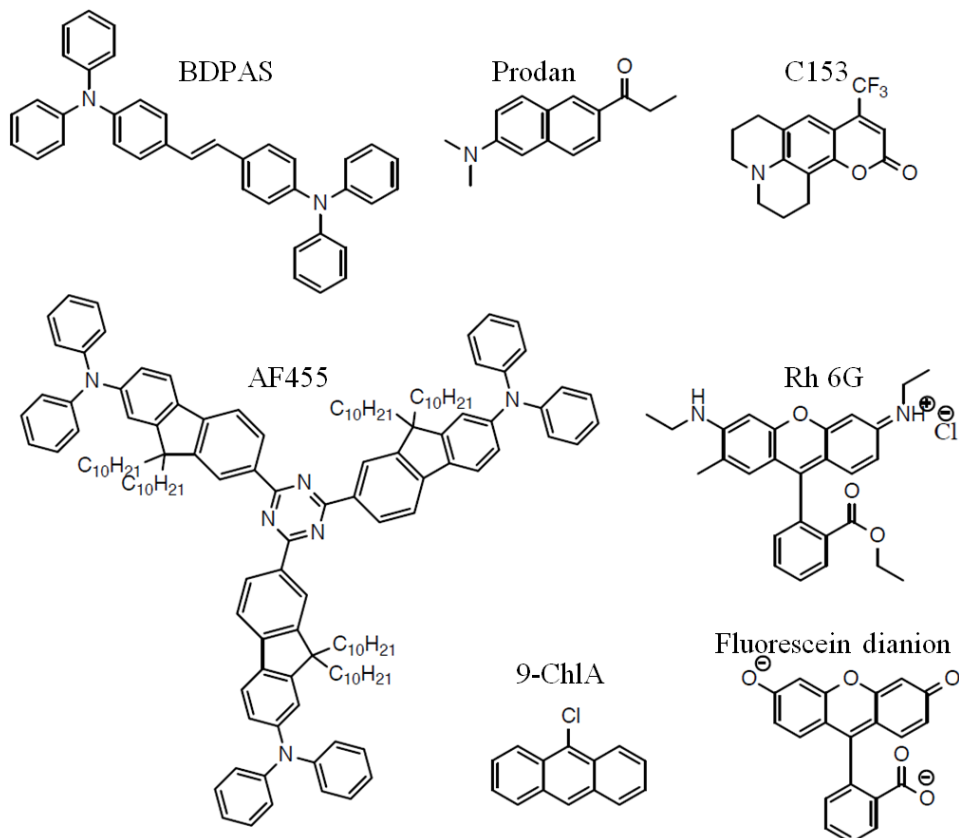


Figure F.1: chemical structure of the 7 chosen chromophores for the 2PA standards set.

BDPAS and 9-Chloroanthracene were dissolved in dichloromethane (DCM), Fluorescein in water buffer pH 11 and Rh6G in methanol (MetOH). Prodan, C153 and AF455 were dissolved in toluene. Taking advantage of a large solvatochromism shift, Prodan and C153 were also dissolved in dimethylsulfoxide (DMSO), whereas AF455 was also dissolved in tetrahydrofuran (THF).

APPENDIX G: 2PA shape function comparison between independent 2PIF measurements

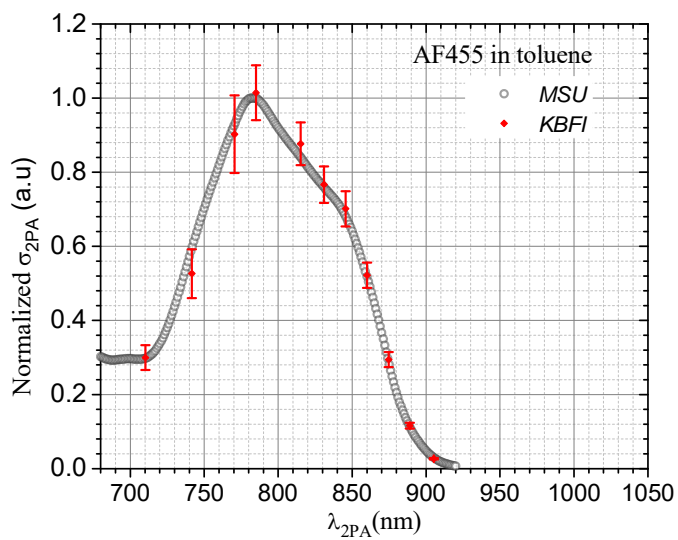


Figure G.2: Comparison of 2PA shape function, obtained independently in MSU and KBFI, for AF455 in toluene.

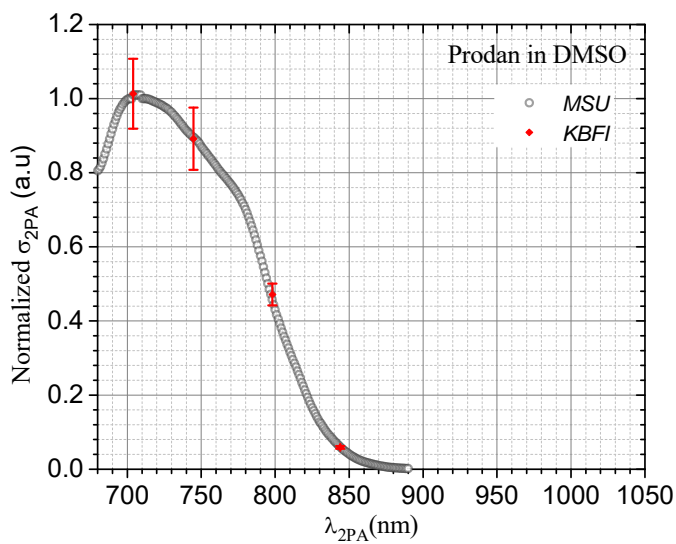


Figure G.3: Comparison of 2PA shape function, obtained independently in MSU and KBFI, for Prodan in DMSO.

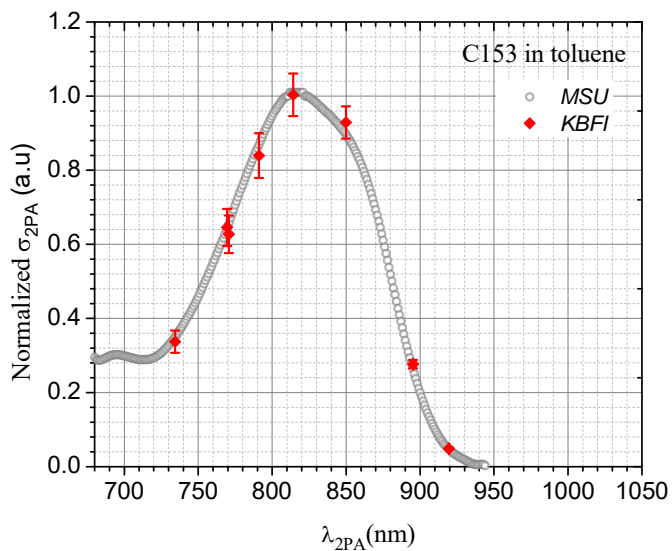


Figure G.4: Comparison of 2PA shape function, obtained independently in MSU and KBFI, for Coumarin 153 in toluene.

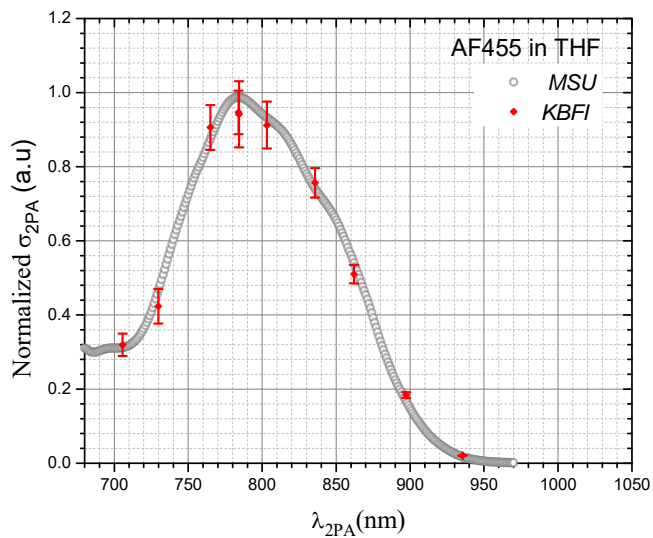


Figure G.5: Comparison of 2PA shape function, obtained independently in MSU and KBFI, for AF455 in THF.

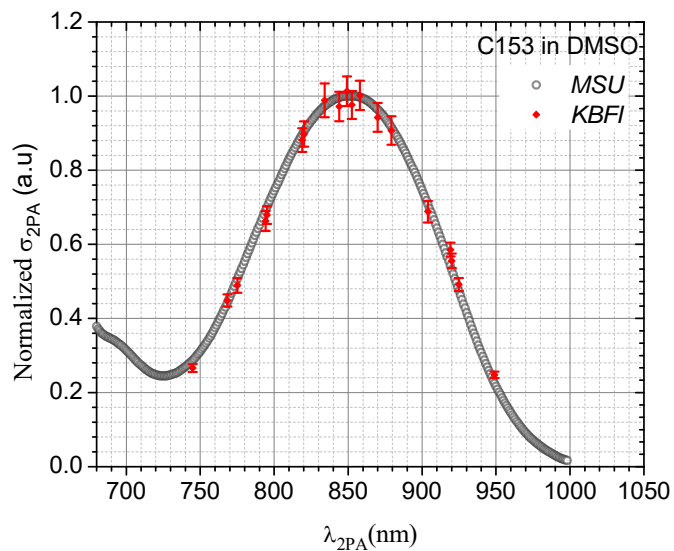


Figure G.6: Comparison of 2PA shape function, obtained independently in MSU and KBFI, for Coumarin 153 in DMSO.

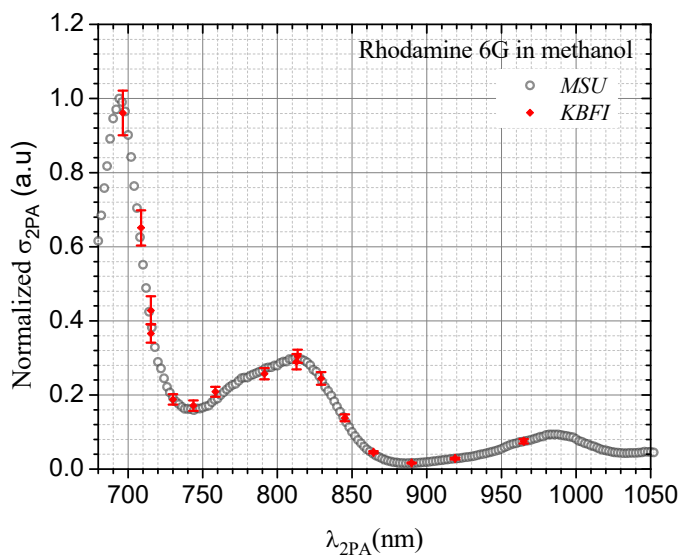


Figure G.7: Comparison of 2PA shape function, obtained independently in MSU and KBFI, for Rhodamine 6G in methanol.

APPENDIX H: Absorption spectra of reference standards

Figures H.1–H.11 present the 2PA cross section (left vertical scale) and molar extinction (second right vertical axis) spectra, as well as permanent dipole moment change upon excitation (first right vertical axis) of the 10 standards ordered by increasing fluorescence wavelength shown in Figure 27. The bottom axis represents the transition wavelength (2PA wavelength), and the top axis represents the 1PA laser wavelength.

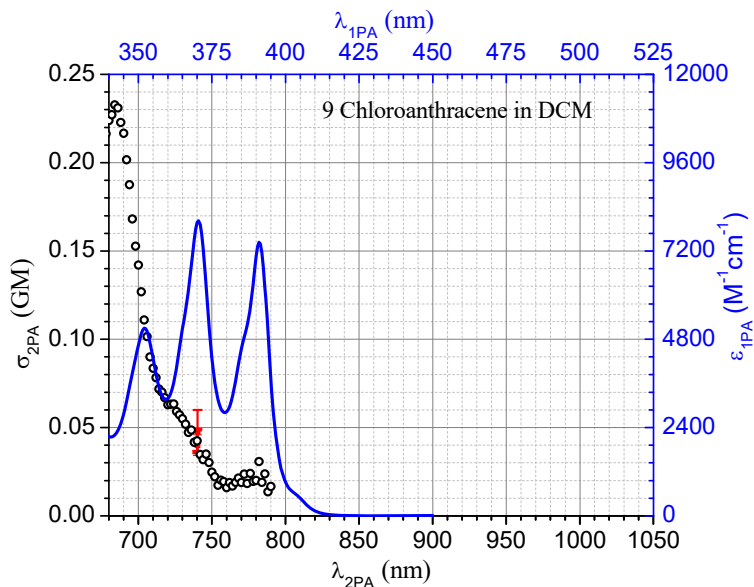


Figure H.1: 2PA cross-section spectrum (black circles), absolute 2PA cross-section measured (red squares with error bar) and extinction coefficient (blue line) ground to excited state for 9-Chloroanthracene in DCM. Because of low and noisy value of the 2PA cross-section spectrum at longer wavelengths, only an upper estimate value for the permanent dipole moment for 0-0 transition of $\sim 0.4 D$ was possible.

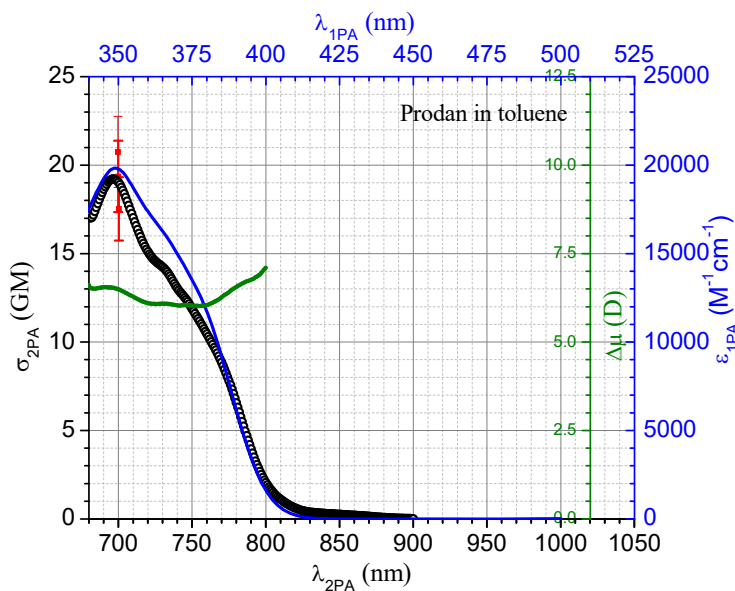


Figure H.2: 2PA cross-section spectrum (black circles), absolute 2PA cross-section measured (red squares with error bar), extinction coefficient (blue line) and difference in permanent dipole moment (green squares) from ground to excited state for Prodan in toluene.

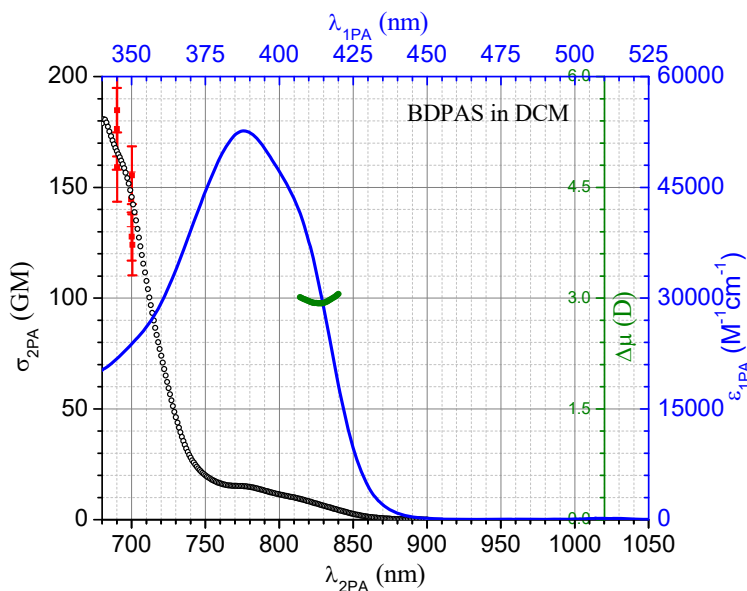


Figure H.3: 2PA cross-section spectrum (black circles), absolute 2PA cross-section measured (red squares with error bar), extinction coefficient (blue line) and difference in permanent dipole moment (green squares) from ground to excited state in the lowest-energy transition 0-0 for BDPAS in DCM.

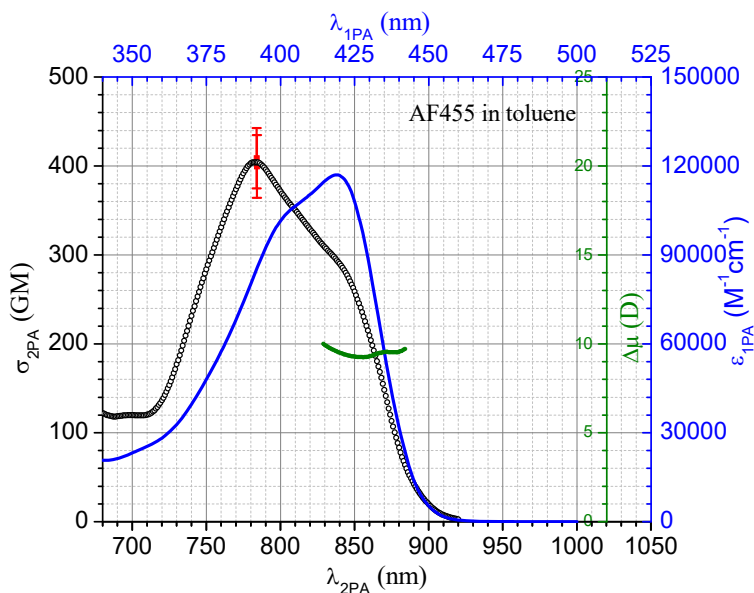


Figure H.4: 2PA cross-section spectrum (black circles), absolute 2PA cross-section measured (red squares with error bar), extinction coefficient (blue line) and difference in permanent dipole moment (green squares) from ground to excited state in lowest-energy transition 0-0 for AF455 in toluene.

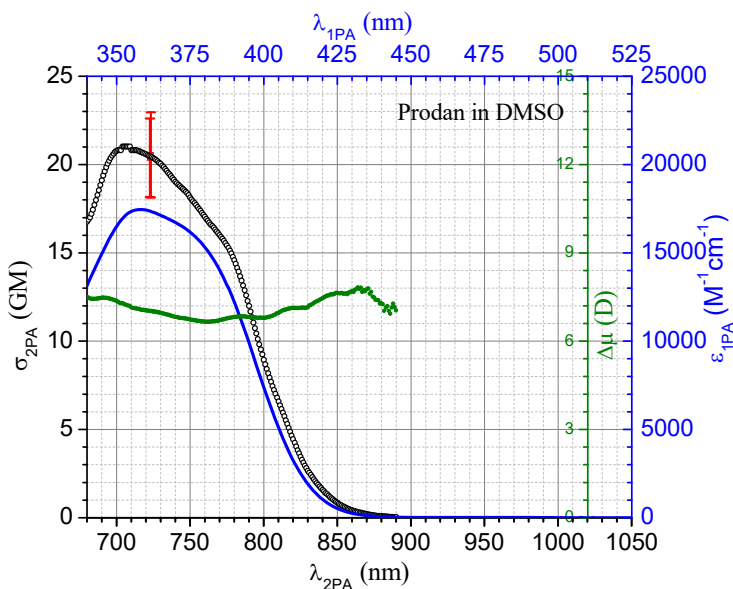


Figure H.5: 2PA cross-section spectrum (black circles), absolute 2PA cross-section measured (red squares with error bar), extinction coefficient (blue line) and difference in permanent dipole moment (green squares) from ground to excited state for Prodan in DMSO.

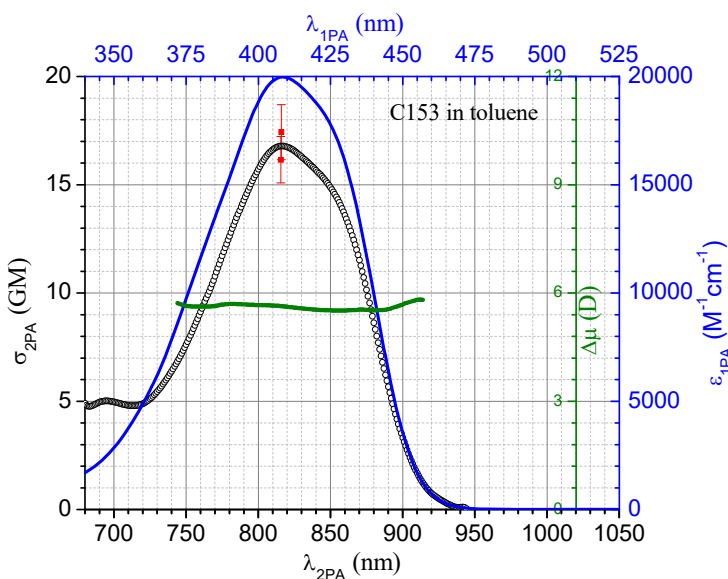


Figure H.6: 2PA cross-section spectrum (black circles), absolute 2PA cross-section measured (red squares with error bar), extinction coefficient (blue line) and difference in permanent dipole moment (green squares) from ground to excited state for Coumarin 153 in toluene.

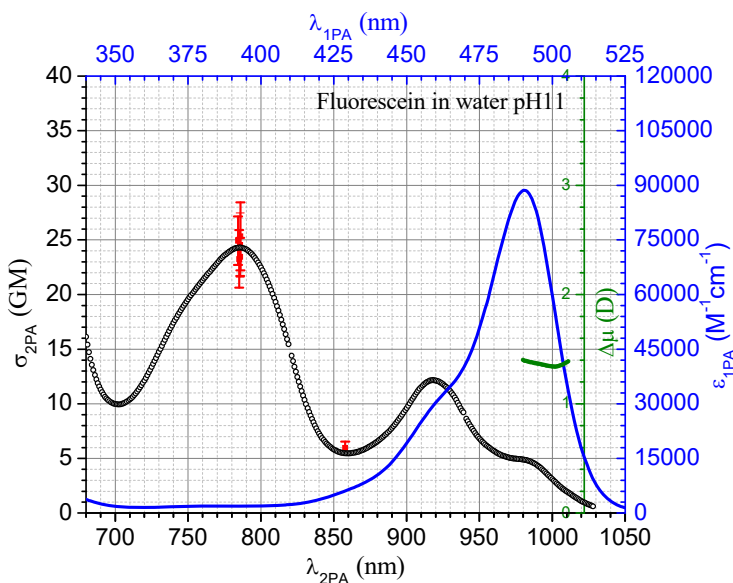


Figure H.7: 2PA cross-section spectrum (black circles), absolute 2PA cross-section measured (red squares with error bar), extinction coefficient (blue line) and difference in permanent dipole moment (green squares) from ground to excited state in the lowest-energy transition 0-0 for Fluorescein in water pH 11.

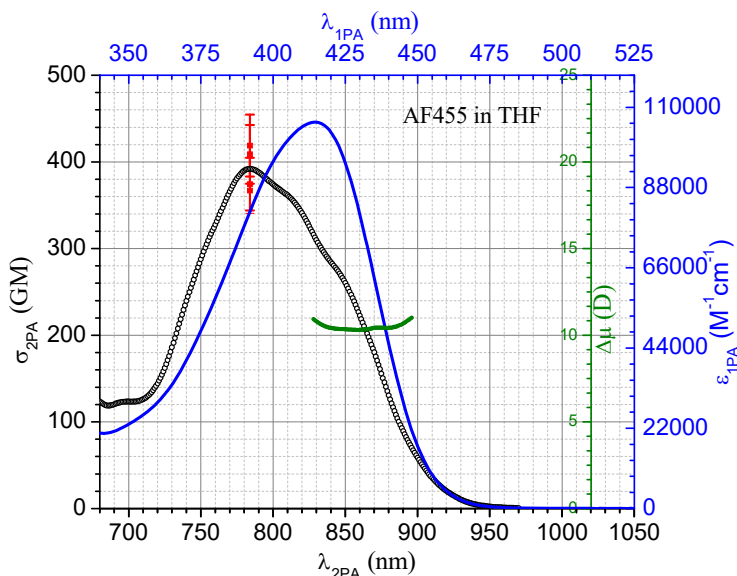


Figure H.8: 2PA cross-section spectrum (black circles), absolute 2PA cross-section measured (red squares with error bar), extinction coefficient (blue line) and difference in permanent dipole moment (green squares) from ground to excited state in the lowest-energy transition 0-0, for AF455 in THF.

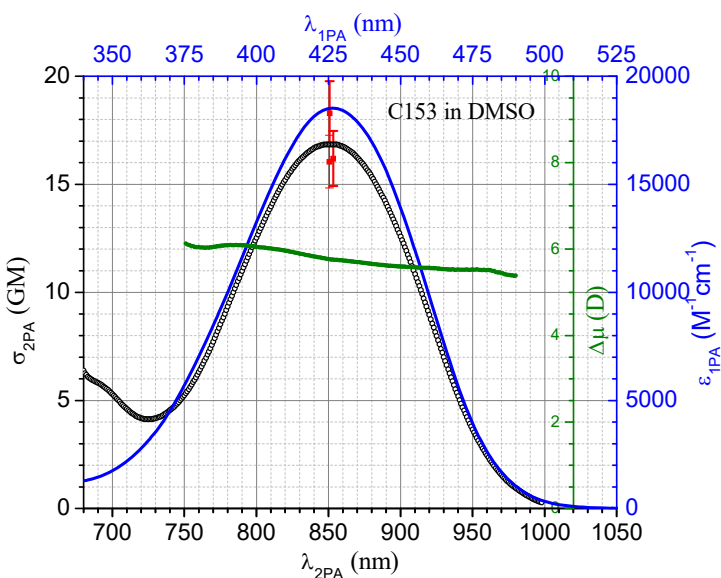


Figure H.9: 2PA cross-section spectrum (black circles), absolute 2PA cross-section measured (red squares with error bar), extinction coefficient (blue line) and difference in permanent dipole moment (green squares) from ground to excited state for Coumarin 153 in DMSO.

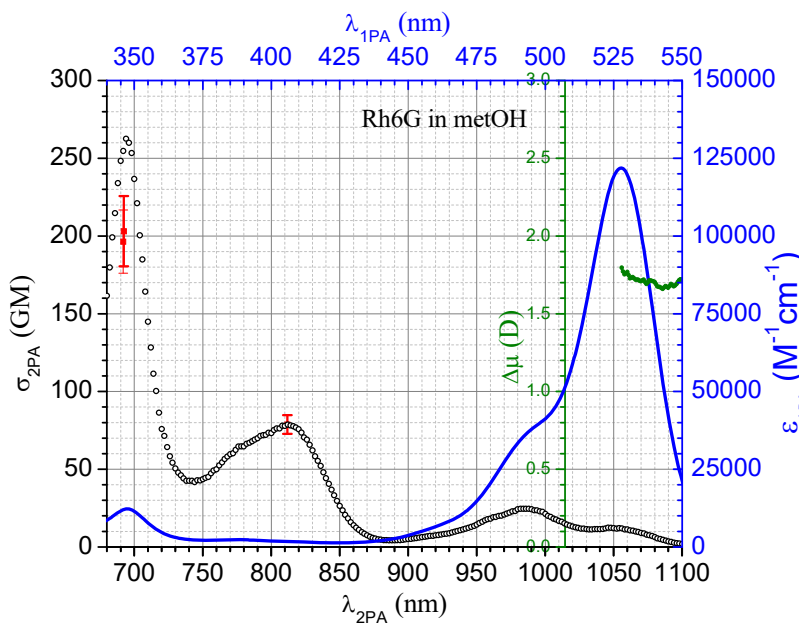


Figure H.10: 2PA cross-section spectrum (black circles), absolute 2PA cross-section measured (red squares with error bar), extinction coefficient (blue line) and difference in permanent dipole moment (green squares) from ground to excited state on the lowest-energy transition 0-0 transition for Rhodamine 6G in methanol.

APPENDIX I: Pair-wise comparison of 2PA cross-section

Table I.1: Deviation in % of the sample relative 2PA cross-section calculated with the reference compared to its absolute value for the same wavelength. Bold values correspond to the maximum of the 2PA spectrum.

Sam.A Sam.B	BDPAS in DCM	9- chl.anthr. in DCM	Prodan in toluene	Prodan in DMSO	C153 in toluene	C153 in DMSO	AF455 in toluene	AF455 in THF	Fluoresce in in buffer pH=11	Rh6G in MetOH
BDPAS in DCM		+6.7% (740nm)	-17.1% (701nm) -28.7% (750nm)	+1.0% (700nm) -0.3% (723nm) -0.6% (740m)	+8.1% (725nm) +2.2% (736nm)					
9-Chl. anthr. in DCM	-6.3% (740nm)		+3.9% (740nm) +13.6% (750nm)							
Prodan in toluene	+20.7% (701 nm) +30.6% (715 nm) +40.2% (750 nm)	-3.7% (740nm) -11.9% (750nm)								
Prodan in DMSO	-0.9% (700 nm) +0.3% (723 nm) +0.6% (740nm)				3.8% (750nm) +1.0% (775nm) +4.2% (816nm)					
C153 in toluene	-7.5% (725nm) -2.2% (736nm)			-3.7% (750nm) -1.0% (775nm) -4.0% (816nm)			+0.3% (784nm) -7.2% (816nm)	+5.3% (784nm) -1.8% (816nm)		
C153 in DMSO									-4.6% (785nm) +6.1% (851nm)	-3.7% (812nm) -4.4% (851nm)
AF455 toluene					-0.3% (784nm) +7.8% (816nm)					
AF455 in THF					-5.0% (784nm) +1.8% (816nm)					
Fluoresce in in buffer pH=7						+4.6% (785 nm) -5.8% (851 nm)				
Rh6G in MetOH						+3.8% (812nm) +4.3% (851nm)				

APPENDIX J: Publication I

de Reguardati, S., Pahapill, J., Mikhailov, A., Stepanenko, Y. and Rebane, A.,

“High-accuracy reference standards for two-photon absorption in the 680-1050 nm wavelength range”

Opt. Express 24(8), 9053-9066 (2016)

High-accuracy reference standards for two-photon absorption in the 680–1050 nm wavelength range

Sophie de Reguardati,¹ Juri Pahapill,¹ Alexander Mikhailov,² Yuriy Stepanenko,^{3,4} and Aleksander Rebane^{1,2,*}

¹National Institute of Chemical Physics and Biophysics, Tallinn, EE 12618, Estonia

²Department of Physics, Montana State University, Bozeman, MT 59717, USA

³Institute of Physical Chemistry, Polish Academy of Sciences, Warsaw 01-224, Poland

⁴Department of Physics, Institute of Experimental Physics, University of Warsaw 02-093, Poland

*rebane@physics.montana.edu

Abstract: Degenerate two-photon absorption (2PA) of a series of organic fluorophores is measured using femtosecond fluorescence excitation method in the wavelength range, $\lambda_{2PA} = 680\text{--}1050$ nm, and ~ 100 MHz pulse repetition rate. The function of relative 2PA spectral shape is obtained with estimated accuracy 5%, and the absolute 2PA cross section is measured at selected wavelengths with the accuracy 8%. Significant improvement of the accuracy is achieved by means of rigorous evaluation of the quadratic dependence of the fluorescence signal on the incident photon flux in the whole wavelength range, by comparing results obtained from two independent experiments, as well as due to meticulous evaluation of critical experimental parameters, including the excitation spatial- and temporal pulse shape, laser power and sample geometry. Application of the reference standards in nonlinear transmittance measurements is discussed.

©2016 Optical Society of America

OCIS codes: (190.0190) Nonlinear optics; (300.6410) Spectroscopy, multiphoton; (190.4710) Optical nonlinearities in organic materials.

References and links

1. J. R. Lakowicz, *Principles of Fluorescence Spectroscopy*, 3rd ed. (Springer, 2006).
2. R. L. Southerland, *Handbook of Nonlinear Optics*, 2nd ed. (Marcel Dekker, 2003).
3. M. Göpper-Maier, "Über Elementarakte mit zwei Quantensprüngen," *Ann. Phys.* **9**(3), 273–294 (1931).
4. J. P. Hermann and J. Ducuing, "Absolute measurement of two-photon cross sections," *Phys. Rev. A* **5**(6), 2557–2568 (1972).
5. C. Xu and W. W. Webb, "Measurement of two-photon excitation cross sections of molecular fluorophores with data from 690 to 1050 nm," *J. Opt. Soc. Am. B* **13**(3), 481–491 (1996).
6. M. A. Albota, C. Xu, and W. W. Webb, "Two-photon fluorescence excitation cross sections of biomolecular probes from 690 to 960 nm," *Appl. Opt.* **37**(31), 7352–7356 (1998).
7. N. S. Makarov, M. Drobizhev, and A. Rebane, "Two-photon absorption standards in the 550–1600 nm excitation wavelength range," *Opt. Express* **16**(6), 4029–4047 (2008).
8. G. G. Dubinina, R. S. Price, K. A. Abboud, G. Wicks, P. Wnuk, Y. Stepanenko, M. Drobizhev, A. Rebane, and K. S. Schanze, "Phenylene vinylene platinum(II) acetylides with prodigious two-photon absorption," *J. Am. Chem. Soc.* **134**(47), 19346–19349 (2012).
9. R. E. Bridges, G. L. Fischer, and R. W. Boyd, "Z-scan measurement technique for non-Gaussian beams and arbitrary sample thicknesses," *Opt. Lett.* **20**(17), 1821–1824 (1995).
10. M. Drobizhev, A. Karotki, M. Kruk, A. Krivokapic, H. L. Anderson, and A. Rebane, "Photon energy upconversion fluorescence in porphyrins: One-photon hot-band absorption versus two-photon absorption," *Chem. Phys. Lett.* **370**(5–6), 690–699 (2003).
11. J. Mütze, V. Iyer, J. J. Macklin, J. Colonell, B. Karsh, Z. Petrášek, P. Schwill, L. L. Looger, L. D. Lavis, and T. D. Harris, "Excitation spectra and brightness optimization of two-photon excited probes," *Biophys. J.* **102**(4), 934–944 (2012).
12. M. G. Velasco, E. S. Allgeyer, P. Yuan, J. Grutzendler, and J. Bewersdorf, "Absolute two-photon excitation spectra of red and far-red fluorescent probes," *Opt. Lett.* **40**(21), 4915–4918 (2015).

13. L.-C. Cheng, N. G. Horton, K. Wang, S.-J. Chen, and C. Xu, "Measurements of multiphoton action cross sections for multiphoton microscopy," *Biomed. Opt. Express* **5**(10), 3427–3433 (2014).
14. A. Rebane, G. Wicks, M. Drobizhev, T. Cooper, A. Trummal, and M. Uudsemaa, "Two-photon voltmeter for measuring a molecular electric field," *Angew. Chem. Int. Ed. Engl.* **54**(26), 7582–7586 (2015).
15. I. L. Arbeloa and P. R. Ojeda, "Molecular forms of rhodamine B," *Chem. Phys. Lett.* **79**(2), 347–350 (1981).
16. D. A. Hinckley, P. G. Seybold, and D. P. Borris, "Solvatochromism and thermochromism of rhodamine solutions," *Spectrochimica Acta* **42A**, 741–754 (1986).
17. S. P. McLroy, E. Cló, L. Nikolajsen, P. K. Frederiksen, C. B. Nielsen, K. V. Mikkelsen, K. V. Gothelf, and P. R. Ogilby, "Two-photon photosensitized production of singlet oxygen: sensitizers with phenylene-ethynylene-based chromophores," *J. Org. Chem.* **70**(4), 1134–1146 (2005).
18. L. Rodriguez, H.-Y. Ahn, and K. D. Belfield, "Femtosecond two-photon absorption measurements based on the accumulating photo-thermal effect and the Rayleigh interferometer," *Opt. Express* **17**(22), 19617–19628 (2009).
19. Y. Bae, J. Song, and Y. Kim, "Photoacoustic study of two-photon absorption in hexagonal ZnS," *J. Appl. Phys.* **53**(1), 615–619 (1982).
20. R. Kannan, L.-S. Tan, and R. A. Vaia, "Two-photon responsive chromophores containing electron accepting cores," US Patent 6,555,682 (2003).
21. R. Kannan, G. S. He, T.-C. Lin, P. N. Prasad, R. A. Vaia, and L.-S. Tan, "Toward highly active two-photon absorbing liquids. Synthesis and characterization of 1,3,5-triazine-based octupolar molecules," *Chem. Mater.* **16**(1), 185–194 (2004).
22. B. Xu, Y. Coello, V. V. Lozovoy, and M. Dantus, "Two-photon fluorescence excitation spectroscopy by pulse shaping ultrabroad-bandwidth femtosecond laser pulses," *Appl. Opt.* **49**(32), 6348–6353 (2010).
23. A. Rebane, M. Drobizhev, N. S. Makarov, G. Wicks, P. Wnuk, Y. Stepanenko, J. E. Haley, D. M. Krein, J. L. Fore, A. R. Burke, J. E. Slagle, D. G. McLean, and T. M. Cooper, "Symmetry breaking in platinum acetylide chromophores studied by femtosecond two-photon absorption spectroscopy," *J. Phys. Chem. A* **118**(21), 3749–3759 (2014).
24. M. Sheik-Bahae, A. A. Said, T.-H. Wei, D. J. Hagan, and E. W. Van Stryland, "Sensitive measurement of optical nonlinearities using a single beam," *IEEE J. Quantum Electron.* **26**(4), 760–769 (1990).
25. M. Rumi and J. W. Perry, "Two-photon absorption: an overview of measurements and principles," *Adv. Opt. Phot.* **2**, 451–518 (2010).

1. Introduction

Spectroscopic reference standards facilitate carrying out measurements of molecular absorption- and scattering cross sections, quantum yields, etc. under circumstances, where absolute methods are overly involved or inapplicable [1]. Reference standards are even more vital in nonlinear-optical spectroscopy [2], where accurate absolute determination of the nonlinear molecular parameters requires knowledge on the instantaneous photon flux, i.e. the number of photons incident on the sample per unit time and per unit area. For this, one would need to perform equally accurate measurements of the spatial- and temporal properties of the excitation beam in a broad range of wavelengths, which, given the notorious inconsistency of tunable lasers, may pose a challenging task.

Degenerate 2-photon absorption (2PA) is a process where two photons of the same wavelength (frequency) and polarization are absorbed simultaneously [3]. The concept of reference standards in the 2PA spectroscopy is well established in the literature [4–7], and consists in calibrating the measurements performed with the sample under study with respect to the measurements performed with a suitable reference under identical conditions. In a generic 2-photon excited fluorescence (2PEF) experiment, one uses a reference standards whose 2PA spectral shape is known to find the so-called 2PA spectral shape correction function, which adjusts for the relative variation of the excitation photon flux in the wavelength range under study. In the second step, the absolute 2PA cross section value, σ_{2PA} , is determined at select wavelengths using a reference standard, whose absolute σ_{2PA} is known, and whose emission spectrum overlaps with that of the system under investigation. The final 2PA spectrum is found by scaling the shape function according to the 2PA cross section. Reference standards are also increasingly used in nonlinear transmittance (NLT) experiments [8], including z-scan [9].

In [7] a set of 2PA fluorophores were characterized using a femtosecond optical parametric amplifier (OPA) operating at 1 kHz pulse repetition rate. However, because the OPA wavelength tuning was inherently discontinuous, and the excitation pulse parameters changed abruptly between the different tuning ranges, especially at the degeneracy point

around 800 nm, this previous data may contain sizable uncertainties. Experimental errors may also occur when multi-photon absorption exhibits dependence on the excitation pulse repetition rate. Since many applications use mode-locked femtosecond oscillators operating at, ~100 MHz, it is advisable that applicability of the 2PA values obtained at 1 kHz [7] is independently ascertained at higher pulse rates. Most importantly, using up to 5 orders of magnitude higher pulse repetition rates is usually accompanied by much lower peak photon flux, which, in turn, means that the relative magnitude one-photon excited fluorescence increases relative to 2PEF signal. This issue becomes most critical in case of potential overlap between the 1PA and 2PA spectra [10]. Nevertheless, due to lack of better alternatives, the data presented in [7] continues to be used under many different conditions, even if the consistency and reliability of the standards is not yet fully verified.

In this work, we strive to substantially improve the accuracy of the reference standards, both in terms of the relative 2PA spectral shape as well as regarding the absolute cross section values. Augmented accuracy is most critical for calibration and optimization of fluorophores used in multi-photon microscopy [11–13], as well as in the emerging area of quantitative 2PA spectroscopy for measuring the strength of intra- and intermolecular electric fields [14] For this purpose, we have constructed two independent experimental setups, using different 76 – 80 MHz pulse repetition rate femtosecond lasers, where one setup is optimized for the measurement of 2PA spectral shapes and the other is optimized for the absolute cross section measurement, and where we have increased the accuracy of characterization of all critical temporal-, spatial- and spectral parameters of the excitation beam. For the 2PA shape measurement, we use a ~80 MHz pulse repetition rate laser that is continuously tunable without gaps over the wavelength range of commonly-used mode-locked femtosecond sources, 680 – 1050 nm. The quadratic dependence is measured with high fidelity for each wavelength, thus minimizing potential artifacts. The new reference fluorophores set comprises both commercial organic dyes such as Prodan, Coumarin 153 (C153), Fluorescein and Rhodamine 590 (Rh 6G), but also two custom-synthesized compounds 4,4'-Bis-(diphenylamino)-stilbene (BDPAS) and 7,7',7''-(1,3,5-triazine-2,4,6-triyl)tris[9,9-didecyl-N,N-diphenyl 9H-Fluoren-2-amine CAS Registry Number, 517874-02-13 (AF455), were the latter two possess a superior peak 2PA value compared to the commercial counterparts. Perylene, Lucifer yellow and chloroanthracenes show relatively low peak 2PA cross section, $\sigma_{2PA} < 10 \text{ GM}$ ($1 \text{ GM} = 10^{-50} \text{ cm}^4 \text{ s photon}^{-1}$), and were therefore not considered in the present set. Solutions of Rhodamine 610 (Rhodamine B), on the other hand, even though showing a relative large peak σ_{2PA} , exhibit undesired dependence of the absorbance on the concentration and temperature, most likely due to the presence of different equilibrium forms (protonated cation, zwitterion and lactone) [15,16], and were therefore excluded from current measurements. The fluorescence emission spectral range, 375 - 600 nm, is chosen to match the emission wavelengths of common fluorescent microscopy probes such as green fluorescent proteins. Finally, in order to cover a sufficiently broad wavelength range, we take advantage of large solvatochromic and fluorosolvatochromic shifts of the 1PA and 2PA spectra of some of the chromophores.

2. Theoretical considerations

When a monochromatic beam of light propagates through a thin slab of 2-photon absorbing medium, then the difference between the input- and output photon flux (in $\text{photon cm}^{-2} \text{ s}^{-1}$) may be expressed as:

$$\Delta I_{2PA} = -\sigma_{2PA} N_c \Delta z I_{2PA}^2, \quad (1)$$

where the σ_{2PA} is in $\text{cm}^4 \text{ s photon}^{-1}$, N_c is the 2-photon fluorophore concentration (in cm^{-3}), Δz is the thickness (in cm) and I_{2PA} is the incident photon flux. In most cases, the flux changes only by a relatively small amount, $\Delta I_{2PA} \ll I_{2PA}$, which makes measurement of ΔI_{2PA} , and,

accordingly, accurate determination σ_{2PA} difficult. Alternatively, one can use the relation between the 2PA cross section and the corresponding 2-photon excitation rate,

$$\dot{n}_{2PA} = \frac{1}{2} \sigma_{2PA} I_{2PA}^2, \quad (2)$$

where the latter is determined from experiment by detecting 2PEF emitted by the chromophores, whereas some other detection schemes involving e.g. phosphorescence [17], generation of heat [18] or acoustic waves [19], have also been demonstrated.

Suppose that the 2PEF medium is excited by a periodic train of ultrashort pulses at the rate g (in Hz), and the wavelength, λ_{2PA} . Then the average fluorescence signal may be expressed as:

$$F_{2PA}(\lambda_{2PA}) = \Delta t_{2PA} \left[g N_c \frac{1}{2} \sigma_{2PA}(\lambda_{2PA}) \Delta z \iint\limits_{2PA} I_{2PA}^2(t, x, y; \lambda_{2PA}) dx dy dt \right] \left[\int_{\lambda_{em}}^{\lambda_{em}} \eta(\lambda_{em}) \phi(\lambda_{em}) d\lambda_{em} \right], \quad (3)$$

where Δt_{2PA} is the fluorescence detector integration time, $\phi(\lambda_{em})$ is the differential quantum efficiency of fluorescence emission at the emission wavelength, λ_{em} , and $\eta(\lambda_{em})$ is the aggregate detection efficiency that accounts for the efficiency of fluorescence collection, spectrometer/diffraction grating through-put, efficiency of the detector, etc. The differential quantum efficiency is defined as,

$$\int_0^{\infty} \phi(\lambda') d\lambda' = Q, \quad (4)$$

where Q is the standard quantum yield, equal to the ratio of the radiative decay rate to the total decay rate of the S_1 state. The quantity enclosed in the first square brackets in Eq. (3) stands for the average number of molecules excited per second, while the quantity inside the second square brackets accounts for the fluorescence signal that is detected within a finite wavelength interval. If the photon flux, $I_{2PA}(t, x, y; \lambda_{em})$, and the parameters, $\eta(\lambda_{em})$ and $\phi(\lambda_{em})$, were known, then the relation Eq. (3) could be immediately used to evaluate the cross section, $\sigma_{2PA}(\lambda_{2PA})$. As was pointed out above, this information is, however, rarely available. At this point it is convenient to present the photon flux as a product of four factors:

$$I_{2PA}(t, x, y; \lambda_{2PA}) = \frac{P_{2PA}(\lambda_{2PA})}{t_{ave} S_{ave}} f_{time}(t) f_{area}(x, y) f_{corr}(\lambda_{2PA}), \quad (5)$$

where P_{2PA} is the total number of photons in the excitation pulse, t_{ave} is the average pulse duration, S_{ave} is the average beam area, f_{time} and f_{area} are the normalized functions describing, respectively, the temporal pulse shape and spatial beam profile and f_{corr} is the so-called wavelength-dependent correction function that quantifies the deviation of the pulse parameters from the average value as a function of λ_{2PA} .

If the Kasha-Vavilov rule is obeyed, then we are allowed to assume that the differential quantum efficiency is independent of the excitation wavelength, and the relative 2-photon absorption spectrum may be obtained then measuring F_{2PA} as function of λ_{2PA} :

$$\sigma_{2PA}^{rel}(\lambda_{2PA}) = c_{norm} \frac{F_{2PA}(\lambda_{2PA})}{P_{2PA}^2(\lambda_{2PA}) f_{corr}^2(\lambda_{2PA})}. \quad (6)$$

Since we are dealing here only with the 2PA spectral shape, we can set the empirical normalization factor, c_{norm} , such that the peak value equals unity, $\max(\sigma_{2PA}^{rel}) = 1$.

To obtain the absolute 2-photon cross section, we need to know the value of the quantity enclosed in the second square bracket in Eq. (3). If we excite the fluorescence by 1-photon

absorption in the same sample, using exact same experimental geometry and same fluorescence detection as in the 2-photon measurement, then the corresponding 1-photon excited fluorescence signal may be expressed as:

$$F_{1PA} = \Delta t_{1PA} \left[(1 - 10^{-OD}) \int_{-\infty}^{\infty} I_{1PA}(x, y) dx dy \right] \left[\int_{\lambda_{\min}}^{\lambda_{\max}} \eta(\lambda_{em}) \phi(\lambda_{em}) d\lambda_{em} \right], \quad (7)$$

where I_{1PA} is the time-average photon flux, Δt_{1PA} is the fluorescence signal integration time and $OD = N_c \sigma_{1PA} \Delta z$ is the optical density of the sample and σ_{1PA} is the 1-photon absorption cross section at the 1-photon excitation wavelength. Here the quantity in the first square brackets represents the number of molecules excited per second, whereas the second term is the same as in Eq. (3). Note that the one-photon excitation rate depends neither on the beam spatial profile nor on its temporal structure. By combining Eqs. (3) and (7), we can express the absolute 2PA cross section as:

$$\sigma_{2PA}(\lambda_{2PA}) = \frac{F_{2PA}(\lambda_{ex}) \Delta t_{1PA}}{F_{1PA}(\lambda_{1PA}) \Delta t_{2PA}} \frac{2(1 - 10^{-OD}) \int_{-\infty}^{\infty} I_{1PA}(x, y) dx dy}{g N_c \Delta z \left[\frac{P_{2PA}(\lambda_{2PA}) f_{corr}(\lambda_{2PA})}{t_{time} S_{area}} \right]^2 \iiint f_{time}^2(t) f_{area}^2(x, y) dx dy dt} \quad (8)$$

3. Experimental

3.1 Materials, linear spectroscopy and sample preparation

Prodan, C153, Fluorescein and Rh 6G were obtained from Aldrich and were used as received. BDPAS was custom-synthesized by K. Schanze group (U of Florida) as described in [8]. AF455 was provided by Dr. S. Tan from the Air Force Research Laboratory. The synthesis of AF455 is described in [20, 21]. All solvents were purchased from Sigma-Aldrich and were used without further purification. Stock solutions were prepared by mixing the solvent with 1–3 mg of dry dye, where the latter was weighed using Mettler-Toledo Model AT2611 analytical balance. Linear absorption spectra were obtained with Shimadzu UV-3600Plus spectrophotometer and corrected fluorescence spectra were measured with Perkin-Elmer Fluorimeter LS55. Extinction coefficients were determined by the dilution method, where a set of daughter solutions with maximum absorbance in the range $OD = 0.5 - 1.5$ were prepared from the stock solution. The samples were contained 1 cm quartz cuvettes. The chromophore concentration used in the 2PA and 1 PA measurements was in the range $10^{-6} - 10^{-3}$ M.

3.2 Measurement of relative 2PA spectral shape function

Schematic of the 2PA spectral shape measurement setup is shown in Fig. 1(a). In this part of the experiment, we use 80-MHz repetition rate femtosecond laser (Spectra-Physics InSight DeepSee) continuously tunable in the 680–1300 nm wavelength range with average output power 0.6–1.5 W. The laser output was spatially-filtered by focusing the beam through a 50 μ m diameter pinhole. To avoid thermal lensing effects in the sample the average laser power was reduced by factor 10 using a 100 Hz chopper wheel. The collimated beam was focused with $f = 400$ mm achromatic lens (Thorlabs) and passed through a motorized variable transmittance circular neutral density filter ($OD = 0.1 - 2.0$). Beam reflected from a flat glass plate positioned in front of the sample was detected with a pyroelectric pulse energy probe (Molelectron) and was used as reference. The variation of the responsivity of the reference detector at different wavelengths was calibrated relative to a thermoelectric probe (Ophir P1) and did not exceed $\pm 2\%$ in the 680–1100 nm range. The focused beam intensity profile at

the sample was measured using a microscope objective and CCD camera (Allied Stingray) in the 680–990 nm range and InGaAs SWIR camera (Xenics Bobcat 320) in the 970–1100 nm range. The measured spot size varied in the range 0.2–0.4 mm depending on the wavelength. The pulse duration was measured with custom-adapted auto-correlator using a scanning delay line (ODL-150, Clark MXR) and 0.1 mm thick BBO crystal set up for non-collinear SHG with computer-controlled phase matching angle adjustment. The laser spectrum was measured with a diffraction grating spectrometer (OceanOptics USB4000). The fluorescence from the sample was collected at 90° angle with respect to the propagation direction and vertical linear polarization of the excitation beam. The fluorescence was directed through a stack of short-pass filters to a photomultiplier (Hamamatsu R777) working in current detection mode. The output voltage from the photomultiplier and the reference detector were directed to respective A/D converters (National Instruments USB6009). The sample solutions were contained in 1–2 mm path length spectroscopic cuvettes to minimize effect of absorption by the solvent. Iris diaphragms were used to monitor alignment of the laser beam.

The relative 2PA cross section spectra were measured by varying the laser wavelength with 2 nm steps in the 680–1100 nm range and by measuring at each wavelength the dependence of the fluorescence signal on the incident photon flux by varying the transmittance through the OD filter in 20 discrete steps. The control of the laser wavelength, setting of the OD filter wheel and acquisition of the fluorescence- and reference signals was accomplished using PC via LabView program. The average time for tuning the laser and collecting the data was about 40–60 s per one wavelength step.

3.3 Measurement of absolute 2PA cross sections

Schematic of the setup is shown in Fig. 1(b). Here we used a 76-MHz pulse repetition rate mode-locked Ti:Sapphire femtosecond oscillator (Coherent Mira 900) pumped by 10 W cw frequency-doubled Nd:YVO₄ laser (Coherent Verdi V-10). The femtosecond laser wavelength was tuned manually in the range 690–960 nm with the average output power varying in the range 0.5–1.5 W.

The fundamental laser spectrum was measured with diffraction grating spectrometer (OceanOptics USB4000). The pulse temporal shape was measured with a modified optical auto-correlator (INRAD 5-14A), where the variable delay was produced by rotating glass plates (glass thickness 1 mm) and non-collinear second harmonic generation was produced in 0.1 mm BBO crystal. The spatial beam profile at the sample location was measured with the CCD-camera based beam profiler (Thorlabs BC106-VIS) (the sample was removed for these measurements).

To minimize detrimental effect of thermal lensing in the optical elements and in the sample, the average fundamental laser power was reduced by factor 10 using a 100 Hz optical chopper (Thorlabs MC2000). The fundamental power reaching the sample was further varied by manually rotating a $\lambda/2$ plate that was positioned in front of a Glan-Taylor polarizer (GL10-B Thorlabs) (Pol). The relative average power of the fundamental beam at the sample was monitored by reflecting a portion of the incident beam to integrating sphere silicon photodetector (Thorlabs S140C) coupled to optical power meter (Thorlabs PM100A). Absolute fundamental power was measured with optical power meter (Coherent FieldMate) with thermoelectric probe (Coherent Powermax PM10) placed directly in front of the sample. Single reflection (~4%) off a glass plate (GP1) was focused on a Type I phase matched BBO crystal that generated second harmonic (blue) light, which was then recombined with the main fundamental wavelength beam using the second glass plate (GP2). At short wavelengths, ~700 nm, the glass plate was replaced by a flipping mirror to compensate for drop in laser output power. A $\lambda/2$ plate in front of the SHG crystal rotated the pump beam polarization to the horizontal direction in order to assure that the second harmonic beam had the same (vertical) polarization as the fundamental beam. After GP2 the two beams followed the same path and were incident on the same spot at sample. The blue beam power was

adjusted by using continuously variable metallic-coated filter wheel (ND1), and the corresponding power was measured with integrating sphere silicon photodetector (Thorlabs S140C) or with standard silicon photodetector (Thorlabs S120VC) placed directly in front of the sample.

A combination of focusing and collimating lenses (L1 - L3) were used to shape both beams so that they have approximately the same spot size, ~ 0.3 mm. A color glass long-pass filter (LPF1) was used to cut off residual short-wavelength pump laser light and a glass short-pass filter (SPF1) was used to cut off residual fundamental wavelength after the SHG crystal.

Fluorescence signal was collected in 90° geometry and focused on the entrance slit of a scanning diffraction grating spectrometer (LOMO MDR-12). Scattered laser light was additionally suppressed by a stack of short-pass color glass filters (SPF2). The fluorescence signal was detected with a photon counting module (Hamamatsu H6240-01) coupled to a frequency counter with PC readout.

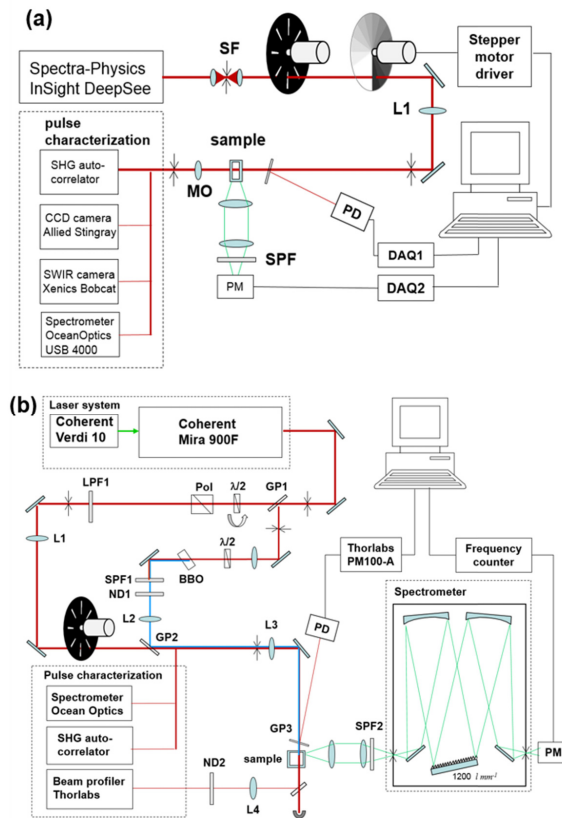


Fig. 1. Schematics of experimental set-ups; (a) Measurement of relative 2PA spectra; (b) Measurement of absolute 2PA cross section. SF – spatial filter; L1, L2, L3, L4 – focusing lenses; MO – microscope objective; ND – neutral density filter wheel; SPF – short-pass glass filter; LPF – long-pass glass filter; GP – glass plate; PM – photomultiplier; DAQ – data acquisition, A/D converters; Pol – Glan-Taylor polarizer; PD – photodetector.

The absolute cross-section was determined at a fixed wavelength by measuring the fluorescence signal on the incident photon flux in both 1PA and 2PA successively and all the laser characterization, e.g. spectral profile, beam profile and temporal profile. Average time needed to evaluate absolute 2PA cross section at 1 wavelength, including stabilizing the laser mode-locking, setting the laser wavelengths and performing the beam characterization measurements, was about 4 h.

4. Results

The normalized fluorescence spectra are shown in Fig. 2. The corresponding peak- and min/max fluorescence wavelengths are listed in Table 1.

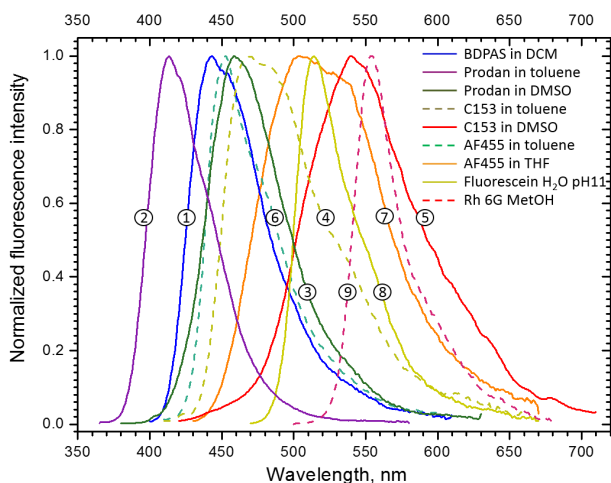


Fig. 2. Corrected fluorescence spectra of (1) BDPAS in methylene chloride; (2) Prodan in toluene; (3) Prodan in DMSO; (4) C153 in toluene; (5) C153 in DMSO; (6) AF455 in toluene; (7) AF455 in THF; (8) Fluorescein in H₂O pH11 buffer; (9) Rh 6G in Methanol.

The 2PA spectral shapes are presented in Fig. 3 by black symbols, and the corresponding absolute cross section measurements are shown as red squares. The shape functions are scaled to give the best match with average absolute cross sections at the select wavelengths. The linear extinction spectra are shown by blue solid line. The two panels (left and right) present the same data in the linear and logarithmic vertical scales. The lower horizontal axis of the plots is calibrated in the wavelength of the 2-photon excitation (λ_{2PA}), while the upper axis is calibrated in 1-photon absorption wavelength (λ_{1PA}). The same data is presented in Table 2 in the Appendix.

Key 2-photon data for all 9 standards, along with the peak molecular extinction coefficient, and estimated maximum fluorophore concentration and the solution stability assessment, is collected in Table 1. The peak cross section value for BDPAS in methylene chloride (1), $\sigma_{2PA} = 175 \pm 14$ GM, is less than was reported earlier [7], which we attribute to relatively rapid photo-degradation and low dark stability of the solution [8]. In our current measurements all precautions were taken by continuously monitoring the sample for signs of potential degradation. Note that BDPAS is especially useful in case of blue-emitting fluorophores, and in the wavelength range, $\lambda_{2PA} = 680 - 860$ nm. At longer wavelengths, the cross section drops below 1 GM. Prodan in toluene (2) and in DMSO (3) have also relatively short wavelength fluorescence emission. These solutions showed no measurable degradation

over a period of several months, even though their peak cross section is also lower, $\sigma_{2PA} \sim 17$ GM. Remarkable feature of C153 in DMSO is that its 2PA and 1PA profiles practically coincide in the range $\lambda_{2PA} = 740 - 1000$ nm. Physical background of this phenomenon was recently discussed in [14]. The peak cross section of Fluorescein (aqueous, pH11) (8) is $\sigma_{2PA} = 26 \pm 1.2$ GM at 780 nm. This is again about factor 2 less than the earlier reported value [7], most likely because this wavelength coincides with degeneracy of the OPA, where the beam parameters may deteriorate. In our current measurement this issue did not occur. We should note that relative 2-photon cross sections reported for Prodan and C153 in [14] were measured using the Fluorescein data from [7], which may have led to over-estimation of σ_{2PA} . Rh 6G in methanol (9) absorbs and emits at the longest wavelengths,

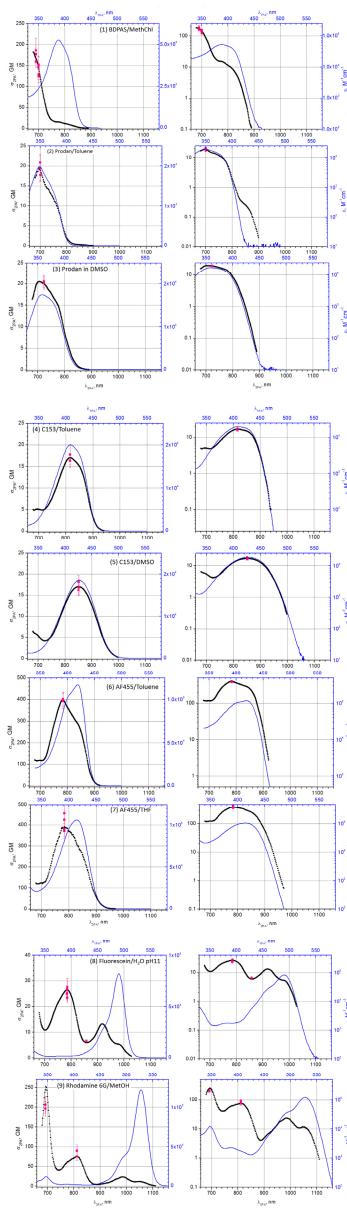


Fig. 3. 2PA spectra of (1) BDPAS in methylene chloride; (2) Prodan in toluene; (3) Prodan in DMSO; (4) C153 in toluene; (5) C153 in DMSO; (6) AF455 in toluene; (7) AF455 in THF; (8) Fluorescein in H₂O pH11 buffer; (9) Rh 6G in methanol.

compared to other fluorophores in the current set. The absolute cross section at 810 nm is, $\sigma_{2PA} = 79 \pm 6$ GM, and correlates well with the value reported in [5]. However, both the absolute value and the shape function are higher at 690 nm. This discrepancy is most likely caused by the narrow spectral band at, $\lambda_{2PA} = 680 - 710$ nm. The spectral FWHM of the excitation pulses in that particular wavelength range was measured to be $\Delta\lambda_{2PA} = 3 - 4$ nm, i.e. is comparable to the half-width of the named band. For comparison, in the earlier measurements the pulses were spectrally about factor of two broader [5], which may explain why the spectral feature appears more pronounced in the current data. We must underline that,

Table 1. 1-photon and 2-photon photophysical properties of the systems studied. The σ_{2PA} and $\Delta\sigma_{2PA}$ values are obtained by averaging over all measurements performed.

	Comp.	Solvent	$\varepsilon (\lambda_{1PA})$	$\min \lambda_{em} - \max \lambda_{em} (\text{peak } \lambda_{em})$	$\sigma_{2PA}(\lambda_{2PA})$	$\Delta\sigma_{2PA}$
			$M^{-1} \text{ cm}^{-1} (\text{nm})$	nm	GM (nm)	$\pm\%$
1	BDPAS	DCM	$52.6 \times 10^3 (388)$	415 – 540 (443)	175 (690) 138 (700)	8 8
2	Prodan	toluene	$19.8 \times 10^3 (349)$	390 – 480 (414)	19 (700)	6
3	Prodan	DMSO	$17.5 \times 10^3 (358)$	420 – 550 (459)	20 (723)	8
4	C153	toluene	$20.5 \times 10^3 (408)$	440 – 600 (468)	17 (816)	5
5	C153	DMSO	$18.5 \times 10^3 (427)$	480 – 650 (540)	17 (851)	7
6	AF455	toluene	$117 \times 10^3 (419)$	430 – 550 (453)	404 (784)	7
7	AF455	THF	$106 \times 10^3 (415)$	450 – 630 (504)	392 (784)	6
8	Fluorescein	H ₂ O	$88.6 \times 10^3 (491)$	490 – 580 (514)	26 (785)	5
		pH11	$8.7 \times 10^3 (322)$		6.5(860)	8
9	Rh 6G	MetOH	$122 \times 10^3 (528)$	580 – 630 (554)	79 (812)	8
			$12.1 \times 10^3 (347)$		202 (692)	8

contrary to 1-photon spectroscopy, where spectral retrieval via deconvolution can be quite effective, inherent nonlinear nature of the 2PA precludes application of such straightforward techniques [22].

5. Evaluation of experimental uncertainty

Main causes of experimental uncertainty in the relative spectral shape measurement are due to (a) deviation from the quadratic dependence of the 2PEF signal on the photon flux and (b) errors in the determination of the temporal- and spatial shape of the laser beam. The quadratic power dependence was ascertained at each wavelength by varying the average incident power over ~ 2 orders of magnitude, and by fitting the resulting 2PEF signal vs. power data, presented in double-logarithmic scale, with a linear function. The measurements accepted have a power law coefficient in the 1.96-2.04 range. Upper panels in Fig. 4 shows the power law coefficient in C153 in DMSO (left) and in Fluorescein (right) obtained in the relative 2PA spectral shape experiment (empty symbols). The power dependence measurement was performed also on the absolute 2PA experimental systems (filled rectangles), and showed very similar behavior. Even though different measurement systems behave slightly differently, the maximum deviation from the exact quadratic dependence does not exceed 3%. In order to further verify the measured spectral shape functions, we performed a relative 2PA shape measurement for a few select standards using the absolute 2PA measurement setup. Lower panels in Fig. 4 show the corresponding normalized shape functions for C153 in DMSO (left) and in Fluorescein (right), measured by the two complementary experiments. The discrepancy between the two measurements does not exceed 4%. This allows us to estimate that the overall uncertainty of the 2-photon shape functions presented here is about 5%. Since the two experiments were truly independent, we conclude that the relative accuracy of measuring the photon flux and, accordingly, the relative beam spatial- and temporal profiles, was also about

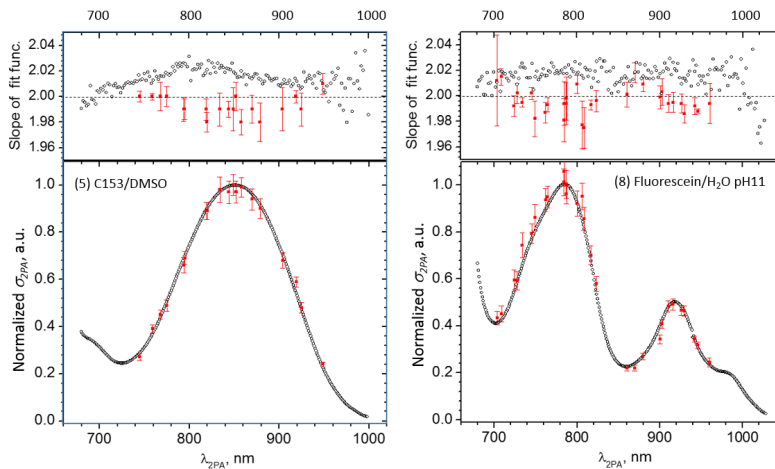


Fig. 4. Comparison between independent 2PEF measurement techniques in two reference samples: C153 in DMSO (left) and Fluorescein in aqueous, pH11 (right). Upper panel: Experimentally determined power law coefficient as a function of laser wavelength measured using the scanning laser setup (empty symbols) and manually-tuned laser setup (filled symbols). Lower panel: 2PA shape functions measured by the scanning laser setup (empty symbols) and manually tuned laser setup (filled symbols). The maximum value of the shape functions is normalized to unity. The manually-tuned data is averaged over 9 measurements in C153 and 3 measurements in Fluorescein.

5% or less. In the case of the absolute cross section measurement, there is an additional uncertainty due to the measurement of the 1-photon excited fluorescence. Firstly, for this measurement, the 1-photon excitation beam should be aligned to illuminate the exact same sample volume as the 2PEF excitation beam. If the beams are even slightly misaligned, then the two fluorescence signals may no longer be collected from the exact same sample volume. Secondly, because the maxima of the 2-photon and 1-photon spectra do not always coincide, when we tune the 2-photon excitation wavelength near the peak of the 2PA spectrum, then the corresponding 1-photon excitation wavelength may be located where the linear absorbance is very low or changes abruptly, thus making it difficult to accurately determine how many photons are absorbed in the sample. When combined with the above 5% error due to the characterization of the excitation beam, we arrived at the estimated maximum uncertainty of the 2-photon cross section value of about 8%.

6. Application notes

How to apply reference standards in the 2PEF-based measurements was described previously in [7]. Here, we would like to briefly discuss the utilization of the reference standards for augmenting nonlinear transmittance-type experiments [2, 9, 24, 25]. According to the Eq. (1), the photon flux passing through a thin layer of 2-photon absorbers decreases in proportion to the number density of the absorbers. In case of finite thickness, it is useful to introduce the effective NLT strength,

$$\kappa_{2PA} = \sigma_{2PA} N_c d, \quad (9)$$

where d is the sample thickness. If d is expressed in cm, the chromophore concentration N_c is given in mM (10^{-3} M) and σ_{2PA} is expressed in GM, then the maximum effective NLT strength would be typically in the range, $\kappa_{2PA} = 1 - 10^2$. The chromophores described here

have been selected to exhibit good solubility in their respective solvents, with the maximum concentration, $\sim 5 - 10$ mM. By using $d = 1$ cm and selecting the standards that have $\sigma_{2PA} > 10$ GM, an sufficiently large value, $\kappa_{2PA} > 10$, may be achieved in the whole wavelength range 680 - 1050 nm. Also, because the reference samples are often exposed to intense laser light, the solutions were evaluated for photo-stability as well as for dark storage stability over a period of about 1 month. Out of the samples tested, only BDPAS in DCM showed an increased photo-induced decomposition [8], which was accompanied by relatively short dark stability of less than ~ 1 week. One might assume that larger κ_{2PA} would allow larger maximum absolute change of the transmittance, $|\Delta T_{\max}|$, which, in turn, would facilitate more accurate determination of σ_{2PA} values. However, depending on the beam parameters, the nonlinear transmittance may exhibit a quite complicated dependence on the incident photon flux [25]. For this reason, special care should be taken not to use excessively large κ_{2PA} values, especially if the sample and the reference have very different NLT signals. Based on practical experience, if the maximum transmittance change of both the sample and the reference is, $|\Delta T_{\max}| < 10\%$, then one can obtain the 2PA spectrum of the sample under study by using the relation,

$$\sigma_{2PA}(\lambda_{2PA}) = \sigma_{2PA}^{ref}(\lambda_{2PA}) \frac{B_{NLT}(\lambda_{2PA})}{B_{NLT}^{ref}(\lambda_{2PA})} \frac{N_c^{ref} d^{ref}}{N_c d}, \quad (10)$$

where σ_{2PA}^{ref} is the 2PA spectrum of the reference standard, N_c^{ref} and d^{ref} are, respectively, the concentration and the thickness of the reference sample and the coefficients B_{NLT} and B_{NLT}^{ref} are obtained from fitting the measured nonlinear transmittance as a function of the number of incident photons with the linear function,

$$f_{lin} = 1 - B_{NLT} \iiint I_{2PA}(t, x, y; \lambda_{2PA}) dx dy dt. \quad (11)$$

Still another potential issue in the NLT measurements stems from near-IR absorption of common solvents. For example, at the wavelengths > 900 nm both toluene and DMSO show peak absorbance, $A_{\max} \sim 0.1$, in 1 cm cuvette. One way to minimize the uncertainty caused by solvent absorption would be to either use the same solvent for the reference as for the system under study, or if that is not feasible, then to subtract from the 2PA spectrum given by the Eq. (10) the artifacts that may be present when the measurement is performed with the neat solvent.

7. Conclusions

We presented absolute two-photon absorption spectra of a series of organic fluorophores in the excitation wavelength range, 680 - 1050 nm. By using stable femtosecond lasers and by cross-checking independently performed measurements, we have achieved accuracy of at least 5% for the shape of the 2PA spectra and 8% for in the absolute 2PA cross section values. This constitutes at least a factor of 4 - 5 improvement compared to the previously established 2-photon reference standards. The chromophores were selected to provide improved solubility and stability and are therefore well suited not only for the 2PEF-based experiments, but also for calibration of nonlinear transmission measurement, which often require higher sample concentration. The new data further alleviates the need for tedious characterization of the excitation laser parameters and allows for quantitative comparison and optimization of molecular probes used in multiphoton microscopy and imaging, for quantifying the multiphoton absorption efficiency of chromophores in different environments, as well as many other applications of nonlinear optics and -spectroscopy.

Appendix

Table 2. 2-photon cross sections (GM) of the dyes at selected wavelengths (nm). The maximum relative error of the numbers shown here is given in Table 1. Please note that the values in Table 1 are obtained directly from measuring the absolute cross section at few select wavelengths, and as shown in Fig. 3, whereas the values shown here are the best fit by scaling the experimentally measured shape function according to the absolute cross section data.

λ_{2PA} (nm)	σ_{2PA} (GM)								
	<i>BDPAS MethCl</i>	<i>Prodan toluene</i>	<i>Prodan DMSO</i>	<i>C153 toluene</i>	<i>C153 DMSO</i>	<i>AF455 toluene</i>	<i>AF455 THF</i>	<i>Fluor. H₂O pH11</i>	<i>Rh6G MetOH</i>
680	179	17	16	4.9	6.4	122	123	17	162
690	166	19	19	5.0	5.8	119	120	12	248
700	146	19	20	5.0	5.3	120	123	11	237
710	108	17	20	4.8	4.6	120	126	11	145
720	74	15	20	4.9	4.2	137	144	13	76
730	46	14	20	5.4	4.2	177	186	16	51
740	28	13	19	6.4	4.5	231	240	19	43
750	20	12	18	7.6	5.2	284	288	21	44
760	16	10	17	9.1	6.3	331	327	23	50
770	15	8.9	16	11	7.7	374	366	24	60
780	15	6.6	14	13	9.3	403	390	26	65
790	13	4.0	12	14	11	396	388	26	70
800	11	2.1	8.7	16	13	372	374	24	73
810	10	1.1	6.4	17	14	350	361	21	78
820	8.3	0.62	4.3	17	15	330	341	16	76
830	6.3	0.39	2.6	16	16	309	310	11	62
840	4.4	0.31	1.5	16	17	290	285	7.8	44
850	2.6	0.26	0.83	15	17	260	260	6.2	26
860	1.3	0.21	0.42	14	17	210	223	5.8	14
870	0.64	0.15	0.20	12	16	148	180	6.2	7.5
880	0.24	0.08	0.09	8.6	15	83	131	7.0	4.7
890		0.04	0.04	5.7	14	42	89	8.3	4.3
900			0.02	3.3	13	20	59	10	5.1
910				1.7	11	7.6	36	12	6.3
920				0.75	9.0	2.8	20	13	7.5
930				0.31	7.0		11	12	8.9
940				0.10	5.2		4.9	9.8	11
950					3.7		2.3	7.3	14
960					2.5		1.1	6.1	18
970					1.6		0.54	5.4	21
980					0.94			5.2	24
990					0.51			4.6	24
1000								3.3	21
1010								2.1	17
1020								1.2	13
1030									11
1040									11
1050									12

Acknowledgments

This work was supported by Ministry of Education and Science, Republic of Estonia grant IUT23-9. Part of this work was supported by European Union ITN project TOPBIO and by NIH Grants R01 GM098083 and 1U01NS094246-01. We thank Jake Lindquist and Caleb Stoltzfus for their help with LabView programming.

APPENDIX K: Publication II

de Reguardati, S., Pahapill, J., Rammo, M. and Rebane, A.,

“Improving the fidelity of two-photon absorption reference standards”

Proc. SPIE 10094 (2017)

Improving the fidelity of two-photon absorption reference standards

S. de Reguardati^a, J. Pahapill^a, M. Rammo^a and A. Rebane^{*a,b}

^aNational Institute of Chemical Physics and Biophysics, Tallinn, Estonia;

^bDepartment of Physics, Montana State University, Bozeman, MT, USA

ABSTRACT

Reference standards with well-defined femtosecond two-photon absorption (2PA) properties facilitate accurate measurement of nonlinear-optical spectra by bypassing tedious characterization of the photon flux. The 2PA standards are increasingly used for developing advanced multi-photon fluorescent probes and, since recently, also for probing intra- and intermolecular electrostatic interactions. We have recently reported 2PA cross section values of a set of common organic dyes in different solvents in 680-1050 nm wavelength range with estimated accuracy of 8%. In the present work, we aim at further improving the accuracy and fidelity of the absolute 2PA cross section data by comparing in a pair-wise manner the relative 2PA efficiency of nine standards with partially overlapping absorption- and fluorescence emission spectra. We measure the relative 2PA-induced fluorescence for each pair under identical excitation conditions, which allows revealing inconsistencies potentially present in the previously published data due to errors in estimating the excitation laser beam spatial- and temporal profile, pulse energy and other critical parameters. Our current measurements confirmed and in some cases improved previously reported error margins thus improving the fidelity of the reference data. We also present refined 2PA cross section data on 9-Chloroanthracene in dichloromethane.

Keywords: two-photon absorption, nonlinear-optical reference standards

1. INTRODUCTION

The process of instantaneous two-photon absorption (2PA) was predicted by Maria Goeppert-Mayer in 1931 [3], who theoretically considered quantum-mechanical probability of a transition from ground electronic state to an excited electronic state via simultaneous absorption of two photons, where the transition energy equals the combined energy of the two photons. The work provided estimate of the peak 2PA cross section of a typical optical absorber, $\sigma_{2PA} = 10^{-50} \text{ cm}^4 \text{ s photon}^{-1}$. This value is now broadly adopted as a convenient unit (GM) of the 2PA efficiency in organic chromophores. In contrast to one-photon absorption (1PA), where the transition probability scales linearly with the average photon flux (number of incident photons per unit area per unit time), the rate of 2PA increases as square of instantaneous photon flux. Because σ_{2PA} is generally rather small, in order to achieve practical efficiency, i.e. a two-photon transition rate comparable to that of 1PA, one would need a high photon flux, on the order of $10^{30} \text{ photon cm}^{-2} \text{ s}^{-1}$. Regular emitters such as incandescent lamps have relatively low brightness, and capability to produce sufficiently high optical intensity became available only after invention of the laser. For this reason, the first observation of 2PA was reported only in 1961 by W. Kaiser and C. G. Garret [4], who used a pulsed ruby laser to illuminate a crystal of CaF_2 containing luminescent Eu^{2+} ions. Recent advances in pulsed lasers and especially due to proliferation of femtosecond mode-locked lasers and optical parametric frequency converters/amplifiers, the utility of 2PA has grown from a mere scientific curiosity into a thriving field of research and applications, covering as diverse areas as biological microscopy, photonic materials processing and medical diagnostics. Driven by these developments, many new molecular systems performing 2PA with increasing efficiency were designed and tested [5 - 9]. However, highly accurate quantitative characterization of the molecular σ_{2PA} and its dependence on the excitation laser wavelength is still posing practical issues. This is because accurate determination of σ_{2PA} requires precise knowledge of the photon flux, which in case of pulsed lasers is still prone to considerable experimental uncertainty. Consequently, the residual experimental errors in 2PA spectroscopy remain large, often exceeding 50-20 %. There are also lingering issues regarding reproducibility of results reported by different laboratories and/or using different measurement techniques.

*arebane@montana.edu, phone: 406-994-7831, fax: 406-994-4452

Frontiers in Ultrafast Optics: Biomedical, Scientific, and Industrial Applications XVII, edited by Alexander Heisterkamp, Peter R. Herman, Michel Meunier, Roberto Osellame, Proc. of SPIE Vol. 10094, 100941Q · © 2017 SPIE · CCC code: 0277-786X/17/\$18 · doi: 10.1117/12.2250443

Proc. of SPIE Vol. 10094 100941Q-1

The tedious characterization of the photon flux could be circumvented if one could calibrate the 2PA measurements with respect to reference standards, where the σ_{2PA} values are previously established with high degree of fidelity. In this case, an accurate measurement of an unknown chromophore or material can be achieved by simply calibrating the data with respect to a known reference standard. Such calibration may be applicable independent of the type of the 2PA measurement, which improves the ability to compare results obtained using different measurement techniques and by different laboratories. Indeed, 2PA cross sections and -spectra obtained in the same chromophore system using the so-called direct z-scan [10] method and the indirect fluorescence excitation method [11-14] are sometimes difficult to reconcile, especially because different experiments may use substantially different photon flux parameters and other excitation conditions. These problems are exacerbated in situations where the excitation photon wavelength needs to be varied in broad range of wavelengths, such as in case of measurement of local electric field [15, 16], and where reproducibility of wavelength-tuneable ultrafast pulsed lasers continues to be an issue.

First report of 2PA standards by Xu and Webb [18] used a ~80-MHz pulse repetition rate mode-locked Ti:Sapphire femtosecond laser and 11 common fluorophores, namely Rhodamine B in methanol, Fluorescein in water buffer pH 11, BIS-MSB in cyclohexane, Coumarin 307 in methanol, Cascade Blue in water, Lucifer Yellow in water, Bodipy in water, DiI in methanol, Indo-1 in water, Dansyl hydrazine in methanol and free DAPI in water. The 2PA cross section measurements were performed in the excitation wavelength range 690 - 1050 nm by exciting fluorescence in fluorophore solution with a tightly focussed laser beam. The evaluation of the absolute 2PA cross-section relied on the knowledge of fluorescence quantum yield, accurate value of which is not always available. Also, the spatial distribution of the incident light was not directly measured thus assumptions were made about the spatial shape of the focussed beam, leading to substantial error of σ_{2PA} values. In [19] the fluorescence excitation approach was expanded to include 5 other fluorophores, and the cross-section spectra were determined by comparison with Fluorescein standard from previous work [18]. In 2008 Makarov et al. [20] carried out measurements of a set of 15 standards using 1 kHz pulse repetition rate femtosecond optical parametric amplifier (OPA) tuneable in a range of wavelengths 550-1600 nm. In this case the excitation beam was only slightly focussed, which allowed for direct measurement of the beam spatial profile. The 2PA fluorescence signal was calibrated relative to 1PA fluorescence in the same sample, which, in combination with a less error-prone determination of the photon flux, gave more reliable σ_{2PA} values with estimated accuracy of 20 - 30%. However, because of a poor day-to-day reproducibility of the low pulse repetition rate source, the 2PA spectral shapes still displayed substantial degree of discrepancy. We have recently further improved the experimental methodology by combining the advantages of high pulse repetition rate femtosecond pulses with the moderate focussing conditions allowing improved accuracy of the spatial beam profiling [21]. The absolute 2PA cross-sections and -spectra were measured for 9 standards, namely 4,4'-bis(diphenylamino)-stilbene (BDPAS) in dichloromethane (DCM), Prodan in toluene, Prodan in dimethylsulfoxide (DMSO), Coumarin 153 in toluene, Coumarin 153 in DMSO, AF455 in toluene, AF455 in tetrahydrofuran (THF), Fluorescein in water buffer pH 11 and Rhodamine 6G (Rh 6G) in methanol (MetOH) in the 680-1050 nm excitation wavelength range. Accuracy of spectral shape profiles was estimated 5% and accuracy of absolute cross sections was 8%. In the present work, we aim to improve the fidelity of the absolute 2PA cross section data by comparing pair-wise the relative 2PA efficiency of the standards with partially overlapping absorption- and fluorescence emission spectra, thus revealing potential inconsistencies caused e.g. by experimental errors in estimating the excitation laser beam parameters. For each pair the relative 2PA cross section was evaluated by measuring the 2PA-induced fluorescence at identical excitation conditions. We are also refining 2PA cross section data of 9-Chloroanthracene in dichloromethane.

2. THEORETICAL CONSIDERATIONS

2.1 Measurement of the absolute cross-section

When a monochromatic beam of light propagates through a thin slab of 2-photon absorbing medium, then the difference between the number of photons at the input and output of the slab may be expressed as:

$$\Delta I_{2PA} = -\sigma_{2PA} N_c \Delta z I_{2PA}^2, \quad (1)$$

where I_{2PA} is the incident photon flux in photons $\text{cm}^{-2} \text{s}^{-1}$, σ_{2PA} is the 2PA cross section in $\text{cm}^4 \text{s photon}^{-1}$, N_c is the concentration of the 2-photon absorbing molecules in cm^{-3} and Δz is the slab thickness in cm. Provided that all other parameters involved are known, σ_{2PA} may be determined directly by measuring the number of the photons absorbed. However, the relative change of the photon flux is often rather small, $\Delta I_{2PA} \ll I_{2PA}$, thus making a direct measurement

both technically involved and subject to systematic and experimental errors. An alternative, so-called indirect way of determining σ_{2PA} is by evaluating the number of absorbed photons using some secondary effect, e.g. though detecting two-photon excited fluorescence (2PEF) i.e. fluorescence photons emitted as a result of 2PA. Even though 2PEF experiment requires knowledge or calibration of the fluorescence detection efficiency and/or of the fluorescence emission quantum yield, this indirect approach has proven to be in certain practical aspects more straightforward and more reliable compared to various direct nonlinear absorption measurements [11, 23, 24].

Let us suppose that the 2PEF medium is excited by a periodic train of ultrashort pulses at the pulse rate of g (in Hz), and at the wavelength λ_{2PA} . Then the average fluorescence signal recorded in a spectral interval centered on a detection wavelength, λ_{reg} , may be expressed as:

$$F_{2PA}(\lambda_{2PA}) = \Delta t_{2PA} \left[g N_c \frac{1}{2} \sigma_{2PA}(\lambda_{2PA}) \Delta z \iiint I_{2PA}^2(t, x, y, \lambda_{2PA}) dx dy dt \right] \left[\int_{\lambda_{reg}} \eta(\lambda_{em}) \varphi(\lambda_{em}) d\lambda_{em} \right], \quad (2)$$

where $I_{2PA}(t, x, y, \lambda_{2PA})$ is the instantaneous photon flux at the laser tuning wavelength λ_{2PA} , Δt_{2PA} is the fluorescence detector integration time, $\varphi(\lambda_{em})$ is the differential quantum efficiency of fluorescence emission at the emission wavelength, λ_{em} , and $\eta(\lambda_{em})$ is the aggregate detection efficiency that accounts for the efficiency of fluorescence collection, spectrometer/diffraction grating output, efficiency of the detector, etc. The quantity inside the square brackets in (2) is related to the fluorescence detection, and its value is generally not known. This may be evaluated, however, by measuring the amount of fluorescence emitted in the same system under 1-photon excitation conditions. If the Kasha-Vavilov rule is obeyed, then we are allowed to assume that the differential quantum efficiency is independent of the mode of excitation. The corresponding linear fluorescence signal is:

$$F_{1PA}(\lambda_{1PA}) = \Delta t_{1PA} \left[(1 - 10^{OD}) \int I_{1PA}(x, y) dx dy \right] \left[\int_{\lambda_{reg}} \eta(\lambda_{em}) \varphi(\lambda_{em}) d\lambda_{em} \right], \quad (3)$$

where I_{1PA} is the time-average photon flux, Δt_{1PA} is the fluorescence signal integration time, $OD = N_c \sigma_{1PA} \Delta z$ is the optical density of the sample and σ_{1PA} is the 1-photon absorption cross section at the 1-photon excitation wavelength λ_{1PA} . By substituting the square brackets from (3) into (2), and by assuming that the 2-photon pulse excitation temporal intensity profile as well as the spatial beam profile are both described by Gaussian functions:

$$I_{2PA}(t, x, y, \lambda_{2PA}) = I_{2PA}^0(\lambda_{2PA}) \exp\left(-4 \ln 2 \frac{t^2}{\tau^2}\right) \exp\left(-4 \ln 2 \frac{x^2}{\Delta x^2}\right) \exp\left(-4 \ln 2 \frac{y^2}{\Delta y^2}\right), \quad (4)$$

we obtain the expression for absolute 2PA cross section:

$$\sigma_{2PA}(\lambda_{2PA}) = \frac{1}{\sqrt{2}} \left(\frac{\pi}{\ln 2} \right)^{3/2} \frac{F_{2PA}(\lambda_{2PA}) P_{1PA}(\lambda_{1PA}) \Delta t_{1PA} (1 - 10^{-OD})}{P_{2PA}^2(\lambda_{2PA}) F_{1PA}(\lambda_{1PA}) \Delta t_{2PA} N_c \Delta z} g \tau \Delta x \Delta y, \quad (5)$$

where P_{1PA} is the total number of photons per second in the 1PA excitation beam and P_{2PA} is the total number of photons in the 2PA excitation pulse.

Relation (5) has been used for evaluation of 2PA cross section and spectra. However, potential experimental errors may still occur, especially due to difficulty of measuring the pulse spatial shape and the pulse duration with sufficient accuracy. Other potential sources of error are due to quantifying both the 1-photon and 2-photon excited fluorescence signal, as well as with limited accuracy and reproducibility of measuring the optical power. Our ultimate goal is to eliminate any potential experimental errors so that the residual uncertainty in determining σ_{2PA} becomes less than a few per cent. Because this task is still practically difficult, we propose instead to verify the fidelity of the current best characterized data set by carrying out a pair-wise comparison between different standards under identical excitation- and detection conditions. If the excitation wavelengths, the photon flux, the beam parameters and the fluorescence detection conditions for two standards, A and B, are the same, then the ratio between the corresponding cross sections may be expressed as:

$$\frac{\sigma_{2PA}^A(\lambda_{2PA})}{\sigma_{2PA}^B(\lambda_{2PA})} = \frac{F_{2PA}^A(\lambda_{2PA}) N_C^B}{F_{2PA}^B(\lambda_{2PA}) N_C^A} \left[\frac{\int_{\lambda_{reg}} \varphi^A(\lambda_{em}) d\lambda_{em}}{\int_{\lambda_{reg}} \varphi^B(\lambda_{em}) d\lambda_{em}} \right]. \quad (6)$$

The ratio between the quantum efficiencies can be obtained e.g. using a spectrofluorimeter [26] set at the same registration wavelength λ_{reg} with the exact same bandwidth, while using sufficiently diluted solutions ($OD_{max} < 0.5$) according to the formula:

$$\varphi(\lambda_{reg}) = \frac{\int f(\lambda) d\lambda}{1 - 10^{-OD(\lambda_{ex})}}, \quad (7)$$

where $f(\lambda)$ represents the fluorescence spectrum and OD is the optical density at the excitation wavelength λ_{ex} . Refractive index of the solvent do not appears in this formula because it cancels out in the relative cross-section expression (6).

By measuring F_{2PA} at an excitation wavelength λ_{2PA} , where the 2PA spectra of A and B have sufficiently mutual overlap and by measuring $\varphi(\lambda_{reg})$ at λ_{reg} , where the corresponding emission spectra also overlap sufficiently well, we can verify the relative 2PA cross-section values that were previously published thus revealing potential discrepancies. We note that since the 2PEF detection is typically performed in a different setup from the differential quantum yield measurement in (7) potential systematic errors may occur due to mismatch in the wavelength calibration of different spectrometers, light source correction functions etc. However, as long as the difference between the absolute cross-section and relative cross-section determination is sufficiently small, e.g. less than 8%, this contribution may be neglected.

3. EXPERIMENTAL

3.1 Description of laser system and measurement setup

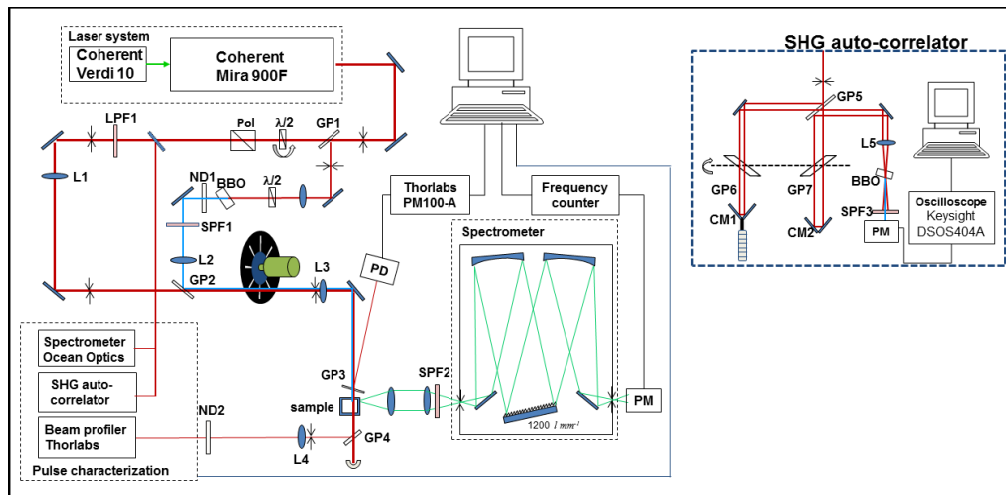


Figure 1. Main panel (left): Schematic of the experimental set-up; Insert (right): schematic of the SHG auto-correlator. L – focusing lenses; ND – neutral density filter wheel; SPF – short-pass glass filter; LPF – long-pass glass filter; GP – glass plate; PM – photomultiplier; PD – photodetector; Pol – Glan-Taylor polarizer; GP – glass plate. Red line stands for the fundamental beam path; blue line stands for the generated SHG beam path. Green lines show the fluorescence detection beam path.

Schematic of the setup is shown in Figure 1. We used a 76-MHz pulse repetition rate mode-locked Ti:Sapphire femtosecond oscillator (Coherent Mira 900) pumped by 10 W cw frequency-doubled Nd:YVO₄ laser (Coherent Verdi V-10). The femtosecond laser wavelength was tuned manually in the range 690 - 960 nm with the average output power varying in the range 0.5 – 1.5 W. A color glass long-pass filter (LPF1) was used to cut off residual short-wavelength emission emanating from the laser output. The fundamental laser spectrum was measured with a diffraction grating spectrometer (OceanOptics USB4000) to which a weak reflection was conveyed through an optical fiber. A combination of focusing and collimating lenses (L1, 500 mm and L3, 150 mm) were used to reduce beam size to ~ 0.3 mm at the sample location and ensure a nearly collimated propagation along the sample pathway. A series of iris diaphragms were used to align the laser beam such that it passed near the center of all lenses. To generate the IPA excitation beam, single reflection (~ 4%) off a glass plate (GP1) was focused on a Type I phase matched BBO crystal that generated second harmonic (blue) light. A $\lambda/2$ plate in front of the SHG crystal rotated the pump beam polarization to horizontal direction in order to assure that SHG had the same (vertical) polarization as the fundamental beam. A glass short-pass filter (SPF1) was used to cut off residual fundamental wavelength after the SHG crystal. A second glass plate (GP2) reflector was used to direct SHG along the same beam path as the main fundamental wavelength beam. At short wavelengths, ~700 nm, the glass plate was replaced by a flip mirror to compensate for decrease in the laser output power. After GP2 the two beams followed the same path and were incident on the same spot at the sample. A combination of focusing and collimating lenses (L2, 125 mm and L3, 150 mm) and a diaphragm place before L3 were used to shape the blue beam such as to have the same or smaller spot size as the red beam.

The spatial profile of the fundamental wavelength beam at the sample location (sample removed) was measured with the CCD- camera based beam profiler (Thorlabs BC106-VIS). The camera and the focusing lens L4 (150 mm) are placed in order to image the beam at the sample location with a magnification of ~ 3. Adjustment and exact magnification factor was done using a 10 mm stage micrometer ruler with 50 μm division (Thorlabs R1L3S1P) at the sample position by inserting it in the sample cell holder. The beam incident on the camera was attenuated by 20 dB with a reflective type neutral filter. A continuously variable neutral density filter wheel ND2 (Thorlabs NDC-100C-4) was placed in front of the camera to further adjust the laser power to avoid saturation. The power reflected by the glass plate GP4 was sufficiently weak to minimize any thermal lensing in the beam profile imaging path. To also minimize potential detrimental effect due to thermal lensing in the sample, especially in tetrahydrofuran (THF) and in methanol solutions, we also recorded the beam profile after passing through the sample, while stirring the solution. If thermal distortions were still observed to change the beam width by 5 - 10% or more, then the average fundamental laser power was reduced by factor 10 using a 100 Hz optical chopper (Thorlabs MC2000) that was inserted before the lens L3, where the spot size was minimum, see Figure 1.

The pulse temporal intensity profile was obtained for each wavelength by using a modified second harmonic autocorrelator (INRAD 5-14A). To acquire the correlation function, the beam was split in two parts on an uncoated glass plate GP5. The resulting beams were reflected back from corner mirrors (CM1, CM2) while passing on their way twice through 1 mm tick rotating glass plates (GP6, GP7) set at 60 degrees with respect to each other and acting as a variable delay between the two beams. The retro reflected beams were again recombined on GP5 and focused with lens L5 (60 mm) to a common spot in 0.1 mm BBO crystal producing a non-collinear second harmonic generation beam. The SHG intensity as a function of the plate rotation angle was detected with a photomultiplier (PM) and digitized with 4 GHz oscilloscope Keysight DSOS404A. A blue glass filter (SGF) was used to reject residual fundamental wavelength. Digitized autocorrelation traces were processed using a Mathematica routine that converted the rotation angle into delay values as well as performed fitting of the data.

Two left panels of Figure 2 (a) show in blue shades the recorded beam profiles at the sample position, after rescaling according to known camera pixel size (6.45 μm) and also by taking into account image magnification factor (~ 3) of the lens. Best fit to experimental data with an asymmetrical Gaussian function is shown in red lines. Since in reality the fitting is not a simple Gaussian, we modified in Equation (5) the product of FWHM of the beam $\Delta x \Delta y$ by introducing a shape correction factor, g_p , that was evaluated based on the asymmetric Gaussian fit model as follows:

$$g_p = \frac{\ln 4 \left[\iint I_{2PA,a,u}(t, x, y, \lambda_{2PA}) dx dy \right]^2}{\pi \iint I_{2PA,a,u}^2(t, x, y, \lambda_{2PA}) dx dy} \quad (8)$$

Estimate of maximum error of the beam shape measurement was calculated by relative quadratic mean between the image and the fit and taking into account 4% due to the estimated accuracy of the magnification factor.

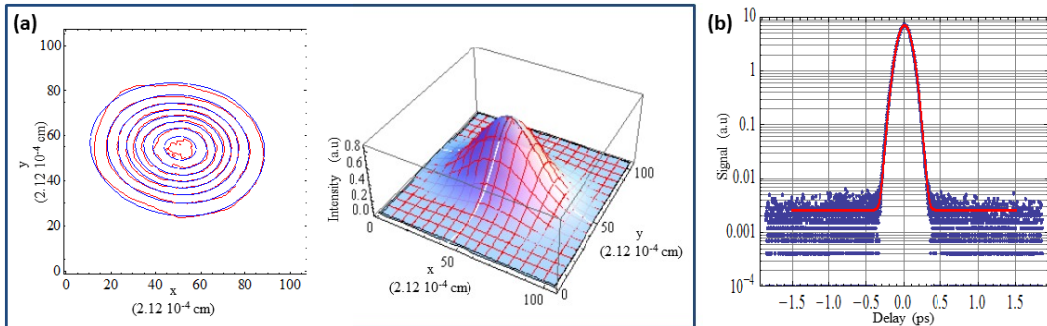


Figure 2. (a) Example of beam profile (red matrix) and its asymmetrical Gaussian fit for $\lambda=812$ nm presented in a topographic (left) and 3D (right) view. (b) Example of autocorrelation function (blue dot) and its Gaussian fit (red line) for $\lambda=784$ nm with Chi-square exceeding 0.999.

The right most panel of Figure 2 (b) shows in blue symbols the oscilloscope trace vs. the delays in picosecond generated between the two beams generated in the auto-correlator. The resulting signal was well fitted with a Gaussian function, showed in red line, for the determination of the laser temporal full-width at half maximum τ . We estimated a maximum experimental error of pulse duration measurement about 2 %, which may result from beam misalignment and detector response nonlinearity in the auto-correlator.

3.2 Sample preparation

Prodan, Coumarin 153 (C153), Fluorescein, 9-Chloroanthracene and Rhodamine 6G (Rh 6G) were obtained from Aldrich and were used as received. 4,4'-Bis(diphenylamino)-stilbene (BDPAS) was custom-synthesized by K. Schanze group (U of Florida) as described in [23]. AF455 was provided by Dr. S. Tan from the Air Force Research Laboratory. The synthesis of AF455 is described in [27, 28]. The pteridine nucleoside analog 6-methylisoxanthopterin (6MI) was purchased from Fidelity Systems, Inc. All solvents were purchased from Sigma-Aldrich and were used without further purification. Stock solutions were prepared by mixing the solvent with 1 -3 mg of dry dye, where the latter was weighed using Mettler-Toledo Model AT2611 analytical balance. Linear absorption spectra were obtained with Shimadzu UV-3600Plus spectrophotometer and corrected fluorescence spectra were measured with Perkin-Elmer Fluorimeter LS55. Extinction coefficients were determined by the dilution method, where a set of daughter solutions with maximum absorbance in the range OD = 0.5 - 1.5 were prepared from the stock solution. The samples were contained 10 mm quartz cuvettes. The chromophore concentration used in the 2PA and 1 PA measurements was in the range 10^{-6} - 10^{-3} M. The concentration was evaluated spectrophotometrically, where the beam path length 1 mm, 2 mm or 10 mm was selected such that peak O.D. was in the range 0.05 - 1.0.

3.3 Experimental procedure for evaluating fluorescence signals

The fundamental power reaching the sample was measured with optical power meter (Coherent FieldMate) with thermoelectric probe (Coherent Powermax PM10) placed directly in front of the sample. Fluorescence signal was collected in 90° geometry and focused on the entrance slit of a scanning diffraction grating spectrometer (LOMO MDR-12) (Figure 1 (a)). Scattered laser light was additionally suppressed by a stack of short-pass color glass filters (SPF2). The fluorescence signal was detected with a photon counting module (Hamamatsu H6240-01) coupled to a frequency counter with PC readout. To assert quadratic power dependence of the 2PEF fluorescent signal F_{2PA} , The relative average power of the fundamental beam at the sample P_{2PA} was further varied by manually rotating a $\lambda/2$ plate that was positioned in front of a Glan-Taylor polarizer (GL10-B Thorlabs) (Pol). The relative average power of the fundamental beam at the sample was monitored by reflecting a portion of the incident beam to integrating sphere silicon photodetector (Thorlabs S140C) coupled to optical power meter (Thorlabs PM100A). Fluorescent signal F_{2PA} and relative average power P_{2PA} were measured simultaneously with 1s integration and 100 acquisitions. The log-log dependence of the resulting average 2PEF F_{2PA} signal on the average relative power P_{2PA} was fitted with a linear function using York method.

Figure 3 (a) shows (black symbols) exemplary power dependence obtained in Coumarin 153 in toluene at 816 nm excitation wavelength. Red line stands for the linear fit, taking into account both vertical and horizontal experimental error bars.

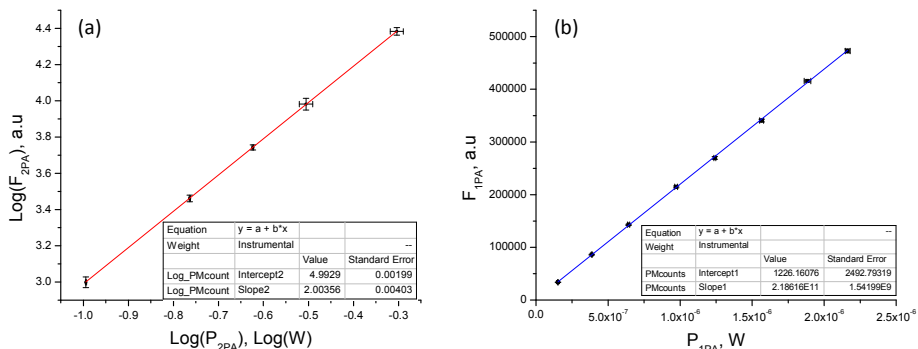


Figure 3. (a) Example of the verification of quadratic power dependence using log-log linear fit of F_{2PA} vs. P_{2PA} recorded for Coumarin 153 in toluene at 816 nm. Experimental data (black point with error bars) are fitted with linear regression using York method (red line) and show a power law coefficient of 2.00. (b) Example of the linear dependence of the fluorescence signal F_{1PA} vs. the blue beam power P_{1PA} after 1-photon absorption recorded for AF455 in toluene at 784 nm. Experimental data (black point with error bars) are fitted with linear regression using York method (red line) with R-squared of 0.999.

The intercept of the fit (*intercept2* in Figure 3 (a)) to the power of 10 was used in Eq. (5) and (6) in the place of the quotient:

$$\frac{F_{2PA}(\lambda_{2PA})}{P_{2PA}^2(\lambda_{2PA})} = 10^{\text{intercept2}} \quad (9)$$

The standard error given by the fit (Figure 3 (a)) was included for both 2PA shape and cross-section error bar estimation. Most of our measurements showed a power law coefficient in the 1.98 - 2.02 range. To a wider tolerance, the measurements accepted have a power law coefficient in the 1.96 - 2.04 range.

The 1-photon excitation beam power was adjusted by using continuously variable metallic-coated filter wheel (ND1), and the corresponding power was measured with integrating sphere silicon photodetector (Thorlabs S140C) or with standard silicon photodetector (Thorlabs S120VC) placed directly in front of the sample. The power was measured immediately before starts of the fluorescence signal acquisition to minimize possible effect of laser power drift. Both power P_{1PA} and fluorescent signal F_{1PA} were measured with an integration time of 1s and over 100 acquisitions. The resulting F_{1PA} signal vs. incoming power P_{1PA} embedded with their dispersion was fitted with a linear function using York method. To verify the linearity of the fluorescence detection, Figure 3 (b) shows average F_{1PA} vs. the average power P_{1PA} (black symbols) for AF455 in toluene at 392 nm excitation wavelength. Blue line stands for the best linear fit.

The slope of the fit (*slope1* in Figure 3 (b)), was used in Eq. (5) in the place of the quotient:

$$\frac{F_{1PA}(\lambda_{1PA})}{P_{1PA}(\lambda_{1PA})} = \text{slope1} \quad (10)$$

The standard deviation given by the fit was included for the 2PA cross-section error bar estimation.

3.4 Measurement of relative quantum yield

The fluorescence detection wavelength, λ_{reg} , was chosen in the region where the two samples spectra overlap and, if possible, where the fluorescence of both samples is close to the respective maximum or at least where the fluorescence spectrum is nearly constant. In order to take into account the dependence of the detector sensitivity on the wavelength,

and to minimize potential impact from inner filter effect, the differential quantum efficiency was calculated for at least 6 different excitation wavelengths, λ_{ex} . These wavelengths were chosen in the overlapping absorbance band of the sample and the reference where the absorbance is preferentially constant at least in an interval ± 1 nm. Only data was used where all values showed good reproducibility. The quantum efficiency was then evaluated by averaging over 6 or more independent values. Nevertheless, it appeared that, even following this rigorous procedure, the differential quantum yield value taken on different times with different solution concentrations changed up to about 5%. Therefore, we continued repeating the differential quantum yield measurements until the discrepancies were rectified.

4. RESULTS AND DISCUSSION

4.1 Absolute cross-section of 9-chloroanthracene in dichloromethane

Our first task was to establish accurate absolute 2PA cross section of 9-Chloroanthracene in dichloromethane. We found $\sigma_{2PA} = 0.043 \pm 0.004$ GM at 740 nm, which is about 1.5 less than the value published in [20]. Figure 4 shows the 2PA spectrum (gray circles), where the shape is reproduced from [20], and the absolute values are corrected according to our current measurement (red squares). The linear extinction spectrum is shown by blue solid line.

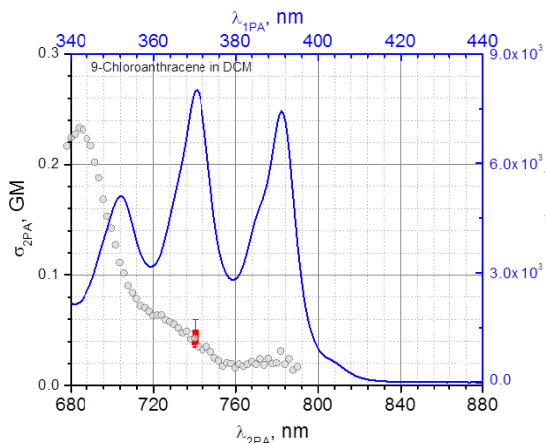


Figure 4. 2PA shape spectrum (grey symbols) and extinction coefficient (blue line) of 9-Chloroanthracene in dichloromethane. Red points correspond to the absolute measurement results to rescale 2PA shape.

Table 1 summarizes the photophysical properties of the previously published standards [21], where we have added current results on 9-Chloroanthracene in dichloromethane. Note that 9-Chloroanthracene has several absorption maxima, and in this case the molar extinction coefficients were estimated at two peaks.

As will be shown below based on the pair-wise comparison of Fluorescein in buffer pH 7 and Coumarin 153 in DMSO, the previously reported absolute 2-photon cross-section for Fluorescein was slightly overestimated. The main difficulty stems from the fact that in this particular fluorophore the 1-photon and 2-photon spectral shapes do not match (see Figure 5 (h)). As a consequence, it is a challenge to find a concentration of the solution suitable simultaneously for one-photon and two-photon measurements. On one hand, the OD must be in the range of 0.05 - 0.2 in the 350 nm region such that 2PEF measurement is feasible. On the other hand, such high concentration leads to a saturated 1PA spectrum even in 1 mm cuvette, thus hampering exact spectrophotometric evaluation of the concentration. A relatively small error in the previous data most likely resulted from such erroneous concentration estimate. The corrected value shown in Table 1 $\sigma_{2PA} = 24.3 \pm 1.2$ GM at 785 nm is lower by 6.5% compared to what was previously published.

Table 1. 1-photon and 2-photon photophysical properties of the systems studied. The σ_{2PA} and $\Delta\sigma_{2PA}$ values are obtained by averaging over all measurements performed. Bold values correspond to correction or add from previous publication [21].

	Comp.	Solvent	$\epsilon (\lambda_{1PA})$	$\min \lambda_{em} - \max \lambda_{em} (\text{peak } \lambda_{em})$	$\sigma_{2PA}(\lambda_{2PA})$	$\Delta\sigma_{2PA}$
			$M^{-1} \text{ cm}^{-1} (\text{nm})$	nm	GM (nm)	$\pm\%$
1	BDPAS	DCM	52.6x10 ³ (388)	415 – 540 (443)	175 (690) 138 (700)	8 8
2	Prodan	toluene	19.8x10 ³ (349)	390 – 480 (414)	19 (700)	6
3	Prodan	DMSO	17.5x10 ³ (358)	420 – 550 (459)	20 (723)	8
4	C153	toluene	20.5x10 ³ (408)	440 – 600 (468)	17 (816)	5
5	C153	DMSO	18.5x10 ³ (427)	480 – 650 (540)	17 (851)	7
6	AF455	toluene	117x10 ³ (419)	430 – 550 (453)	404 (784)	7
7	AF455	THF	106x10 ³ (415)	450 – 630 (504)	392 (784)	6
8	Fluorescein	H ₂ O pH11	88.6x10 ³ (491)	490 – 580 (514)	24 (785)	5
			8.7x10 ³ (322)		6.0 (858)	8
9	Rh 6G	MetOH	122x10 ³ (528)	580 – 630 (554)	79 (812)	8
			12.1x10 ³ (347)		202 (692)	8
10	9-Chloroanthracene	DCM	8.02x10 ³ (370) 7.44x10 ³ (391)	386-477 (416)	0.043 (740)	8

4.2 Pair-wise comparison or the relative 2PA efficiency

Figure 5 shows the 2PA and 1PA spectra, along with the fluorescence emission spectra for select 9 pairs (out of 10 pairs studied): (a) 9-Chloroanthracene in DCM vs. Prodan in toluene, (b) 9-Chloroanthracene in DCM vs. BDPAS in DCM, (c) BDPAS in DCM vs. Prodan in in DMSO, (d) BDPAS in DCM vs. Coumarin 153 in toluene, Prodan in in DMSO vs. Coumarin 153 in toluene, (f) Coumarin 153 in toluene vs. AF455 in THF, (g) Coumarin 153 in toluene vs. AF455 in toluene, (h) Coumarin 153 in DMSO vs. Rhodamine 6G in methanol and (i) Coumarin 153 in DMSO vs. Fluorescein in water buffer pH 11. As mentioned already, one of the criteria for choosing the particular pairs was sufficient overlap between their respective absorption spectra (solid lines). The second criterion was overlap between the fluorescence spectra (dash lines). Common fluorescence detection wavelength is indicated by vertical straight line.

The pair-wise relative 2PA was then compared with the ratio between the absolute σ_{2PA} values for the same excitation wavelength. The discrepancy between the two ratios values at selected wavelengths expressed in % terms is presented in Table 2. Coumarin 153 in toluene cross-section was measured relatively to 4 other standards: BDPAS in DCM (Figure 5 (d)), Prodan in DMSO (Figure 5 (e)), AF455 in THF (Figure 5 (f)) and AF455 in toluene (Figure 5 (g)). The discrepancy ranges from -7.5 % to +5.3 %. At the 2PA peak $\lambda_{2PA} = 816$ nm we report a deviation of -4 % relatively to Prodan in DMSO, -1.8% relatively to AF455 in THF and -7.2 % relatively to AF455 in toluene which might suggest that the absolute cross-section is slightly lower than the value published in [20]. A systematic error may arise here from erroneous differential quantum yield measurements, especially since our 2PA shape was already verified with a substantially smaller maximum error of 5 % [21]. However, this deviation is still less than the 8 %, thus confirming our previous absolute two-photon cross-sections for Coumarin 153 in toluene. For BDPAS in dichloromethane there is relatively poor overlap with the absorption and fluorescence of Prodan in toluene, which may be responsible of marked deviations. Indeed, their 1PA absorption maximum are displaced by ~40 nm making it difficult to find a suitable common excitation wavelength, and their fluorescent maximum are also shifted by 30 nm leading to a difficult choice of the common λ_{reg} . With our choice $\lambda_{reg} = 457$ nm, we found a deviation of -17.1% at 701 nm and -28.7% at 750 nm excitation. Thus this example allows visualizing the limits of accuracy in the use of reference standard regarding spectral mismatch. Relative to Prodan in DMSO, the deviation from the absolute value is +1.0 % at 700 nm. With 4 selected wavelengths in the 720 - 740 nm region, the deviations are in the ranging from 0.3 % relatively to Prodan in toluene at 723 nm, to 8.1 % relatively to Coumarin 153 in toluene at 725nm. Therefore our absolute 2PA cross-section value for BDPAS in dichloromethane is as well validated. Conversely, assuming that the absolute 2-photon cross-section spectra for Coumarin 153 in toluene and BDPAS in DCM are exact, then using those two standards (Figure 5 (c) and (e)) we found for Prodan in DMSO a deviation of -0.9% at its 2PA peak at 700 nm. Otherwise, the deviation does not exceed 4.6 % in the 700 – 816 nm, which confirm the fidelity of this standard. AF455 in THF and in toluene were both compared to Coumarin in toluene and showed at their 2PA peak a deviation of -0.3% for AF455 in toluene and -5.0 % for AF455 in THF.

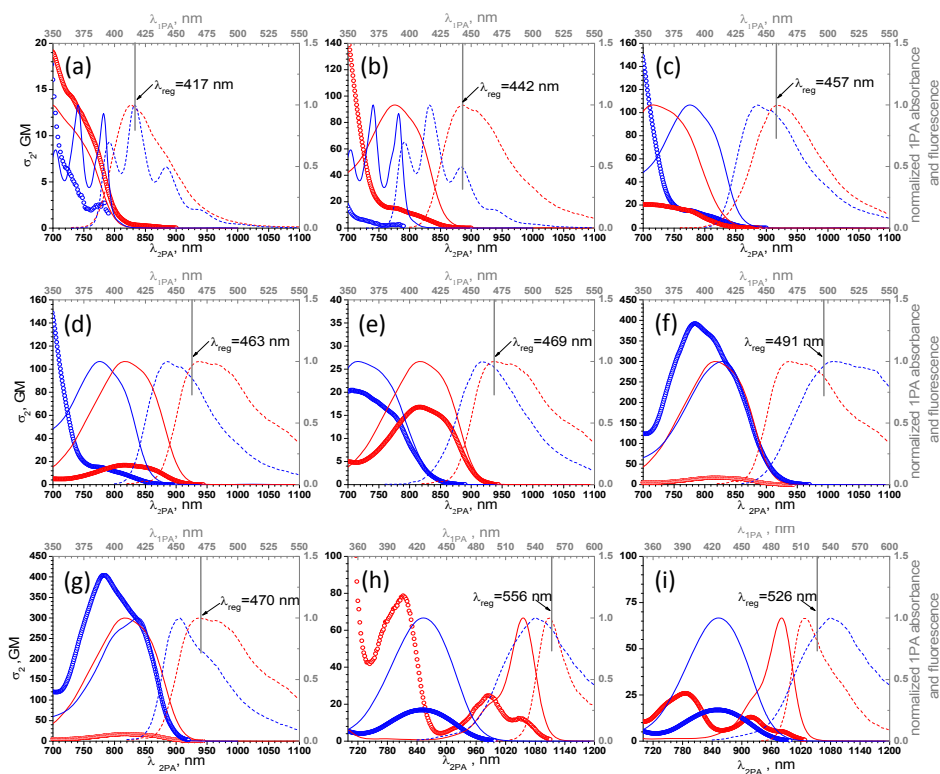


Figure 5. Normalized 1-photon absorption (line, right and top axis), normalized fluorescence spectra (dash, right and top axis) and 2PA spectra (circle, bottom and left axis) of: (a) 9-Chloroanthracene in DCM (blue) vs. Prodan in toluene (red); (b) 9-Chloroanthracene in DCM (blue) vs. BDPAS in DCM (red); (c) BDPAS in DCM (blue) vs. Prodan in in DMSO (red); (d) BDPAS in DCM (blue) vs. Coumarin 153 in toluene (red); (e) Prodan in DMSO (blue) vs. Coumarin 153 in toluene (red); (f) AF455 in THF (blue) vs. Coumarin 153 in toluene (red); (g) AF455 in toluene (blue) vs. Coumarin 153 in toluene (red); (h) Coumarin in DMSO vs. Fluorescein in water buffer pH 11 (red); (i) Coumarin 153 in DMSO (blue) vs. Rhodamine 6G in methanol (red). The common chosen fluorescence detection wavelength λ_{reg} for each pair is also indicated.

Comparison of 9-Chloroanthracene in DCM to BDPAS in DCM at 740 nm gave a deviation of -6.3% . Relative to Prodan in toluene the deviation was $+3.9\%$ at 740 nm and $+13.6\%$ at 750 nm. We have to point out that the 2PA shape for 9-Chloroanthracene is slightly noisy for longer wavelength and therefore the resulting deviation is higher at 750 nm. The good agreement found at 740 nm confirmed our absolute measurement for 9-Chloroanthracene at this wavelength. Conversely, the relative cross-section determined for Prodan in toluene with respect to 9-Chloroanthracene in DCM is 3.7% off the absolute determined one, therefore we are allowed to assert that the high deviation found for Prodan in toluene relatively to BDPAS in DCM is the consequence of the poor overlap in their emission spectra and that the absolute 2PA spectrum determined for Prodan in toluene is accurate. Coumarin 153 in DMSO gave at 851 nm a deviation $+6.1\%$ relatively to Fluorescein in water buffer pH 11 and -3.7% relatively to Rhodamine 6G. Conversely, Rhodamine 6G in methanol showed a deviation at its 2PA peak of $+3.8\%$ relatively to Coumarin 153 in DMSO and Fluorescein showed a deviation at its 2PA peak of $+4.6\%$ relatively to Coumarin in DMSO. Therefore, all these deviations are smaller than the 8% error thus confirming the accuracy to our absolute measurements.

Table 2. Deviation in % of the sample relative 2PA cross-section calculated with the reference compared to its absolute value for the same wavelength. Bold values correspond to the maximum of the 2PA spectrum.

Sam.A Sam B	BDPAS in DCM	9-chl.anthr. in DCM	Prodan in toluene	Prodan in DMSO	C153 in toluene	C153 in DMSO	AF455 in toluene	AF455 in THF	Fluorescein in buffer pH=11	Rh6G in MetOH
BDPAS in DCM		+6.7% (740nm)	-17.1% (701nm) -28.7% (750nm)	+1.0% (700nm) -0.3% (723nm) -0.6% (740m)	+8.1% (725nm) +2.2% (736nm)					
9-chl. anthr. in DCM	-6.3% (740nm)		+3.9% (740nm) +13.6% (750nm)							
Prodan in toluene	+20.7% (701 nm) +30.6% (715 nm) +40.2% (750 nm)	-3.7% (740nm) -11.9% (750nm)								
Prodan in DMSO	-0.9% (700 nm) +0.3% (723 nm) +0.6% (740nm)				3.8% (750nm) +1.0% (775nm) +4.2% (816nm)					
C153 in toluene	-7.5% (725nm) -2.2% (736nm)			-3.7% (750nm) -1.0% (775nm) -4.0% (816nm)			+0.3% (784nm) -7.2% (816nm)	+5.3% (784nm) -1.8% (816nm)		
C153 in DMSO									-4.6% (785nm) +6.1% (851nm)	-3.7% (812nm) -4.4% (851nm)
AF455 toluene					-0.3% (784nm) +7.8% (816nm)					
AF455 in THF					-5.0% (784nm) +1.8% (816nm)					
Fluorescein in buffer pH=7						+4.6% (785 nm) -5.8% (851 nm)				
Rh6G in MetOH						+3.8% (812nm) +4.3% (851nm)				

4.3 Two-photon cross-section spectrum of 6MI

6-methylisoxanthopterin (6MI) is a fluorescent analog to DNA base guanine with the fluorescence emission in the 450 nm region with high quantum yield and 1PA peak at 343 nm. It has found use as promising fluorophore probe for monitoring DNA and RNA conformations. Because living cells absorb light in the ranges from 200 - 360 nm

overlapping with the 6MI spectrum, it is of increasing interest to explore the 2-photon absorption properties of this system [32, 33].

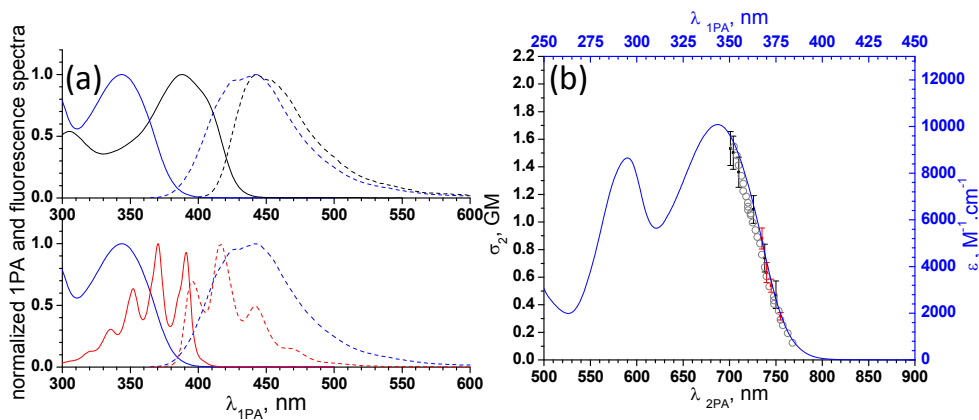


Figure 6. (a) Comparison of normalized 1-photon absorption and fluorescence spectra between 6MI in phosphate buffer pH=7 with two adapted standards: BDPAS in DCM (upper panel) and 9-chloroanthracene in DCM (lower panel). (b) rescaled 2PA shape spectrum (grey circles, left and bottom axis) and extinction coefficient spectrum (blue line, right and top axis) of 6MI in phosphate buffer pH=7. Relative cross-section with respect to BDPAS in DCM (black) and to 9-Chloroanthracene in DCM (red).

6MI was dissolved in 1M phosphate buffer pH 7. This solvent was chosen to simulate human cell environment but also to avoid ionization of the N3 proton of 6MI whose pKa is approximately 8.3. BDPAS and 9-chloroanthracene were used as reference. 6MI samples were prepared with a rather high concentration of $\sim 10^{-4}$ M. The relative quantum yield and 2PA cross-section were determined at 442 nm. Figure 6 (a) shows the normalized 1PA and fluorescence spectra of 6MI in the phosphate buffer compared to the same of BDPAS in dichloromethane (upper panel) and 9-Chloroanthracene in dichloromethane (lower panel). Figure 6 (b) presents the measured 2PA shape spectrum (grey circles) of 6MI in the 700 - 750 nm range. 1PA spectrum (blue line) is shown for comparison. At its maximum at 700 - 704 nm the 2PA cross section is ~ 1.5 GM. The σ_{2PA} values at different wavelengths are collected in Table 3 and shown Figure 6 (b) by black squares when determined relative to BDPAS in DCM and by red squares when 9-Chloroanthracene in DCM was used as reference standard. The 2PA shape spectrum was rescaled to match with the measured cross-section values, the resulting best fit 2PA cross-sections are also shown in Table 3.

Table 3. 2-photon cross-section of 6MI in phosphate buffer pH 7 calculated using a reference standard at different wavelength.

Reference	σ_{2PA} (λ_{2PA}) GM (nm)	σ_{2PA} from best match shape rescale GM (nm)
BDPAS in DCM	1.53 ± 0.10 (701)	
	1.50 ± 0.10 (704)	1.54 (704)
	1.36 ± 0.10 (710)	1.41 (710)
	1.09 ± 0.09 (726)	0.98(726)
	0.74 ± 0.06 (738)	0.67 (738)
	0.47 ± 0.04 (750)	0.39 (750)
9-Chloroanthracene in DCM	0.88 ± 0.08 (735)	0.76 (735)
	0.63 ± 0.07 (740)	0.61 (740)
	0.54 ± 0.05 (745)	0.50 (745)
	0.32 ± 0.03 (755)	0.29 (755)

We conclude that in the spectral region studied 2PA follows the 1PA profile, i.e. 2PA transition is most likely to the same excited singlet state as the 1PA band. By extrapolation, the peak 2PA is ~ 1.7 GM at 690 nm.

4.4 Additional potential issues with standard selection

We strive to substantially improve the accuracy of the reference standard and their fidelity. In that regards, standards should be selected such as to facilitate their use, i.e. they should show large 2PA cross-section, be well soluble in ambient conditions (minimal aggregation) and the solutions should be stable both in the dark as well as under stringent illumination conditions. Some of the previously reported standards fail to fulfill these requirements and are therefore omitted from our current set. For instance, Rhodamine 610 (Rhodamine B), which was proposed in [11, 15], appears in different solvents as a mixture of at least three different forms: (a) intensely colored protonated cation form; (b) zwitterion and (c) colorless lactone [29, 30]. In water, the equilibrium between zwitterion and lactone form has $pK_a = 8.3$ whereas in methanol the equilibrium between zwitterionic and cationic form has $pK_a = 3.1$. Moreover the proportion of the different forms of Rhodamine B depends on temperature and concentration. We found that in methanol, with increasing concentration, the equilibrium is displaced toward the cationic form due to increases of the acidity and is visible in the 1-photon absorption spectrum for concentration as low as 10^{-5} M by a bathochromic shift of the maximum peak. This effect might be avoided by the use of few triethylamine drops. In deuterated water, zwitterionic form tends to aggregate at concentrations as low as 10^{-5} M as manifested by a distinct change of the 1-photon absorption spectrum with the rise of the dimer absorbance peak at 523 nm. This effect appears in slightly more concentrated solution in pure water [31]. Therefore water or heavy water solutions of Rhodamine B can be considered as transition systems between solutions of monomers and aggregates in the whole range of usual studies. Perylene, Lucifer yellow and chloroanthracenes show relatively low peak 2PA cross section, $\sigma_{2PA} < 10$ GM and were excluded from the set as well. Because some of the biological markers absorb in the far-UV region, we reconsidered 9-Chloroanthracene as a standard. It has also an advantage of a greater stability (>1 month) compared to 4,4'-bis-(diphenylamino)stilbene (BDPAS), which has low stability in solution, about 1 week.

5. CONCLUSION

We presented a detailed study of absolute two-photon absorption cross sections of a series of organic fluorophores in the excitation wavelength range, 680-1050 nm. We measured the relative 2PA-induced fluorescence for 10 pairs of standards under identical excitation conditions, which has revealed some minor inconsistencies in the previously published data, most likely due to errors in estimating the excitation laser beam spatial- and temporal profile, pulse energy and other critical parameters. Our current measurements confirmed the 8% maximum error margin and in some cases improved the previously reported results, thus augmenting the overall fidelity of the reference data. We also present refined 2PA cross section data on 9-Chloroanthracene in dichloromethane.

6. ACKNOWLEDGMENTS

This work was supported by Ministry of Education and Science, Republic of Estonia grant IUT23-9. A.R. and A. M. acknowledge support from AFOSR grant FA9550-16-1-0189.

REFERENCES

- [1] Lakowicz, J. R., [Principles of Fluorescence Spectroscopy, 3rd edition], Springer (2006).
- [2] Southerland, R. L., [Handbook of Nonlinear Optics, 2nd edition], Marcel Dekker (2003).
- [3] Göpper-Maier, M., "Über Elementarakte mit zwei Quantensprüngen," *Ann. Phys.* 401 (3), 273–294 (1931).
- [4] Kaiser, M. and Garrett, C. G. B., "Two-Photon Excitation in $\text{CaF}_2:\text{Eu}^{2+}$," *Phys. Rev. Lett.* 7(6), 229-231 (1961).
- [5] Ventelon, L., Blanchard-Desce, M., Moreaux, L. and Mertz, J., "New quadrupolar fluorophores with high two-photon excited fluorescence," *Chem. Commun.* 20, 2055-2056 (1999).
- [6] Schmitt, J., Heitz, V., Sour, A., Bolze, F., Ftouni, H., Nicoud, J-F., Flamigni, L. and Ventura, B., "Diketopyrrolopyrrole-Porphyrin Conjugates with High Two-Photon Absorption and Singlet Oxygen Generation for Two-Photon Photodynamic Therapy," *Angew. Chem. Int. Ed. Engl.* 54(1), 169-173 (2015).

- [7] Wang, Y., Hu, R., Xi, W., Cai, F., Wang, S., Zhu, Z., Bai, R. and Qian, J., "Red emissive AIE nanodots with high two-photon absorption efficiency at 1040 nm for deep-tissue in vivo imaging," *Biomed. Opt. Express* 6(10), 3783-3794 (2015).
- [8] Liu, H-W., Zhang, X-B, Zhang, J., Wang, Q-Q., Hu, X-X., Wang, P. and Tan, W., "Efficient Two-Photon Fluorescent Probe with Red Emission for Imaging of Thiophenols in Living Cells and Tissues," *Anal. Chem.* 87(17), 8896-8903 (2015).
- [9] Yue, X., Armijo, Z., King, K., Bondar, M. V., Morales, A. R., Frazer, A., Mikhailov, I. A., Przhonska, O. V. and Belfield, K. D., "Steady-state and femtosecond transient absorption spectroscopy of a new two-photon absorbing fluorine-containing quinolizinium cation membrane probes," *ACS Appl. Mater. Interfaces* 7(4), 2833-2846 (2015).
- [10] Sheik-Bahae, M., Said, A. A., Wei, T.-H., Hagan, D. J. and Van Stryland, E. W., "Sensitive measurement of optical nonlinearities using a single beam," *IEEE J. Quantum Electron.* 26(4), 760-769 (1990).
- [11] Denk, W., Strickler, J. H. and Webb, W. W., "Two-photon laser scanning fluorescence microscopy," *Science* 248, 73-76 (1990).
- [12] Xu, C., Zipfel, W., Shear, J. B., Williams, R. M. and Webb, W. W., "Multiphoton fluorescence excitation: new spectral windows for biological nonlinear spectroscopy," *Proc. Natl. Acad. Sci. U.S.A.* 93, 10763-10768 (1996).
- [13] Wokosin, D. L. and White, J. G., "Optimization of the design of a multiple-photon excitation laser scanning fluorescence imaging system" *Proc. SPIE* 2984, 25-29 (1997).
- [14] Zipfel, W. R., Williams, R. M. and Webb, W. W., "Nonlinear magic: multiphoton microscopy in the biosciences," *Nat. Biotechnol* 21, 1369-1377 (2003).
- [15] Drobizhev, M., Makarov, N. S., Tillo, S. E., Hughes, T. E. and Rebane, A., "Two-photon absorption properties of fluorescent proteins" *Nat. Methods.* 8, 393-399 (2011).
- [16] Rebane, A., Wicks, G., Drobizhev, M., Cooper, T., Trummal, A. and Uudsemaa, M., "Two-photon voltmeter for measuring a molecular electric field," *Angew. Chem. Int. Ed. Engl.*, 54 (26), 7582-7586 (2015).
- [17] Hermann, J. P. and Ducuing, J., "Absolute measurement of two-photon cross sections," *Phys. Rev. A.* 5, 2557-2568 (1972).
- [18] Xu, C. and Webb, W. W., "Measurement of two-photon excitation cross sections of molecular fluorophores with data from 690 to 1050 nm," *J. Opt. Soc. Am. B* 13, 481-491 (1996).
- [19] M. A. Albota, C. Xu, W. W. Webb, "Two-photon fluorescence excitation cross sections of biomolecular probes from 690 to 960 nm," *Appl. Opt.* 37, 7352-7356 (1998).
- [20] Makarov, N. S., Drobizhev, M. and Rebane, A., "Two-photon absorption standards in the 550-1600 nm excitation wavelength range," *Opt. Express* 16(6), 4029-4047 (2008).
- [21] de Reguardati, S., Pahapill, J., Mikhailov, A., Stepanenko, Y. and Rebane, A., "High-accuracy reference standards for two-photon absorption in the 680-1050 nm wavelength range" *Opt. Express* 24(8), 9053-9066 (2016).
- [22] Rumi, M. and Perry, J. W. "Two-photon absorption: an overview of measurements and principles," *Adv. Opt. Photonics* 2, 451-518 (2010).
- [23] Dubinina, G. G., Price, R. S., Abboud, K. A., Wicks, G., Wnuk, P., Stepanenko, Y., Drobizhev, M., Rebane, A. and Schanze, K. S., "Phenylene vinylene platinum(II) acetylides with prodigious two-photon absorption," *J. Am. Chem. Soc.* 134 (47), 19346-9 (2012).
- [24] Bridges, R. E., Fischer, G. L. and Boyd, R. W., "Z-scan measurement technique for non-Gaussian beams and arbitrary sample thicknesses," *Opt. Lett.* 20 (17), 1821-1824 (1995).
- [25] Gu, B., Ji, W., Patil, P. S., Dharmaparakash, S. M. and Wang, H. T., "Two-photon-induced excited-state absorption: Theory and experiment," *Appl. Phys. Lett.* 92, 091118 (2008).
- [26] Würth, C., Grabolle, M., Pauli, J., Spieles, M. and Resch-Genger, U., "Relative and absolute determination of fluorescence quantum yields of transparent samples," *Nat. Protoc.*, 8 (8), 1535-1550 (2013).
- [27] Kannan, R., Tan, L.-S. and Vaia, R. A., "Two-photon responsive chromophores containing electron accepting cores," *US Patent* 6,555,682 (2003).
- [28] Kannan, R., He, G. S., Lin, T.-C., Prasad, P. N., Vaia, R. A. and Tan, L.-S., "Toward highly active two-photon, absorbing liquids. Synthesis and characterization of 1,3,5-triazine-based octupolar molecules," *Chem. Mater.* 16 (1), 185-194 (2004).
- [29] Arbeloa, I. L., Ojeda, P. R., "Molecular forms of rhodamine B," *Chem. Phys. Lett.* 79, 347-350 (1981).

- [30] Hinckley, D. A., Seybold, P. G., Borris, D. P., "Solvatochromism and thermochromism of rhodamine solutions," *Spectrochim. Acta A Mol. Spectrosc.* 42, 741-754 (1986).
- [31] Mchedlov-Petrosyan, N. O. and Kholin, Y. V., "Aggregation of Rhodamine B in water," *Russ. J. of App. Chem.*, 77 (3), 414-422 (2004).
- [32] Cho, S. H., Chang, W. S., Kim, K. R. and Hong, J. W., "Measurement of UV absorption of single living cell for cell manipulation using NIR femtosecond laser," *Appl. Surf. Sci.* 255 (9), 4974-4978 (2009).
- [33] Siede, W. and Doetsch, P. W., [DNA Damage Recognition], CRC Press (2005).

APPENDIX L: Publication III

Mikhaylov, A., Lindquist, J. R., Callis, P. R., Kohler, B., Pahapill, J., **de Reguardati, S.**, Rammo, M., Uudsemaa, M., Trummal, A. and Rebane, A.,

“Femtosecond two-photon absorption spectra and permanent electric dipole moment change of tryptophan, 2-aminopurine and related intrinsic and synthetic fluorophores”

Proc. SPIE 10069 (2017)

Femtosecond two-photon absorption spectra and permanent electric dipole moment change of tryptophan, 2-aminopurine and related intrinsic and synthetic fluorophores

Alexander Mikhaylov^a, Jake R. Lindquist^a, Patrik R. Callis^b, Bern Kohler^{b, c}, Juri Pahapill^d, Sophie de Reguardati^d, Matt Rammo^d, Merle Uudsemaa^d, Aleksander Trummal^d and Aleksander Rebane^{a, d*}

^a Department of Physics, Montana State University, Bozeman, MT, USA; ^b Department of Chemistry & Biochemistry, Montana State University, Bozeman, MT, USA; ^c Department of Chemistry, The Ohio State University, Columbus, OH, USA; ^d National Institute of Chemical Physics and Biophysics, Tallinn, Estonia

ABSTRACT

Two-photon absorption (2PA) cross sections for 2-aminopurine (2AP), 7-methyl guanosine (7MG), 6-methyl isoxanthopterin (6MI), isoxanthopterin (IXP), 3-methylindole (3MI) and tryptophan (L-trp) are measured for excitation wavelengths between 550 and 810 nm using two independent methods: femtosecond two-photon excited fluorescence (2PEF) and femtosecond nonlinear transmission (NLT). For all systems we find that in the long-wavelength region of the lowest-energy one-photon allowed singlet-singlet transition the 2PA spectral profiles follow the one-photon absorption spectral profiles, thus indicating the strongly dipolar nature of the transition. We use the measured 2PA cross sections to estimate the corresponding permanent electric dipole moment change and find the values to vary in the range 1 to 5 D. These experimental findings are corroborated by quantum-chemical computations.

Keywords: two-photon absorption, DNA base fluorescent analogs, amino acids fluorescent labels, permanent electric dipole moment

1. INTRODUCTION

Fluorescence spectroscopy, including nonlinear-optical techniques using multi-photon excitation can provide useful information about complex behavior of biomolecules such as DNA and proteins. To overcome issues due to low fluorescence emission of natural nucleic acids, one can take advantage of synthetic analogs,¹⁻⁵ which exhibit high fluorescence yields while keeping at the same time many of the key intrinsic properties of the originals, e.g. Watson-

*arebane@montana.edu, phone: 406-994-7831, fax: 406-994-4452

Crick hydrogen bonding within the double helix structure. Recently, there has been interest in using fluorescent DNA base and amino acids analogs for two-photon excited fluorescence imaging⁶⁻⁸. However, to fully realize the potential advantages of two-photon excitation of fluorescent DNA analogs, one needs reliable quantitative information about the two-photon absorption (2PA) cross section values as well as about the dependence of 2PA on excitation wavelength. In this paper we perform femtosecond two-photon absorption study of 2-aminopurine (2AP), 7-methyl guanosine (7MG), 6-methyl isoxanthopterin (6MI), isoxanthopterin (IXP), 3-methylindole (3MI) and tryptophan (L-trp). As solvents, we use distilled water (for L-trp, 3MI, 2AP), a mixture of water and glycerol (for 2AP), phosphate buffer (for 6MI), a mixture of NH₃ and water (for IXP), pH7 aqueous buffer (for 7MG), methanol (for 2AP) and dimethyl sulfoxide (for 2AP). Our goal is to perform comprehensive measurements that would provide more reliable data compared to what has been published previously⁹⁻¹⁷. Due to the complicated photophysics that occurs in amino acids and related molecules theoretical methods even being extremely useful cannot always explain and predict all properties of these systems¹⁸⁻²⁴. In earlier experimental studies absolute 2PA cross sections were measured either at some individual wavelengths^{13,16,25-27} or only a relative 2PA profile was reported^{28,29}. Even more limited data are available about the permanent dipole moment changes in these systems^{11,12,15,30}. We use 2-photon excited fluorescence (2PEF) and nonlinear transmission (NLT) methods to measure the 2PA cross sections over a broad range of excitation wavelengths 550 - 810 nm. We use our data to estimate the permanent electric dipole moment change upon the transition from the ground electronic state to the lowest-energy excited singlet electronic state. For 2AP, the experimental results are compared to quantum chemical calculations to elucidate the permanent dipole moment changes in different solvent environments.

2. EXPERIMENTAL

Detailed descriptions of the 2PEF and NLT experiments has been provided previously^{31,32}. Briefly, a Ti:Sapphire femtosecond laser Coherent Libra operated at 1 kHz repetition rate and producing pulses with duration ~ 90 fs pumped an optical parametric amplifier (OPA) Light Conversion OPerA Solo (pulse durations at the OPA output are 200-300 fs). The OPA output wavelengths were tuned in the region 550–810 nm with 1 nm steps. The approximate OPA pulse spectral width was ~ 15–35 nm (measured with spectrometer Ocean Optics USB-4000). 2PEF signals were measured using spectrometer Jobin Yvon Horiba TRIAX ISA 550 with liquid nitrogen cooled detector CCD Jobin Yvon Horiba TRIAX ISA Spectrum 1. The relative excitation laser pulse energy was measured using pyroelectric detector Moletron P4-45, followed by Princeton Applied Research PAR 113 amplifier, and the signal was then digitized using DAQ card NI USB-6212 and processed using a LabView program. The power exponent of the dependence of the fluorescence signal on the incident pulse energy was confirmed with 5 nm wavelength step for the whole range within accuracy 1.95 - 2.05 for all compounds. The 2PA shapes were measured with 1 nm steps. Averaging was used to obtain the final spectral profiles. For the NLT measurements the laser repetition rate was reduced to 100 Hz and the OPA beam was focused with a long focal length lens. Two glass plates positioned before and after the sample reflected ~ 8% of light to silicon photodetectors Thorlabs DET 36A. Signals from the two detectors were digitized using DAQ card NI PCI-6110 connected through NI BNC-2110 and the data was processed using a LabView program to determine the dependence of the sample transmittance on the incident photon flux. The absolute power was measured using power meter Ophir Nova 2 with thermoelectric probe Ophir 3A SH. Both the 2PEF and NLT measurements were performed relative to 2PA reference standards^{31,33}. For the 2PA shape correction in the range 550-720 nm 9-chloroanthracene in dichloromethane was applied³¹, and for 680-810 nm range fluorescein in pH11 aqueous buffer was used³³, in the intermediate overlapping region 680-720 nm an averaged correction from both standards was applied. The absolute two-photon cross sections were measured relative to bis-diphenylaminostilbene (BDPAS) in dichloromethane³³ for 6MI, while for all other samples 9-chloroanthracene in dichloromethane was used as reference³¹. Relative quantum yields were measured using fluorescence spectrometer PerkinElmer LS50B. Both 1PEF and 2PEF signals were collected at 450 nm.

2AP, 7MG, IXP, 3MI and L-trp were purchased from Sigma-Aldrich (98% or higher purity) and were used as received. 6MI nucleoside was purchased from Fidelity Systems, Inc. (Gaithersburg, MD, USA) and was used as received. Distilled water was used to prepare aqueous solutions. Methanol (MeOH), dimethyl sulfoxide (DMSO) and glycerol were of HPLC grade and were used as received from Sigma-Aldrich. Ultrasonification was applied to prepare solutions of compounds with poor solubility. The solutions were filtered using 0.45 μ m filters. Concentrations of final solutions were determined spectro-photometrically using spectrophotometer PerkinElmer Lambda 950. Samples for the 2PEF and NLT experiments were contained in 1 cm or 10 cm path length quartz spectroscopic cuvettes, respectively.

3. COMPUTATIONAL METHODS

To determine the properties of 1PA and 2PA spectra and the values of permanent dipole moment change $\Delta\mu$ of 2AP the linear and quadratic response function calculations were carried out using the DALTON program package^{34,35}. These calculations were preceded by full geometry optimizations using Gaussian09 software³⁶.

The line shapes of the 1PA spectra were obtained by applying Gaussian broadening function to the corresponding stick spectra based on the calculated oscillator strengths and excitation energies:

$$\varepsilon = \frac{\sqrt{\pi} e^2 N_A 2\sqrt{\ln 2}}{1000 \ln(10) c^2 m_e} \frac{f_i}{FWHM} \exp \left[-4 \ln 2 \left(\frac{\bar{\nu} - \bar{\nu}_i}{FWHM} \right)^2 \right] \quad (1)$$

where e is the elementary charge, N_A is Avogadro's constant, c is the speed of light in vacuum, m_e is the mass of an electron, f_i is the calculated oscillator strength, $FWHM$ is a full width at half maximum of the spectral line of the molecule and $\bar{\nu}_i$ is the calculated excitation energy.

The expression for calculation of 2PA cross-sections σ_{2PA} for $S_0 \rightarrow S_1$ transition is given by:

$$\sigma_{2PA} = \frac{4 \pi^3 \alpha a_0^5}{c} \frac{\omega^2}{\pi \left(\frac{FWHM}{z} \right)} \delta \quad (2)$$

where α is the fine structure constant, a_0 is Bohr radius, ω is the calculated photon energy (half of the transition energy) and δ is the two-photon transition probability obtained from DALTON. Experimental FWHM values (1PA: 0.53 eV for methanol and DMSO, 0.58 eV for water; 2PA: 0.27 eV for methanol and DMSO, 0.29 eV for water) were used for calculation of molar extinction coefficients ε and the cross-sections σ_{2PA} . To convert to Göppert-Mayer units the value of σ_{2PA} from Eq. 2 should be multiplied by 10^{50} .

The ground state optimized geometries were used for TD-DFT excited state calculations to obtain vertical excitation properties. The modified version³⁷ of range-separated CAM-B3LYP hybrid functional and valence triple- ζ basis set augmented with one set of polarization and diffuse exponents on all atoms (*m*CAM-B3LYP/6-311++G(d,p) with $\alpha=0.08$, $\beta=0.92$, and $\mu=0.15$) were used for all excited state calculations. Solvent effects were accounted for by implementing gas-phase supermolecule approach and by using discrete-continuum approximation in the framework of the polarized continuum model PCM.

4. RESULTS AND DISCUSSION

The measured 2PA spectra (black symbols) along with linear extinction (one-photon absorption) spectra (red solid lines) are presented in Fig. 1. The 2PA cross section values were measured at several wavelengths (green solid symbols). Solid blue dots represent results of the NLT measurements. Estimated accuracy is within 30%.

The peak 2PA wavelengths shift slightly depending on solvent, following the same shift observed in the corresponding 1PA spectrum (see Table 1). The peak 2PA cross section σ_{2PA} for L-trp in water is 1 GM, for 3-MI in water it is 1.2 GM, for IXP in NH₃ and water 3:1 mixture it is 4 GM, for 6MI it is 1.7 GM, for 3-MI in water it is 1.2

GM and for 7-MG in pH7 aqueous buffer it is 3.6 GM. The maximum σ_{2PA} for 2AP varies from 0.24 GM in both H₂O and MeOH to 0.4 GM in DMSO and 2.4 GM in a Glycerol and H₂O 10:1 mixture. All results are summarized in Table 1. All 2PA spectra were measured for the lowest energy transitions. Those are spanning 550-720 nm excitation wavelengths range for 2AP in different solvents (Fig. 1 a-d). At the excitation wavelengths > 700 nm the value of σ_{2PA} drops below our detection limit. It is important to mention that for 2AP there is the well established tautomerism for the ground state^{38,39}. Relative weights of each conformer (and as a result fluorescence) might be strongly affected by solvent interaction effects^{5,38,39}. 2PA spectrum for 6MI in phosphate aqueous buffer pH7 also spans range between 580-810 nm. 2PA spectrum of IXP in NH₃ and water 1:3 mixture is more structured and covers the excitation wavelengths range from 550 nm to 800 nm. In contrast to IXP, the 2PA spectrum for 6MI is peaked at 700 nm and goes down at wavelengths shorter than 600 nm. Additionally to the 2PEF method, we perform NLT measurement for L-trp and conclude that σ_{2PA} at 550 nm is about 1.5 GM. Results of both methods are consistent within 30%. The numbers derived from the NLT are most probably affected by excited state absorption that results in overestimated σ_{2PA} values. Small maximum achievable molar concentrations (only about 5mM) limited our capability of the NLT measurements for 3MI. From the NLT we could only get some estimation for the cross section upper limit: the peaked σ_{2PA} should be below 2 GM.

To the best of our knowledge, there is no consistency in literature about σ_{2PA} values for L-trp. In earlier experiments¹³ it was found that for L-trp σ_{2PA} at 530 nm is around 0.16 GM, while other authors claimed it is 0.03 GM¹⁴ and 0.005 GM¹⁰ at 532nm. For 6-MI it was reported²⁶ that σ_{2PA} is around 2.5 GM at 700 nm. In one paper¹⁶ it was reported that σ_{2PA} at 584 nm for 2AP in aqueous solution is 0.2 GM that correlates well with our result.

2PA cross section σ_{2PA} relates some important molecular parameters allowing getting insights about changes of them upon transition between ground and excited states. In general, all highly lying energy states contribute to transition amplitude between initial and final states, but one also should include a contribution of the direct two-photon transition between the two states, which strength is proportional to the permanent dipole moment change amplitude^{28,40}. For 2AP in all considered solvents 2PA shapes follow very closely 1PA profiles. That is also true for the red sides of 2PA spectra for L-trp, 3-MI, 7-MG, IXP and 6MI. Such behavior is usually typical for highly dipolar non-symmetric molecules, when one-photon and two-photon transitions are both allowed. It gives rise to an assumption that the two-level model of 2PA might be applicable here⁴¹. According to this model, the 2PA cross section σ_{2PA} at excitation wavelength λ_{2PA} ($\lambda_{2PA} = 2 \lambda_{1PA} = 2 \lambda$) can be expressed in terms of parameters of initial and final molecular quantum states only. Then, for the amplitude of the permanent dipole moment change between the ground state and the final excited state, $\Delta\mu$ (in Debye), one gets (for details see e.g. supplementary information section in³²)

$$\Delta\mu(\lambda) = \frac{13650}{n^2 + 2} \left[\frac{n\sigma_{2PA}(2\lambda)}{\varepsilon_M(\lambda)\lambda} \right]^{1/2}, \quad (3)$$

where n is the index of refraction, ε_M is the molar extinction coefficient in M⁻¹cm⁻¹ and σ_{2PA} is expressed in GM and λ in nm.

Obtained by using that approach $\Delta\mu$ values are presented in Table 1. There is a significant spread of $\Delta\mu$ values in literature for considered compounds that were measured mainly using Stark effect spectroscopy. Applying the Ooshika-Lippert-Mataga relation^{42,43}, D. Pierce and S. Boxer¹² concluded that for L-trp $\Delta\mu$ is around 5D (for so-called L_a transition). Employing a similar approach, E. Jalviste and N. Ohta³⁰ found for indole the same transition corresponds to $\Delta\mu$ of 5.6 D, while for 3MI $\Delta\mu$ is 7.2D. Note that Stark spectroscopy values are reported without accounting for the local field correction factor. T. Nordlund with colleagues¹¹ measured the spectral shifts for 2AP in a series of solvents. From those experiments they concluded that 2AP in water and glycerol stand out compared to all other considered media resulting in large $\Delta\mu$ (up to 8D). It was assumed that such a drastic difference was observed in these two particular solvents due to some specific chromophore-solvent interactions, presumably hydrogen bonding. It is interesting that in our measurements $\Delta\mu$ values for 2AP in glycerol and water mixture are significantly higher compared to other solvents that might be another indication of forming a specific interaction.

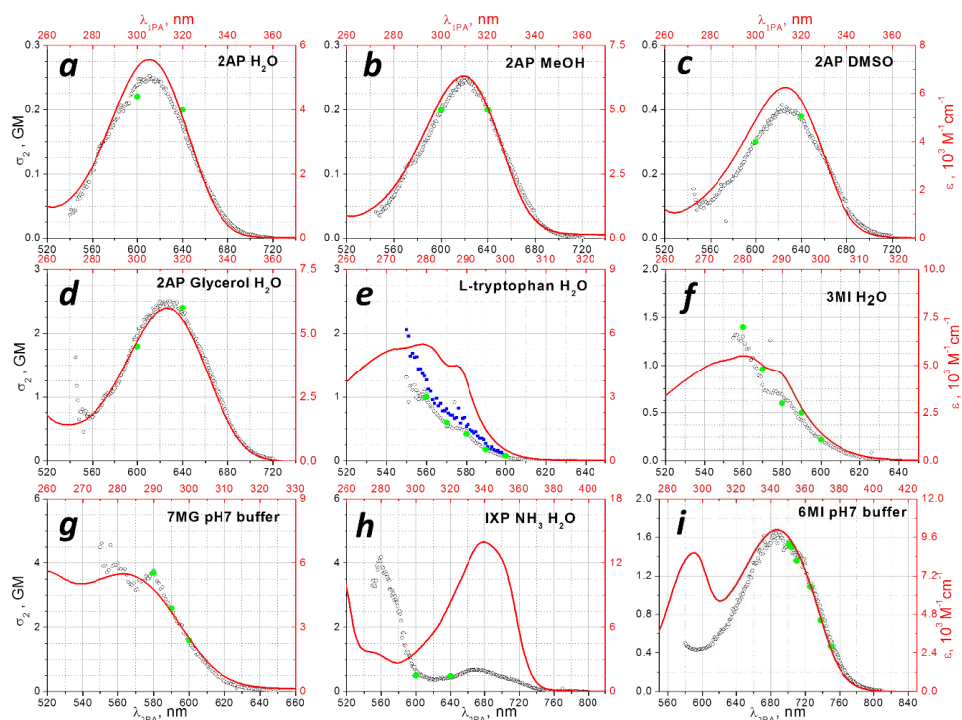


Figure 1. Two-photon absorption (2PA) spectra of 2-aminopurine (2AP) in distilled water (a), methanol (MeOH) (b), dimethyl sulfoxide (DMSO) (c), glycerol and distilled water mixture 10:1 (d); L-tryptophan in distilled water (e), 3-methyl indole (3-MI) in distilled water (f), 7-methylguanosine (7MG) in aqueous pH 7 buffer (g), isoxanthopterin (IXP) in NH_3 and distilled water mixture 1:3 (h), 6-methyl isoxanthopterin (6MI) in water phosphate pH 7 buffer (i). Left vertical axis represent 2PA cross section values σ_2 in Goepfert-Mayer units GM. Right vertical axis show extinction coefficient values ϵ in $\text{M}^{-1}\text{cm}^{-1}$ units. The lower horizontal scales correspond to the two-photon excitation wavelength λ_{2PA} , while the upper scales represent one-photon wavelength λ_{1PA} (both in nm). Black circles show 2PA profiles measured using the 2PEF relative method, while green dots indicate wavelengths where the cross sections σ_2 were measured; blue symbols illustrate 2PA spectrum obtained from the NLT method (all 3 sets of data correspond to the left vertical and lower horizontal axis). Solid red lines are linear absorption spectra (correspond to right vertical and upper horizontal axis). For 6MI absolute cross sections were measured using an independent setup and method described in details in ³³.

Table 1. Summary of one-photon and two-photon optical parameters of measured compounds. Literature (shown with references) and measured extinction coefficients at maximum ϵ expressed in inverse Mole \cdot cm. Peak wavelengths in absorption and emission showed as λ_{abs} and λ_{em} respectively. Maximum two-photon absorption cross sections σ_{2PA} in Goepfert-Mayer units GM were measured using two-photon excited fluorescence (2PEF) and nonlinear transmission (NLT) techniques (see text for details); corresponding peak values, $\sigma_{2PA} \text{2PEF}(\lambda_{\text{exc}})$ and $\sigma_{2PA} \text{NLT}(\lambda_{\text{exc}})$ showed at peak excitation wavelengths λ_{exc} . Transition dipole moment changes $\Delta\mu$ in Debye units D are calculated according to Eq. 3 (see text). †results of independent measurements using a setup and method described in ³³.

Comp.	Solvent	ϵ_s , $M^{-1}cm^{-1}$	λ_{abs} , nm	λ_{em} , nm	σ_{2PA} 2PEF(λ_{exc}), GM	σ_{2PA} NLT(λ_{exc}), GM	$\Delta\mu$, D
L-trp	dist H ₂ O	5500 ⁴⁴	279	362	1(550), 0.4(580)	1.5(550), 0.7(580)	2.6±0.3
3MI	dist H ₂ O	5500 ⁴⁴	280	374	1.2(550), 0.5(580)	< 2.0	2.8±0.2
7MG	pH 7 buffer	5500 ⁴⁵	258/281	393	3.6 (560), 1.8 (600)		2.8±0.5
IXP	NH ₃ H ₂ O 1:3	14000 ⁴⁴	340	422	4(550), 0.4(600), 0.7(670)		1.4±0.2
6MI	phosphate pH7 buffer	10090	343		1.53(701) [†] , 1.5(704) [†] , 1.36 (710) [†] , 1.09(726) [†] , 0.74 (738) [†] , 0.47(750) [†] , 0.3(750)		2.8±0.2
2AP	dist H ₂ O	5560	305	370	0.2 (612)		1.5±0.3
2AP	MeOH	6310	310	372	0.2(622)		1.1±0.2
2AP	DMSO	5930	313	375	0.4 (626)		1.8±0.2
2AP	glycerol H ₂ O 10:1	6250	313	378	2.4 (628)		4.6±0.2

The structures of 2-aminopurine and water clusters used for gas-phase excited state calculations and for solute representation of cluster-continuum approach are presented in Fig. 2.

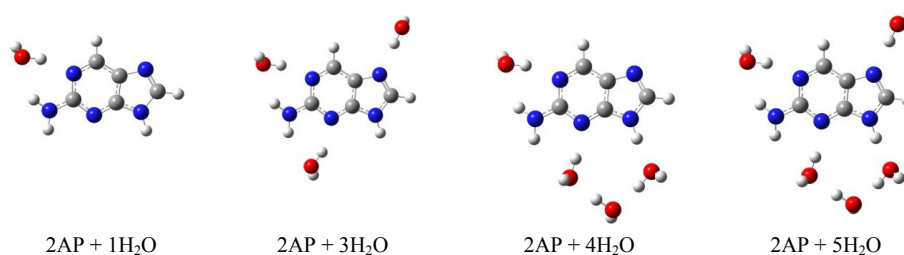


Figure 2. The structures of 2-aminopurine and water clusters.

The computational values of 1PA and 2PA spectral properties in water, DMSO, and methanol are presented in Table 2.

Table 2. Summary of computational 1PA/2PA optical parameters and transition dipole moment changes $\Delta\mu$.

Compound	Solvent	Model	ϵ , $M^{-1}cm^{-1}$	λ_{abs} , nm	σ_{2PA} (λ_{exc}), GM	$\Delta\mu$, D
2AP	H ₂ O	2AP + 1 H ₂ O (gas phase)	5132	296	0.4 (593)	0.7
		2AP + 3 H ₂ O (gas phase)	4885	306	0.4 (611)	1.0
		2AP + 4 H ₂ O (gas phase)	5343	298	0.2 (597)	1.2
		2AP + 5 H ₂ O (gas phase)	5286	299	0.3 (598)	1.6
		2AP (PCM)	7006	294	0.5 (589)	2.7
		2AP + H ₂ O (PCM)	6600	298	0.5 (596)	2.7
		2AP + 3 H ₂ O (PCM)	6479	303	0.5 (607)	2.9
		2AP + 4 H ₂ O (PCM)	6884	300	0.4 (600)	2.5
		2AP + 5 H ₂ O (PCM)	6758	301	0.4 (602)	2.7
2AP	MeOH	2AP (PCM)	7653	294	0.5 (589)	2.7
2AP	DMSO	2AP (PCM)	8367	295	0.6 (591)	2.8

The comparison of the data presented in Tables 1 and 2 reveals that the closest match between experimental and computational values for aqueous 2AP is observed for the gas-phase cluster model of 2AP incorporating 5 water molecules. In case of pure implicit or mixed explicit/implicit solvation the computational values of ϵ , σ_{2PA} and $\Delta\mu$ are somewhat higher than the corresponding experimental values. The same is also true for 2AP in methanol and DMSO environment. Based on the present computational results it is too early to draw the final conclusions on the influence of specific solvation on spectral properties of fluorescent nucleobase analog 2AP.

5. CONCLUSIONS

Femtosecond 2PA cross section values σ_{2PA} and wavelength dependence in the region of lowest-energy singlet transition of L-trp and DNA fluorescent base analogs 3MI, 7MG, IXP, 6MI and 2AP in different solvents were measured in excitation wavelength range 550-810 nm using both indirect fluorescence excitation method and direct nonlinear transmission method. All compounds studied have rather small maximum σ_{2PA} that varies from 0.2 GM for 2AP to 4 GM for IXP. It was found that for the lowest energy transitions the 2PA shapes follow very closely corresponding 1PA profiles for 2AP in different solvents; for L-trp, 3MI, 7MG, IXP and 6MI the same is observed for the longer wavelength side of the absorption tail. Assuming that in these cases the two level model can be applied to describe the two-photon transitions, changes of permanent dipole moments between the ground and first excited states $\Delta\mu$ were calculated based on the measured σ_{2PA} values and was found to be between 1.1 and 4.6 D. For 2AP experimental $\Delta\mu$ values correlate with the results of quantum-chemical calculations carried out on gas phase clusters with 1 to 5 water molecules using DALTON program.

6. ACKNOWLEDGMENTS

This work was supported by Ministry of Education and Science, Republic of Estonia grant IUT23-9. A.R. and A. M. acknowledge support from AFOSR grant FA9550-16-1-0189.

REFERENCES

- [1] Wilson, J.N., and Kool, E.T., "Fluorescent DNA base replacements: Reporters and sensors for biological systems.," *Organic & biomolecular chemistry* 4(23), 4265–4274 (2006).
- [2] Sinkeldam, R.W., Greco, N.J., and Tor, Y., "Fluorescent analogs of biomolecular building blocks: Design, properties, and applications," *Chemical Reviews* 110(5), 2579–2619 (2010).
- [3] Wilhelmsson, L.M., "Fluorescent nucleic acid base analogues.," *Quarterly reviews of biophysics* 43(2010), 159–183 (2010).
- [4] Tanpure, A.A., Pawar, M.G., and Srivatsan, S.G., "Fluorescent nucleoside analogs: Probes for investigating nucleic acid structure and function," *Israel Journal of Chemistry* 53(6–7), 366–378 (2013).
- [5] Jones, A.C., and Neely, R.K., "2-aminopurine as a fluorescent probe of DNA conformation and the DNA-enzyme interface.," *Quarterly reviews of biophysics* 2(2015), 1–36 (2015).
- [6] Li, J., Zhang, Y., Zhang, H., Xuan, X., Xie, M., Xia, S., Qu, G., and Guo, H., "Nucleoside-Based Ultrasensitive Fluorescent Probe for the Dual-Mode Imaging of Microviscosity in Living Cells," *Analytical Chemistry* 88(10), 5554–5560 (2016).
- [7] Yang, Z., Zhao, N., Sun, Y., Miao, F., Liu, Y., Liu, X., Zhang, Y., Ai, W., Song, G., et al., "Highly selective red- and green-emitting two-photon fluorescent probes for cysteine detection and their bio-imaging in living cells," *Chemical Communications* 48(28), 3442 (2012).
- [8] Manders, E.M.M., Kimura, H., and Cook, P.R., "Direct imaging of DNA in living cells reveals the dynamics of chromosome formation," *Journal of Cell Biology* 144(5), 813–821 (1999).
- [9] Rehms, A.A., and Callis, P.R., "Resolution of La and Lb bands in methyl indoles by two-photon spectroscopy," *Chemical Physics Letters* 140(1), 83–89 (1987).
- [10] Hefetz, Y., Dunn, D. A., Deutsch, T. F., Buckley, L., Hillenkamp, F., Kochevar, I.E., "Laser Photochemistry of DNA: Two-Photon Absorption and Optical Breakdown Using High-Intensity, 532-nm Radiation," *J. Am. Chem. Soc* 112, 8528–8532 (1990).
- [11] Evans, K., Xu, D., Kim, Y., and Nordlund, T.M., "2-Aminopurine optical spectra: Solvent, pentose ring, and DNA helix melting dependence," *Journal of Fluorescence* 2(4), 209–216 (1992).
- [12] Pierce, D.W., and Boxer, S.G., "Stark effect spectroscopy of tryptophan.," *Biophysical journal* 68(4), 1583–1591 (1995).
- [13] Meshalkin, Y.P., "Two-photon absorption cross sections of aromatic amino acids and proteins.," *Kvantovaya electronica* 23(6), 551–552 (1996).

- [14] Sengupta, P., Balaji, J., Mukherjee, S., Philip, R., Kumar, G.R., and Maiti, S., "Determination of the absolute two-photon absorption cross section of tryptophan" 4262, 336–339 (2001).
- [15] Kang, C., Korter, T.M., and Pratt, D.W., "Experimental measurement of the induced dipole moment of an isolated molecule in its ground and electronically excited states: Indole and indole- H₂O," *Journal of Chemical Physics* 122(17), 0–8 (2005).
- [16] Lane, R.S.K., and Magennis, S.W., "Two-photon excitation of the fluorescent nucleobase analogues 2-AP and tC," *RSC Advances* 2(30), 11397 (2012).
- [17] Lane, R.S.K., Jones, R., Sinkeldam, R.W., Tor, Y., and Magennis, S.W., "Two-photon-induced fluorescence of isomorphous nucleobase analogs," *ChemPhysChem* 15(5), 867–871 (2014).
- [18] Salem, M.A., and Brown, A., "Two-photon absorption in fluorescent protein chromophores: TDDFT and CC2 results," *Journal of Chemical Theory and Computation* 10(8), 3260–3269 (2014).
- [19] Callis, P.R., "Perturbation selection rules for multiphoton electronic spectroscopy of neutral alternant hydrocarbons," *The Journal of Chemical Physics* 78(1), 16 (1983).
- [20] Callis, P.R., "Molecular orbital theory of the 1Lb and 1La states of indole," *The Journal of Chemical Physics* 95(6), 4230–4240 (1991).
- [21] Hahn, D.K., and Callis, P.R., "Lowest triplet state of indole: An ab initio study," *The Journal of Physical Chemistry A* 101(14), 2686–2691 (1997).
- [22] Burova, T.G., Nurlygayanova, M.N., and Ten, G.N., "Quantum-mechanical calculation of the intensity distributions in spectra of resonance hyper-Raman scattering and two-photon absorption of indole and skatole," *Optics and Spectroscopy* 117(4), 582–588 (2014).
- [23] Brisker-Klaiman, D., and Dreuw, A., "Explaining level inversion of the La and Lb states of indole and indole derivatives in polar solvents," *ChemPhysChem* 16(8), 1695–1702 (2015).
- [24] Samanta, P.K., and Pati, S.K., "Theoretical understanding of two-photon-induced fluorescence of isomorphous nucleoside analogs," *Phys. Chem. Chem. Phys.* 17(15), 10053–10058 (2015).
- [25] Stanley, R.J., Hou, Z., Yang, A., and Hawkins, M.E., "The two-photon excitation cross section of 6MAP, a fluorescent adenine analogue," *Journal of Physical Chemistry B* 109(8), 3690–3695 (2005).
- [26] Katilius, E., and Woodbury, N.W., "Multiphoton excitation of fluorescent DNA base analogs," *Journal of biomedical optics* 11(4), 44004 (2014).
- [27] Herbrich, S., Al-Hadhuri, T., Gericke, K.H., Shternin, P.S., Smolin, A.G., and Vasyutinskii, O.S., "Two-color two-photon excited fluorescence of indole: Determination of wavelength-dependent molecular parameters," *Journal of Chemical Physics* 142(2), (2015).
- [28] Callis, P.R., Scott, T.W., and Albrecht, A.C., "Polarized two-photon fluorescence excitation studies of pyrimidine," *The Journal of Chemical Physics* 75(10), 1312–931 (1981).
- [29] Williams, S.A., and Callis, P.R., "Two-photon electronic spectra of nucleotides," *SPIE Proceedings* 1204(1204), 332–343 (1990).

- [30] Jalviste, E., and Ohta, N., "Stark absorption spectroscopy of indole and 3-methylindole," *Journal of Chemical Physics* 121(10), 4730–4739 (2004).
- [31] Makarov, N.S., Drobizhev, M., and Rebane, A., "Two-photon absorption standards in the 550-1600 nm excitation wavelength range," *Optics express* 16(6), 4029–4047 (2008).
- [32] Dubinina, G.G., Price, R.S., Abboud, K.A., Wicks, G., Wnuk, P., Stepanenko, Y., Drobizhev, M., Rebane, A., and Schanze, K.S., "Phenylene vinylene platinum(II) acetylides with prodigious two-photon absorption," *Journal of the American Chemical Society* 134(47), 19346–19349 (2012).
- [33] de Reguardati, S., Pahapill, J., Mikhailov, A., Stepanenko, Y., and Rebane, A., "High-accuracy reference standards for two-photon absorption in the 680–1050 nm wavelength range," *Optics Express* 24(8), 9053 (2016).
- [34] Aidas, K., Angeli, C., Bak, K.L., Bakken, V., Bast, R., Boman, L., Christiansen, O., Cimiraglia, R., Coriani, S., et al., "The Dalton quantum chemistry program system," *Wiley Interdisciplinary Reviews: Computational Molecular Science* 4(3), 269–284 (2014).
- [35] "Dalton, a molecular electronic structure program," Dalton2015, <<http://daltonprogram.org>>.
- [36] Frisch, M. J.; Trucks, G. W.; Schlegel, H. B.; Scuseria, G. E.; Robb, M. A.; Cheeseman, J. R.; Scalmani, G.; Barone, V.; Mennucci, B.; Petersson, G. A.; Nakatsuji, H.; Caricato, M.; Li, X.; Hratchian, H. P.; Izmaylov, A. F.; Bloino, J.; Zheng, G.; Sonnenb, D.J., "Gaussian 09, Revision E.01," Gaussian, Inc., Wallingford, CT (2009).
- [37] Okuno, K., Shigeta, Y., Kishi, R., Miyasaka, H., and Nakano, M., "Tuned CAM-B3LYP functional in the time-dependent density functional theory scheme for excitation energies and properties of diarylethene derivatives," *Journal of Photochemistry and Photobiology A: Chemistry* 235, 29–34 (2012).
- [38] Neely, R.K., Magennis, S.W., Dryden, D.T.F., and Jones, A.C., "Evidence of tautomerism in 2-aminopurine from fluorescence lifetime measurements," *Journal of Physical Chemistry B* 108(45), 17606–17610 (2004).
- [39] Lobsiger, S., Blaser, S., Sinha, R.K., Frey, H.-M., and Leutwyler, S., "Switching on the fluorescence of 2-aminopurine by site-selective microhydration," *Nature Chemistry* 6(11), 989–993 (2014).
- [40] Dick, B., and Hohlneicher, G., "Importance of initial and final states as intermediate states in two-photon spectroscopy of polar molecules," *Journal of Chemical Physics* 76(12), 5755–5760 (1982).
- [41] Rebane, A., Drobizhev, M., Makarov, N.S., Beuerman, E., Tillo, S., and Hughes, T., "New all-optical method for measuring molecular permanent dipole moment difference using two-photon absorption spectroscopy," *Journal of Luminescence* 130(9), 1619–1623 (2010).
- [42] Ooshika, Y., "Absorption spectra of dyes in solution," *Journal of the physical society of Japan* 9(4), 594–602 (1954).
- [43] Mataga, N., Kaifu, Y., and Koizumi, M., "Solvent Effects upon Fluorescence Spectra and the Dipolemoments of Excited Molecules," *Bulletin of the Chemical Society of Japan* 29(4), 465–470 (1956).

- [44] Fasman, G.D., [Handbook of biochemistry and molecular biology] , 3rded., CRC Press, Cleveland, OH (1976).
- [45] Stoychev, G., Kierdaszuk, B., and Shugar, D., "Interaction of Escherichia coli purine nucleoside phosphorylase (PNP) with the cationic and zwitterionic forms of the fluorescent substrate N(7)-methylguanosine," *Biochimica et Biophysica Acta - Protein Structure and Molecular Enzymology* 1544(1-2), 74-88 (2001).

**DISSERTATIONS DEFENDED AT
TALLINN UNIVERSITY OF TECHNOLOGY ON
NATURAL AND EXACT SCIENCES**

1. **Olav Kongas**. Nonlinear Dynamics in Modeling Cardiac Arrhythmias. 1998.
2. **Kalju Vanatalu**. Optimization of Processes of Microbial Biosynthesis of Isotopically Labeled Biomolecules and Their Complexes. 1999.
3. **Ahto Buldas**. An Algebraic Approach to the Structure of Graphs. 1999.
4. **Monika Drews**. A Metabolic Study of Insect Cells in Batch and Continuous Culture: Application of Chemostat and Turbidostat to the Production of Recombinant Proteins. 1999.
5. **Eola Valdre**. Endothelial-Specific Regulation of Vessel Formation: Role of Receptor Tyrosine Kinases. 2000.
6. **Kalju Lott**. Doping and Defect Thermodynamic Equilibrium in ZnS. 2000.
7. **Reet Koljak**. Novel Fatty Acid Dioxygenases from the Corals *Plexaura homomalla* and *Gersemia fruticosa*. 2001.
8. **Anne Paju**. Asymmetric oxidation of Prochiral and Racemic Ketones by Using Sharpless Catalyst. 2001.
9. **Marko Vendelin**. Cardiac Mechanoenergetics *in silico*. 2001.
10. **Pearu Peterson**. Multi-Soliton Interactions and the Inverse Problem of Wave Crest. 2001.
11. **Anne Menert**. Microcalorimetry of Anaerobic Digestion. 2001.
12. **Toomas Tiivel**. The Role of the Mitochondrial Outer Membrane in *in vivo* Regulation of Respiration in Normal Heart and Skeletal Muscle Cell. 2002.
13. **Olle Hints**. Ordovician Scolecodonts of Estonia and Neighbouring Areas: Taxonomy, Distribution, Palaeoecology, and Application. 2002.
14. **Jaak Nõlvak**. Chitinozoan Biostratigraphy in the Ordovician of Baltoscandia. 2002.
15. **Liivi Kluge**. On Algebraic Structure of Pre-Operad. 2002.
16. **Jaanus Lass**. Biosignal Interpretation: Study of Cardiac Arrhythmias and Electromagnetic Field Effects on Human Nervous System. 2002.
17. **Janek Peterson**. Synthesis, Structural Characterization and Modification of PAMAM Dendrimers. 2002.
18. **Merike Vaher**. Room Temperature Ionic Liquids as Background Electrolyte Additives in Capillary Electrophoresis. 2002.
19. **Valdek Mikli**. Electron Microscopy and Image Analysis Study of Powdered Hardmetal Materials and Optoelectronic Thin Films. 2003.
20. **Mart Viljus**. The Microstructure and Properties of Fine-Grained Cermets. 2003.
21. **Signe Kask**. Identification and Characterization of Dairy-Related *Lactobacillus*. 2003.
22. **Tiiu-Mai Laht**. Influence of Microstructure of the Curd on Enzymatic and Microbiological Processes in Swiss-Type Cheese. 2003.

23. **Anne Kuusksalu.** 2–5A Synthetase in the Marine Sponge *Geodia cydonium*. 2003.
24. **Sergei Bereznev.** Solar Cells Based on Polycrystalline Copper-Indium Chalcogenides and Conductive Polymers. 2003.
25. **Kadri Kriis.** Asymmetric Synthesis of C₂-Symmetric Bimorpholines and Their Application as Chiral Ligands in the Transfer Hydrogenation of Aromatic Ketones. 2004.
26. **Jekaterina Reut.** Polypyrrole Coatings on Conducting and Insulating Substrates. 2004.
27. **Sven Nõmm.** Realization and Identification of Discrete-Time Nonlinear Systems. 2004.
28. **Olga Kijatkina.** Deposition of Copper Indium Disulphide Films by Chemical Spray Pyrolysis. 2004.
29. **Gert Tamberg.** On Sampling Operators Defined by Rogosinski, Hann and Blackman Windows. 2004.
30. **Monika Übner.** Interaction of Humic Substances with Metal Cations. 2004.
31. **Kaarel Adamberg.** Growth Characteristics of Non-Starter Lactic Acid Bacteria from Cheese. 2004.
32. **Imre Vallikivi.** Lipase-Catalysed Reactions of Prostaglandins. 2004.
33. **Merike Peld.** Substituted Apatites as Sorbents for Heavy Metals. 2005.
34. **Vitali Syritski.** Study of Synthesis and Redox Switching of Polypyrrole and Poly(3,4-ethylenedioxythiophene) by Using *in-situ* Techniques. 2004.
35. **Lee Põllumaa.** Evaluation of Ecotoxicological Effects Related to Oil Shale Industry. 2004.
36. **Riina Aav.** Synthesis of 9,11-Secosterols Intermediates. 2005.
37. **Andres Braunbrück.** Wave Interaction in Weakly Inhomogeneous Materials. 2005.
38. **Robert Kitt.** Generalised Scale-Invariance in Financial Time Series. 2005.
39. **Juss Pavelson.** Mesoscale Physical Processes and the Related Impact on the Summer Nutrient Fields and Phytoplankton Blooms in the Western Gulf of Finland. 2005.
40. **Olari Ilison.** Solitons and Solitary Waves in Media with Higher Order Dispersive and Nonlinear Effects. 2005.
41. **Maksim Säkki.** Intermittency and Long-Range Structurization of Heart Rate. 2005.
42. **Enli Kiipli.** Modelling Seawater Chemistry of the East Baltic Basin in the Late Ordovician–Early Silurian. 2005.
43. **Igor Golovtsov.** Modification of Conductive Properties and Processability of Polyparaphenylene, Polypyrrole and polyaniline. 2005.
44. **Katrin Laos.** Interaction Between Furcellaran and the Globular Proteins (Bovine Serum Albumin β -Lactoglobulin). 2005.
45. **Arvo Mere.** Structural and Electrical Properties of Spray Deposited Copper Indium Disulphide Films for Solar Cells. 2006.

46. **Sille Ehala.** Development and Application of Various On- and Off-Line Analytical Methods for the Analysis of Bioactive Compounds. 2006.
47. **Maria Kulp.** Capillary Electrophoretic Monitoring of Biochemical Reaction Kinetics. 2006.
48. **Anu Aaspõllu.** Proteinases from *Vipera lebetina* Snake Venom Affecting Hemostasis. 2006.
49. **Lyudmila Chekulayeva.** Photosensitized Inactivation of Tumor Cells by Porphyrins and Chlorins. 2006.
50. **Merle Uudsemaa.** Quantum-Chemical Modeling of Solvated First Row Transition Metal Ions. 2006.
51. **Tagli Pitsi.** Nutrition Situation of Pre-School Children in Estonia from 1995 to 2004. 2006.
52. **Angela Ivask.** Luminescent Recombinant Sensor Bacteria for the Analysis of Bioavailable Heavy Metals. 2006.
53. **Tiina Lõugas.** Study on Physico-Chemical Properties and Some Bioactive Compounds of Sea Buckthorn (*Hippophae rhamnoides* L.). 2006.
54. **Kaja Kasemets.** Effect of Changing Environmental Conditions on the Fermentative Growth of *Saccharomyces cerevisiae* S288C: Auxo-accelerostat Study. 2006.
55. **Ildar Nisamedtinov.** Application of ^{13}C and Fluorescence Labeling in Metabolic Studies of *Saccharomyces* spp. 2006.
56. **Alar Leibak.** On Additive Generalisation of Voronoï's Theory of Perfect Forms over Algebraic Number Fields. 2006.
57. **Andri Jagomägi.** Photoluminescence of Chalcopyrite Tellurides. 2006.
58. **Tõnu Martma.** Application of Carbon Isotopes to the Study of the Ordovician and Silurian of the Baltic. 2006.
59. **Marit Kauk.** Chemical Composition of CuInSe_2 Monograin Powders for Solar Cell Application. 2006.
60. **Julia Kois.** Electrochemical Deposition of CuInSe_2 Thin Films for Photovoltaic Applications. 2006.
61. **Ilona Oja Ačik.** Sol-Gel Deposition of Titanium Dioxide Films. 2007.
62. **Tiia Anmann.** Integrated and Organized Cellular Bioenergetic Systems in Heart and Brain. 2007.
63. **Katrin Trummal.** Purification, Characterization and Specificity Studies of Metalloproteinases from *Vipera lebetina* Snake Venom. 2007.
64. **Gennadi Lessin.** Biochemical Definition of Coastal Zone Using Numerical Modeling and Measurement Data. 2007.
65. **Enno Pais.** Inverse problems to determine non-homogeneous degenerate memory kernels in heat flow. 2007.
66. **Maria Borissova.** Capillary Electrophoresis on Alkylimidazolium Salts. 2007.
67. **Karin Valmsen.** Prostaglandin Synthesis in the Coral *Plexaura homomalla*: Control of Prostaglandin Stereochemistry at Carbon 15 by Cyclooxygenases. 2007.

68. **Kristjan Piirimäe**. Long-Term Changes of Nutrient Fluxes in the Drainage Basin of the Gulf of Finland – Application of the PolFlow Model. 2007.
69. **Tatjana Dedova**. Chemical Spray Pyrolysis Deposition of Zinc Sulfide Thin Films and Zinc Oxide Nanostructured Layers. 2007.
70. **Katrin Tomson**. Production of Labelled Recombinant Proteins in Fed-Batch Systems in *Escherichia coli*. 2007.
71. **Cecilia Sarmiento**. Suppressors of RNA Silencing in Plants. 2008.
72. **Vilja Mardla**. Inhibition of Platelet Aggregation with Combination of Antiplatelet Agents. 2008.
73. **Maie Bachmann**. Effect of Modulated Microwave Radiation on Human Resting Electroencephalographic Signal. 2008.
74. **Dan Hüvonen**. Terahertz Spectroscopy of Low-Dimensional Spin Systems. 2008.
75. **Ly Villo**. Stereoselective Chemoenzymatic Synthesis of Deoxy Sugar Esters Involving *Candida antarctica* Lipase B. 2008.
76. **Johan Anton**. Technology of Integrated Photoelasticity for Residual Stress Measurement in Glass Articles of Axisymmetric Shape. 2008.
77. **Olga Volobujeva**. SEM Study of Selenization of Different Thin Metallic Films. 2008.
78. **Artur Jõgi**. Synthesis of 4'-Substituted 2,3'-dideoxynucleoside Analogues. 2008.
79. **Mario Kadastik**. Doubly Charged Higgs Boson Decays and Implications on Neutrino Physics. 2008.
80. **Fernando Pérez-Caballero**. Carbon Aerogels from 5-Methylresorcinol-Formaldehyde Gels. 2008.
81. **Sirje Vaask**. The Comparability, Reproducibility and Validity of Estonian Food Consumption Surveys. 2008.
82. **Anna Menaker**. Electrosynthesized Conducting Polymers, Polypyrrole and Poly(3,4-ethylenedioxythiophene), for Molecular Imprinting. 2009.
83. **Lauri Ilison**. Solitons and Solitary Waves in Hierarchical Korteweg-de Vries Type Systems. 2009.
84. **Kaia Ernits**. Study of In₂S₃ and ZnS Thin Films Deposited by Ultrasonic Spray Pyrolysis and Chemical Deposition. 2009.
85. **Veljo Sinivee**. Portable Spectrometer for Ionizing Radiation "Gammamapper". 2009.
86. **Jüri Virkepu**. On Lagrange Formalism for Lie Theory and Operadic Harmonic Oscillator in Low Dimensions. 2009.
87. **Marko Piirsoo**. Deciphering Molecular Basis of Schwann Cell Development. 2009.
88. **Kati Helmja**. Determination of Phenolic Compounds and Their Antioxidative Capability in Plant Extracts. 2010.
89. **Merike Sõmera**. Sobemoviruses: Genomic Organization, Potential for Recombination and Necessity of P1 in Systemic Infection. 2010.

90. **Kristjan Laes.** Preparation and Impedance Spectroscopy of Hybrid Structures Based on CuIn₃Se₅ Photoabsorber. 2010.
91. **Kristin Lippur.** Asymmetric Synthesis of 2,2'-Bimorpholine and its 5,5'-Substituted Derivatives. 2010.
92. **Merike Luman.** Dialysis Dose and Nutrition Assessment by an Optical Method. 2010.
93. **Mihhail Berezovski.** Numerical Simulation of Wave Propagation in Heterogeneous and Microstructured Materials. 2010.
94. **Tamara Aid-Pavlidis.** Structure and Regulation of BDNF Gene. 2010.
95. **Olga Bragina.** The Role of Sonic Hedgehog Pathway in Neuro- and Tumorigenesis. 2010.
96. **Merle Randrüüt.** Wave Propagation in Microstructured Solids: Solitary and Periodic Waves. 2010.
97. **Marju Laars.** Asymmetric Organocatalytic Michael and Aldol Reactions Mediated by Cyclic Amines. 2010.
98. **Maarja Grossberg.** Optical Properties of Multinary Semiconductor Compounds for Photovoltaic Applications. 2010.
99. **Alla Maloverjan.** Vertebrate Homologues of Drosophila Fused Kinase and Their Role in Sonic Hedgehog Signalling Pathway. 2010.
100. **Priit Pruunsild.** Neuronal Activity-Dependent Transcription Factors and Regulation of Human *BDNF* Gene. 2010.
101. **Tatjana Knjazeva.** New Approaches in Capillary Electrophoresis for Separation and Study of Proteins. 2011.
102. **Atanas Katerski.** Chemical Composition of Sprayed Copper Indium Disulfide Films for Nanostructured Solar Cells. 2011.
103. **Kristi Timmo.** Formation of Properties of CuInSe₂ and Cu₂ZnSn(S,Se)₄ Monograin Powders Synthesized in Molten KI. 2011.
104. **Kert Tamm.** Wave Propagation and Interaction in Mindlin-Type Microstructured Solids: Numerical Simulation. 2011.
105. **Adrian Popp.** Ordovician Proetid Trilobites in Baltoscandia and Germany. 2011.
106. **Ove Pärn.** Sea Ice Deformation Events in the Gulf of Finland and This Impact on Shipping. 2011.
107. **Germo Väli.** Numerical Experiments on Matter Transport in the Baltic Sea. 2011.
108. **Andrus Seiman.** Point-of-Care Analyser Based on Capillary Electrophoresis. 2011.
109. **Olga Katargina.** Tick-Borne Pathogens Circulating in Estonia (Tick-Borne Encephalitis Virus, *Anaplasma phagocytophilum*, *Babesia* Species): Their Prevalence and Genetic Characterization. 2011.
110. **Ingrid Sumeri.** The Study of Probiotic Bacteria in Human Gastrointestinal Tract Simulator. 2011.
111. **Kairit Zovo.** Functional Characterization of Cellular Copper Proteome. 2011.

112. **Natalja Makarytsheva.** Analysis of Organic Species in Sediments and Soil by High Performance Separation Methods. 2011.
113. **Monika Mortimer.** Evaluation of the Biological Effects of Engineered Nanoparticles on Unicellular Pro- and Eukaryotic Organisms. 2011.
114. **Kersti Tepp.** Molecular System Bioenergetics of Cardiac Cells: Quantitative Analysis of Structure-Function Relationship. 2011.
115. **Anna-Liisa Peikolainen.** Organic Aerogels Based on 5-Methylresorcinol. 2011.
116. **Leeli Amon.** Palaeoecological Reconstruction of Late-Glacial Vegetation Dynamics in Eastern Baltic Area: A View Based on Plant Macrofossil Analysis. 2011.
117. **Tanel Peets.** Dispersion Analysis of Wave Motion in Microstructured Solids. 2011.
118. **Liina Kaupmees.** Selenization of Molybdenum as Contact Material in Solar Cells. 2011.
119. **Allan Olsper.** Properties of VPg and Coat Protein of Sobemoviruses. 2011.
120. **Kadri Koppel.** Food Category Appraisal Using Sensory Methods. 2011.
121. **Jelena Gorbatšova.** Development of Methods for CE Analysis of Plant Phenolics and Vitamins. 2011.
122. **Karin Viipsi.** Impact of EDTA and Humic Substances on the Removal of Cd and Zn from Aqueous Solutions by Apatite. 2012.
123. **David Schryer.** Metabolic Flux Analysis of Compartmentalized Systems Using Dynamic Isotopologue Modeling. 2012.
124. **Ardo Illaste.** Analysis of Molecular Movements in Cardiac Myocytes. 2012.
125. **Indrek Reile.** 3-Alkylcyclopentane-1,2-Diones in Asymmetric Oxidation and Alkylation Reactions. 2012.
126. **Tatjana Tamberg.** Some Classes of Finite 2-Groups and Their Endomorphism Semigroups. 2012.
127. **Taavi Liblik.** Variability of Thermohaline Structure in the Gulf of Finland in Summer. 2012.
128. **Priidik Lagemaa.** Operational Forecasting in Estonian Marine Waters. 2012.
129. **Andrei Errapart.** Photoelastic Tomography in Linear and Non-linear Approximation. 2012.
130. **Külliki Krabbi.** Biochemical Diagnosis of Classical Galactosemia and Mucopolysaccharidoses in Estonia. 2012.
131. **Kristel Kaseleht.** Identification of Aroma Compounds in Food using SPME-GC/MS and GC-Olfactometry. 2012.
132. **Kristel Kodar.** Immunoglobulin G Glycosylation Profiling in Patients with Gastric Cancer. 2012.
133. **Kai Rosin.** Solar Radiation and Wind as Agents of the Formation of the Radiation Regime in Water Bodies. 2012.

134. **Ann Tiiman.** Interactions of Alzheimer's Amyloid-Beta Peptides with Zn(II) and Cu(II) Ions. 2012.
135. **Olga Gavrilova.** Application and Elaboration of Accounting Approaches for Sustainable Development. 2012.
136. **Olesja Bondarenko.** Development of Bacterial Biosensors and Human Stem Cell-Based *In Vitro* Assays for the Toxicological Profiling of Synthetic Nanoparticles. 2012.
137. **Katri Muska.** Study of Composition and Thermal Treatments of Quaternary Compounds for Monograin Layer Solar Cells. 2012.
138. **Ranno Nahku.** Validation of Critical Factors for the Quantitative Characterization of Bacterial Physiology in Accelerostat Cultures. 2012.
139. **Petri-Jaan Lahtvee.** Quantitative Omics-level Analysis of Growth Rate Dependent Energy Metabolism in *Lactococcus lactis*. 2012.
140. **Kerti Orumets.** Molecular Mechanisms Controlling Intracellular Glutathione Levels in Baker's Yeast *Saccharomyces cerevisiae* and its Random Mutagenized Glutathione Over-Accumulating Isolate. 2012.
141. **Loreida Timberg.** Spice-Cured Sprats Ripening, Sensory Parameters Development, and Quality Indicators. 2012.
142. **Anna Mihhalevski.** Rye Sourdough Fermentation and Bread Stability. 2012.
143. **Liisa Arike.** Quantitative Proteomics of *Escherichia coli*: From Relative to Absolute Scale. 2012.
144. **Kairi Otto.** Deposition of In₂S₃ Thin Films by Chemical Spray Pyrolysis. 2012.
145. **Mari Sepp.** Functions of the Basic Helix-Loop-Helix Transcription Factor TCF4 in Health and Disease. 2012.
146. **Anna Suhhova.** Detection of the Effect of Weak Stressors on Human Resting Electroencephalographic Signal. 2012.
147. **Aram Kazarjan.** Development and Production of Extruded Food and Feed Products Containing Probiotic Microorganisms. 2012.
148. **Rivo Uiboupin.** Application of Remote Sensing Methods for the Investigation of Spatio-Temporal Variability of Sea Surface Temperature and Chlorophyll Fields in the Gulf of Finland. 2013.
149. **Tiina Kriščiunaite.** A Study of Milk Coagulability. 2013.
150. **Tuuli Levandi.** Comparative Study of Cereal Varieties by Analytical Separation Methods and Chemometrics. 2013.
151. **Natalja Kabanova.** Development of a Microcalorimetric Method for the Study of Fermentation Processes. 2013.
152. **Himani Khanduri.** Magnetic Properties of Functional Oxides. 2013.
153. **Julia Smirnova.** Investigation of Properties and Reaction Mechanisms of Redox-Active Proteins by ESI MS. 2013.
154. **Mervi Sepp.** Estimation of Diffusion Restrictions in Cardiomyocytes Using Kinetic Measurements. 2013.

155. **Kersti Jääger**. Differentiation and Heterogeneity of Mesenchymal Stem Cells. 2013.
156. **Victor Alari**. Multi-Scale Wind Wave Modeling in the Baltic Sea. 2013.
157. **Taavi Päll**. Studies of CD44 Hyaluronan Binding Domain as Novel Angiogenesis Inhibitor. 2013.
158. **Allan Niidu**. Synthesis of Cyclopentane and Tetrahydrofuran Derivatives. 2013.
159. **Julia Geller**. Detection and Genetic Characterization of *Borrelia* Species Circulating in Tick Population in Estonia. 2013.
160. **Irina Stulova**. The Effects of Milk Composition and Treatment on the Growth of Lactic Acid Bacteria. 2013.
161. **Jana Holmar**. Optical Method for Uric Acid Removal Assessment During Dialysis. 2013.
162. **Kerti Ausmees**. Synthesis of Heterobicyclo[3.2.0]heptane Derivatives *via* Multicomponent Cascade Reaction. 2013.
163. **Minna Varikmaa**. Structural and Functional Studies of Mitochondrial Respiration Regulation in Muscle Cells. 2013.
164. **Indrek Koppel**. Transcriptional Mechanisms of BDNF Gene Regulation. 2014.
165. **Kristjan Pilt**. Optical Pulse Wave Signal Analysis for Determination of Early Arterial Ageing in Diabetic Patients. 2014.
166. **Andres Anier**. Estimation of the Complexity of the Electroencephalogram for Brain Monitoring in Intensive Care. 2014.
167. **Toivo Kallaste**. Pyroclastic Sanidine in the Lower Palaeozoic Bentonites – A Tool for Regional Geological Correlations. 2014.
168. **Erki Kärber**. Properties of ZnO-nanorod/In₂S₃/CuInS₂ Solar Cell and the Constituent Layers Deposited by Chemical Spray Method. 2014.
169. **Julia Lehner**. Formation of Cu₂ZnSnS₄ and Cu₂ZnSnSe₄ by Chalcogenisation of Electrochemically Deposited Precursor Layers. 2014.
170. **Peep Pitk**. Protein- and Lipid-rich Solid Slaughterhouse Waste Anaerobic Co-digestion: Resource Analysis and Process Optimization. 2014.
171. **Kaspar Valgepea**. Absolute Quantitative Multi-omics Characterization of Specific Growth Rate-dependent Metabolism of *Escherichia coli*. 2014.
172. **Artur Noole**. Asymmetric Organocatalytic Synthesis of 3,3'-Disubstituted Oxindoles. 2014.
173. **Robert Tsanev**. Identification and Structure-Functional Characterisation of the Gene Transcriptional Repressor Domain of Human Gli Proteins. 2014.
174. **Dmitri Kartofelev**. Nonlinear Sound Generation Mechanisms in Musical Acoustic. 2014.
175. **Sigrid Hade**. GIS Applications in the Studies of the Palaeozoic Graptolite Argillite and Landscape Change. 2014.
176. **Agne Velthut-Meikas**. Ovarian Follicle as the Environment of Oocyte Maturation: The Role of Granulosa Cells and Follicular Fluid at Pre-Ovulatory Development. 2014.

177. **Kristel Hälvin**. Determination of B-group Vitamins in Food Using an LC-MS Stable Isotope Dilution Assay. 2014.
178. **Mailis Päri**. Characterization of the Oligoadenylate Synthetase Subgroup from Phylum Porifera. 2014.
179. **Jekaterina Kazantseva**. Alternative Splicing of *TAF4*: A Dynamic Switch between Distinct Cell Functions. 2014.
180. **Jaanus Suurväli**. Regulator of G Protein Signalling 16 (RGS16): Functions in Immunity and Genomic Location in an Ancient MHC-Related Evolutionarily Conserved Synteny Group. 2014.
181. **Ene Viiard**. Diversity and Stability of Lactic Acid Bacteria During Rye Sourdough Propagation. 2014.
182. **Kristella Hansen**. Prostaglandin Synthesis in Marine Arthropods and Red Algae. 2014.
183. **Helike Lõhelaid**. Allene Oxide Synthase-lipoxygenase Pathway in Coral Stress Response. 2015.
184. **Normunds Stivrīnš**. Postglacial Environmental Conditions, Vegetation Succession and Human Impact in Latvia. 2015.
185. **Mary-Liis Kütt**. Identification and Characterization of Bioactive Peptides with Antimicrobial and Immunoregulating Properties Derived from Bovine Colostrum and Milk. 2015.
186. **Kazbulat Šogenov**. Petrophysical Models of the CO₂ Plume at Prospective Storage Sites in the Baltic Basin. 2015.
187. **Taavi Raadik**. Application of Modulation Spectroscopy Methods in Photovoltaic Materials Research. 2015.
188. **Reio Põder**. Study of Oxygen Vacancy Dynamics in Sc-doped Ceria with NMR Techniques. 2015.
189. **Sven Siir**. Internal Geochemical Stratification of Bentonites (Altered Volcanic Ash Beds) and its Interpretation. 2015.
190. **Kaur Jaanson**. Novel Transgenic Models Based on Bacterial Artificial Chromosomes for Studying BDNF Gene Regulation. 2015.
191. **Niina Karro**. Analysis of ADP Compartmentation in Cardiomyocytes and Its Role in Protection Against Mitochondrial Permeability Transition Pore Opening. 2015.
192. **Piret Laht**. B-plexins Regulate the Maturation of Neurons Through Microtubule Dynamics. 2015.
193. **Sergei Žari**. Organocatalytic Asymmetric Addition to Unsaturated 1,4-Dicarbonyl Compounds. 2015.
194. **Natalja Buhhalko**. Processes Influencing the Spatio-temporal Dynamics of Nutrients and Phytoplankton in Summer in the Gulf of Finland, Baltic Sea. 2015.
195. **Natalia Maticiu**. Mechanism of Changes in the Properties of Chemically Deposited CdS Thin Films Induced by Thermal Annealing. 2015.
196. **Mario Öeren**. Computational Study of Cyclohexylhemicucurbiturils. 2015.
197. **Mari Kalda**. Mechanoenergetics of a Single Cardiomyocyte. 2015.

198. **Ieva Grudzinska.** Diatom Stratigraphy and Relative Sea Level Changes of the Eastern Baltic Sea over the Holocene. 2015.
199. **Anna Kazantseva.** Alternative Splicing in Health and Disease. 2015.
200. **Jana Kazarjan.** Investigation of Endogenous Antioxidants and Their Synthetic Analogues by Capillary Electrophoresis. 2016.
201. **Maria Safonova.** SnS Thin Films Deposition by Chemical Solution Method and Characterization. 2016.
202. **Jekaterina Mazina.** Detection of Psycho- and Bioactive Drugs in Different Sample Matrices by Fluorescence Spectroscopy and Capillary Electrophoresis. 2016.
203. **Karin Rosenstein.** Genes Regulated by Estrogen and Progesterone in Human Endometrium. 2016.
204. **Aleksei Tretjakov.** A Macromolecular Imprinting Approach to Design Synthetic Receptors for Label-Free Biosensing Applications. 2016.
205. **Mati Danilson.** Temperature Dependent Electrical Properties of Kesterite Monograin Layer Solar Cells. 2016.
206. **Kaspar Kevvai.** Applications of ¹⁵N-labeled Yeast Hydrolysates in Metabolic Studies of *Lactococcus lactis* and *Saccharomyces Cerevisiae*. 2016.
207. **Kadri Aller.** Development and Applications of Chemically Defined Media for Lactic Acid Bacteria. 2016.
208. **Gert Preegel.** Cyclopentane-1,2-dione and Cyclopent-2-en-1-one in Asymmetric Organocatalytic Reactions. 2016.
209. **Jekaterina Služenikina.** Applications of Marine Scatterometer Winds and Quality Aspects of their Assimilation into Numerical Weather Prediction Model HIRLAM. 2016.
210. **Erkki Kask.** Study of Kesterite Solar Cell Absorbers by Capacitance Spectroscopy Methods. 2016.
211. **Jürgen Arund.** Major Chromophores and Fluorophores in the Spent Dialysate as Cornerstones for Optical Monitoring of Kidney Replacement Therapy. 2016.
212. **Andrei Šamarin.** Hybrid PET/MR Imaging of Bone Metabolism and Morphology. 2016.
213. **Kairi Kasemets.** Inverse Problems for Parabolic Integro-Differential Equations with Instant and Integral Conditions. 2016.
214. **Edith Soosaar.** An Evolution of Freshwater Bulge in Laboratory Scale Experiments and Natural Conditions. 2016.
215. **Peeter Laas.** Spatiotemporal Niche-Partitioning of Bacterioplankton Community across Environmental Gradients in the Baltic Sea. 2016.
216. **Margus Voolma.** Geochemistry of Organic-Rich Metalliferous Oil Shale/Black Shale of Jordan and Estonia. 2016.
217. **Karin Ojamäe.** The Ecology and Photobiology of Mixotrophic Alveolates in the Baltic Sea. 2016.
218. **Anne Pink.** The Role of CD44 in the Control of Endothelial Cell Proliferation and Angiogenesis. 2016.

219. **Kristiina Kreek.** Metal-Doped Aerogels Based on Resorcinol Derivatives. 2016.
220. **Kaia Kukk.** Expression of Human Prostaglandin H Synthases in the Yeast *Pichia pastoris*. 2016.
221. **Martin Laasmaa.** Revealing Aspects of Cardiac Function from Fluorescence and Electrophysiological Recordings. 2016.
222. **Eeva-Gerda Kobrin.** Development of Point of Care Applications for Capillary Electrophoresis. 2016.
223. **Villu Kikas.** Physical Processes Controlling the Surface Layer Dynamics in the Stratified Gulf of Finland: An Application of Ferrybox Technology. 2016.
224. **Maris Skudra.** Features of Thermohaline Structure and Circulation in the Gulf of Riga. 2017.
225. **Sirje Sildever.** Influence of Physical-Chemical Factors on Community and Populations of the Baltic Sea Spring Bloom Microalgae. 2017.
226. **Nicolae Spalatu.** Development of CdTe Absorber Layer for Thin-Film Solar Cells. 2017.
227. **Kristi Luberg.** Human Tropomyosin-Related Kinase A and B: from Transcript Diversity to Novel Inhibitors. 2017.
228. **Andrus Kaldma.** Metabolic Remodeling of Human Colorectal Cancer: Alterations in Energy Fluxes. 2017.
229. **Irina Osadchuk.** Structures and Catalytic Properties of Titanium and Iridium Based Complexes. 2017.
230. **Roman Borožnjak.** A Computational Approach for Rational Monomer Selection in Molecularly Imprinted Polymer Synthesis. 2017.
231. **Sten Erm.** Use of Mother-Daughter Multi-Bioreactor Systems for Studies of Steady State Microbial Growth Space. 2017.
232. **Merike Kriisa.** Study of ZnO:In, Zn(O,S) and Sb₂S₃ Thin Films Deposited by Aerosol Methods. 2017.
233. **Marianna Surženko.** Selection of Functional Starter Bacteria for Type I Sourdough Process. 2017.
234. **Nkwusi God'swill Chimezie.** Formation and Growth of Cu₂ZnSnS₄ Monograin Powder in Molten CdI₂. 2017.